STRAIN RATE EFFECT ON HIGH PERFORMANCE FIBER REINFORCED CEMENTITIOUS COMPOSITES USING SLIP HARDENING HIGH STRENGTH DEFORMED STEEL FIBERS

by

Dong joo Kim

A dissertation submitted in partial fulfillment
of the requirements for the degree of
Doctor of Philosophy
(Civil Engineering)
in The University of Michigan
2009

Doctoral Committee:

Professor Sherif El-Tawil, Co-Chair
Emeritus Professor Antoine E. Naaman, Co-Chair
Professor Anthony M. Waas
Associate Professor Gustavo J. Parra-Montesinos

DEDICATION

To My family

ACKNOWLEDGMENTS

The author wish to express his profound gratitude and sincere appreciation to Professors Antoine E. Naaman and Sherif El-Tawil, co-chairs of my doctoral thesis committee, for invaluable suggestions, guidance, and tremendous support throughout my doctoral studies. The author sincerely has enjoyed his research with them.

The author also appreciates the committee members of his doctoral dissertation, Profs. Gustavo J. Parra-Montesinos and Anthony M. Waas, for reviewing his thesis, giving valuable comments, and supporting test materials and equipments.

Special thanks are due to his colleagues, including Kittinun Sirijaroonchai, Shih-Ho Chao, Supat Suwwanakarn, Kapil Khandelwal, Chung-Chan Hung and Phillip Park, for their friendship and help.

The author also would like to express his special thanks to lab technician Robert Fischer, Robert Spence and Jan Pantolin for fabricating the test set-up, specimen molds and repairing the fiber producing machine.

Finally, the author sincerely appreciates his family who encouraged and supported him continuously. The author dedicates this work to his wife and daughter.

TABLE OF CONTENTS

LIST OF FIGURES

LIST OF TABLES

ABSTRACT

The objective of this research is to develop an understanding of the high strain rate response of High Performance Fiber Reinforced Cementitious Composites (HPFRCC). The research is divided into four parts. In the first, HPFRCC with high tensile strength (>10MPa) and ductility (>0.5%) is developed by using slip hardening fibers within a high strength mortar. Two types of fibers, twisted and hooked, are used in volume fractions ranging from 1 to 2%. The large slip capacity of twisted fibers during pullout generates large pullout energy (large equivalent bond strength), and thus leads to high strain capacity composites with multiple micro-cracks. In the second part, experiments are performed to investigate the effect of strain rate on fiber pullout and composite response. The rate sensitivity of HPFRCC in tension depends on fiber type, volume fraction and matrix strength (or composition). As the strain rate increases, HPFRCC with twisted fibers exhibits a pronounced, beneficial strain rate effect, i.e. a higher tensile strength is achieved with no reduction in strain capacity. In contrast, HPFRCC with hooked fiber show no clear strain rate effect. In the third part of this work, a new impact test system that employs suddenly released elastic strain energy is developed to enable impact testing for cementitious composites with large-sized specimen. A prototype system that was simulated and built is only 1.5m in height and can generate a high rate impact pulse. Compared to current impact test system, the new setup is inexpensive, small, portable, safe and easy to operate. Finally, the source of strength enhancement for cement-based

materials under high rate compressive loadings was investigated through computational simulation models. The observed strain rate effect or mortar under compression is primarily, but not totally, due to lateral inertial effects under high rate loading and the pressure dependent nature of cementitious materials. The test and simulation results show that it is possible to develop a high performance cementitious composite with 1% to 2% volume fraction of fibers that has high energy absorption capacity and that can therefore be used to mitigate the effect of extreme loading such as earthquakes, impact, and blast.

CHAPTER I

INTRODUCTION

1.1 GENERAL

Recent disasters around the world have heightened the interest in improving the resistance of structures subjected to seismic, impact and blast load conditions. High Performance Fiber Reinforced Cementitious Composites (HPFRCC) have the potential to be a viable solution for improving the resistance of buildings and other infrastructure components because of their high ductility, durability and energy absorption capacity compared with normal concrete and/or Fiber Reinforced Concrete (FRC). As suggested by Naaman and Reinhardt (1996), the term "high performance" implies an optimized combination of HPFRCC properties, such as quasi strain hardening behavior, small crack width, as well as improved strength, toughness, energy absorption, stiffness, durability, and corrosion resistance, as shown in Fig. 1.1. When concrete, mortar or FRC are subjected to tension, they eventually crack and quickly lose all ability to transfer tensile stresses across the crack. In contrast, HPFRCC materials exhibit multiple cracking after first cracking along with hardening behavior, i.e., the strength continues to increase after first cracking. In other words, the maximum post-cracking strength σ_{pc} is higher than

the first cracking strength σ_{cc}.

$$\sigma_{pc} \geq \sigma_{cc} \quad [1.1]$$

The ability of HPFRCC to strain harden is highly dependent on the matrix, fiber type and the bond properties at the interface between the matrix and fibers. Many researchers have successfully achieved strain-hardening behavior through various tailoring techniques that involved control of fiber, matrix and bond properties.

The promising superior performance of HPFRCC is based on its observed static mechanical properties; however, there has been little research to characterize completely the behavior of HPFRCC under higher strain rates. Since the behavior of fiber, matrix and the bond at the interface between them is likely dependent upon the rate of loading, it is expected that the response of HPFRCC is also rate dependent. Therefore, there is an urgent need to develop a better understanding of strain rate effects on HPFRCC. This is necessary information in order to successfully utilize HPFRCC in structures subjected to dynamic loading conditions.

An impact test method is needed to investigate the response of HPFRCC under high strain rates. A number of techniques are currently available for exploring material behavior under high strain rate loading. Commonly used methods can be classified into three main types, according to the way by which the load is generated, as shown in Fig. 1.2.

1) Method based on Potential energy, e.g. Charpy pendulum method, Izod test and Drop-weight impact tests. In these methods, a moving weight is used to generate the impact. Various strain rates can be achieved in the drop weight method by changing the drop height of the weight. The Charpy and Izod methods cannot generate a stress-strain

curve because displacement is not measured. The drop weight method does not typically generate high strain rates (i.e., $\dot{\varepsilon}_{max} \approx 1 \sim 5/sec$). (Fig. 1.2a)

2) Methods based on Kinetic energy, e.g. Hopkinson-Bar technique, Gas gun impact test. These methods can generate high strain rates (i.e., $\dot{\varepsilon}_{max} \approx 100 \sim 1000/sec$). However, they are expensive, dangerous to operate, and utilize large-size test set-ups. (Fig. 1.2b)

3) Methods based on Hydraulic pressure, e.g. hydraulic impact test machine. These machines can precisely measure material properties at strain rates that represent seismic loading condition (i.e., $\dot{\varepsilon} = 0.1/sec$) and can generate higher strain rate with more expensive machines. However, they cannot be conveniently used to investigate the effect of higher strain rates due to their limited load capacity and high cost. (Fig. 1.2c)

Although existing high rate test methods have been used extensively in the past, there is a need to develop new techniques that overcome the various draw backs mentioned above. Given the limitations of existing high rate of loading methods, a new test set-up was developed in this work. Unlike any of the previously classified methods, the developed system can generate impact load through the sudden release of stored elastic strain energy. The primary advantages of the new setup are that it is small, portable and inexpensive to build. (Fig. 1.2d)

1.2 RESEARCH SIGNIFICANCE

Although HPFRCC is an effective solution for improving ductility, durability and load carrying capacity of buildings and other infrastructure components under static load condition, its performance under dynamic loading is not yet well understood. In

particular, it is not clear if HPFRCC will maintain their strain hardening behavior at higher strain rates. This research provides much needed information about this topic.

The developed impact test system, term here on, Strain Energy Impact Test System [SEITS], creates a new category of impact test systems that overcome the combined limitations of the existing test systems.

1.3 LITERATURE REVIEW AND BACKGROUND

A general literature review is provided in this Chapter. Detailed research background information is provided in each Chapter.

1.3.1 Strain rate effect on mortar and concrete

In general, the dynamic strength of concrete in both compression and tension is relatively insensitive under the transition strain rates, i.e., critical strain rate. Ross et al. (1996) reported that these transition strain rates are between 1~10 /sec for tension and 60~80 /sec for compression as shown in Fig 1.3. After the transition strain rates there are large dynamic strength increases.

Many researchers have reported the effect of strain rate on mortar and concrete. Ross et al. (1989) demonstrated that the tensile strength of mortar at strain rates of 10 to 100 /sec is approximately 1.5 to 3 times that of the tensile strength at quasi-static strain rates, however, the tensile strength of concrete tested at these same strain rates is 4 to 6 times the tensile strength at quasi-static strain rates. Tedesco and Ross (1993) reported that the tensile strength of concrete appears to show significant strain rate effects at strain rates of 1.0 /sec and beyond, the concrete tensile strength is proportional to strain rate to the one-third power($\dot{\varepsilon}^{1/3}$). Ross (1995) reported that the critical strain rate in concrete is

approximately 5 /sec for tension and is approximately 60 /sec for compression. It was also reported that the tensile behavior of concrete under high strain rate is more sensitive than that for compressive behavior. Ross (1996) also investigated the moisture and strain rate effect on concrete strength. He found that wet concrete experiences appreciable increases in strength at all strain rates both below and above transition region for the dry concrete. He suggested that the static strength decreases in wet concrete as compared to dry concrete because the presence of moisture forcing the gel particles apart and reducing the van der waals forces.

Nemat-Nasser and Deng (1994) explained the effect of strain rate on the compressive strength of concrete by using the wing crack model, which is based on fracture mechanics. It was shown that the experimentally observed change in the compressive failure stress with increasing strain rate might be a consequence of the generation and dynamic growth of interacting between micro-cracks, compression-induced tensile micro cracks. They used the Split Hopkinson Pressure Bar in their tests.

Strain rate effects on other material properties of concrete in addition to compressive strength were investigated by Bischoff and Perry (1991, 1995). They carried out static loading ($\dot{\varepsilon} = 6.6 \sim 7.2 \times 10^{-6} / \sec$) in a hydraulic test machine, and used drop hammer testing for impact loading ($\dot{\varepsilon} = 5.2 \sim 9.0 / \sec$). Based on their tests, they reported the effect of strain rate on compressive strength, axial strain at maximum strength, volumetric strain, energy absorption capacity, and modulus. The compressive strength increased by 50~60% during impact loading and axial strain at maximum strength was observed to increase between 14% and 36%. The maximum volumetric strain increased 11 to 36% and energy absorption capacity at failure showed an increase between 64% and

118% at high strain rate. However, it was reported that the initial elastic modulus is not strain rate sensitive.

Dynamic Increase Factors (DIF) for concrete was reported by Malvar and Crawford (1998). They reported that the DIF can be more than 2 in compression and more than 6 in tension for very high strain rates ($\dot{\varepsilon} = 1000/\sec$). They also confirmed that the DIF is a bilinear function of the strain rate in a log-log plot.

Klepaczko (2003) provided an overall review of experimental test results about high strain rate effect on concrete. He reported that the highest rate sensitivity is found in tension and the smallest in compression and the rate sensitivity in the shear mode is closer to the tension case.

1.3.2 Single fiber pullout behavior under high speed loading

Gokoz and Naaman (1981) investigated the effect of strain rate on the pullout behavior of fibers in mortar. They carried out fiber pullout test in static ($v = 4.2 \times 10^{-3} cm/\sec$) and high loading speed ($v = 300 cm/\sec$) for three types of fibers (smooth steel, glass and polypropylene). They developed a special experimental procedure that allowed them to pull out a group of fibers simultaneously as shown in Fig. 1.4.

They concluded that glass fibers generally failed at all loading velocities and steel fibers generally maintained fiber pullout mode at all loading velocities. However, PP showed a mixed behavior strongly dependent on the loading velocity. They concluded that PP fibers are very sensitive to the loading velocity, but steel fibers are in sensitive to the loading velocity. They also reported that post peak response of steel fibers, which is representative of frictional effects, is almost insensitive to loading velocity, i.e., friction

between fiber and matrix is insensitive to the loading velocity. It should be noted that the steel fibers used were smooth steel fibers.

Banthia and Trottier (1991) investigated pull out resistance of deformed steel fibers embedded in cement based matrices. Static ($v = 8.46 \times 10^{-4} cm/\sec$) pullout test was performed by using an Instron test machine and dynamic ($v = 150 cm/\sec$) pullout response was investigated by using a Charpy type pendulum impact tester. It was found that the deformed steel fibers embedded in cementitious matrices in general support a higher load under impact than under static pullout and that the pullout energy is also greater under impact provided the fiber failure mode is maintained from static to impact loading as shown in Fig 1.5.

Yang and Li (2005) examined the rate dependence in engineered cementitious composites. PVA fibers were used in single fiber pullout tests, which revealed strong rate dependency of PVA fiber pullout behavior. The pullout speed ranged between $v = 10^{-4} cm/\sec$ and $v = 1 cm/\sec$. It was reported that a strong rate dependency in chemical bond strength, G_d, is evident at the highest pullout speed and that G_d could be 5 times higher than the static values as shown in Fig. 1.6.

1.3.3 Strain rate effect on FRC response

It is well known that fiber reinforcement in mortar and concrete increases matrix toughness and energy dissipation. Therefore, there is consensus that the use of fiber reinforced concrete increases impact resistance under dynamic and impact loading conditions. Many researches have investigated strain rate effects in FRC as discussed next.

Naaman and Gopalaratnam (1983) investigated the impact properties of steel fiber

reinforced concrete in bending as shown in Fig. 1.7 and 1.8. Three-point bending test were conducted at four different rates of loading. The loading velocities were $4.23\times10^{-3} cm/\sec$, $0.826 cm/\sec$, $70 cm/\sec$, and $100 cm/\sec$. Tests at the higher two velocities were performed using the Dynatup drop-weight tower. In their test, for both the static and dynamic tests, identical specimens were used in similar loading and support conditions to avoid size effect. Based on their experimental test results, they concluded that the higher the volume fraction of fibers and the higher their aspect ratio as shown in Fig 1.7, the more sensitive is the composite to the rate of loading. They also noted that composites made from weaker matrices exhibit a higher sensitivity to loading rate than those made with stronger matrices as shown in Fig. 1.8.

Rostasy and Hartwich (1985) conducted compressive tests to investigate the influence of high strain rates on the strength and deformation of fiber reinforced concrete. It was found that dynamic strength ($\dot{\varepsilon}_{dyn} \Big/ \dot{\varepsilon}_{stat} \approx 10^4$) is about 20 % higher than the static strength, and the dynamic ultimate strain increases by 10 to 20 % over the static as shown in Fig. 1.9.

Nammur and Naaman (1986) reported strain rate effects on the tensile properties of fiber reinforced concrete. They observed that the pre-cracking strength of fiber reinforced concrete as well as the strain at peak stress both increase with increasing strain rates and the post-cracking strength of fiber reinforced concrete also increases with strain rate. However, they also observed that the displacement at failure decreases with increasing strain rates.

Kormeling and Reinhardt (1987) used the split Hopkinson Pressure Bar method to investigate high strain rate effects on steel fiber concrete in uniaxial tension. Three testing

strain rates were used: $\dot{\varepsilon} = 1.25 \times 10^{-6} / \sec$, $\dot{\varepsilon} = 2.5 \times 10^{-3} / \sec$ and $\dot{\varepsilon} = 1.5 - 20 / \sec$. There was a significant increase of tensile strength of plain and steel fiber concrete due to high strain rates. The fracture energy and strain at maximum stress also increased at higher strain rates.

Banthia et al. (1993) reported that the fiber reinforced cement based composites were found to be stronger and tougher under impact and that the improvements were more pronounced at higher fiber volume fractions. They used a modified charpy pendulum machine to perform high strain rate testing with three types of fibers (Carbon, Steel and Polypropylene). In related research, Banthia et al. (1996) concluded that fiber reinforcement is indeed effective in improving fracture energy absorption under impact; however, the improvement is dependent on the type and geometry of fiber and is not as pronounced as observed under static conditions. Fiber types used in that experimental test program are hooked-end, crimped and twin cone steel fibers.

Lok and Zhao (2004) conducted compressive tests to investigate the impact response of steel fiber reinforced concrete using a Split Hopkinson Pressure Bar (SHPB). Steel Fiber Reinforced Concrete(SFRC) specimens were tested at strain rate between about 20 and 100 /sec produced by impact from two specially designed striker bars on the SHRP facility ; different impact load durations were produced using these striker bars. It was found that post peak ductility of SFRC is clearly absent at strain rates exceeding 50 /sec because matrix fragments can no longer bond onto the steel fibers.

Wei et al. (2005) studied the dynamic uniaxial compressive responses of Steel Fiber Reinforced High Strength Concrete (SFRHSC) and Steel Fiber Reinforced Ultra-High Strength Concrete (SFRUHSC) subjected to high velocity impact loading. They achieved

strain rates of about 10 /sec to 100 /sec in a 74mm diameter SHPB. It was indicated that SFRHSC and SFRUHSC had obvious strain sensitive behavior and that the SFRHSC and SFRUHSC exhibited relatively good ductility at high strain rate. It should be noticed that the critical strain rate ($\dot{\varepsilon}_{cr} = 41 \sim 50/s$) is similar to the result from Lok and Zhao (2004).

1.3.4 Strain rate effect on HPFRCC

Yang and Li (2005) reported a strong rate dependence in engineered cementitious composite (PVA-ECC), a subclass of HPFRCC. They performed a uniaxial tensile test with different strain rate ($\dot{\varepsilon} = 10^{-5} \sim 10^{-1}/s$) to investigate the rate dependency in PVA-ECC by using hydraulic test machine. The tensile stress-strain curves of PVA-ECC as a function of strain rate are shown in Fig 1.10.

Douglas and Billington (2005) also examined rate dependence in high-performance fiber reinforced cement-based composites for seismic application. Cylindrical specimens of PVA-ECC were subjected to monotonic compression, monotonic tension, and reversed-cyclic tension and compression at varying strain rates. It was reported that while tensile strength increases with strain rate, the ductility decreases under seismic loading rate. In addition, tensile strength is increased by 12% and the modulus of elasticity is increased by 22%.

In contrast to the findings of Yang and Li (2005), and Douglas and Billington (2005), Maalej et al (2005) reported that the tensile strain capacity in their tests was insensitive to strain rate. They conducted tests on a hybrid-fiber ECC (1.5 volume percentage and polyethylene and 0.5 volume percentage steel fibers). However, they noted that the tensile strength increased remarkably with increasing strain rate.

1.3.5 Current impact test techniques

Cantwell and Mortan (1991) divided impact test techniques into two types: low velocity impact by a large mass and high velocity impact by a small mass. Examples of the former method include the Charpy pendulum method, Izod test and Drop-weight impact test, while examples of the latter include the gas-gun impact test and the Hopkinson-bar technique. Another classification is possible based on the means by which impact load is generated : methods based on potential energy (e.g. izod, charpy, drop weight), based on kinetic energy (e.g. SHPB & gas gun), based on hydraulic pressure, and based on elastic strain energy stored in an energy bar (as proposed in Chapter VII).

The Charpy impact test method was originally designed for testing metals and this system is mainly used for estimating energy absorption capacity and toughness. The amount of energy absorption during impact can be estimated by using the force-time recorded history. The test specimen is usually a thick beam with a notch, therefore, it is difficult to define strain rate and to obtain a meaningful stress-strain relationship. The Izod impact test method also has the same disadvantages as the Charpy impact test.

The drop weight setup utilizes potential energy of a weight dropped from a pre-determined height to create impact. This test method can have a wide range of test geometries and unlike the Charpy & Izod tests; it can be used to obtain force-deformation history. This method does require a considerable height in order to have enough potential energy to cause complete failure of the test specimen, but this, of course, is a function of the specimen geometry and material properties. The maximum strain rate achieved by this method is around $\dot{\varepsilon} = 1 - 5/\sec$.

One of the most popular impact test methods for high velocity impact is the Split

Hopkinson Pressure Bar (SHPB). In 1872, Hopkinson proposed this method to investigate the effect of strain rate effect on the compressive behavior of metals. This system consists of two long elastic bars holding a short cylindrical specimen between them by friction. When a striker bar projected by a gas gun hits the incident bar, a compressive stress wave is generated and transferred into the specimen. When the compressive stress wave arrives at the interface between the incident bar and the specimen, a reflection stress wave is generated, which reflects back toward the impact end. The remainder of the stress wave is transferred into the specimen and the transmitter bar. Both stress and strain history of the specimen and strain rate are determined based on the strain history of strain gages attached to the two split pressure bars. Detailed information on how the stress and strain history of the specimen can be computed is given in Chapter VIII.

In the past 140 years, there have been many modifications and adaptations of the Hopkinson pressure bar system to make it suitable for other loading conditions and materials. Nemat Nasser et al. (1991) introduced novel techniques to render the classical Split Hopkinson Bar suitable for dynamic recovery experiments. Staab and Gilat (1990) introduced a direct tensile Split Hopkinson Bar apparatus by using strain energy stored in the pressure bar. Ross et al. (1995) used a large diameter (51mm) split hopkinson pressure bar to investigate the effect of strain rate on the tensile and compressive properties of plain concrete specimens. Lok et al. (2002) proposed a new loading method to eliminate oscillation while maintaining uniform deformation of the specimen to overcome problems associated with a large diameter bar. They reduced the pressure bar length by using specially designed strikers. Recently, Brara and Klepaczko (2004)

introduced a new experimental technique based on the Hopkinson Pressure Bar by using only one pressure bar as shown in Fig 1.13. The maximum strain rate in the new experimental set up which was equipped with six high frequency and high resolution charged coupled device cameras is 100 /sec.

Although the Split Hopkinson Pressure Bar is a popular test system, many researchers have chosen low velocity impact by a large mass because of the size restriction imposed by minimum specimen size, i.e., the greater the diameter of the specimen, the longer the bar. Radomski (1981) investigated the properties of FRC materials by application of the rotating impact machine. The main limitation in rotating impact test system was that that system was originally designed for small metal specimen. Therefore, the specimen size was not enough to represent the material properties. Bischoff and Perry (1995) used the drop hammer test rig to investigate the strain rate effect in concrete and they could reach a strain rate of 5~9 /sec. Banthia et al. (1996) introduced a simple impact machine by modifying the pendulum method. He used the rotational drop weight method to conduct impact tests on concrete in uniaxial tension. In this test system, he could obtain load-time response, but could not extract the load-displacement response.

One of the hurdles to test HPFRCC under high strain rate is that there are no standardized test techniques for it (Banthia, 2005). Another complication is that the specimen must be of sufficient size to represent the distribution of fiber in HPFRCC. Moreover, the strain rate is dependant upon not only loading rate but also on specimen gage length.

1.4 OBJECTIVES AND TASKS

The overall goal of this research is to improve the robustness, toughness, and

durability of civil infrastructure under various extreme loads such as earthquakes, impacts and blasts through the development and application of HPFRCC. There are four major objectives and related tasks as outlined next and shown in Fig 1.12.

Objective 1: To develop High Performance Fiber Reinforced Cementitious Composites with high strength and ductility using minimal fiber volume fraction.

The high cost of HPFRCC has been a critical obstacle in their widespread commercial application. Each 1% of steel fibers by volume usually cost more than the entire cement matrix. Therefore, it is necessary to minimize the fiber volume contents to encourage wide spread adoption of this new material. In this dissertation, slip hardening fibers are employed to achieve strain hardening behavior of HPFRCC under tension with a small amount of fibers, typically less than 2% by volume. The specific tasks necessary to achieve this objective are: to investigate correlation between fiber pullout behavior and tensile response of Fiber Reinforced Cementitious Composites [FRCC] (Chapter II); to develop tensile strain hardening FRC composite with high tensile strength and high ductility using less than 2% fiber volume fraction (Chapter III); and, to compare the performance of different fibers in identical matrices under flexural load (Chapter IV).

Objective 2: To investigate strain rate effect on the behavior of High Performance Fiber Reinforced Cementitious Composites [HPFRCC]

There is currently little information on the behavior of HPFRCC under various strain rates, i.e., strain rate effect on the behavior of HPFRCC. It is therefore necessary to develop new information on the influence of strain rate on HPFRCC response.

The specific tasks required to achieve this objective are: to investigate the loading rate effect on pullout behavior of two deformed steel fibers (Chapter V); and, to

investigate rate-dependent tensile behavior of HPFRCC according to the types of fiber, matrix compositions and fiber volume contents (Chapter VI).

Objective 3: To develop a new impact test system using elastic strain energy

Current popular impact test methods, e.g., Drop Weight and Split Hopkinson Pressure Bar, are expensive and also require large lab space, which has limited their widespread applicability. The objective of this part in the dissertation is to develop a new test setup that overcomes the limitations of traditional test techniques. (Chapter VII)

Objective 4: To investigate the source of dynamic strength enhancement in mortar subjected to rapid compressive loading

There is a common belief that high strain rate causes cement-based materials, such as concrete and mortar, to become stronger in compression. However, there appears to be a lack of agreement in the literature about the source of the rate effect. The objective of this part of the work is to obtain a better understanding of the source of dynamic strength enhancement in cement-based materials. (Chapter VIII)

1.5 STRUCTURE OF THE DISSERTATION

This dissertation contains four main parts, as shown in Fig. 1.12, corresponding to the four main objectives outlined in the previous section: Part 1 is composed of three chapters (II, III, and IV); Part 2 is composed of two chapters (V and VI); and, Part 3 and Part 4 are composed of Chapter VII and VIII, respectively. The dissertation is therefore divided into nine chapters. Each chapter is prepared as a conference or journal paper, therefore, there are common figures appearing in several chapters. The main focus of each chapter described below.

Chapter I. Introduction

This chapter consists of a brief overview of the contents of this thesis, as well as the objectives and significance of this research.

Chapter II. Correlation between fiber pullout and tensile response of FRCC

This chapter investigates the influence of single fiber pullout behavior on the tensile response of FRCC. Two slip hardening fibers, Hooked (H-) and Twisted (T-) fiber, with completely different pullout mechanisms are investigated to understand the influence of the pullout mechanism on pullout energy, equivalent bond strength, and resulting tensile response of FRCC.

Chapter III. High tensile strength strain-hardening FRC Composites with less than 2% fiber content

By utilizing the information developed in Chapter II, high tensile strength strain-hardening FRC Composites, with more than 10 MPa tensile strength and 0.5% strain capacity, are developed by using 2% T- fiber by volume in high strength mortar (84 MPa). The performance of H- and T- fibers in high strength matrix are compared in this chapter.

Chapter IV. Comparative flexural behavior of four FRC Composites

This chapter compares the flexural performance of four different types of fiber (T-, H-, SPECTRA, and PVA fiber) within identical matrices. Two fiber volume contents are used: 0.4% and 1.2%. The influence of fibers on load carrying capacity, energy absorption capacity, and ductility are evaluated.

Chapter V. Loading rate effect on pullout behavior of deformed steel fibers

This chapter investigates the loading rate effect on single fiber pullout behavior and provides a basis to better understand the effect of strain rate on the tensile properties of fiber reinforced cement composites. Based on the results of previous Chapters (II, III, and

IV), two types of high strength deformed steel fibers (H- and T- fibers) known to have slip hardening behavior under static pullout loading are selected. The pullout behavior of those fibers is investigated under four different loading rates ranging from static to seismic by using a hydraulic testing machine.

Chapter VI. Rate-dependent tensile behavior of High Performance Fiber Reinforced Cementitious Composites

This chapter investigates the strain rate effect on the response of HPFRCC at the composites level while chapter V shows the influence of loading rate on fiber pullout behavior. Two high strength deformed steel fibers (H- and T- fibers), three matrices (low, medium, and high strength mortar), and two fiber volume contents (1% and 2%) are the parameters used in this investigation. Four strain rates ranging from static to seismic are applied by using a hydraulic machine. Here the term "seismic loading rate" refers only to the magnitude of the rate, but no consideration is given to cyclic or reversal loading condition. The effect of fibers, matrices, and fiber volume contents on the strain rate sensitivity of HPFRCC is investigated.

Chapter VII. New impact test system using elastic strain energy

An innovative device that is inexpensive, safe and accurate is proposed here for high strain rate testing. The developed device belongs to a new category of impact test systems. This new device employs elastic strain energy accumulated in a bar to generate a stress wave that creates the desired impact pulse from sudden strain energy release.

Chapter VIII. Source of strength enhancement for cement-based materials under high rate compressive loadings

This chapter investigates the source of strength enhancement for cement-based

materials, e.g., concrete and mortar, by using computational simulation models based on the Split Hopkinson Pressure Bar technique. Influential parameters are identified and attempts are made to shed light on some controversial issues surrounding the interpretation of high strain rate test data.

Chapter IX. Summary, conclusions and future work

This chapter provides a summary of the main conclusions drawn from the four main parts: 1) development of HPFRCC with high strength and ductility; 2) strain rate effects on HPFRCC; 3) new impact test system using elastic strain energy; and, 4) source of strength enhancement for cement-based materials under high rate compressive loadings. In addition, several recommendations for future work are provided.

PUBLICATIONS FROM THIS DISSERTATION

In this thesis, Chapter II, III, IV, V and VI have been published, and Chapter VII and VIII will soon be submitted for publications. Citations are as follows:

D. Kim, S. El-Tawil, and A. E. Naaman, "Correlation between single fiber pullout behavior and tensile response of FRC Composites with high strength steel fiber," in Proceedings of Rilem International Workshop on High Performance Fiber Reinforced Cement Composites – HPFRCC5, Germany, H.W. Reinhardt and A.E. Naaman, Co-Editors, RILEM Proceedings, Pro. 53, S.A.R.L., Cachan, France, July 2007, pp. 67-76, **(Chapter II)**

D. Kim, A. E. Naaman, and S. El-Tawil, "High tensile strength strain hardending FRC Composites with less than 2% fiber content," in Proceeding of Second International Symposium on Ultra High Performance Concrete, Germany, E. Fehling, M. Schmidt and S. Stűrwald, Co-Editor, Kassel University Press GmbH, Heft 10, No. 10, March 2008, pp. 169-176, **(Chapter III)**

D. Kim, A. E. Naaman, and S. El-Tawil, "Comparative flexural behavior of four fiber reinforced cementitious composites", Cement and Concrete Composites, Vol.30, No.10, November 2008, pp.917-928, **(Chapter IV)**

D. Kim, S. El-Tawil, and A. E. Naaman, "Loading rate effect on pullout behavior of deformed fiber", ACI Materials Journal, Vol. 105, No. 6, Nov.-Dec. 2008, pp.576-584. **(Chapter V)**

D. Kim, S. El-Tawil, and A. E. Naaman, "Rate-dependent tensile behavior of high performance fiber reinforced cementitious composites", Materials and Structures, ISSN 1359-5997 (in print), 1871-6873 (online), May 21, 2008, **(Chapter VI)**

D. Kim, S. El-Tawil, and A. E. Naaman, "New impact test system using elastic strain energy", International Journal of Impact Engineering, (to be submitted), **(Chapter VII)**

D. Kim, K. Sirijaroonchai, S. El-Tawil, and A. E. Naaman, "Numerical simulation of Split Hopkinson Pressure Bar test methods for concrete under compression", International Journal of Impact Engineering, 2008, (submitted), **(Chapter VIII)**

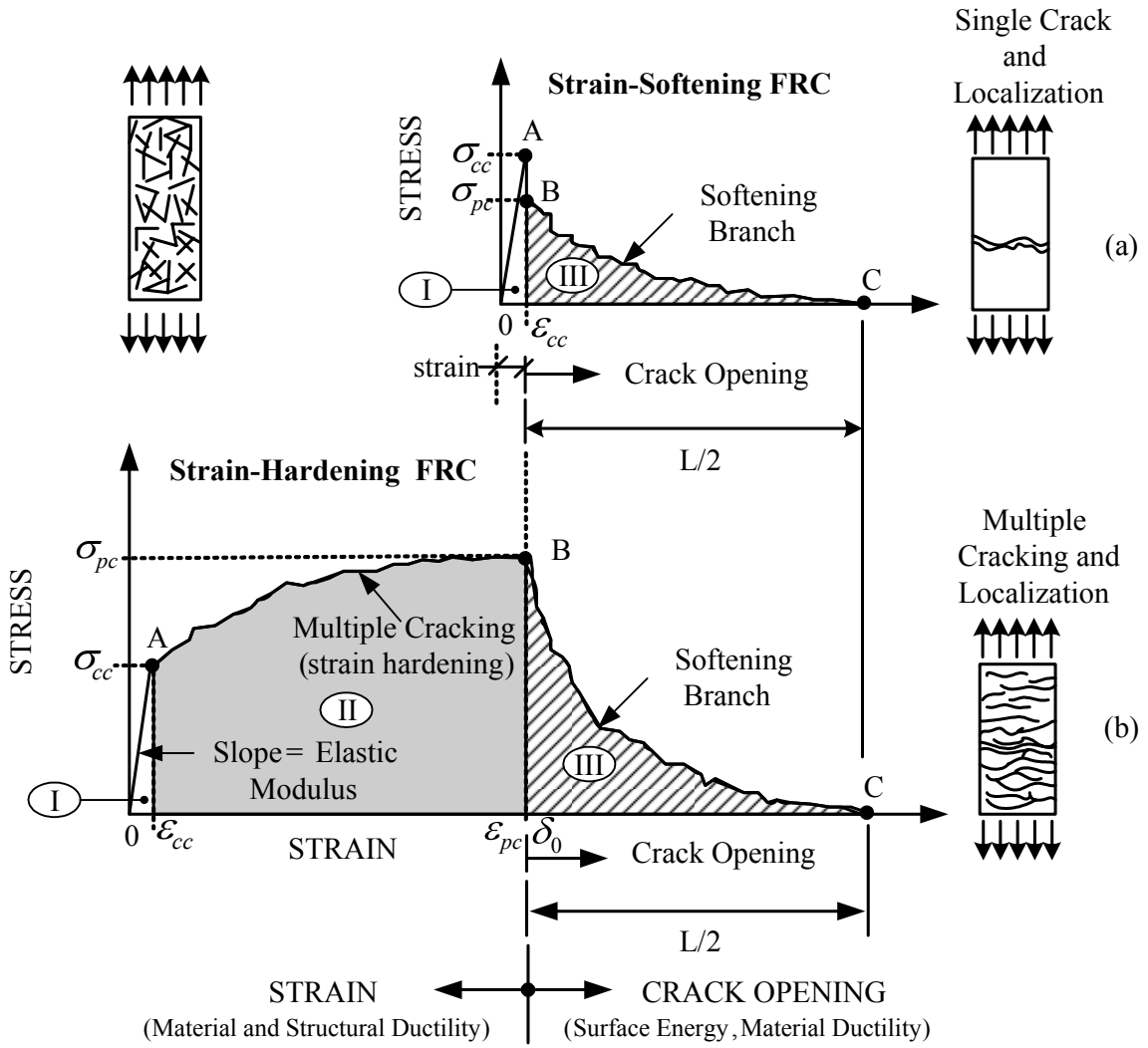

Fig. 1.1- Typical stress-strain or elongation curve in tension up to complete separation: (a) Conventional strain-softening FRC composites; (b) Strain-hardening FRC composite or HPFRCC (Naaman and Reinhardt, 1996)

(a) Method based on Potential energy

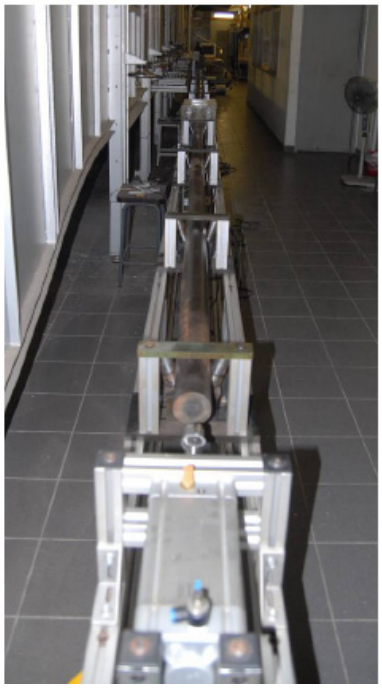

(b) Method based on Kinetic energy

(c) Method based on Hydraulic pressure

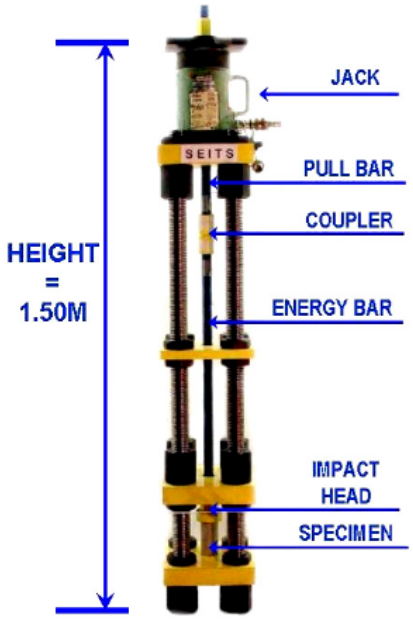

(d) Developed method based on Strain Energy

Fig. 1.2- Impact load generating methods

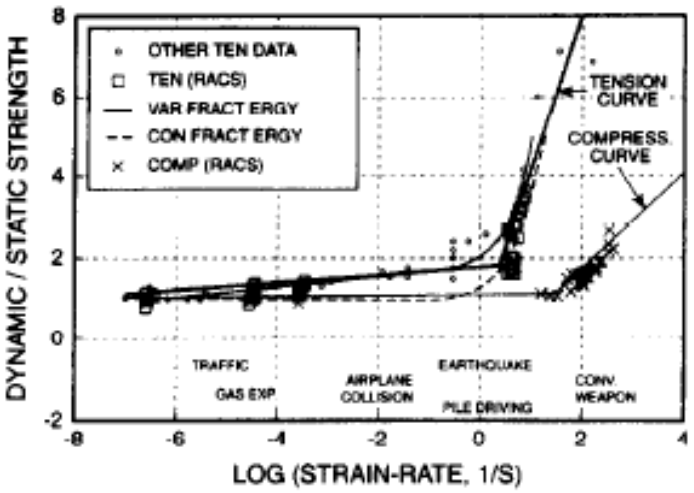

Fig. 1.3- Example of strain rate data for concrete, Ross 1996

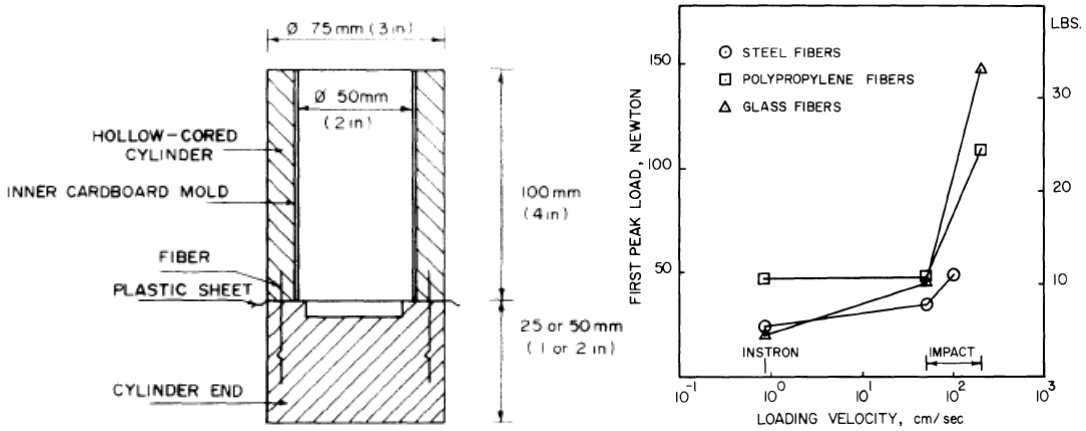

Fig 1.4- Fiber pullout specimen and rate sensitivity of peak pullout load (Gokoz and Naaman, 1981)

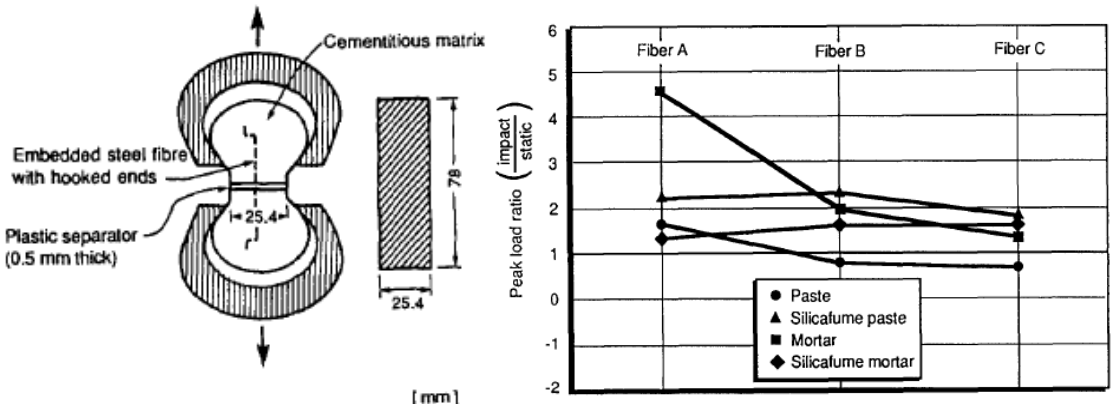

Fig 1.5- Single fiber pullout specimen and rate sensitivity of peak pullout load (N. Banthia and J.F. Tronttier, 1991)

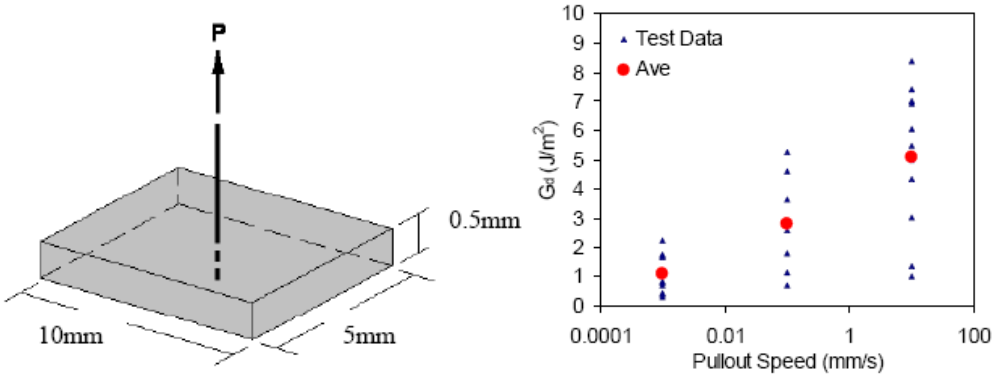

Fig 1.6- PVA single fiber pullout specimen and rate dependency in chemical bond strength (Yang and Li, 2005)

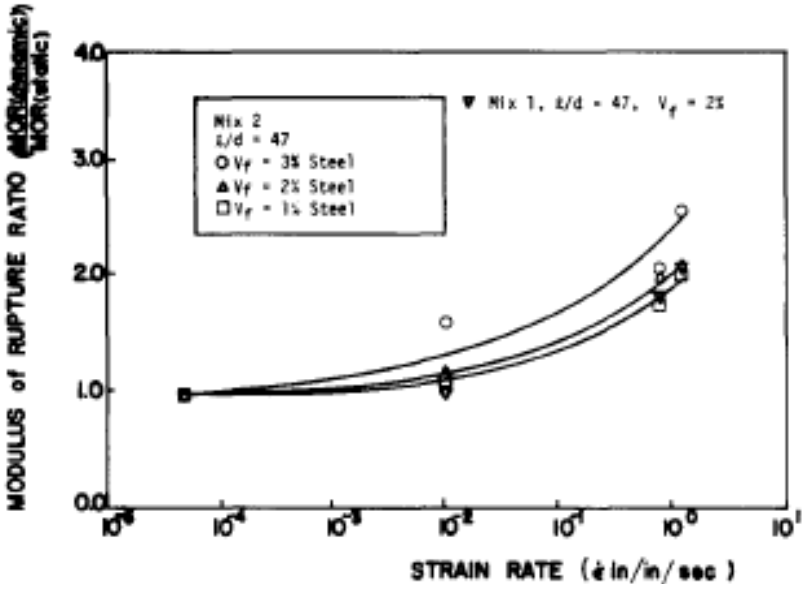

Fig. 1.7- Strain rate effect on Modulus of Rupture in different fiber volume ratio (Naaman and Gopalaratnam, 1983)

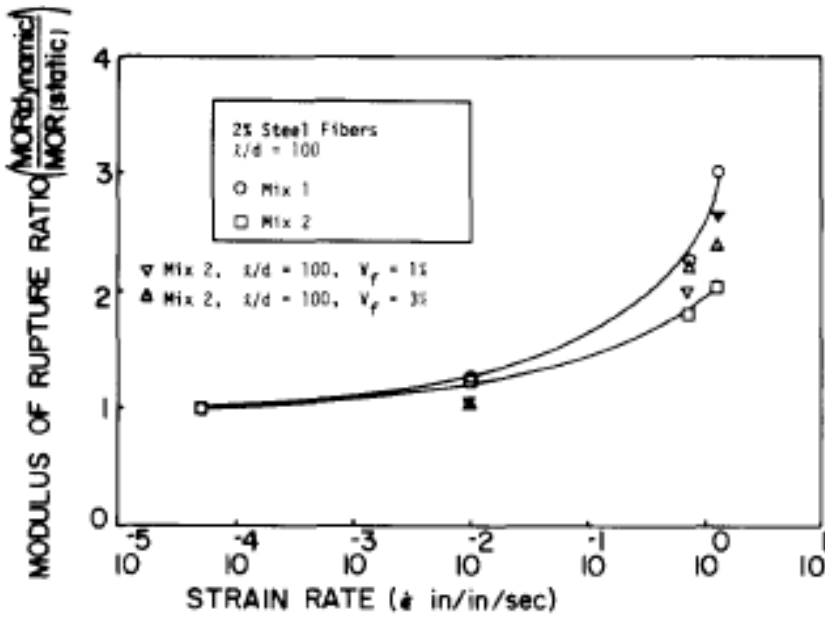

Fig. 1.8- Strain rate effect on MOR in different matrix (Naaman and Gopalaratnam, 1983)

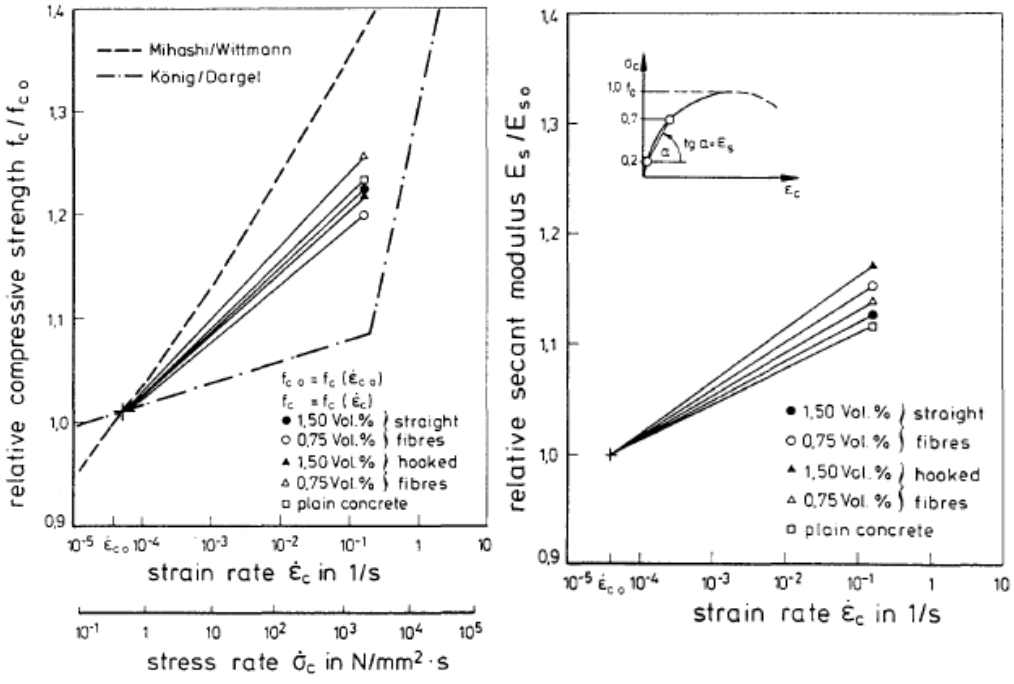

Fig. 1.9- Strain rate effect on compressive strength and modulus of elasticity in SFRC (F. S. Rostasy and K. Hartwich, 1985)

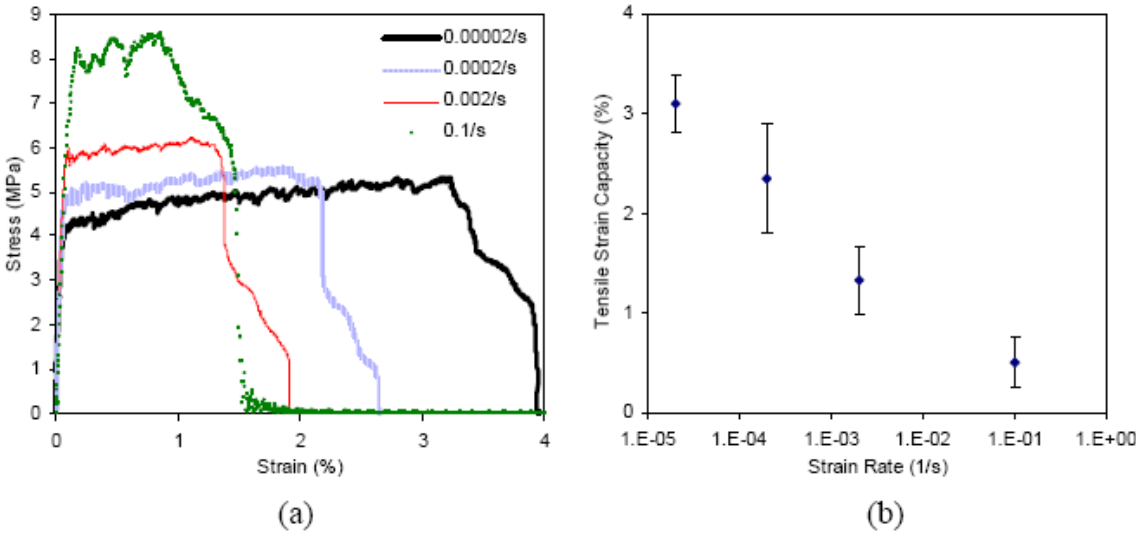

Fig. 1.10- Rate dependency in PVA-ECC : (a) tensile stress-strain curve and (b) tensile ductility versus strain rate relation (Yang and Li, 2005)

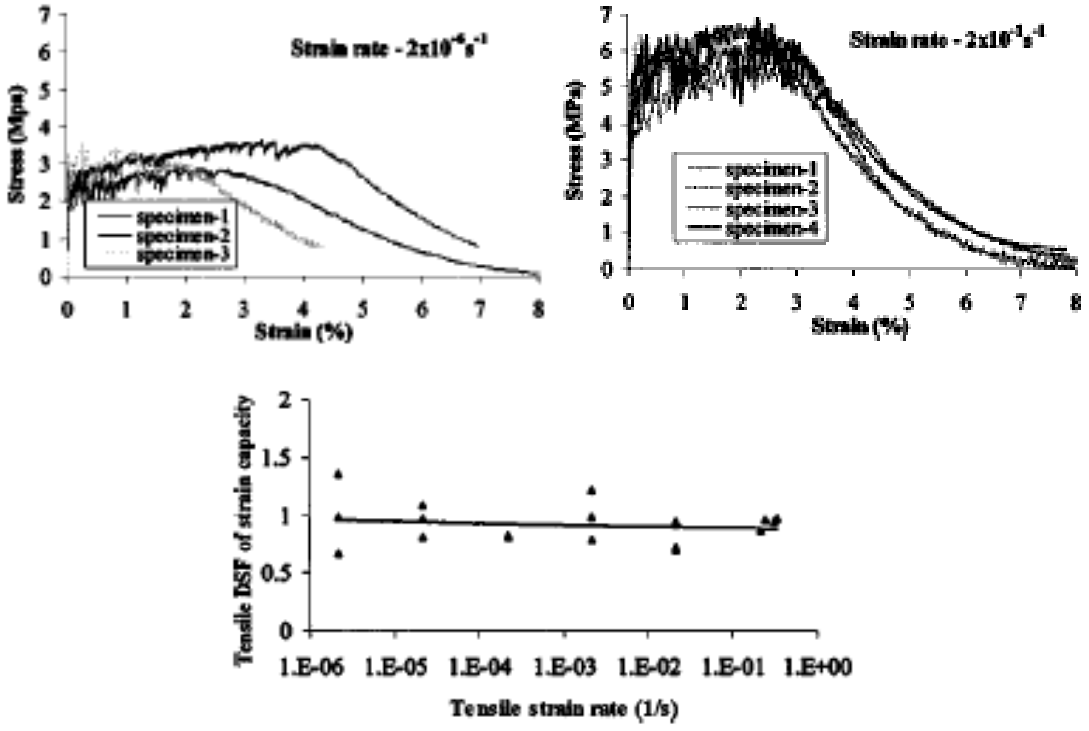

Fig 1.11- Rate dependency in hybrid-fiber ECC (Maalej et al, 2005)

Fig. 1.12- Structure of the Dissertation

REFERENCES

Banthia, N. and Trottier, J.-F., "Test methods for flexural toughness characterization of Fiber Reinforced Concrete : Some concerns and a proposition," ACI Materials Journal, Vol. 92, No. 1, Jan.-Feb. 1995, pp.1-10.

Banthia, N., and Trottier, J.-F., "Deformed steel fiber – cementitious matrix bond under impact," Cement and Concrete Research, Vol. 21, No. 1, 1991, pp.158-168.

Banthia, N., Chokri, K., Ohama, Y., and Mindess, S., "Fiber-Reinforced Cement Based Composites Under Tensile Impact," Advanced cement based materials ISBN 1065-7355, Vol. 94, No. 1, 1993, pp. 131-141.

Banthia, N., Mindess, S., and Trottier, J.-F., "Impact resistance of steel fiber reinforced concrete," ACI Materials Journal, Vol. 93, No. 5, Sep.-Oct. 1996, pp.472-479

Bantia, N., "Impact resistance of HPFRCC," Proceedings, HPFRCC-2005 International Workshop, Honolulu, Hawaii, USA, 2005

Bischoff, P. H., and Perry, S. H., "Compressive behavior of concrete at high strain rates," Materials and Structures, Vol. 91, No. 24, 1991, pp.425-450.

Bischoff, P. H., and Perry, S. H., "Impact behavior of plain concrete loaded in uniaxial compression," ASCE Journal of engineering mechanics, Vol. 121, No. 6, June 1995, pp.685-693.

Brara, A., and Klepaczko, J. R., "Dynamic tensile behavior of concrete : Experimental and Numerical analysis," ACI Materials Journal, Vol. 101, No. 2, Mar.-April 2004, pp.162-167

Cantwell, W. J., and Morton, J., "The impact resistance of composite materials – a review," Composites, Vol. 22, No. 5, 1991, pp.347-362

Douglas, K. S., and Billington, S. L., "Rate dependence in High-performance fiber reinforced cement-based composites for seismic application," in Proceedings, HPFRCC-2005 International Workshop, Honolulu, Hawaii, USA, 2005

Gokoz, U., and Naaman, A. E., "Effect of Strain Rate on the Pull-Out Behavior of Fibers in Mortar," International Journal of Cement Composites, Vol. 3, No. 3, Aug. 1981, pp.187-202.

Kim, D., Naaman, A.E., and El-Tawil, S., "Comparative flexural behavior of four fiber reinforced cementitious composites", Cement and Concrete Composites, Vol.30, No.10, November 2008, pp.917-928, (Chapter IV)

Kim, D., Naaman, A.E., and El-Tawil, S., "Correlation between single fiber pullout behavior and tensile response of FRC Composites with high strength steel fiber," in Proceedings of Rilem International Workshop on High Performance Fiber Reinforced Cement Composites – HPFRCC5, Germany, H.W. Reinhardt and A.E. Naaman, Co-Editors, RILEM Proceedings, Pro. 53, S.A.R.L., Cachan, France, July 2007, pp. 67-76, (Chapter II)

Kim, D., Naaman, A.E., and El-Tawil, S., "High tensile strength strain hardending FRC Composites with less than 2% fiber content," in Proceeding of Second International Symposium on Ultra High Performance Concrete, Germany, E. Fehling, M. Schmidt and S. Stűrwald, Co-Editor, Kassel University Press GmbH, Heft 10, No. 10, March 2008, pp. 169-176, (Chapter III)

Kim, D., Naaman, A.E., and El-Tawil, S., "Loading rate effect on pullout behavior of deformed fiber", ACI Materials Journal, 2008 (in print), (Chapter V)

Kim, D., Naaman, A.E., and El-Tawil, S., "New impact test system using elastic strain energy", International Journal of Impact Engineering, *(to be submitted),* (Chapter VII)

Kim, D., Naaman, A.E., and El-Tawil, S., "Numerical simulation of Split Hopkinson Pressure Bar test methods for concrete under compression", International Journal of Impact Engineering, 2008 *(submitted)*, (Chapter VIII)

Kim, D., Naaman, A.E., and El-Tawil, S., "Rate-dependent tensile behavior of high performance fiber reinforced cementitious composites", Materials and Structures, ISSN 1359-5997 (in print), 1871-6873 (online), May 21, 2008, (Chapter VI)

Klepaczko, J. R., "On a very high rate sensitivity of concrete failure at high loading rates and impact," Proceedings of International Symposium, Brittle Matrix Composites 7, ZTUREK RSI and Woodhead Publ., Warsaw 2003.

Lok, T. S., and Zhao, P.J., "Impact response of steel fiber-reinforced concrete using a Split Hopkinson Pressure Bar," ASCE Journal of materials in civil engineering, Vol. 16, No. 1, Jan.-Feb. 2004, pp.54-59.

Lok, T. S., Li, X. B., Liu, D., and Zhao, P.J., "Testing and response of Large Diameter Brittle Materials subjected to High strain rate," ASCE Journal of materials in civil engineering, May-June 2002, Vol. 14, No. 3, pp.262-269

Maalej, M., Quek, S. T., and Zhang, J., "Behavior of Hybrid-Fiber Engineered Cementitious Composites Subjected to Dynamic Tensile Loading and Projectile Impact," ASCE Journal of Materials in civil engineering, Vol. 17, No. 2, April 2005, pp.143-152.

Malvar, L. J., and Crawford, J. E., "Dynamic increase factors for Concrete," Twenty-eighth DDESB Seminar, Orlando, FL, august 1998.

Naaman, A. E., and Reinhardt, H. W., "Characterization of High Performance Fiber Reinforced Cement Composites," Proceedings, 2nd International Workshop on HPFRCC, Chapter 41, in High Performance Fiber Reinforced Cement Composites: HPFRCC 2, A.E. Naaman and H. W. Reinhardt, Editors, RILEM, No. 31, E. & FN Spon, London, 1996, pp. 1-24.

Naaman, A.E, El-Tawil, S., and Kim, D., "Strain Energy Impact Test System [SEITS] for characterizing material response under high strain rates," (Application No. 61/038,174) Provisional US Patent application. (Filed March 20, 2008)

Nammur, G. G. and Naaman, A. E., "Strain Rate Effects on Tensile Properties of Fiber Reinforced Concrete," Proceedings of MRS Symposium on "Cement Based Composites: Strain Rate Effects on Fracture," S. Mindess, Editor, Materials Research Society, Vol. 64, Pittsburgh, 1986, pp.97-118.

Nemat-Nasser, S., and Deng, H., "Strain-rate effect on brittle failure in compression," Acta metallurgica et materialia, ISSN 0956-7151, Vol. 42, No. 3, 1994, pp.1013-1024.

Nemat-Nasser, S., Isaacs, J. B., and Starrett, J. E., "Hopkinson technique for dynamic recovery experiment," Proceedings, Mathematical and Physical Sciences, Vol. 435, No. 1894, Nov. 8, 1991, pp.371-391.

Radomski, W., "Application of the rotating impact machine for testing fibre-reinforced concrete," International Journal of Cement Composites and Lightweight Concrete, Vol. 3, No. 1, 1981, pp. 3-12

Ross, C. A., Jerome, D. M., Tedesco, J. W., and Hughes, M. L., "Moisture and Strain rate effects on Concrete strength," ACI Materials Journal, Vol. 93, No. 3, May-June 1996, pp.293-300.

Ross, C. A., Tedesco, J. W., and Kuennen, S. T., "Effects of strain rate on concrete strength," ACI Materials Journal, Vol. 92, No. 1, Jan.-Feb. 1995, pp37-47

Ross, C. A., Thomson, P. Y., and Tedesco, J. W., "Split-Hopkinson Pressure-Bar test on Concrete and Mortar in Tension and Compression," ACI Materials Journal, Vol. 86, No. 5, Sep.-Oct. 1989, pp.475-481.

Rostásy, F. S. and Hartwich, K., "Compressive strength and deformation of steel fiber reinforced concrete under high rate of strain," International Journal of Cement Composites and Lightweight Concrete, V. 7, No. 1, 1985, pp.21-28

Staab, G. H., and Gilat, A., "A direct-tension Split Hopkinson Bar for high strain-rate testing," Proceedings, SEM spring conference on experimental mechanics, Columbus, Ohio, USA, 1990.

Tedesco, J. W., Ross, C. A. and Kuennen, S. T., "Experimental and Numerical Analysis of High Strain Rate Splitting Tensile Tests," ACI Materials Journal, Vol. 90, No. 2, Mar-April 1993, pp.162-169.

Wei, S., Chunjie, J., and Jianzhong, L., "Behavior of steel fiber reinforced high and ultra-high strength concrete at high strain rate," Proceedings, HPFRCC-2005 International Workshop, Honolulu, Hawaii, USA, 2005

Yang, E. and Li, V. C., "Rate dependence in Engineered Cementitious Composites," in Proceedings, Proceedings of International RILEM Workshop on HPFRCC in Structural Applications, Published by RILEM SARL, pp. 83-92, 2006.

CHAPTER II

CORRELATION BETWEEN FIBER PULLOUT AND TENSILE RESPONSE OF FRCC [1]

ABSTRACT

This chapter describes the results of experimental tests designed to correlate the pull-out response of two types of high strength steel fibers [Hooked and Torex fibers] with the tensile response of fiber reinforced cement composites using such fibers. The focus is mostly on HPFRCC or strain-hardening composites in tension and the parameter studied includes fiber type. Experimental results reveal that a strong correlation exists between pull-out behavior and tensile response, especially in terms of the extent of slip before bond decays and the strain-capacity of the composite prior to localization. While the bond strength is important, the extent of slip prior to bond softening is also most critical. It is concluded that extensive slip hardening in the fiber pullout behavior leads to high strain capacity composites with multiple micro-cracks.

[1] D. Kim, S. El-Tawil, and A. E. Naaman, "Correlation between single fiber pullout behavior and tensile response of FRC Composites with high strength steel fiber," in Proceedings of Rilem International Workshop on High Performance Fiber Reinforced Cement Composites – HPFRCC5, Germany, H.W. Reinhardt and A.E. Naaman, Co-Editors, RILEM Proceedings, Pro. 53, S.A.R.L., Cachan, France, July 2007, pp. 67-76

2.1 INTRODUCTION

The tensile behavior of fiber reinforced cement composites (FRCCs) depends on numerous parameters including the matrix and fiber properties and the bond at the fiber-matrix interface. Compared with conventional FRC composites, high performance FRC composites (HPFRCC) are characterized by a strain-hardening behavior in tension accompanied by multiple cracking. Such characteristic leads to high ductility, durability, and energy absorption capacity.

The condition to develop strain hardening and multiple cracking behavior is simple to set, namely; the post cracking strength of composites should be higher that their first cracking strength (Naaman [1987] and Naaman and Reinhardt [1996]). Moreover, the slip hardening in single fiber pullout behavior, should it exist, is believed to be a key for the strain-hardening behavior of the composite (Sujivorakul and Naaman [2003]). Both Torex (twisted fibers of polygonal cross-section) and Hooked ends steel fibers show slip-hardening behavior under pull-out, primarily because of the plastic energy capacity of steel (Sujivorakul et al. [2000] and Naaman [1999]). However, the extent of slip before bond decay is very different for both types of fibers (Sujivorakul [2002]). The main objective of this chapter is to evaluate the correlation that exists between the extent of slip before bond decay in a single fiber pullout, and the tensile response of a composite made with such fiber. Experimental test results are provided and analyzed using equivalent bond strength derived from the fiber pullout energy.

2.2 PULLOUT MECHANISM AND PULLOUT ENERGY

Fiber pullout resistance is based on the bond mechanisms at the interface between fiber and matrix. Bond characteristics between fiber and matrix generally comprise

adhesion, friction and mechanical components. The pullout resistance of deformed steel fibers is primarily controlled by the mechanical component, whereas that of smooth steel fiber is mainly dependent upon the frictional component. The Hooked steel fiber is one of the most widely used steel fibers, which utilize the plastic energy of deformation of steel (Naaman and Najm [1991]); however, it uses only a small portion of fiber length to enhance pullout resistance as induced by the formation of two plastic hinges at the end hook. Plastic hinge formation results in slip-hardening response up to a certain slip (S1 in Fig. 2.1a). The pullout mechanism of Torex fiber is based on the untwisting torsional moment resistance of the fiber which is distributed throughout the fiber embedment length (Naaman and Sujivorakul [2001]). Therefore, everything else being equal, the extent of slip of a Torex fiber before bond decays (S2 in Fig. 2.2a) is much higher than that of a Hooked fiber (S1 in Fig. 2.1a), i.e. S2 >> S1. This big difference in slip capacity leads to a substantial increase in pullout energy during single fiber pullout and in improved energy absorption capacity of the composite.

2.3 PULLOUT ENERGY AND EQUIVALENT BOND STRENGTH

To achieve strain-hardening behavior, the maximum post-cracking strength, σ_{pc}, should be higher than the first cracking strength, σ_{cc} (Naaman [1987] and Naaman and Reinhardt [1996]). The post-cracking strength is directly dependent on the average bond strength at the fiber matrix interface, which is assumed to be a constant over a relatively small level of slip. Assuming that the bond strength remains a constant over the entire embedment length, the authors suggest that equivalent bond strength can be calculated from the pullout energy obtained from a single fiber pullout test

If the equivalent bond strength is assumed constant, the shape of the pullout load

versus slip curve will be triangular such as shown in the middle part of Figs. 2.1, 2.2. Using the pullout energy (area under each curve) leads to the equivalent bond strength for a typical Hooked and Torex steel fiber as illustrated in Fig. 2.1c, 2.2c. It is observed that, even if the maximum pullout load is the same for two fibers, their equivalent bond strength can be significantly different depending on their pullout energy. Mathematically, the equivalent bond strength can be estimated from the following equations.

$$E_{pullout} = P\Delta/2 = \left(\pi d_f \tau_{eq} \times \left(L_f/2\right)\right) \times \left(L_f/2\right)/2 = \tau_{eq} \times \pi d_f L_f^{\,2}/8$$

$$\rightarrow \ \tau_{eq} = 8E_{pullout} \Big/ \pi d_f L_f^{\,2} \qquad [2.1]$$

2.4 EQUIVALENT BOND STRENGTH AND TENSILE BEHAVIOR

The equivalent bond strength concept makes it possible and simple to utilize the equations for first-cracking strength and post-cracking strength based on the mechanics of composite materials suggested by Naaman [1972, 1987] because these equations assume a constant bond strength.

Typical stress-elongation curve of a strain-hardening FRC composite is shown in Fig. 2.3. Multiple cracking occurs along the strain hardening portion of the curve. The strain capacity at maximum stress is based on both the number of multiple cracks and the width of cracks. These can also be estimated, assuming the equivalent bond strength is known as described next. The equations suggested by Naaman [1972, 1987] for first cracking strength and the post cracking strength are used here:

First cracking strength : $\sigma_{cc} = \sigma_{mu}\left(1 - V_f\right) + \alpha \tau_{eq} V_f \left(L_f/d_f\right)$ [2.2]

Post cracking strength: $\sigma_{pc} = \lambda \tau_{eq} V_f \left(L_f/d_f\right)$ [2.3]

The average crack spacing and crack width derived for the case of continuous

reinforcement (Naaman [1970, 2000]) are assumed to apply here provided an equivalent bond strength is used. Note that the equation can also be put in terms of the specific surface of fiber reinforcement. Thus, assuming a tensile prism model leads to:

Average crack spacing: $\Delta L_{av} = \eta \frac{A_m \sigma_m}{p\tau_{eq}} = \eta \frac{A_m \sigma_m}{\left(N_F \cdot \pi d_f\right)\tau_{eq}}$ [2.4]

Crack opening due to fiber stretch:

$$W_{st} = \Delta L_{ax}\left[\left(\varepsilon_f\right)_{ax} - \left(\varepsilon_m\right)_{ax}\right]$$

$$= \Delta L_{av}\left[\frac{N}{A_f E_f} - \frac{p\tau}{4A_f E_f}\Delta L_{av}\right] - \Delta L_{av}\left[\frac{p\tau \times \Delta L_{av}}{4A_m E_m} - \varepsilon_{SH}\right]$$

$$\cong \Delta L_{av}\frac{N}{A_f E_f} \quad [2.5]$$

where, V_f = fiber volume fraction, L_f = fiber length, d_f = fiber diameter, L_f/d_f = fiber aspect ratio, σ_{mu} = tensile strength of matrix, τ_{eq} = equivalent bond strength, $\left(\varepsilon_f\right)_{av}$ = Average strain in fiber, $\left(\varepsilon_m\right)_{av}$ = Average strain in matrix, $\left(\sigma_f\right)_{av}$ = Average strain in fiber, $\left(\sigma_m\right)_{av}$ = Average strain in matrix, p = total fiber perimeter (i.e., sum of perimeters of all fibers per unit volume), N_f = Number of fibers crossing a unit area of matrix, A_m = area of matrix in tensile prism model, W_{st} = Crack opening due to fiber stretch, A_f = average area of fibers crossing a unit area of composites, E_m = Matrix modulus of elasticity, E_f = Fiber modulus of elasticity, N = Applied Load, α = factor equal to the product of several coefficient for considering average stress, random distribution, fiber orientation, λ = factor equal to the product of several coefficients for considering average pullout length, group reduction, orientation effect, η = factor for the

range between minimum and maximum crack spacing ($1 \le \eta \le 2$).

2.5 EXPERIMENTS

Experimental tests were carried out to investigate the correlation between single fiber pullout behavior and the tensile behavior of strain-hardening FRC composites (HPFRCC). Hooked and Torex steel fibers were investigated since they both show slip-hardening behavior under pullout but with significantly different slip capacity before bond decay.

2.5.1 Materials

The matrix mix properties are shown in Table 2.1 and the key properties of the fibers are shown in Table 2.2.

Note that the reason for which VMA (viscosity modifying agent) was used is because this project was in support of another project involving the use of self-consolidating HPFRCC for application in seismic resistant structures. VMA is added to the matrix to increase viscosity, reduce fiber segregation and ensure uniform fiber distribution during mixing.

2.5.2 Single Fiber Pullout Test

The geometry of pullout test specimen and test set up are shown in Fig. 2.4. This test simulates the case of fibers bridging the crack surface of a tensile prism and undergoing the different pullout mechanisms influencing slip capacity and fiber pullout energy. In performing single fiber pullout test, extreme care should be taken in gripping the fiber as close as possible to the free surface of the prism to minimize the effect of deformation from fiber elongation.

2.5.3 Tensile Test

The tensile behavior of HPFRCC is highly dependent on the fiber reinforcing parameters and the equivalent bond stress. Tests on tensile prisms were carried out to correlate with results on pullout load and energy obtained from tests using single fiber pullout. Tensile test specimen (double-dogbone shaped) and test set-up are shown in Fig. 2.5. Cross section dimensions of specimen are 2 x 1 in. (50 x 25 mm) and the elongation (thus strain) was measured over a gage length of 7 in (= 178 mm) using the average reading of 2 LVDTs.

The fiber volume fraction was 2% in both Hooked and Torex fiber reinforced specimen and the same matrix composition (compressive strength 7ksi (48.3 MPa)) was used to eliminate the influence of any other parameters. The direct tensile test as shown in Fig. 2.5 allows identification of the following characteristics: first cracking strength, post cracking strength, strain capacity, cracking behavior, and strain energy to peak stress.

2.6 RESULTS

2.6.1 Single Fiber Pullout behavior

Single fiber pullout test were performed and the results are shown in Fig. 2.6. The embedded length was taken as 0.59 in (15 mm). The pullout response of Torex fibers shows considerable slip before bond decays (more than 0.4 inch (10 mm)). In contrast, high strength Hooked fibers slipped less than 0.05 inch (1.27 mm) before the resistance started to decay. The typical shapes of both Torex and Hooked fibers before and after the pullout test are shown Fig. 2.6g, h.

Both Hooked and TOREX fibers have comparable mechanical bond resistance when computed from the peak pull-out load (Fig. 2.6a, b)**.** If the fiber tensile stress under pull-out is plotted versus slip (Fig. 2.6c, d), then the pull-out stress until a slip of 0.03 in. (0.76

mm) is about the same in the two fibers, that is, about 190 ksi (1311 MPa). The slip at the peak stress for the Hooked fiber is 0.03 in. (0.76 mm) and is followed by a rapid decay; however, after that slip, the Torex fibers show dramatic enhancement in both stress and slip up to a slip of about 0.45 in (11.4 mm), which represents 76% of embedded fiber length (Fig. 2.6e, f).

This big difference in slip capacity leads to a considerable difference in pullout energy. Pullout energy was calculated from the average pullout load versus slip curves of Hooked and Torex fibers. The pullout work obtained for Torex fiber was = 13.568 lb-in (1533 N-mm) is more than twice that obtained for Hooked fibers (5.921 lb-in = 669 N-mm).

Even though there is a big difference in pullout energy between Hooked and Torex fibers, it should be noted that the slip capacity at peak stress of Hooked fiber before bond decays (0.03 inch = 0.76 mm) is still sufficient to induce significant multiple cracking in a tensile composite. Since fiber embedment length varies from 0 to $L_f/2$ at any crack section, an average bond stress along the fiber embedment length is used in estimating the composite tensile behavior.

The equivalent bond stress was calculated from the experimentally measured pullout work using Eq. [2.1]. The equivalent bond stress is thus a constant that is assumed to be slip-independent.

$$\underline{\text{Hooked Fiber}}:\ \tau_{eq} = \frac{8 \times PulloutWork}{\pi d_f {L_f}^2} = \frac{8 \times 5.921}{\pi (0.4/25.4) 1.18^2} = 686\,psi = 4.73\,MPa \qquad [2.6]$$

$$\underline{\text{Torex Fiber}}:\ \tau_{eq} = \frac{8 \times PulloutWork}{\pi d_f {L_f}^2} = \frac{8 \times 13.568}{\pi (0.3/25.4) 1.18^2} = 2100\,psi = 14.49\,MPa \qquad [2.7]$$

These values will be used later on to explain some aspects of the tensile response and

crack distribution in composites subjected to tension.

2.6.2 Tensile behavior

Tensile test results are shown in Fig. 2.7 and Table 2.3. Both Hooked and Torex fiber reinforced specimens with 2% fiber volume ratio show strain hardening behavior. Three specimens were tested for each series, and the averages are discussed next. For the hooked fiber reinforced tensile prisms, the first cracking strength was 0.575 ksi (3.97 MPa), the post-cracking strength was 0.783 ksi (5.40 MPa) and the corresponding strain was 0.33%. Torex fiber reinforced specimens showed a higher load carrying capacity: first cracking strength = 0.826 ksi (5.70 MPa), post-cracking strength = 1.157 ksi (7.98 MPa)), and a strain of 0.47% at peak stress. It is clear in this comparison between Hooked and Torex steel fibers that, everything else being equal, the Torex fiber leads to a significantly better performance in terms of both strength and strain capacity prior to decay.

Note also that the cracking behavior of the tensile specimen with Torex fibers is quite different from that with Hooked fibers as shown in Fig. 2.8. For the Torex fiber reinforced specimen, the average number of observed cracks is 60 and the average crack spacing is 2.96 mm (= 177.8/60); the average crack opening at post cracking strength 1.157 ksi (= 7.98 MPa) is 13.92 μm (Table 2.7, Fig. 2.8). For the Hooked fiber reinforced specimen, the average number of observed cracks was 15, and their average spacing was 11.85 mm; the average crack width was 39.12 μm (Table 2.7, Fig. 2.8).

2.7 COMPARISON BETWEEN EXPERIMENTALLY OBSERVED AND ANALYTICALLY PREDICTED CRACK SPACING AND WIDTH

Predicted theoretical values of crack spacing and crack width for Torex and Hooked

fiber reinforced tensile specimens are calculated using Equations [2.4], [2.5] in which the equivalent bond strength is obtained from Eqs. [2.6], [2.7]. In estimating theoretical crack widths due to the average tensile strain in the fiber, the post-cracking strength was used to calculate the applied tensile force N, for both Torex and Hooked fibers. The corresponding values of crack widths are given in Table 2.4, and compared to the experimental observations. On the other hand, Fig. 8 illustrates examples of residual crack width observed.

2.7.1 Torex Fiber

Average number of fibers at bridging a typical cross section of the tensile prism:

$$N_f = \alpha_2 \frac{4V_F}{\pi d_f{}^2} A_c = 0.5 \times \frac{4 \times 0.02}{3.14 \times 0.011811023^2} \times 2 = 182 ea$$

Average crack spacing Eq. [2.4]:

$$\Delta L_{average} = 1.5 \times \frac{(2 - 0.04) \times 0.504}{(182 \times \pi \times (0.3/25.4)) \times 2.1} = 0.1045 inch = 2.66 mm$$

Predicted number of cracks: $Gagelength/Crackspacing = 7/0.1045 = 67 ea$

Crack opening due to fiber stretch Eq. [2.5]:

$$W_{st} = \Delta L_{av} \frac{N}{A_r E_r} = \mu \frac{A_m \sigma_{mu}}{(N_f \cdot \pi d_f)\tau_{eq}} \times \frac{\sigma_{pc} A_c}{A_r E_r}$$

$$= 1.5 \times \frac{(2 - 0.04) \times 0.504}{(182 \times \pi \times (0.3/25.4)) \times 2.1} \times \frac{1.157 \times 2}{0.04 \times 29000} = 0.000208 inch = 0.0053 mm = 5.3 \mu m$$

2.7.2 Hooked Fiber

Average number of fibers bridging a typical cross section of the tensile prism:

$$N_f = \alpha_2 \frac{4V_F}{\pi d_f{}^2} A_c = 0.5 \times \frac{4 \times 0.02}{3.14 \times 0.015748^2} \times 2 = 103 ea$$

Average crack spacing Eq. [2.4] :

$$\Delta L_{average} = 1.5 \times \frac{(2 - 0.04) \times 0.504}{(103 \times \pi \times (0.4/25.4)) \times 0.686} = 0.424 inch = 10.77 mm$$

Predicted number of cracks: $Gagelength/Crackspacing = 7/0.424 = 16 ea$

Crack opening due to fiber stretch Eq. [2.5]:

$$W_{st} = \Delta L_{av} \frac{N}{A_r E_r} = \mu \frac{A_m \sigma_{mu}}{(N_f \cdot \pi d_f) \tau_{eq}} \times \frac{\sigma_{pc} A_c}{A_r E_r}$$

$$= 1.5 \times \frac{(2 - 0.04) \times 0.504}{(103 \times \pi \times (0.4/25.4)) \times 0.686} \times \frac{0.783 \times 2}{0.04 \times 29000}$$
$$= 0.00057 inch = 0.0145 mm = 14.53 \mu m$$

The above analytical calculations for the crack spacing are very close to the results observed in the experimental tensile tests (Tables 2.3, 2.4) suggesting that the analytical procedure used here can be very useful. The results confirm that the better tensile response of specimens reinforced with Torex fibers is due to the high equivalent bond strength that develops along the entire fiber embedment length. This high equivalent bond strength is due to the large slip capacity before bond softening in the fiber pullout versus slip behavior of Torex fiber.

2.8 CONCLUSIONS

This study investigated the correlation between single fiber pullout and tensile response of FRC composites with high strength steel Torex and Hooked fibers. Even though both Torex and Hooked fibers show slip-hardening behavior due to their mechanical bond, the extent of slip prior to bond softening (or decay) is very different for each fiber. Differences in the slip capacity are theorized to be partly responsible for the observed differences in strain capacity and multiple cracking development in the FRC

composites. The following specific conclusions may be drawn from the limited study described herein:

- The combined effects of high slip-hardening capacity and high slip before bond decay in fiber pullout behavior helps achieve strain-hardening FRC composites with higher strain capacity in tension and better multiple cracking developments.
- Torex fiber shows slip-hardening behavior up to 76 % of the fiber embedment length. This large slip capacity significantly increases the energy required to pull out the fiber.
- The high pullout energy of Torex fibers leads to a high equivalent bond strength, which can be used to predict crack spacing at crack saturation in strain-hardening FRC composites.
- The very fine crack widths at saturated micro cracking associated with Torex fibers implies that Torex reinforced composites are likely to have excellent durability.

Table 2.1- Composition of matrix mixtures by weight ratio and compressive strength

Matrix	Cement (Type III)	Fly ash	Sand (Flint)	Silica Fume	Super - Plasticizer	VMA	Water	$f_c^{'}$, ksi (MPa)
Mortar	1.00	0.15	1.00	-	0.009	0.006	0.35	7 (49)

Table 2.2- Properties of Fibers used in this study

Fiber Type	Diameter in (mm)	Length in(mm)	Density g/cc	Tensile strength ksi (MPa)	Elastic Modulus ksi (GPa)
Hooked	0.016 (0.4)	1.18 (30)	7.9	304 (2100)	29000 (200)
Torex	0.012 (0.3)*	1.18 (30)	7.9	400 (2760)**	29000 (200)

* Equivalent diameter ** Tensile strength of the fiber after twisting

Table 2.3- Tensile test results

	TOREX FIBER 2%	HOOKED FIBER 2%
First Cracking strength, σ_{cc}	0.826ksi = 5.70MPa	0.575ksi = 3.97MPa
Post Cracking strength, σ_{pc}	1.157ksi = 7.98MPa	0.783 ksi = 5.40MPa
Strain capacity at peak stress, ε_{pc}	0.47%	0.33%
Number of cracks	60	15
Average crack spacing	0.116inch = 2.96mm	0.467inch =11.85mm
Crack opening at Post Cracking (Based on strain capacity and Number of Cracks)	13.92μm	39.12μm
Permanent average crack width	9.06μm	22.12μm
Crack opening due to fiber stretch	13.92–9.06=4.86μm	39.12–22.12 = 17μm

Table 2.4- Comparison of cracking behavior between predicted and actual test results

	Torex Fiber 2%		Hooked Fiber 2%	
	Predicted	Actual	Predicted	Actual
Crack spacing	2.66mm	2.96mm	10.77mm	11.85mm
Number of cracks	67 ea	60 ea	16 ea	15 ea
Crack opening due to fiber stretch	5.3 μm	4.86 μm	14.53 μm	17.00 μm

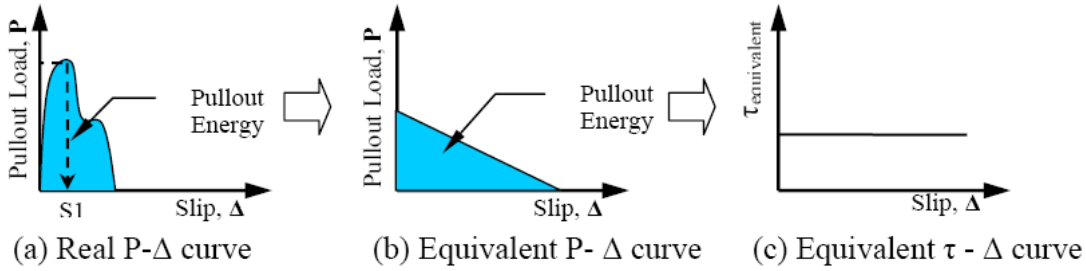

Fig. 2.1- Hooked fiber pullout behavior

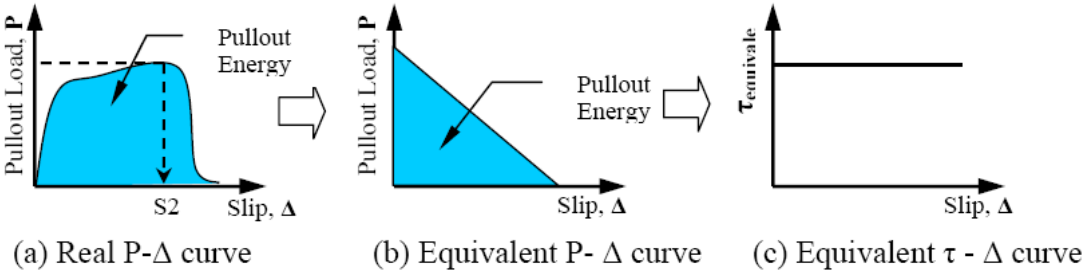

Fig. 2.2- Torex fiber pullout behavior

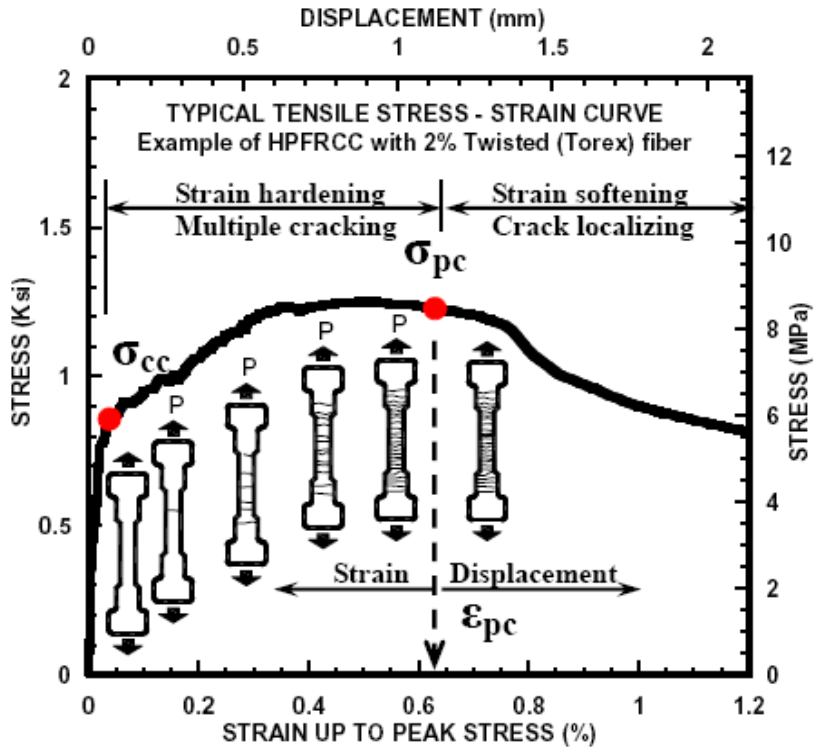

Fig. 2.3- Typical tensile stress – strain (or elongation) curve of HPFRCC

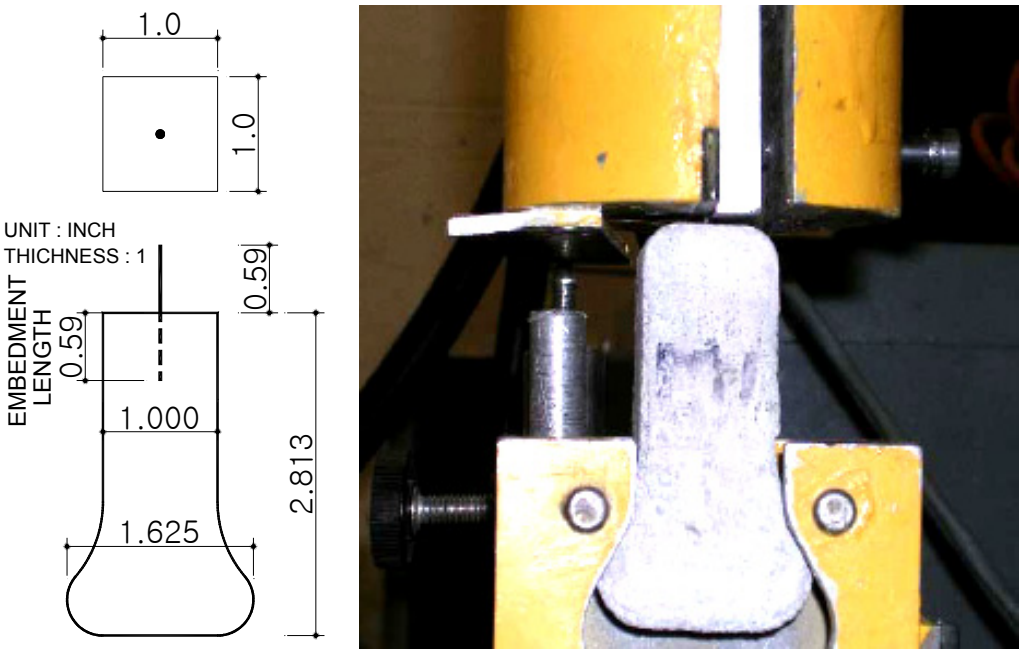

Fig. 2.4- Pull out test specimen and setup

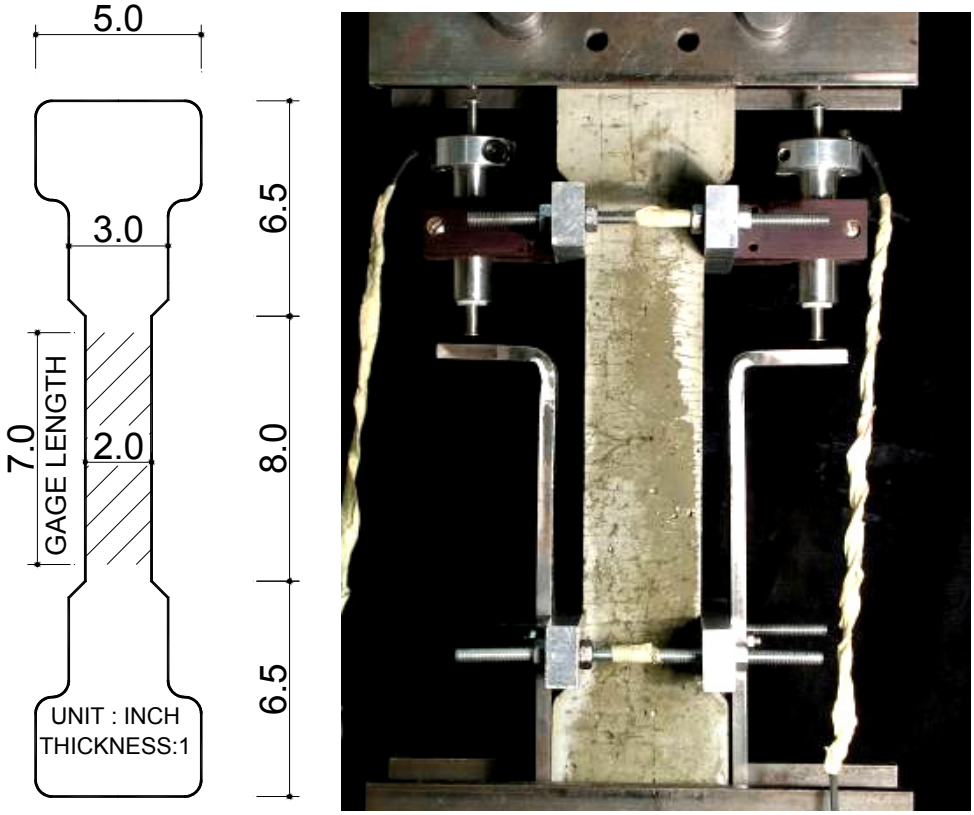

Fig. 2.5- Tensile test specimen and setup

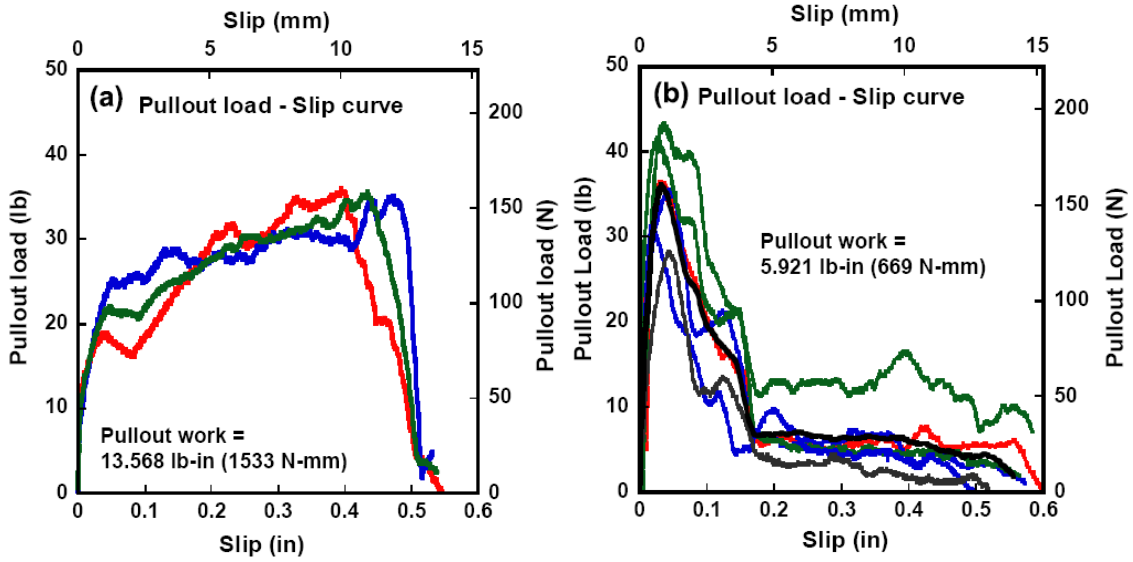

(a) Torex fiber pullout load – slip (b) Hooked fiber pullout load - slip

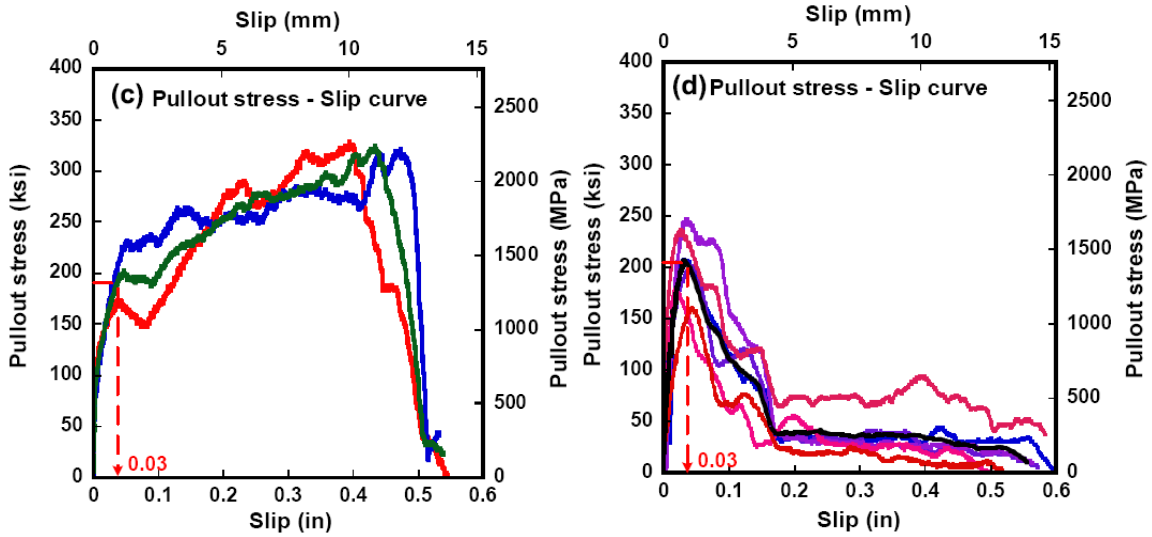

(c) Torex fiber pullout stress – slip (d) Hooked fiber pullout stress – slip

Fig. 2.6- Single fiber pullout test results (continued)

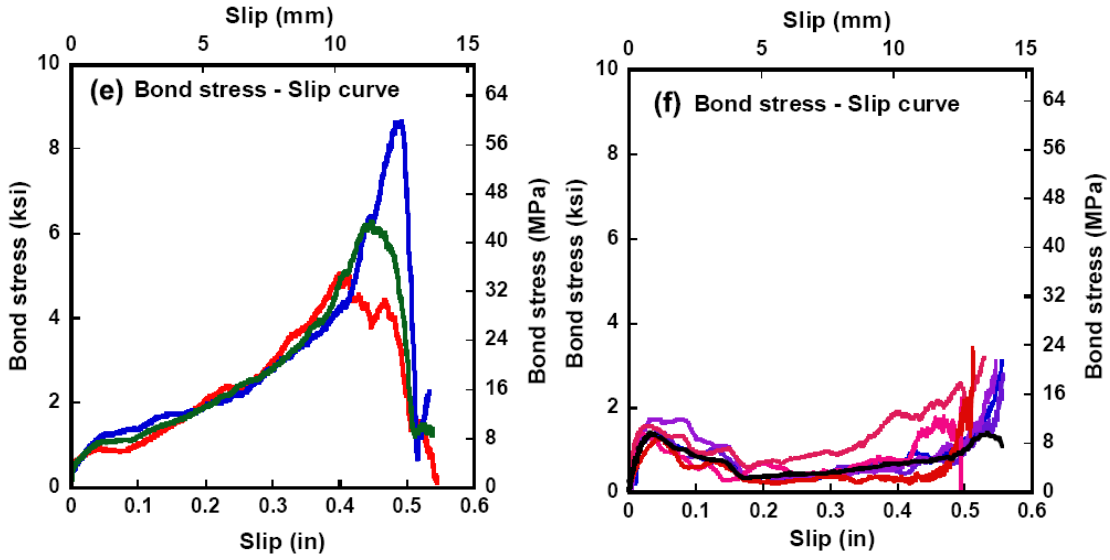

(e) Torex fiber bond stress – slip (f) Hooked fiber bond stress – slip

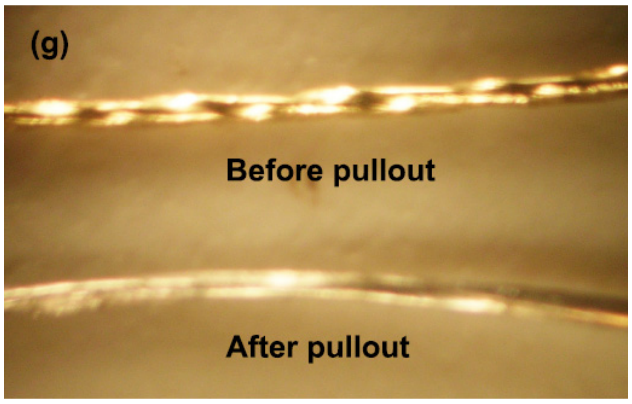

(g) Deformation of Torex fiber during pullout

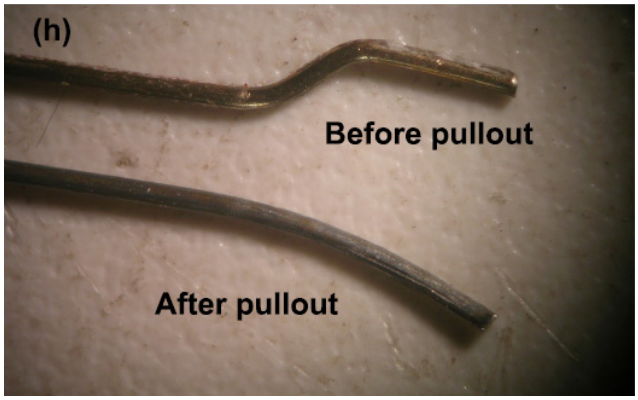

(f) Deformation of Hooked fiber during pullout

Fig. 2.6- Single fiber pullout test results

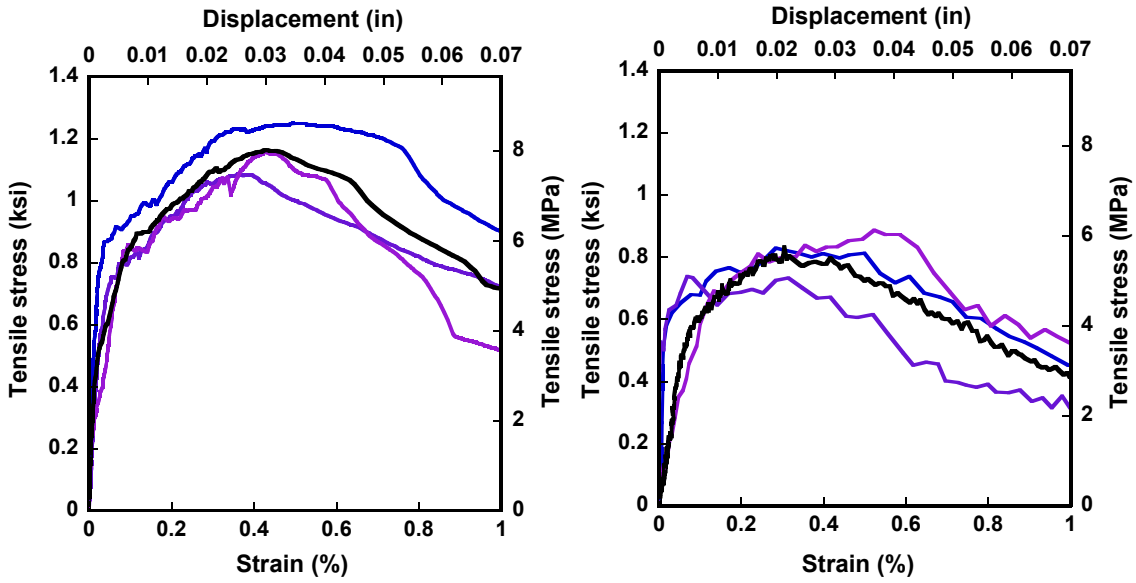

(a) Torex Fiber 2% (b) Hooked Fiber 2%

Fig. 2.7- Tensile stress – strain curve

Cracking spacing and pattern of Torex fiber 2% reinforced specimen

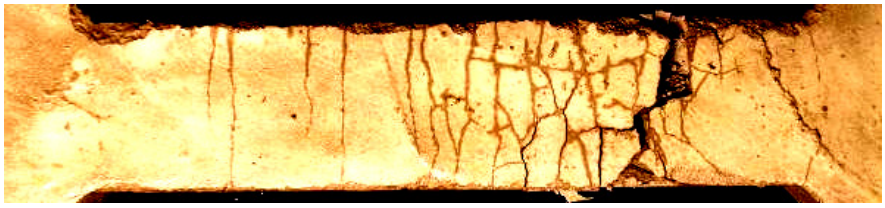

Cracking spacing and pattern of Hooked fiber 2% reinforced specimen

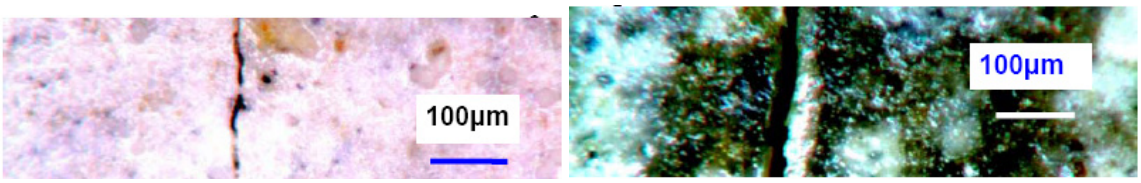

Crack width of Torex fiber 2% and Hooked fiber 2% reinforced specimen

Fig. 2.8- Cracking pattern and crack width

REFERENCES

Naaman, A.E, "A Statistical Theory of Strength for Fiber Reinforced Concrete," Ph.D. Thesis, Massachusetts Institute of Technology, 1972, 196 pages.

Naaman, A.E., "Ferrocement & Laminated Cementitious Composites", Techno Press 3000, Ann Arbor, Michigan, 2000

Naaman, A.E., "Fibers with Slip-Hardening Bond," in High Performance Fiber Reinforced Cement Composites – HPFRCC 3,' H.W. Reinhardt and A.E. Naaman, Editors, RILEM Pro 6, RILEM Publications S.A.R.L., Cachan, France, May 1999, pp. 371-385.

Naaman, A.E., "High Performance Fiber Reinforced Cement Composites," Concrete Structures for the future, IABSE Symposium, Paris, France, September 1987, pp. 371-376

Naaman, A.E., "Reinforcing Mechanisms in Ferrocement," M.S. Thesis, Massachusetts Institute of Technology, Civil Engineering Department, 1970, 152 pages.

Naaman, A.E., and Najm, H., "Bond-Slip Mechanics of steel Fibers in Concrete," ACI Materials Journal, Vol. 88, No.2, April 1991, pp. 135-145.

Naaman, A.E., and Reinhardt, H.W., "Characterization of High Performance Fiber Reinforced Cement Composites," Proceedings of 2nd International Workshop on HPFRCC, Chapter 41, in High Performance Fiber Reinforced Cement Composites: HPFRCC 2, A.E. Naaman and H.W. Reinhardt, Editors, RILEM, No. 31, E. & FN Spon, London, 1996, pp. 1-24.

Naaman, A.E., and Sujivorakul, C., "Pull-out Mechanism of Twisted Steel Fibers Embedded in Concrete "Proceedings of International Conference on Applications of Shotcrete, Tasmania, Australia, April 2001.

Sujivorakul, C, and Naaman, A.E., "Tensile Response of HPFRC Composites using Twisted Polygonal Steel Fibers", accepted for publication in proceedings of Fiber Reinforced Concrete: Innovation for Value, ACI Convention, Toronto, ACI Special Publication, in print, 2003.

Sujivorakul, C., "Development of High Performance Fiber Reinforced Cement Composites using Twisted Polygonal Steel Fibers," Ph.D. Thesis, 2002, University of Michigan, Ann Arbor.

Sujivorakul, C., Waas, A.M., and Naaman, A.E., "Pullout Response of a Smooth Fiber with End Anchorage," Journal of Engineering Mechanics, American Society of Civil Engineers, Vol. 126, No. 9, September 2000, pp.986-993.

CHAPTER III

HIGH TENSILE STRENGTH STRAIN-HARDENING FRC COMPOSITES WITH LESS THAN 2% FIBER CONTENT [2]

ABSTRACT

Tensile strain hardening FRC composite with a tensile strength exceeding 10 MPa and a tensile strain capacity close to 0.5% was developed using only 2% fiber volume fraction in high strength matrix (84 MPa). Two high strength steel fibers, Hooked and Torex fiber, of tensile strength exceeding 2000 MPa were selected. In single fiber pullout tests, both fibers showed slip-hardening behavior without fiber failure, and the Torex fiber showed high slip capacity before bond decay generating large amount of pullout work or energy. In direct tensile tests of bell-shaped specimens, the use of both high strength steel Hooked and Torex fiber led to strain hardening-behavior. In some cases, strain-hardening was achieved with a fiber volume fraction of only 1%. However, there were clear differences in the cracking behavior of the composite depending on the type of fiber. With Torex fibers at 2% fiber content, the crack spacing was less than 4.5 mm and

[2] D. Kim, A. E. Naaman, and S. El-Tawil, "High tensile strength strain hardending FRC Composites with less than 2% fiber content," in Proceeding of Second International Symposium on Ultra High Performance Concrete, Germany, E. Fehling, M. Schmidt and S. Stűrwald, Co-Editor, Kassel University Press GmbH, Heft 10, No. 10, March 2008, pp. 169-176

crack width prior to maximum load was less than 21 microns; the corresponding values for the high strength hooked fiber were 6.5 mm and 29 microns respectively.

3.1 INTRODUCTION

Much research has worked to increase the strength and ductility of concrete and cementitious composites. As a result, high performance concretes (HPC) and ultra-high performance concretes (UHPC) were developed with the aid of water reducing agents, chemical admixtures, and the addition of very fine fillers. HPC and UHPC are usually first characterized by their compressive strength. Initially HPC had compressive strengths ranging between 40 and 70 MPa. For UHPC, strengths in excess of 200 MPa have been attained. Such high strength is expected to reduce the required section size of reinforced and prestressed concrete structural members such as bridge girders, beams and columns. However UHPCs are extremely brittle in both tension and compression. Adding fibers to such matrices improves their ductility and fracture properties. So far, ultra high performance fiber reinforced cement (UHPFRC) composites cannot achieve strain-hardening behavior in tension without using high fiber contents (ranging from 5% to 11% by volume) such as in the examples of SIFCON (slurry infiltrated fiber concrete), SIMCON (slurry infiltrated mat concrete) and $CEMTEC_{multiscale}$ (Multiscale Cement Technical Composites). The properties and applications of SIFCON were first reported by Lankard (1985). The tensile and compressive behavior of SIMCON were reported by Krstulovic and Al-Shannag (1997) and Krstulovic and Malak (1999).

Naaman and Homrich (1989) described experimental studies on the tensile behavior of SIFCON and proposed a model predicting the ascending branch of its tensile stress-

strain curve. Naaman et al. (1992) also investigated the flexural behavior of reinforced concrete beams in a SIFCON matrix. Rossi (2005) introduced new cement composites called $CEMTEC_{multiscale}$ by using three different types of steel fibers with 11% total fiber volume fraction; Rossi et al (2005) reported that $CEMTEC_{multiscale}$ can achieve 50-58 MPa modulus of rupture in bending and more than 200 MPa compressive strength. Recently, several researchers reported on the mechanical, compressive and time dependent behavior of UHPFRC (Habel et al. (2006), Graybeal (2007), and Habel et al. (2006)). Behloul (2007) described many applications of Ductal, a type of UHPFRC with moderate fiber content, in bridges and footbridges and showed that Ductal technology can achieve 200 MPa compressive strength, 45 MPa flexural strength and 11 MPa tensile strength**.**

Since each 1% of steel fibers usually cost more than the entire cement matrix, there is urgent need to minimize the cost of the composite for practical applications. The main objective of this study was to develop a tensile strain hardening Fiber Reinforced Cementitious (SH-FRC) composites with a tensile strength exceeding 10 MPa, a corresponding tensile strain capacity close to 0.5%, and a fiber content less than 2% by volume. The compressive strength of the matrix described in this study was about 84 MPa. While higher compressive strengths could have been used, they would generate significantly higher fiber bond strengths (adhesive, frictional and mechanical) which lead in some cases to failure of the fibers upon matrix cracking and during fiber pull-out. To minimize fiber failure, two steel fibers of tensile strength exceeding 2000 MPa were selected; one fiber was circular in cross-section and hooked at its ends, and the other was triangular in cross-section and twisted along its longitudinal axis (here called Torex).

Pull-out tests of single fibers were carried out as well as direct tensile tests on cement matrices containing 1% and 2% fibers by volume.

3.2 SLIP HARDENING AND STRAIN HARDENING

Strong correlation between single fiber pullout behavior and tensile behavior of FRC composites was reported in Chapter II (also by Kim et al. in 2007). Used two types of high strength deformed steel fibers, high strength Hooked and Torex fiber, they showed that slip hardening pullout behavior with large slip capacity before bond decay helps achieve strain-hardening FRC composites with high strain capacity in tension accompanied by multiple micro cracks.

Figs. 3.1a and 3.1b show typical single fiber pullout behavior of Hooked and Twisted fiber, respectively. Although both deformed Hooked and Twisted fibers, show slip hardening behavior, the slip capacity of Twisted fiber is much higher than that of Hooked fiber as illustrated in Fig. 3.1. The higher slip capacity of Twisted (Torex) fiber originates from the unique untwisting pullout mechanism which engages the whole embedded length of fiber during fiber pullout, while only a small portion of the fiber length is engaged in hooked fibers (Naaman 1999, Alwan et al. 1999, Sujiravorakul 2001).

The amount of pullout work (or energy) during the pullout described in Fig. 3.1 depends on slip capacity and can be interpreted to derive an equivalent bond strength with the assumption that bond strength remains constant along the fiber embedded length for the selected slip. For any given slip capacity, a different equivalent bond strength can be determined, including the case where the slip is the maximum observed in a typical pull-out test. Kim et al. (2007) suggested equation [3.1] to calculate the equivalent bond strength assuming the maximum slip is equal to the fiber embedded length.

$$\tau_{equivalent} = \frac{8E_{PULLOUT}}{\pi d_f L_f^{\,2}} \qquad [3.1]$$

where, $E_{PULLOUT}$ is Pullout energy, d_f : Fiber diameter and L_f : Fiber length.

Fig. 3.2 shows typical tensile behavior of an FRC composite using Twisted (Torex) fiber with 2% fiber content by volume. Clear strain hardening behavior is observed; the tensile load resistance after first cracking strength σ_{cc} steadily increases up to post cracking strength σ_{pc} and is accompanied with multiple micro-cracks. It is clear that the slip hardening behavior in fiber pullout helps achieve strain hardening behavior in tension.

3.3 EXPERIMENTAL PROGRAM

As mentioned above, two types of high strength steel fibers (Hooked and Twisted) with slip hardening pull-out behavior, were used in a high strength cementitious matrix (84MPa) with 1% and 2% fiber by volume. Single fiber pullout tests and direct tensile tests were carried out using a servo-controlled hydraulic testing machine (MTS810).

3.3.1 Materials

The matrix mix composition and proportions are shown in Table 3.1 and the properties of fibers are shown in Table 3.2. It should be noted that VMA (Viscosity Modifying Agent) was added to the matrix to increase viscosity and ensure uniform fiber distribution in the matrix. The compressive strength of the matrix was measured from 100x200 mm cylinders and this matrix composition is self-consolidating mixture.

3.3.2 Test set-ups and procedure

The geometry of pullout test specimen and test set-up is shown in Fig. 3.3. The embedment length of the fiber was 15mm (= 0.59 inch) and the fiber was placed at the

center of the specimen. The specimen's axis was located along the loading axis and the fiber axis; the fiber was gripped firmly to prevent any slip in the gripping device. The geometry of the double bell end-shaped tensile test specimen and test set up are shown in Fig. 3.4 (Naaman et al. 2007). Two layers of steel wire mesh were used to reinforce the bell shaped ends to minimize failure at the grips and out of the gage length. The gage length was selected to be 178mm (=7 inch), between two infrared markers; displacement between the markers was measured using a non-contacting motion measuring instrument (OPTOTRAK System) placed at about one meter from the specimen; the measurement accuracy was 0.001 mm.

3.3.3 Test results

Pullout load - slip response curves of the high strength steel Hooked and Twisted fiber are shown in Figs. 3.5a and 3.5b, respectively. Note that while the pullout load axis has the same scale for both fibers, the tensile stress induced in the fiber is different because they have different cross-sections. Figure 3.5c compares the average curve derived for each fiber, plotted as pullout tensile stress in the fiber versus slip. It can be observed that the twisted fiber, in which the tensile stress reaches 2000 MPa, is significantly more efficient than the hooked fiber for which the maximum tensile stress reaches 1600 MPa. The average pullout energy (area under the pullout curve) was determined and the equivalent bond strength for each fiber was calculated from Eq. [3.1]. The pullout energy of the Torex fiber was 1635.50 N-mm while that of the Hooked fiber was 713.67 N-mm. The corresponding equivalent bond strength was 15.4 MPa for Torex fiber and 5.05 MPa for high strength Hooked fiber, respectively.

Tensile stress – strain curves and photos illustrating the number of cracks and crack

spacing in each test series are given in Fig. 3.6. Average numerical values of several parameters describing tensile response such as first cracking strength, maximum post cracking strength, strain capacity at maximum post cracking strength and number of cracks (and related crack spacing) are shown in Table 3.3. These values are averaged from at least three specimens. Figure 3.7 illustrates and compares graphically some of the parameters of Table 3.3.

3.4 EVALUATION OF THE EXPERIMENTAL RESULTS

The tensile stress – strain curves observed for all test series showed strain hardening behavior and multiple cracking characteristics, for both 1% and 2% fiber content by volume. While both fibers were effective in developing tensile strain hardening response of the composite, the twisted fiber was much more effective than the hooked fiber (Table 3.3 and Fig. 3.7). For a volume fraction of 2%, the test series with Twisted (Torex) fibers achieved a maximum post-cracking stress of 10.8 MPa, at a strain of about 0.45%, with an average crack spacing of 4.5 mm and an average crack width of 21 micrometer.

3.5 CONCLUSIONS

This study investigated the performance of high strength Hooked and Twisted (Torex) fiber in a high strength cementitious matrix (84 MPa) in both pullout and tensile test.

Although both Hooked and Twisted (Torex) fibers show slip hardening behavior under pullout due to their mechanical bond, Twisted (Torex) fiber led to an equivalent bond strength about 3 times that of the Hooked fiber.

In tensile tests, the use of both Hooked and Twisted (Torex) fiber reinforced specimens led to strain hardening behavior. However, Twisted (Torex) fiber was much more effective than the hooked fiber in terms of maximum tensile strength, strain

capacity and number of cracks within gage length.

Finally, with Twisted (Torex) fibers at 2% fiber content by volume in a high strength cementitious matrix (84MPa), the objective of achieving SH-FRC composites with post-cracking direct tensile strength of about 10 MPa and strain capacity close to 0.5% was attained. At time of this writing a new level of 17 MPa has also been achieved in a SIFCON strain-hardening FRC composite with a fiber volume fraction of 4%, and is being used as a reference base for the next level.

Table 3.1- Composition of Matrix Mixtures by weight ratio and compressive strength

Cement (Type III)	Fly ash	Sand (Flint)	Silica Fume	Super - Plasticizer	VMA	Water	f_c' (MPa)
0.80	0.20	1.00	0.07	0.04	0.012	0.26	84

Table 3.2- Properties of Fibers used in this study

Fiber Type	Diameter (mm)	Length (mm)	Density (g/cc)	Tensile strength, (MPa)	Elastic Modulus, (GPa)
Hooked	0.38	30	7.9	2300	200
Twisted	0.3*	30	7.9	2760**	200

* Equivalent diameter ** Tensile strength of the fiber after twisting

Table 3.3- Average experimental results obtained from the tensile tests

Fiber type & Volume fraction	First cracking strength	Post Cracking Strength	Strain Capacity	Number of cracks	Crack Spacing	Average Crack Width
	(MPa)	(MPa)	(%)	(EA)	(mm)	(micrometer)
Hooked 1%	4.299	5.207	0.301	15	11.85	37
Hooked 2%	5.143	7.562	0.387	27	6.56	29
Twisted 1%	4.264	5.499	0.616	23	7.74	49
Twisted 2%	6.997	10.778	0.452	39	4.56	21

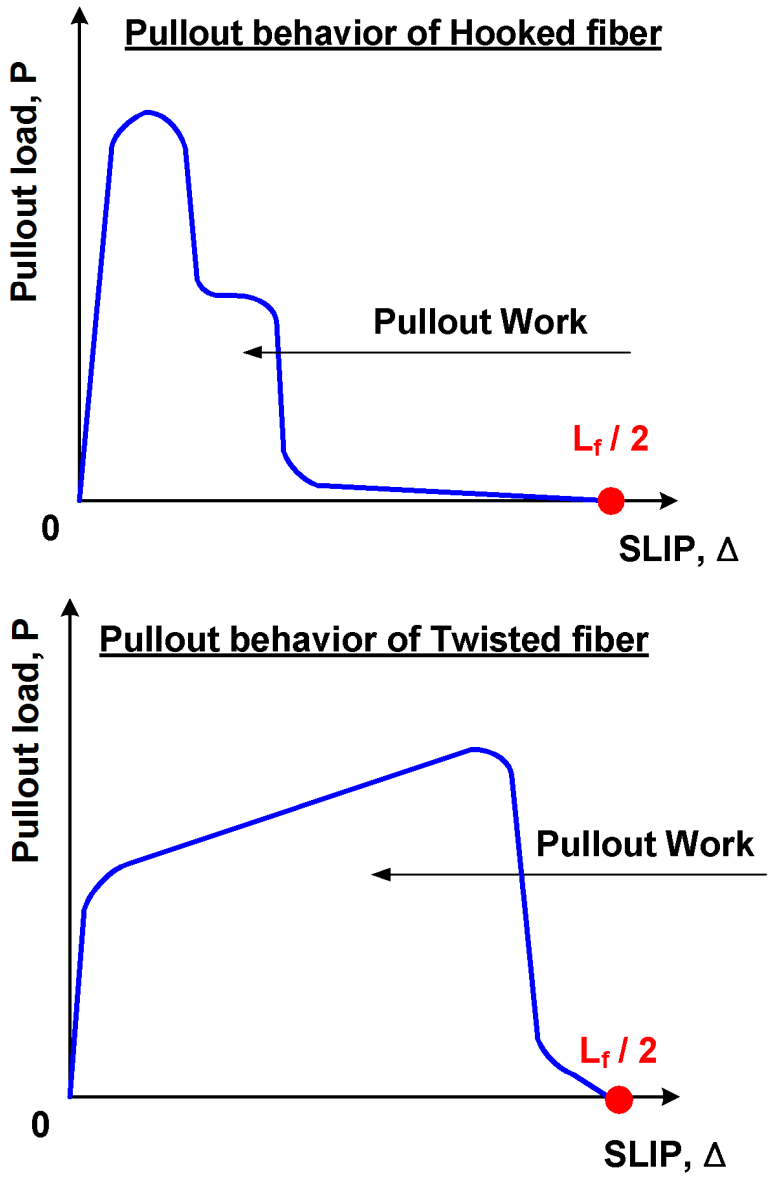

Fig. 3.1- Typical pullout behavior of Hooked and Twisted fiber

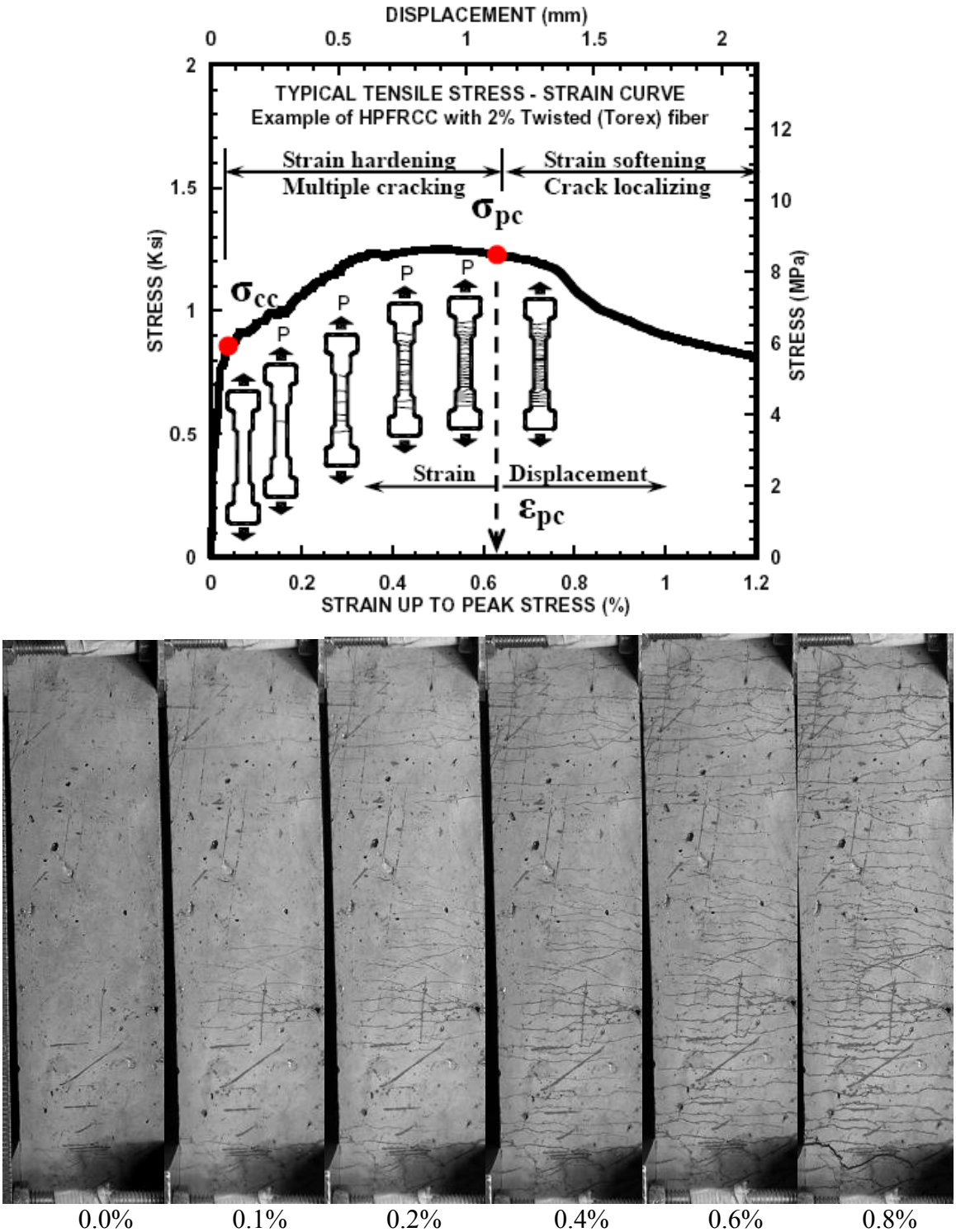

Fig. 3.2- Typical tensile behavior of Twisted (Torex) fiber reinforced composites. a) Tensile stress-strain response up to peak stress. b) Cracking behavior at different strain levels

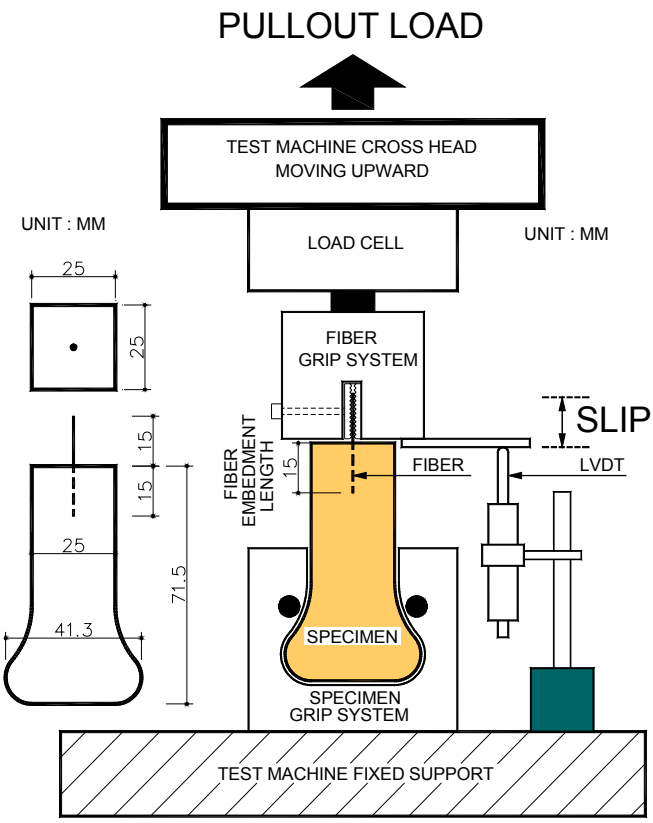

Fig. 3.3- Pull out test specimen and setup

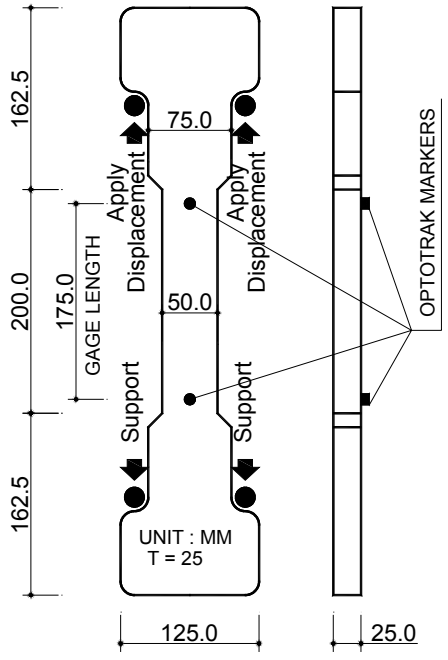

Fig. 3.4- Tensile test specimen and setup

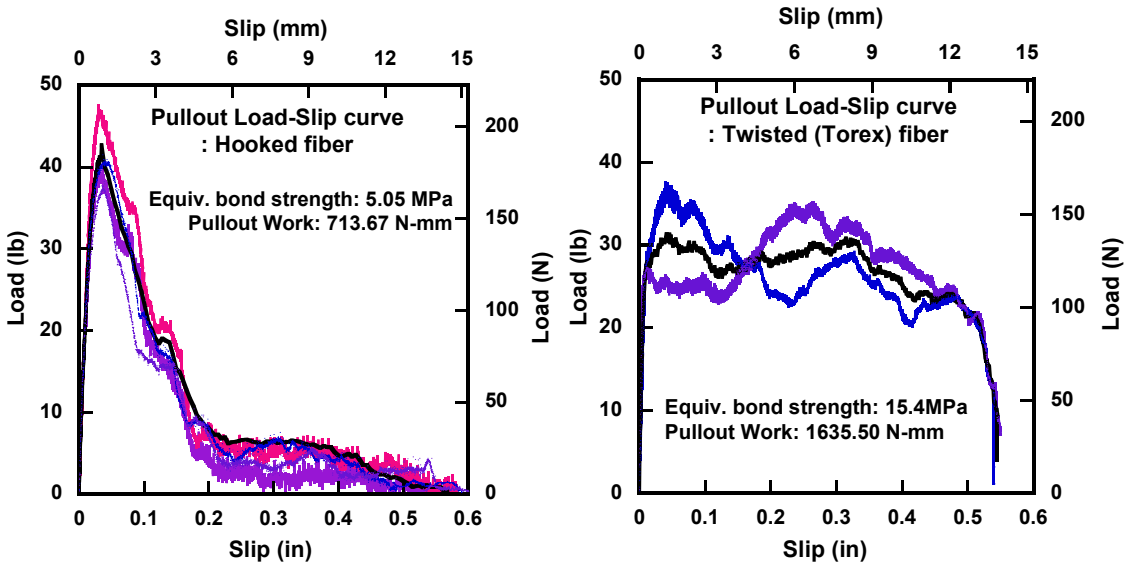

(a) Pullout Load - Slip curve, Hooked fiber (b) Pullout Load - Slip curve, Twisted fiber

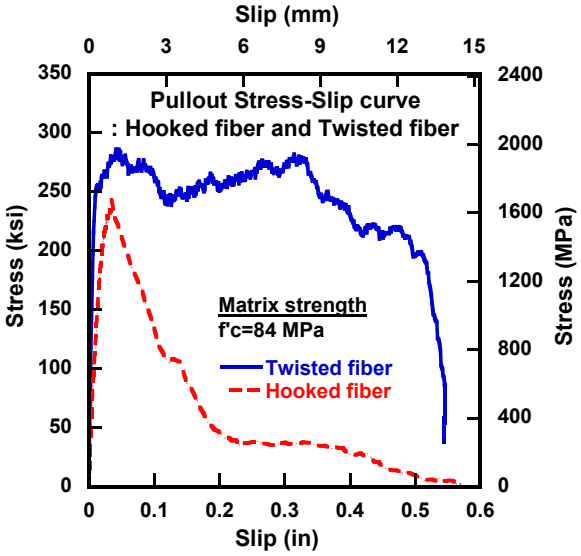

(c) Average Pullout Stress - Slip curve for both Hooked and Twisted fiber

Fig. 3.5- Pullout behavior of both Hooked and Twisted fiber

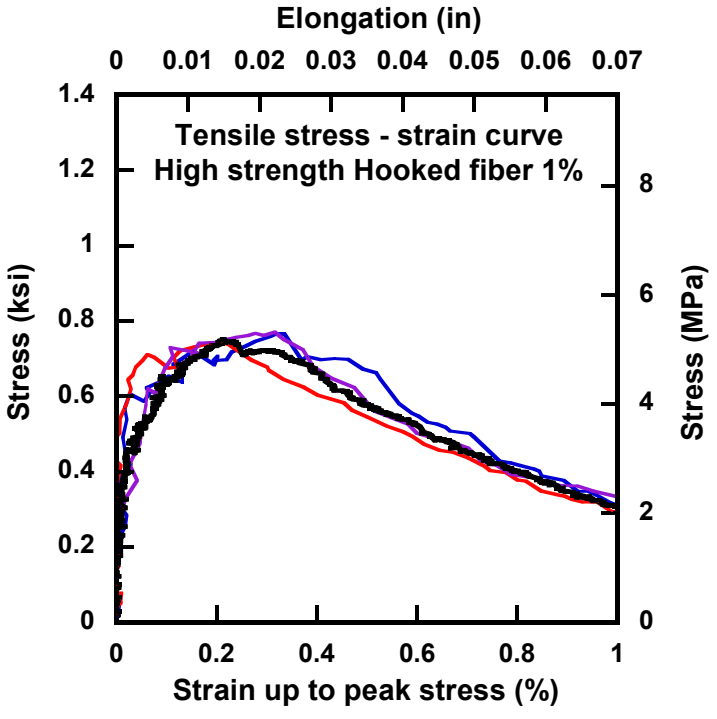

(a) High strength Hooked fiber 1%

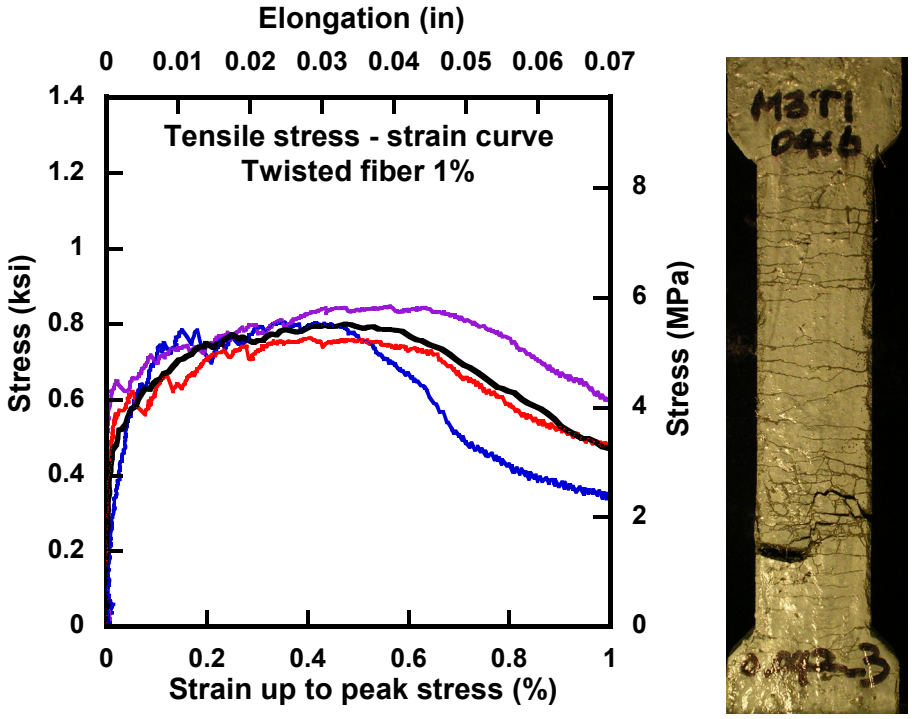

(b) Twisted (Torex) fiber 1%

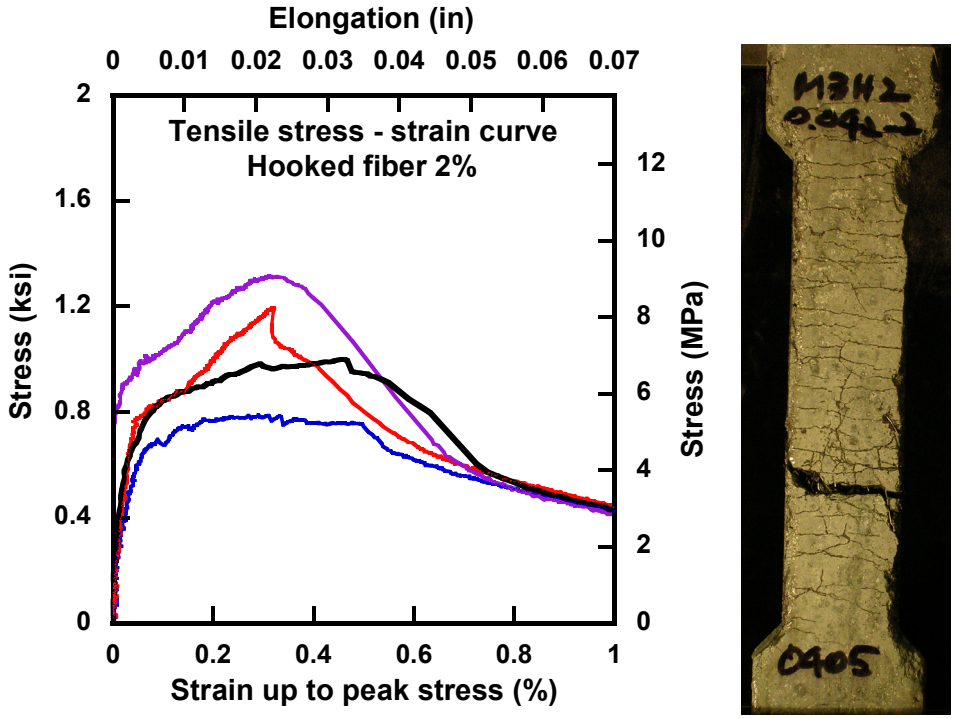

(c) High strength Hooked fiber 2%

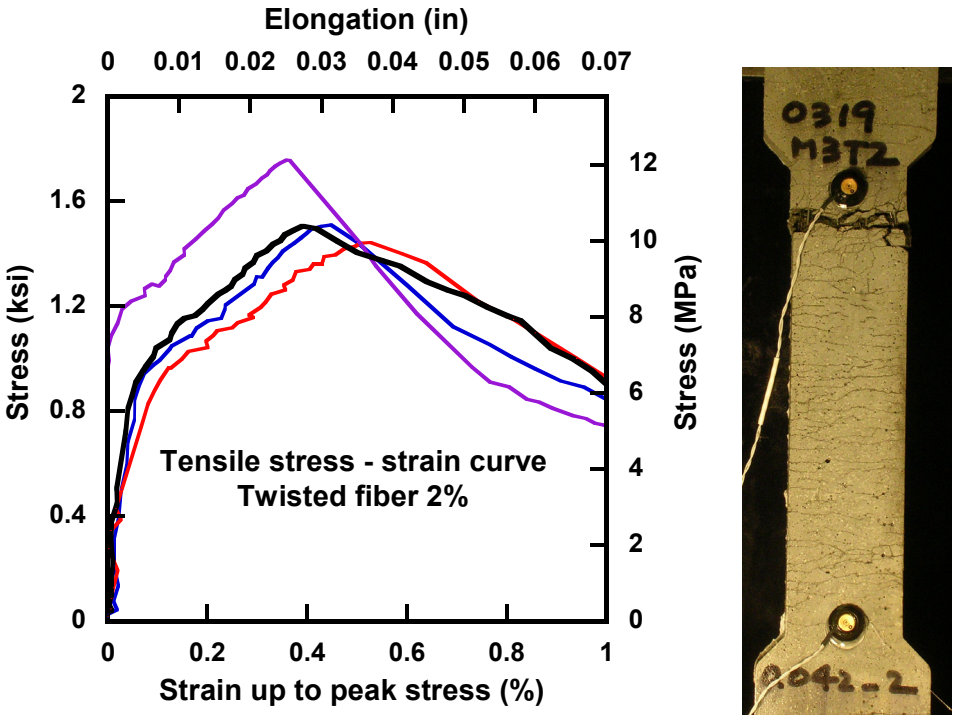

(d) Twisted (Torex) fiber 2%

Fig. 3.6- Tensile stress – strain curve and cracking behaviour

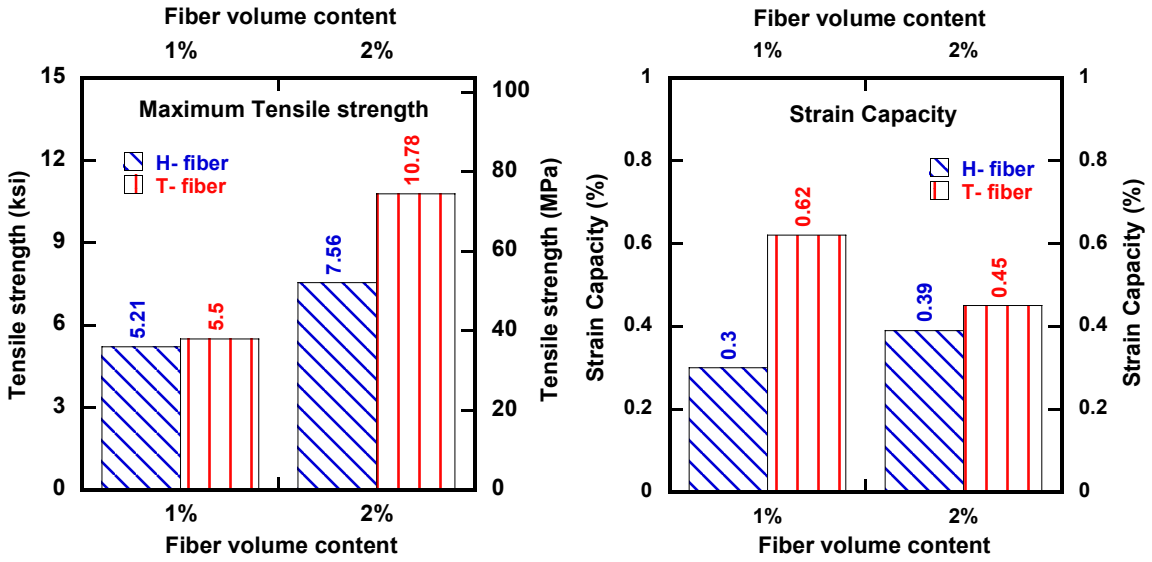

(a) Maximum Tensile strength (b) Strain capacity

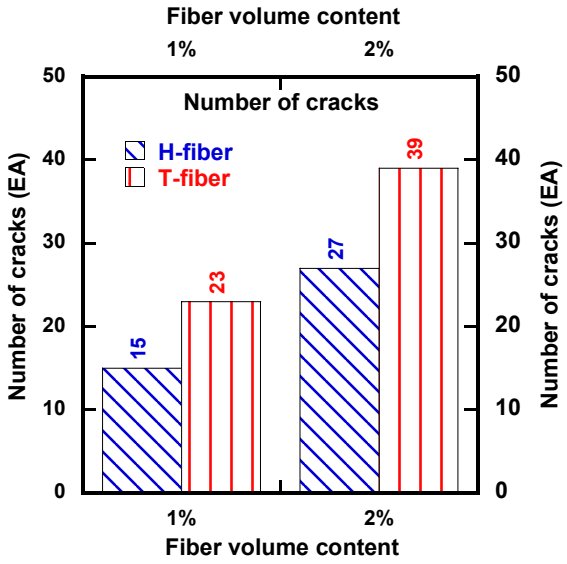

(c) Number of cracks

Fig. 3.7- Effect of fiber type and volume fraction

REFERENCES

Alwan, J. M. Naaman, A. E., and Guerrero, P., "Effect of Mechanical Clamping on the Pull-out Response of Hooked Steel Fibers Embedded in Cementitious Matrices.," Concrete Science and Engineering, Vol. 1, Mar. 1999, pp. 15-25

Graybeal, B. A., "Compressive behavior of Ultra-High-Performance Fiber-Reinforced Concrete," ACI Materials Journal, Vol. 104, No. 2, Mar.-April 2007, pp. 146-152.

Habel, K., Denarie, E. And Brühwiller, E., "Time dependent behavior of elements combing ultra-high performance fiber reinforced concretes (UHPFRC) and reinforced concrete," Materials and Structures, Vol. 39, No. 5, June 2006, pp. 557-569.

Habel, K., Viviani, M., Denarie, E. And Brühwiller, E., "Development of the mechanical properties of an Ultra-High Performance Fiber Reinforced Concrete (UHPFRC)," Cement and Concrete Research, Vol. 36, Issue 7, July 2006, pp. 1362-1370.

Kim, D., El-Tawil, S. and Naaman, A.E, "Correlation between single fiber pullout behavior and tensile response of FRC composites with high strength steel fiber", in Prints, HPFRCC5, Mainz, Germany, July 10-13, 2007, pp. 67-76.

Krstulovic-Opara, N. and Al-shannag M. J., "Compressive behaviour of Slurry Infiltrated Mat Concrete," ACI Materials Journal, Vol. 96, No. 3, May-June 1999, pp. 367-378.

Krstulovic-Opara, N. and Malak, S., "Micromechanical Tensile behaviour of Slurry Infiltrated Continuous-Fiber-Mat Reinforced Concrete (SIMCON)," ACI Mat. Journal, 94(5), Sep.-Oct. 1997, pp. 373-384.

Lankard., D. R., "Slurry Infiltrated Fiber Concrete (SIFCON) : Properties and Applications," Very high strength cement based materials, Vol. 42, Materials Res. Society, Pittsburgh, 1985, pp. 277-286.

Naaman, A. E. and Homrich, J. R., "Tensile Stress-Strain Properties of SIFCON," ACI Material Journal, Vol. 86, No. 3, May-June 1989. pp. 244-251.

Naaman, A. E., "Fibers with slip-hardening Bond," in High Performance Fiber Reinforced Cement Composites – HPFRCC 3," H.W. Reinhardt and A.E. Naaman, Editers, RILEM Pro 6, RILEM Publications S.A.R.L., Cachan, France, May 1999, pp. 371-385.

Naaman, A. E., Fischer, G. and Krstulovic-Opara, N., "Measurement of Tensile properties of fiber reinforced concrete : Draft submitted to ACI Committee 544," HPFRCC5, Mainz, Germany, July 10-13, 2007, pp. 3-12. Give here the exact proceedings. You have them.

Naaman, A. E., Reinhardt, H. W. and Fritz, C., "Reinforced Concrete Beams with SIFCON Matrix," ACI Structural Journal, Vol. 89, No. 1, Jan.-Feb. 1992, pp. 79-88.

Rossi, P., "Development of new cement composite materials for construction," Proceedings of the Institution of Mech. Engineers, Part L, Jnl. of Materials: Design and Applications, 219(1), 2005, pp. 67-74.

Rossi, P., Arca, A., Parant, E. And Fakhri, P., "Bending and Compressive behaviors of a new cement composites," Cement and Concrete Research, 35(1), Jan. 2005, pp. 27-33.

Sujiravorakul, C., “Development of High Performance Fiber Reinforced Cement Composites Using Twisted Polygonal Steel Fibers,” Ph.D. thesis, University of Michigan, Ann Arbor, Feb. 2001. 230pages.

CHAPTER IV

COMPARATIVE FLEXURAL BEHAVIOR OF FOUR FIBER REINFORCED CEMENTITIOUS COMPOSITES [3]

ABSTRACT

This chapter investigates the flexural behavior of Fiber Reinforced Cementitious Composites [FRCC] with four different types of fibers and two volume fraction contents (0.4% and 1.2%) within a nominally identical mortar matrix (56 MPa compressive strength). The four fibers are high strength steel twisted (T-), high strength steel hooked (H-), high molecular weight polyethylene Spectra (SP-) and PVA fibers. The tests were carried out according to ASTM standards. The T-fiber specimens showed best performance in almost all aspects of behavior including load carrying capacity, energy absorption capacity and multiple cracking behavior, while the PVA fiber specimens exhibited comparatively the worst performance in all aspects of response. The only category in which SP-fiber specimens outperformed T-fiber specimens was deflection capacity, where SP-specimens exhibited the highest deflection at maximum load. By comparing the test results to data from an additional test program involving the use of a

[3] D. Kim, A. E. Naaman, and S. El-Tawil, "Comparative flexural behavior of four fiber reinforced cementitious composites", Cement and Concrete Composites, Vol.30, No.10, November 2008, pp.917-928.

higher strength mortar (84 MPa) with both H- and T-fibers, it is shown that, again, T-fibers perform significantly better than H-fibers in a higher strength matrix. The test results from both experimental programs were used to critique the new ASTM standard [C 1609/C 1609M – 05], and a few suggestions were made for improving the applicability of the standard to deflection hardening FRCCs.

4.1 INTRODUCTION

The addition of a relatively small quantity of short random fibers to a cementitious matrix is known to improve the mechanical response of the resulting product, commonly known as Fiber Reinforced Cementitious Composite (FRCC). FRCCs have the potential of exhibiting higher strength and ductility in comparison to unreinforced mortar or concrete, which fail in tension right after the formation of a single crack. The performance of FRCC could be improved to the point where it can exhibit deflection hardening response in bending accompanied by multiple cracks after initial cracking. In such a case, FRCC are known as deflection hardening FRCC, or DHFRCC. Naaman (2002) discussed the relationship between DHFRCC and strain-hardening FRCC in direct tension. He showed that in order for the bending response to be deflection hardening, the average post cracking strength in tension should be about only a third of the cracking strength. Thus, a much smaller amount of fibers is required to obtain deflection-hardening response than to obtain strain-hardening behavior. Furthermore, Naaman (2002) formulated an equation for the critical volume fraction of fibers to achieve deflection-hardening behavior. Recently, Soranakom and Mobasher (2008) also discussed the correlation of tensile and flexural responses of FRCC and provided closed form equations to predict flexural behavior of FRCC based on its uniaxial tension and

compression response. They also suggested that the tensile behavior of FRCC can be back-calculated from convenient flexural tests.

The performance of FRCC depends on many factors, such as fiber material (e.g., strength, stiffness, Poisson's ratio), fiber geometry (e.g., smooth, end hooked, crimped, twisted), fiber volume content, matrix properties (e.g., strength, stiffness, Poisson's ratio) and interface properties (e.g., adhesion, frictional and mechanical bond). Clearly, for a given matrix, the type and quantity of fibers are key parameters influencing the performance of FRCC and their cost. Everything else being equal, using a low fiber volume fraction, while still attaining strain hardening or deflection hardening response, is attractive from the cost point of view.

Although many researchers have conducted bending tests and reported the flexural response of FRCC, most used different sizes of specimen, matrix composition, and fiber and volume content in their experiments. Often, only one fiber type or material was considered and no attempt was made to compare performance with other fibers types or materials. Also, some researchers did not follow standard test procedures, e.g. as specified by ASTM. In addition, most of experimental studies that investigated the effect of fiber types were performed approximately a decade ago. Therefore, the types of fiber investigated in prior research are quite different from the high performance fibers used in this study. This situation made it difficult for the writers to isolate the effect of fiber type on the flexural performance of FRCC and motivated the experimental study reported in this paper, which focused on the flexural performance of FRCC involving four high performance fibers within a nominally identical mortar matrix (56 MPa compressive strength).

The main objective of this research is to investigate the influence of fiber type and fiber volume content on the bending response of four FRCCs. Testing and analysis of results were carried out according to ASTM standard C 1609/C 1609M – 05 (2006). The research is geared towards mixtures showing deflection hardening behavior with low to moderate fiber contents, here, 0.4% and 1.2% by volume. To gain further insight into the effect of matrix strength, the results of this research are compared to test results from a related program involving the use of a higher strength matrix (84 MPa compressive strength). The test results lead to some suggestions to improve current standard ASTM C 1609.

4.2 BENDING BEHAVIOR OF FRCC BEAMS

Much research on the bending behavior of FRCC has been carried out over the past four decades in the US and elsewhere. Soroushian and Bayasi (1991) investigated the effect of fiber-type on the general performance of fiber reinforced concrete. They used different types of steel fibers, including straight-round, crimped-round, crimped-rectangular, hooked-single, and hooked-collated fibers with 2% fiber volume content. They reported that the overall workability was independent of fiber type except for crimped fiber. They also noted that hooked fibers showed better performance than straight and crimped fibers.

Gopalaratnam et al. (1991) pointed out the importance of accurate deflection measurement in estimating toughness and other parameters describing flexural behavior of FRCC. They also noted that the effect of fiber type, fiber volume fraction and specimen size could be discerned from toughness measures. Balaguru et al. (1992) investigated the flexural toughness of FRCC with deformed steel fibers using the

procedure for deflection measurement suggested by Gopalaratnam et al. (1991). They investigated three types of fibers: hooked-end, corrugated and end deformed steel fibers. In computing toughness, they used the I5 and I10 indices defined according to the ASTM C 1018 (1998) procedure. Their results indicated that the toughness indices did not reflect the variations observed in the load-deflection curves. They also noted that, of the three types of fibers investigated, hooked-end fibers were the most effective in improving toughness.

Banthia and Trottier (1995) pointed out several difficulties in both ASTM C 1018 and JSCE SF-4 methods for FRC toughness characterization and suggested an alternative technique. For the former method (ASTM C 1018), they discussed the difficulty of measuring deflection correctly, and accurately identifying the first cracking point. For the latter (JSCE SF – 4), they showed that the Flexural Toughness (FT) factor depends upon the geometry of the specimen and noted that the end–point used in the computation, at span-over-150, is arbitrary and actually much greater than the deflection at serviceability.

Several points necessary to estimate the performance of deflection hardening FRCC were discussed by Naaman (2002). In addition to the Toughness Index for describing the toughness of FRCC, he recommended using the average post cracking strength or surface energy as additional parameters. He also defined ductility as the ratio of total energy consumed up to a certain point to the elastic energy and mentioned that the scale effect and testing procedure could influence multiple cracking in strain hardening or deflection hardening FRCC.

Chandrangsu and Naaman (2003) compared the performance of three different fibers, Twisted (Torex), Spectra and PVA fiber, in both tensile and bending response using two

different specimen sizes. The length of the fibers was 30mm for Torex fibers, 38mm for Spectra fibers, and 12mm for PVA fiber. The smaller bending specimens had a 75mm×12.5mm thin rectangular section with 225mm span length, while the larger size bending specimens had a 100mm×100mm square section with 300mm span length. The twisted (Torex) fibers generated best performance in both tensile and bending test among the three fibers considered. In addition, a strong size effect was noticed especially in the bending test, in terms of strength and deflection. The smaller bending specimens showed 80% higher modulus of rupture, and 500% higher deflection (actual displacement not normalized) at maximum load compared with the larger specimens.

4.3 PARAMETERS DESCRIBING FLEXURAL BEHAVIOR OF FRCC

The bending behavior of FRCC can generally be classified as either deflection softening, [(a) curve in Fig. 4.1] or deflection hardening [(b) curve in Fig. 4.1] (Naaman and Reinhardt, (2006)). FRCC showing deflection hardening behavior generate a higher load carrying capacity after first cracking compared with normal concrete or deflection-softening FRCC. In this research, the first cracking point is defined as the point where nonlinearity in the load–deflection curve becomes evident. This point is termed 'Limit of Proportionality (*LOP*)' according to the previous ASTM standard C 1018 – 97 (1998). The new ASTM standard C 1609/C 1609M – 05 (2006) uses the first peak point, defined as a point where the slope is zero, which is inappropriate for use with materials exhibiting deflection hardening with multiple micro cracks. In other words, it is hard to pinpoint the first peak strength as required by ASTM standard C 1609/C 1609M – 05 (2006) if the bending behavior of the material shows stable deflection hardening as shown in the upper curves of Fig. 4.1. Therefore, *LOP* is used in this work instead of first peak strength. The

load value at *LOP* is termed P_{LOP} and the corresponding deflection value is δ_{LOP} in Fig. 4.1. The stress obtained when the first cracking load is inserted into Equation [4.1] is defined as the first crack strength, f_{LOP}. The energy equivalent to the area under the load-deflection curve up to *LOP* is defined as first-crack toughness $Tough_{LOP}$. This definition is consistent with the ASTM standard definition for toughness at various points of the load-deflection curve, as explained farther below. From ASTM C 1609/C 1609M – 05 (2006), the stress at LOP is obtained from:

$$f_{LOP}=P_{LOP}.\ \frac{L}{bh^2} \qquad [4.1]$$

where, L is span length, b is the width of specimen and h is the height of specimen.

The 'Modulus of Rupture (*MOR*)' is defined as the point where softening starts to occur after point *LOP* as shown in Fig. 4.1. Besides the *LOP* and *MOR* points, six other points are defined as follows:

d5 : Point at a deflection of 3.0 times δ_{LOP},

d10 : Point at a deflection of 5.5 times δ_{LOP},

d20 : Point at a deflection of 10.5 times δ_{LOP},

L/600 : a net deflection equal to 1/600 of the span. [0.5mm (0.02in) for a specimen clear span of 300mm (12in)]

L/150 : a net deflection equal to 1/150 of the span. [2mm (0.08in) for a specimen clear span of 300mm (12in)]

L/100 : a net deflection equal to 1/100 of the span. [3mm (0.12 in) for a specimen clear span of 300mm (12in)]

The ASTM Standard C 1609 recommends the *L/600* and *L/150* points. However, it was found in this investigation that these points are insufficient to fully differentiate

behavior between different fibers, and one additional point was added, namely *L/100*. For all tested specimens, load, stress and toughness (energy) quantities were computed from the test results for the six points listed above in addition to *LOP* and *MOR*. To facilitate referring to various quantifies, the prefixes *P*, *f*, *δ*, *Tough* are used to designate load, stress, displacement and toughness associated with a specific point (as was done for *LOP*).

4.4 EXPERIMENTAL PROGRAM

The matrix used for all specimens had a nominal compressive strength of 8.1 ksi (56 MPa). The fibers used were high strength steel twisted (T-), high strength steel hooked (H-), high molecular weight polyethylene Spectra (SP-), and PVA fibers and were applied in two fiber volume contents (0.4% and 1.2 %) leading to eight series of bending specimens designated as shown in Table 4.1. Two specimens per series were prepared for T- and H-fiber series, while three specimens per series were used in the SP- and PVA-fiber series. Fewer specimens were used in the T- and H-fiber series because prior tests showed very consistent results. Table 4.2 provides the mortar mixture composition for the matrix used and its average compressive strength. Fiber properties are given in Table 4.3, and Fig. 4.2 shows pictures of the T-, H-, SP- and PVA fibers used. A servo-hydraulic testing machine (MTS 810) running in displacement control was used to conduct the bending tests. To reduce testing time, the rate of net displacement increase was taken as 0.25mm/min (0.01 inch/min), which is somewhat higher than the rate of 0.10mm/min (0.004 inch/min) recommended in ASTM C 1609/C 1609M – 05 (2006).

4.4.1 Materials and Specimen Preparation

A Hobart type laboratory mixer was used to prepare the mix. Cement, fly-ash and

sand were first dry-mixed for about 2 minutes. Water mixed with superplasticizer and Viscosity Modifying Agent (VMA), was then added gradually and mixed for another 5 to 10 minutes. The VMA was added into the matrix mixture to increase viscosity, prevent fiber sinking and improve fiber distribution as noted by Ozyurt et al. (2007). When the mortar started to show adequate flowability and viscosity, both of which are necessary for good workability and uniform fiber distribution, fibers were dispersed carefully by hand into the mortar mixture. The cementitious mixture with fibers was then carefully placed in a mold by using a wide scoop and vibrated using a high frequency vibrating table. Sufficient time of vibration was provided to guarantee suitable consolidation and to prevent fiber protrusion from the finished surface. During mixing and placing of the fresh mixture, no steel fiber gravitation was observed and uniform fiber distribution was apparent. Specimen casts were covered with plastic sheets and stored at room temperature for 24 hours prior to demolding. The specimens were then placed in a water tank for an additional 4 weeks. All specimens were tested in a dry condition at the age of 32 days, which allowed 4 days for drying in a laboratory environment. Two to three layers of polyurethane were sprayed on the surface of the specimens after drying to facilitate crack detection.

4.4.2 Test set-ups and procedure

The geometry of the test specimen and the test setup are shown in Fig. 4.3. The size of beam used is 100×100×350 mm (4×4×14 in) in accordance with ASTM standard C 1609/C 1609M – 05. The clear span is 300mm (12 in). Before testing, specimens are rotated 90^{o} from their casting position to reduce the effects of casting direction on the test results. A special test frame was used to measure the center deflection as shown in Fig.

4.3. This frame made it possible to eliminate extraneous deformations such as deformation from seating or twisting of the specimen. The frame was located at mid-depth of the specimen using four screws at points A and B as shown in Fig. 4.3. Only two of the screws provided a fixed restraint against displacement, while the two other allowed horizontal displacement. Deflection was measured from an LVDT attached to the frame and the load signal was measured from a load cell directly attached to the bottom of the cross head. A 5 Hz data acquisition frequency was used to record static load and deflection signals.

4.4.3 Test results and General discussion

The flexural response of all test series is illustrated by the load – deflection curves in Fig. 4.4. Each load – deflection curve in the figure is averaged from two or three specimens as previously discussed. Detailed information about the test results are also documented in Tables 4.4 and 4.5, which give averaged values of the parameters characterizing the flexural behavior of FRCC at the 8 points previously defined.

Two different scales are used for the load axes of the graphs in Figs 4.4a and 4.4b, since a significant difference in load carrying capacity was noted for the different fiber volume contents studied. As illustrated in Fig. 4.4a, even though the test series demonstrated a wide range of performance, all test series with 1.2% fiber volume content exhibited deflection hardening behavior. Of the series with 0.4% fiber volume content (Fig. 4.4b), three series (T04, H04, and SP04) generated deflection hardening behavior while only PVA04 resulted in deflection softening response. The deflection hardening series (T04, H04, and SP04) exhibited similar load – deflection responses, unlike the test series with 1.2 % fiber volume content, which exhibited different load-deflection

characteristics.

In comparing the flexural performance according to the type of fiber, the load – deflection curves in Figs. 4.4a and 4.4b illustrate that T-fiber reinforced specimens produced the highest load carrying capacity and *MOR* compared with other series. However, SP-fiber specimens showed the best deflection capacity at *MOR*. The *MOR* for T-fiber specimens was almost three times higher than that observed for specimens with PVA fiber at both fiber volume contents.

The cracking behavior (crack width, spacing, number, shape) of FRCC specimens is investigated because it is one of the main parameters characterizing the performance of each fiber type. It is clear from Fig. 4.5 that there is a large variation in the cracking response based on fiber type and volume content. Indeed, all test series showed multiple cracks except series PVA04, which responded in a deflection-softening manner as previously indicated. Generally, specimens with higher fiber volume content exhibited more cracks than specimens with lower fiber volume content. In addition, specimens with T- and SP-fibers exhibit the highest number of cracks. Specimens with PVA fibers produced only 2-3 cracks in specimens with 1.2% fiber volume content and only one major crack (with immediate localization) in specimens with 0.4% fiber volume content. Details of the multiple cracking responses of the T12 and SP12 series are shown in Fig. 4.5 (i) and (j).

4.4.4 Load Carrying Capacity (Equivalent Bending Stress)

The effect of fiber type on the equivalent bending stress is illustrated in Fig. 4.6. Eight equivalent bending stress values were calculated from the bending loads at different deflection points using equation (1). The deflection points were selected from the load –

deflection curves of the test series as previously explained. Figs. 4.6(a) and 4.6(c) describe the development of flexural load resistance in the ascending range of the load – deflection curves, while Figs. 4.6(b) and 4.6(d) illustrate the effect of fiber type on the different softening tendencies of load resistance in the descending range of the load – deflection curves.

Fig. 4.6(a) shows the equivalent bending stress in the test series with 1.2% fiber volume content up to and including the *L/600* deflection point, while Fig 4.6(b) shows the equivalent bending stress at *MOR*, *L/150* and *L/100*. This same arrangement is used for series with 0.4% fiber volume content in Figs 4.6(c) and 4.6(d).

In Fig. 4.6(a), the effect of the types of fiber on the equivalent bond strength at *LOP* is not apparent for all series with 1.2% fiber volume content. For example, f_{LOP}, is 2.62MPa for T12, 2.60MPa for H12, 2.76MPa for SP12 and 3.13MPa for PVA12. A more noticeable effect of fiber type is observed as the deflection increases following *LOP*. This result shows that the effect of fiber reinforcement is activated primarily after *LOP* through fiber bridging and that the bridging forces are highly dependent upon the type of fiber. The equivalent elastic bending strength values at other deflection points of interest, *d5*, *d10*, *d20* and *L/600* are documented in Table 4.4 and plotted in Fig. 4.6(a); for example, $f_{L/600}$ is 11.06MPa for T12, 9.64MPa for H12, 6.85MPa for SP12 and 4.62MPa for PVA12. The same trend is also evident at *MOR* as shown in Fig. 4.6(b). Clearly, in terms of strength at *MOR*, T-fibers perform the best while PVA fibers perform the worst. The ratio of their *MOR* is approximately three at 1.2% fiber content, and four at 0.4% fiber content.

Deflection points *L/150* and *L/100* were primarily intended to sample response in the

softening range. While softening at these deformation levels is achieved in most series, Series SP12 is an exception and is still in the hardening range at *L/150* and *L/100*. Displacement at maximum load, δ_{MOR}, for SP12 is 3.05mm (Table 4.4), which is higher than $\delta_{L/100}$ *(= 3mm)*, reflecting the extreme ductility of this series. On the contrary, series PVA12 did not show any residual strength at *L/100* in Fig. 4.6(b) since PVA12 loses most of its load carrying capacity at *L/150*. Breakage of PVA fibers was clearly observed at the major crack opening in PVA series, while, in contrast, series with other fiber types exhibited fiber pullout.

The variation of the equivalent bending stress in the test series with 0.4% fiber volume contents is illustrated in Fig. 4.6(c) and (d). As for the case of lower fiber content, little variation of f_{LOP} with fiber type was observed, although f_{LOP} stresses were somewhat lower than those with higher fiber volume content. As previously indicated, and as shown in Fig. 4.4(b) and Fig. 4.6(c), only PVA04 underwent deflection softening behavior, while all other series exhibited deflection hardening response in spite of the low fiber volume content. The equivalent bending stress values at other pertinent deflection points in the ascending range of the load – deflection curve are also shown in Fig. 4.6(c) and Table 4.5.

Unlike series with a higher fiber volume content, Series T04, H04 and SP04 had similar values of f_{MOR}. For example, as shown in Fig. 4.6(d), f_{MOR} is 7.61MPa, 6.97MPa, 7.89MPa respectively. Fig 4b and Fig. 4.6d show that the softening branches for series T04, H04 and S04 are also quite similar. In contrast, f_{MOR} (= 1.73MPa) is much lower in PVA04, which softens much more quickly than its three other counterparts, as previously indicated.

4.4.5 Energy Absorption Capacity (Toughness)

There is need for high energy absorbing materials that will mitigate the hazards for structures subjected to dynamic loads, such as seismic, impact and blast. Thus comparing energy absorption capacity provides useful information for such applications. The effect of fiber type on energy absorption capacity is illustrated in Fig. 4.7 using toughness values, defined as the area up to a certain deflection under the load – deflection curve. Fig. 4.7(a) shows the effect of fiber type on the toughness of the test series with 1.2% fiber volume content up to and including the *L/600* point (essentially along the ascending branch of the curve), while Fig. 4.7(b) illustrates the toughness as a function of fiber type at *MOR*, *L/150* and *L/100* deflection points on the descending branch of the curve except for series SP12. The same arrangement is used for the series with 0.4% fiber volume content in Figs 4.7(c) and 4.7(d).

As shown in Fig. 4.7(a), toughness values of different fiber reinforced specimens at *LOP* are almost same in all series with 1.2% fibers. The same observation is true for deflection points *d5* and *d10*. However, noticeable differences between specimens with different types of fiber start to occur at *d20* and beyond because the load resistance increases. For example, at point *L/600* in ascending range of load – deflection curve, toughness values are 13.823 N-m for T12, 12.171 N-m for H12, 8.838 N-m for SP12 and 6.479N-m for PVA12, respectively. Thus, for toughness values up to *L/600*, specimens with T-fibers provide the toughest response, while PVA fiber provides the lowest toughness, with H-fiber and SP-fiber specimens in between. As shown in Fig. 4.7(b) and Table 4.4, the same general trend can be observed at *L/150* and *L/100*. However, the situation is different at *MOR*, where specimens with SP-fibers outperform T-fiber specimens and absorb significantly more energy. This is, of course, attributed to the

extreme ductility of Series SP12 in the hardening range.

The variation of toughness in specimens T04, SP04 and H04 is lower than for their counterparts with 1.2% fibers. In addition, different trends were observed. For example, H-fiber specimens slightly outperform specimens with T-fibers at *MOR*. In addition, specimens with SP-fibers continue to outperform T-fiber specimens at *L/150* and *L/100*, which did not occur at 1.2% volume fraction.

4.4.6 Deflection Characteristics

Structural ductility is a function of deflection capacity, which is the motivation for the study in this section. Deflection, δ_{LOP}, at *LOP* is clearly not dependent on the type of fiber or fiber volume content as shown in Fig. 4.8 and Table 4.4 and 4.5. In contrast, the deflection at maximum load, δ_{MOR} is highly dependent upon the type of fiber and volume content. For example, as shown in Fig. 4.8(a), δ_{MOR} is 1.2mm for T12, 0.9mm for H12, 3.05mm for SP12, and 0.6mm for PVA12. Here, SP12 outperforms all other series, again because of its extended deflection hardening range. The best performance for the low fiber content also occurs in specimens with SP- fibers, where δ_{MOR} is 1.0mm for T04, 1.2mm for H04, 1.6mm for SP04, and 0.3mm for PVA04, as shown in Fig. 4.8 (b). In general, it is obvious that the deflection capacity is strongly influenced by fiber content only in the specimens with SP-fibers. In other words, the deflection of specimens at maximum resistance with T-, H- and PVA fibers exhibited lower dependence on fiber content than specimens with SP-fibers.

4.4.7 Strength Ratio and Toughness Ratio

To provide a general idea about the comparative performance of fibers, the strength and toughness of all test series were normalized by the values of PVA fiber reinforced

series, since the strength and toughness of PVA fiber reinforced specimens were the lowest. This was not done for the lower volume fraction because PVA04 produced deflection softening behavior. Strength ratio and toughness ratio are illustrated in Fig. 4.9.

The three equivalent bending stresses for the 1.2% series, $f_{L/600}$, f_{MOR} and $f_{L/150}$, were divided by the equivalent bending stress of PVA fiber reinforced specimen**.** As shown in Fig. 4.9(a), T12 generates an equivalent bending stress at $\delta_{L/600}$ and δ_{MOR} of 2.39 and 2.77 times that of PVA12, respectively. When the deflection reaches $\delta_{L/150}$, T12 showed a strength capacity that is 9.18 times that of PVA12.

The toughness ratio of various series compared to that with PVA fibers at 1.2% fiber content is illustrated in Fig. 4.9 (b). Toughness ratios at $\delta_{L/600}$ and $\delta_{L/150}$ deflections are in following order; T- > H- > SP- > PVA fibers. T12 produced the highest toughness ratio, i.e. 3.70 and 2.13, at deflections $\delta_{L/600}$ and $\delta_{L/150}$, respectively. In comparing toughness, $Tough_{MOR}$, at maximum resistance, SP12 showed the highest toughness ratio due to its high deflection capacity δ_{MOR}.

4.5 COMPARATIVE PERFORMANCE OF TWISTED (T-) AND HOOKED (H-) FIBER IN HIGH STRENGTH MATRIX

As an additional experimental investigation, the performance of FRCC in bending with the same high strength steel T- and H- fibers in a high strength mortar matrix was evaluated. The compressive strength of the matrix was 84 MPa. Two fiber volume contents (1.0% and 2.0%) were used and three specimens were tested in each series. The test series are identified as T10-H, T20-H, H10-H, H20-H for the two types of fiber and the two fiber contents, respectively, where the appended '-H' at the end of each designation refers to the high strength matrix. Investigating the effect of matrix strength on the same key composite strength and toughness values described above (Figs. 4.6 and

4.7) with a lower strength matrix provides further insight into the behavior of FRCCs.

Average load-deflection curves and photos of typical cracking behavior for the high strength matrix series are shown in Fig. 4.10a. As observed in the other tests discussed above, T- fiber specimens showed both higher load carrying capacity and energy absorption capacity than H- fiber specimens, and generated significantly better cracking response.

Load carrying capacity and energy absorption capacity for the high strength matrix series are compared in Figs. 4.10 (b) and 4.10 (c). As shown in Fig. 4.10(b), f_{MOR} is 29.42 MPa for T20-H, 22.21 MPa for H20-H, 16.78 MPa for T10-H, and 6.58 MPa for H10-H. It is observed from Fig. 4.10(b) that T-fibers are more effective than H-fibers in the presence of a higher strength matrix. It also appears, when comparing Figs. 4.10b and 4.10c with Figs. 4.6 and 4.7, that, generally speaking, a higher strength matrix leads to improved FRCC performance. For example, f_{MOR} is 13.08 MPa for T12 with the lower strength matrix (56 MPa) and 16.78 MPa for T10-H with the higher strength matrix (84 MPa). Similarly, the toughness at L/100 for the T10-H (high strength matrix) is higher than the corresponding toughness of T12 for the lower strength matrix, yet it has a smaller volume fraction of fibers.

Overall, it is observed that increasing the matrix compressive strength increases the performance of T-fibers significantly more than that of H-fibers. That is, T-fibers take better advantage of the higher strength matrix.

4.6 COMMENTS ON CURRENT ASTM STANDARD C 1609/C 1609M- 05

The ASTM Standard C 1609/C 1609M – 05 (2006) replaces its predecessor ASTM Standard C 1018 – 97 (1992). While the new standard is certainly an improvement over

the older one in some respects, there are a number of difficulties that arise when the new standard is applied to deflection hardening composites.

The C 1609 Standard recommends estimating toughness as the "energy equivalent to the area under load – deflection curve up to a net deflection of 1/150 of the span". For deflection hardening response, especially in situations involving large deformation in the deflection hardening range (in excess of L/150), such as observed here in the SP series, the situation becomes more complicated because the computed toughness may not then truly represent the energy absorption capacity of the material. It is therefore suggested that the computations of toughness be extended to L/100 and even L/50 if the case justifies it. More research is needed to determine the end deflection point, such as L/150, L/100 and L/50.

Another difficulty with the C 1609 Standard pertains to the definition of LOP, which is defined as the first point on the load versus deflection curve where the slope is zero. Clearly, deflection-softening FRCC will exhibit such response. On the other hand, deflection hardening FRCC may not show such a load drop and may not possess a point on their load – deflection curve where a zero slope is meaningful in the sense suggested by the C 1609 Standard. Take, for example, Fig. 4.11, where the load–deflection curves are not averages but typical examples from each test series. In Fig. 4.11(a), PVA12 clearly shows an LOP point in accordance with C 1609; however, such a point with zero slope cannot be meaningfully detected on the load deflection curves of T12, H12 and SP12. Even at low fiber volume content of 0.4 %, T04 and H04 show no clear load drop, whereas SP04 and PVA04 both show a load drop with definable LOP. Together, these observations imply that a first peak point cannot always be found in the initial portion of

a load – deflection curve if the specimen shows stable deflection hardening response, i.e. without a sudden load drop after LOP. With this in mind, LOP is more generally applicable than the first peak point in describing the flexural behavior of deflection hardening FRCC. Fig. 4.11(c) illustrates that although there is no point where the slope is zero in the initial part of the load-deflection curve of T12, by magnifying the scale of the deflection axis, a possible LOP point (that is, deviation from linearity but without zero slope) can be found.

4.7 CONCLUSIONS

This research investigated the flexural behavior of FRCC employing four different types of fibers with two volume fraction contents (0.4% and 1.2%) in an identical matrix. The four fiber types were high strength steel twisted (T -), high strength steel hooked (H -), high molecular weight polyethylene Spectra (SP -) and PVA fibers. All test series showed deflection-hardening behavior except specimens with 0.4% PVA fibers, and very different performance levels were noted in terms of load carrying capacity [equiv. bending strength], energy absorption capacity [toughness] and cracking behavior [number of cracks], as a function of fiber type and volume content. The following observations and conclusions can be made based on the limited experimental study conducted.

- Deflection hardening FRCC behavior can be obtained for low volume fractions (0.4%) of T-, SP- and H- fibers.
- T-fiber specimens showed the highest load carrying capacity or *MOR* at 1.2% fiber volume contents, that is, 13.08 MPa. The order of performance in terms of equivalent bending strength, f_{MOR}, is observed to be as follows: T- > H- > SP- > PVA fibers.

- At large deflections of $\delta_{L/150}$ and $\delta_{L/100}$, T-fiber specimens exhibited the highest energy absorption capacity. The order of performance at this deflection level is as follows: T- > H- > SP- > PVA fibers.
- Spectra (SP-) fibers generated the highest deflection capacity at maximum resistance, δ_{MOR}.
- Although all fibers (T-, H-, SP- and PVA fiber) showed multiple cracking during deflection hardening response when used at 1.2 % fiber volume fraction, significantly different cracking behavior was observed. T- and SP- fiber specimens generated many cracks while PVA specimens generated only 2-3 cracks, and H- fiber specimens showed a number of cracks that is in between. The order of performance in terms of cracking behavior is as follows: T- > SP- > H- > PVA fiber.
- Comparison between the test program with a lower strength matrix and another test program with a higher strength matrix shows that increasing the matrix compressive strength increases the performance of T- fiber specimens significantly more than that of H- fiber specimens. In other words, T- fibers are able to take better advantage of a higher strength matrix than H- fibers.

The test results were used to critique the new ASTM Standard C 1609/C 1609M – 05 (2006). In particular, it was noted that there are difficulties in applying the new standard to deflection hardening materials. Two suggestions were made:

- Computations of toughness should be extended to L/100 and even L/50 if the case justifies it.
- A first peak point cannot always be found in the initial portion of a load – deflection

curve, especially if the specimen shows stable deflection hardening response. Therefore, the LOP as defined in the previous standard (ASTM Standard C 1018 – 97 (1998)) is more generally applicable and should be used instead.

Table 4.1-Matrix of test program

Matrix	Fiber volume contents	T- fiber	H- fiber	SP- fiber	P- fiber
Mortar	1.2%	T12	H12	SP12	PVA12
	0.4%	T04	H04	SP04	PVA04

Table 4.2–Composition of matrix mixtures by weight ratio and compressive strength

Cement*	Fly Ash°	Sand** (Flint)	Super - Plasticizer	VMA***	Water	$f_c^{'}$, ksi (MPa)
1.00	0.15	1.00	0.009	0.006	0.35	8.1 (55.9)

* ASTM Type 3 Portland Cement; ** ASTM 50-70;
*** Viscosity Modifying Agent; ° TYPE C

Table 4.3– Properties of Fibers

Fiber Type	Diameter in (mm)	Length in(mm)	Density g/cc	Tensile strength ksi (MPa)	Elastic Modulus ksi (GPa)
High strength steel Torex	0.012 (0.3)*	1.18 (30)	7.9	320 (2206)**	29000 (200)
High strength steel Hooked	0.015 (0.38)	1.18 (30)	7.9	304 (2100)	29000 (200)
Spectra	0.0015 (0.038)	1.50 (38)	0.97	374 (2585)	16960 (117)
PVA #13	0.0078 (0.2)	0.472 (12)	1.3	140 (1000)	4203 (29)

* Equivalent diameter ** Tensile strength of the fiber after twisting

Table 4.4- Average values of parameter in Flexural behavior of FRCC (V_f = 1.2%)

		UNIT	T12	H12	SP12	PVA12
LOP	P_{LOP}	N	9005	8927	9487	10756
	f_{LOP}	MPa	2.62	2.60	2.76	3.13
	δ_{LOP}	mm	2.4E-2	2.3E-2	2.4E-2	2.6E-2
	$Tough_{LOP}$	N-m	0.116	0.112	0.078	0.147
d5	P_{d5}	N	17886	16054	11410	10814
	f_{d5}	MPa	5.20	4.67	3.32	3.15
	δ_{d5}	mm	7.2E-2	7.0E-2	7.3E-2	7.9E-2
	$Tough_{d5}$	N-m	0.789	0.726	0.613	0.747
d10	P_{d10}	N	23084	20420	14489	11433
	f_{d10}	MPa	6.71	5.94	4.21	3.33
	δ_{d10}	mm	1.3E-1	1.3E-1	1.3E-1	1.5E-1
	$Tough_{d10}$	N-m	2.051	1.804	1.405	1.481
d20	P_{d20}	N	29566	25070	18325	13185
	f_{d20}	MPa	8.60	7.29	5.33	3.83
	δ_{d20}	mm	2.5E-1	2.4E-1	2.6E-1	2.8E-1
	$Tough_{d20}$	N-m	5.226	4.466	3.415	3.114
L/600	$P_{L/600}$	N	38014	33157	23553	15880
	$f_{L/600}$	MPa	11.06	9.64	6.85	4.62
	$\delta_{L/600}$	mm	0.5	0.5	0.5	0.5
	$Tough_{L/600}$	N-m	13.823	12.171	8.838	6.479
MOR	P_{MOR}	N	44982	39843	34483	16212
	f_{MOR}	MPa	13.08	11.59	10.03	4.72
	δ_{MOR}	mm	1.2	0.9	3.05	0.6
	$Tough_{MOR}$	N-m	44.117	28.453	90.679	7.384
L/150	$P_{L/150}$	N	40214	31522	31736	4379
	$f_{L/150}$	MPa	11.70	9.17	9.23	1.27
	$\delta_{L/150}$	mm	2.0	2.0	2.0	2.0
	$Tough_{L/150}$	N-m	78.889	69.328	54.402	21.316
L/100	$P_{L/100}$	N	33517	20771	34053	0
	$f_{L/100}$	MPa	9.75	6.04	9.90	0
	$\delta_{L/100}$	mm	3.0	3.0	3.0	3.0
	$Tough_{L/100}$	N-m	116.608	94.015	88.424	22.755

Table 4.5– Average values of parameter in Flexural behavior of FRCC (V_f = 0.4%)

		UNIT	T04	H04	SP04	PVA04
LOP	P_{LOP}	N	7823	8788	7714	9408
	f_{LOP}	MPa	2.28	2.56	2.24	2.74
	δ_{LOP}	mm	3.2E-2	2.6E-2	1.9E-2	2.5E-2
	$Tough_{LOP}$	N-m	0.129	0.128	0.077	0.123
d5	P_{d5}	N	12576	12982	9944	7141
	f_{d5}	MPa	3.66	3.78	2.89	2.08
	δ_{d5}	mm	9.6E-2	7.7E-2	5.7E-2	7.4E-2
	$Tough_{d5}$	N-m	0.779	0.708	0.442	0.531
d10	P_{d10}	N	16130	14530	11080	4962
	f_{d10}	MPa	4.69	4.23	3.22	1.44
	δ_{d10}	mm	1.8E-1	1.4E-1	1.0E-1	1.4E-1
	$Tough_{d10}$	N-m	1.922	1.615	0.930	0.898
d20	P_{d20}	N	18799	17502	13337	5539
	f_{d20}	MPa	5.47	5.09	3.88	1.61
	δ_{d20}	mm	3.4E-1	2.7E-1	2.0E-1	2.6E-1
	$Tough_{d20}$	N-m	4.673	3.689	2.107	1.552
L/600	$P_{L/600}$	N	21628	19612	19843	4748
	$f_{L/600}$	MPa	6.29	5.70	5.77	1.38
	$\delta_{L/600}$	mm	0.5	0.5	0.5	0.5
	$Tough_{L/600}$	N-m	8.247	8.063	7.243	2.927
MOR	P_{MOR}	N	26151	23970	27130	5935
	f_{MOR}	MPa	7.61	6.97	7.89	1.73
	δ_{MOR}	mm	1.0	1.2	1.6	0.3
	$Tough_{MOR}$	N-m	21.399	22.922	35.239	2.086
L/150	$P_{L/150}$	N	19017	18705	24113	0
	$f_{L/150}$	MPa	5.53	5.44	7.01	0.00
	$\delta_{L/150}$	mm	2.0	2.0	2.0	2.0
	$Tough_{L/150}$	N-m	43.433	41.057	43.798	4.360
L/100	$P_{L/100}$	N	14227	12195	16271	0
	$f_{L/100}$	MPa	4.14	3.55	4.73	0.00
	$\delta_{L/100}$	mm	3.0	3.0	3.0	2.0
	$Tough_{L/100}$	N-m	60.179	56.365	63.920	4.360

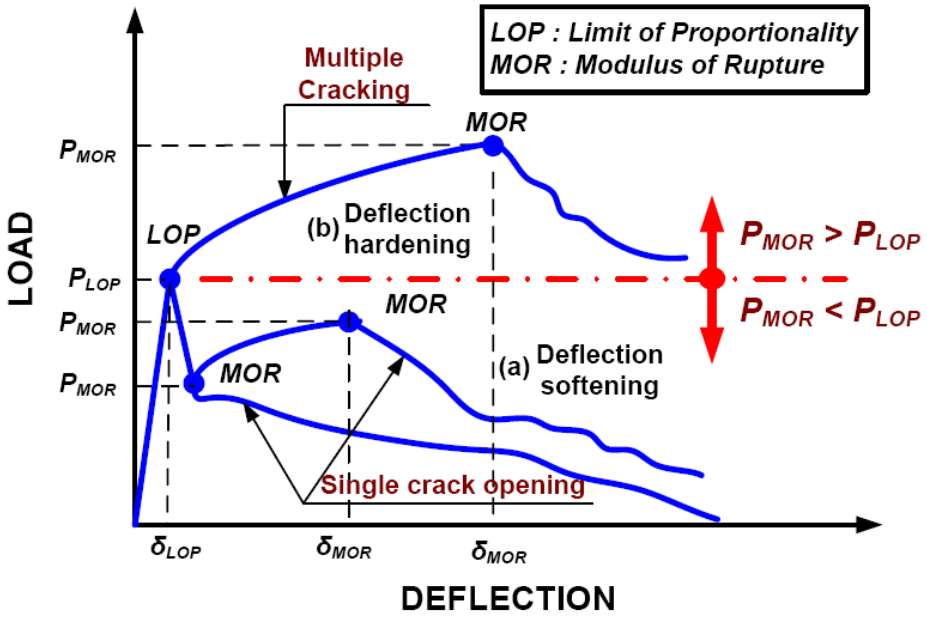

Fig. 4.1 – Typical load – deflection response curves of FRCC

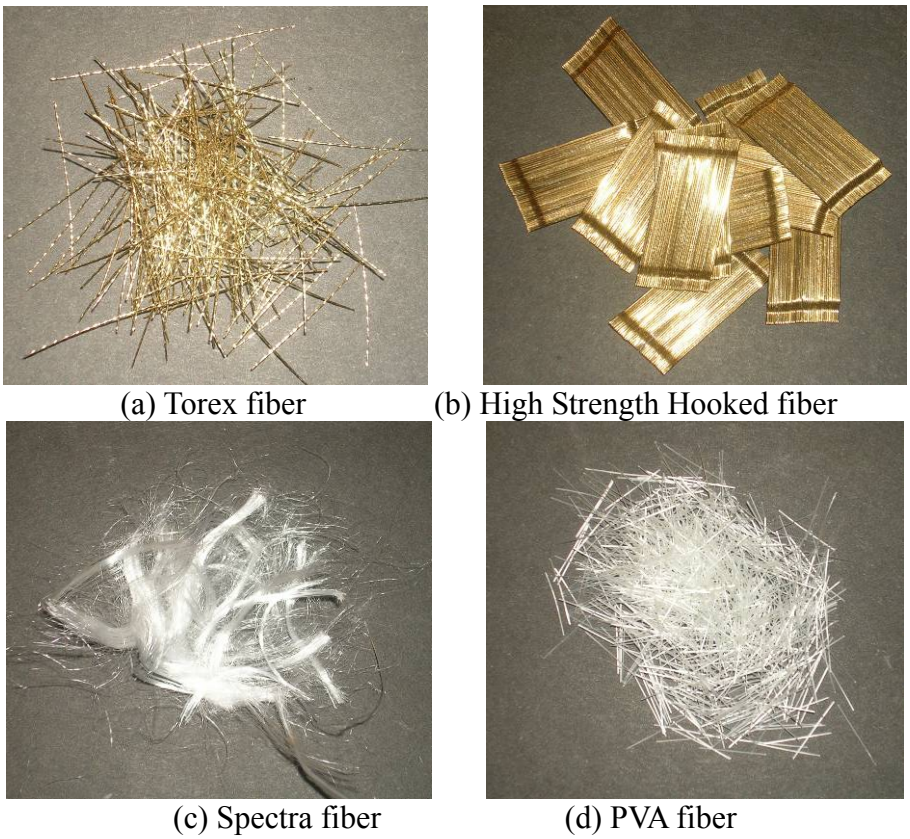

(a) Torex fiber (b) High Strength Hooked fiber

(c) Spectra fiber (d) PVA fiber

Fig. 4.2 – Pictures of fibers; Torex, High strength Hooked, Spectra and PVA fiber

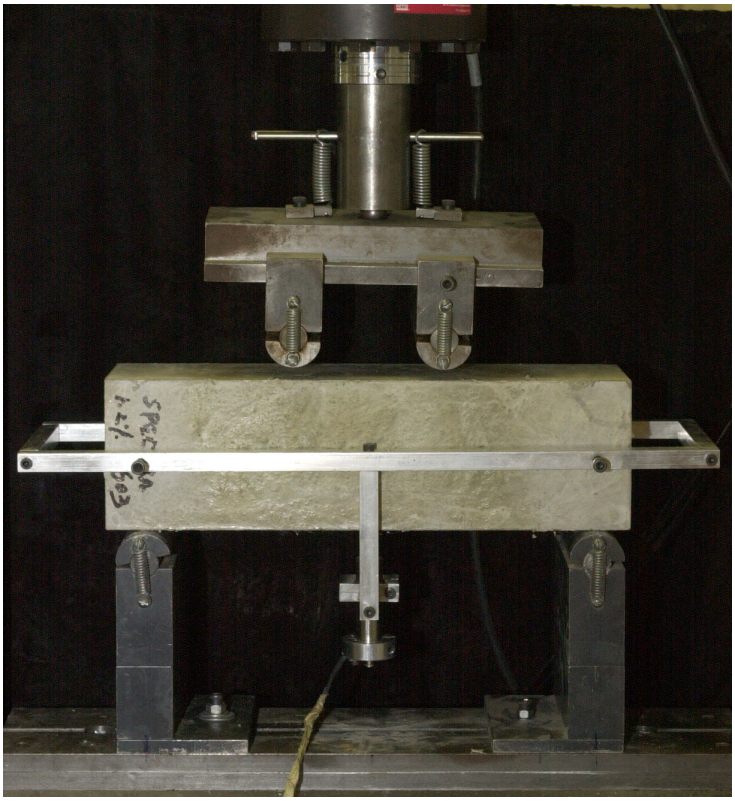

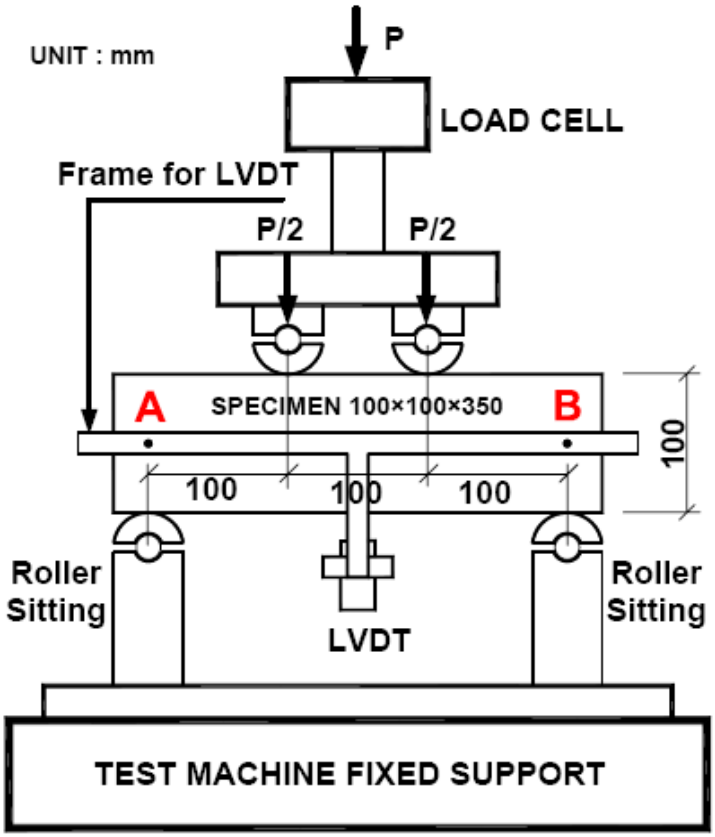

Fig. 4.3 – Test specimen and set – up

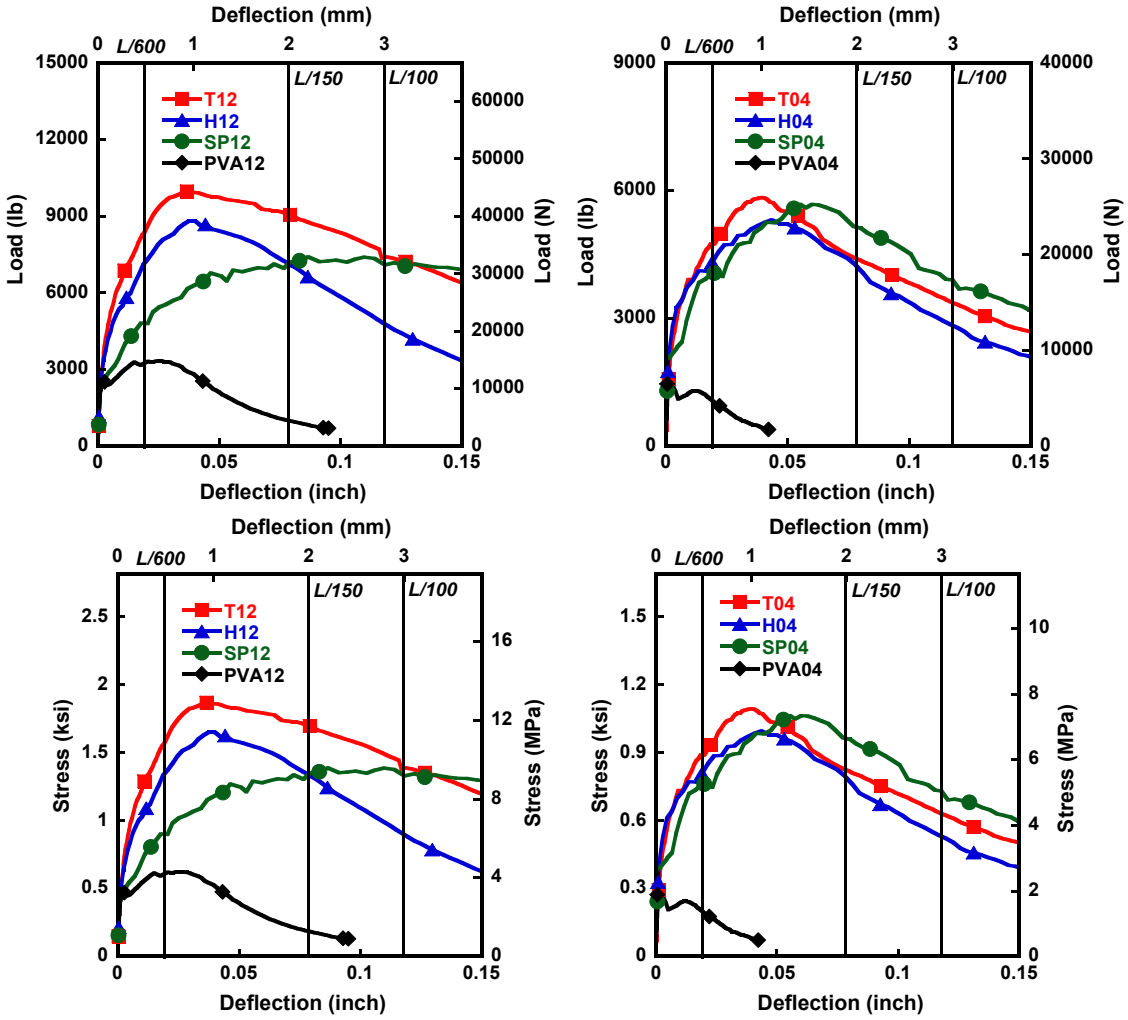

(a) Fiber volume content 1.2% (b) Fiber volume content 0.4%

Fig. 4.4 – Bending test results with medium strength mortar

(a) T12

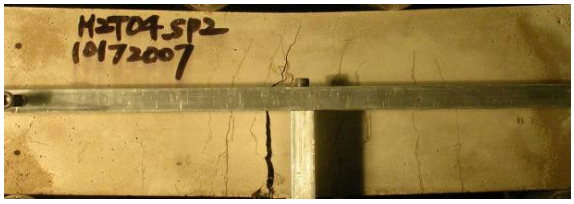

(b) T04

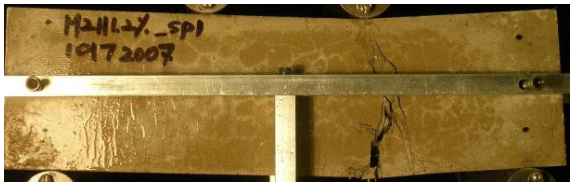

(c) H12

(d) H04

(e) SP12

(f) SP04

(g) PVA12

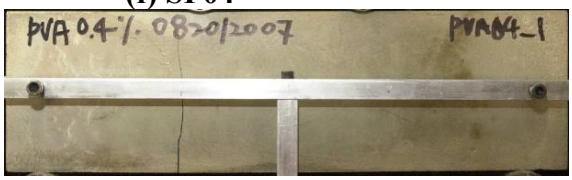

(h) PVA04

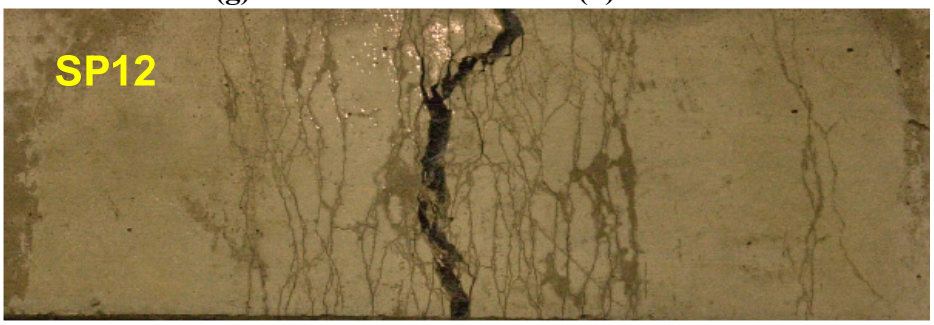

(i) Multiple cracking behaviors of SP12 (from tension side of the specimen)

(j) Multiple cracking behaviors of T12 (from tension side of the specimen)

Fig. 4.5 – Cracking behavior of FRCC under bending

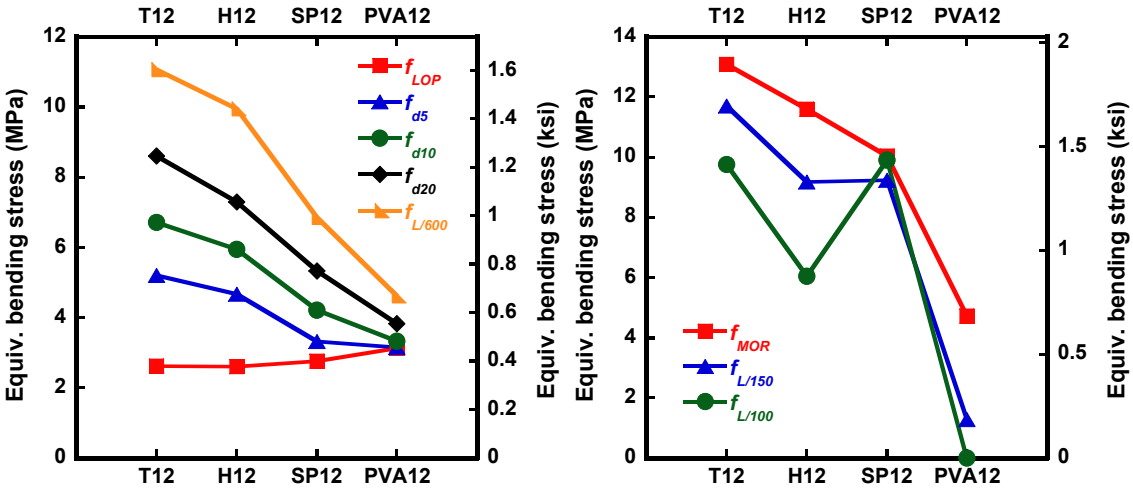

(a) Prior to maximum load, $V_f = 1.2\%$ (b) After maximum load, $V_f = 1.2\%$

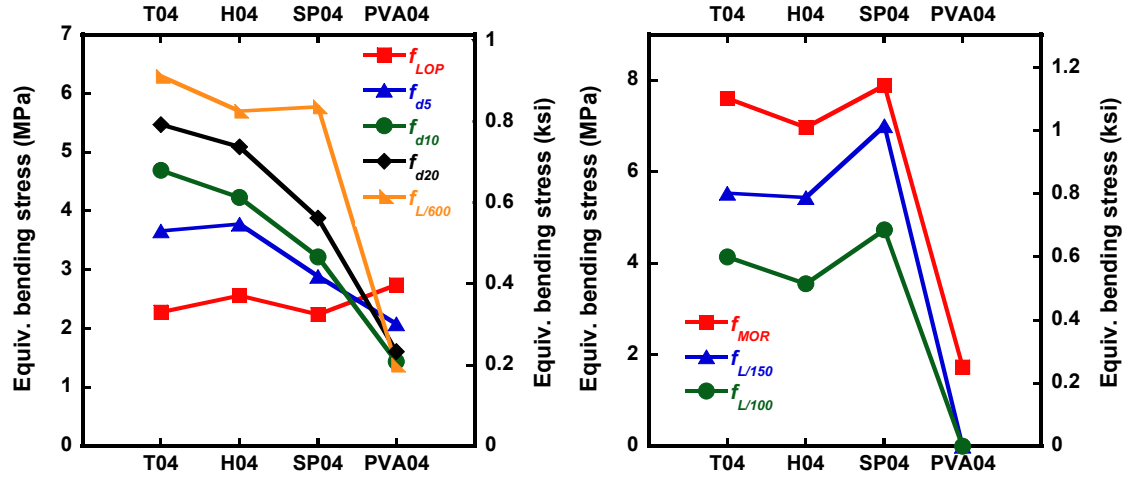

(c) Prior to maximum load, $V_f = 0.4\%$ (d) After maximum load, $V_f = 0.4\%$

Fig. 4.6 – Effect of fiber type on equivalent bending stress

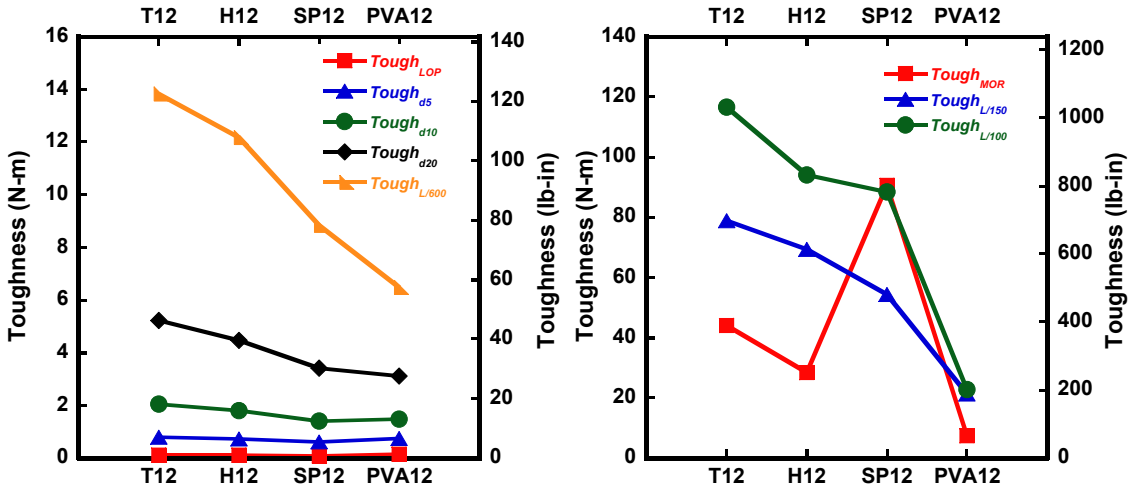

(a) $V_f = 1.2\%$

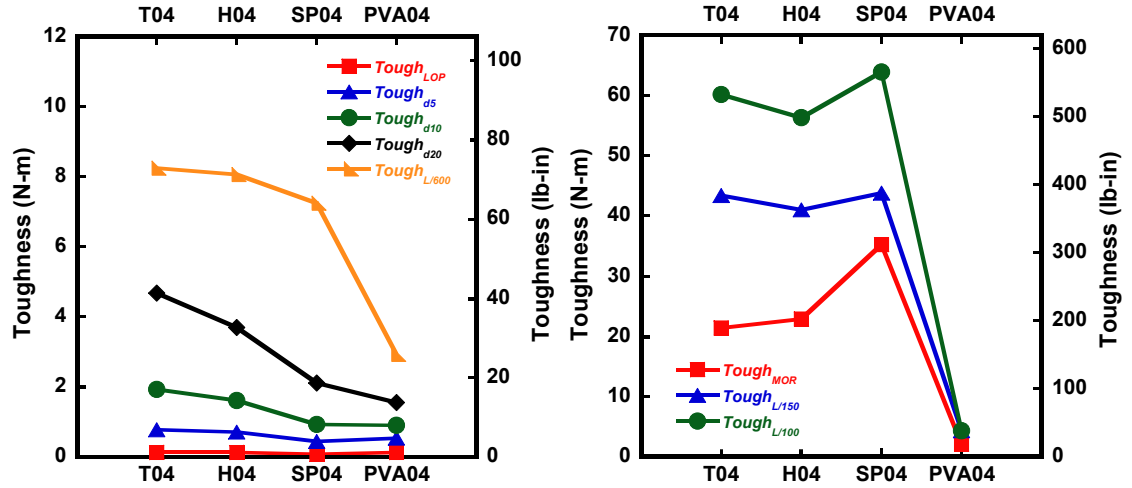

(b) $V_f = 0.4\%$

Fig. 4.7 – Effect of fiber type on toughness

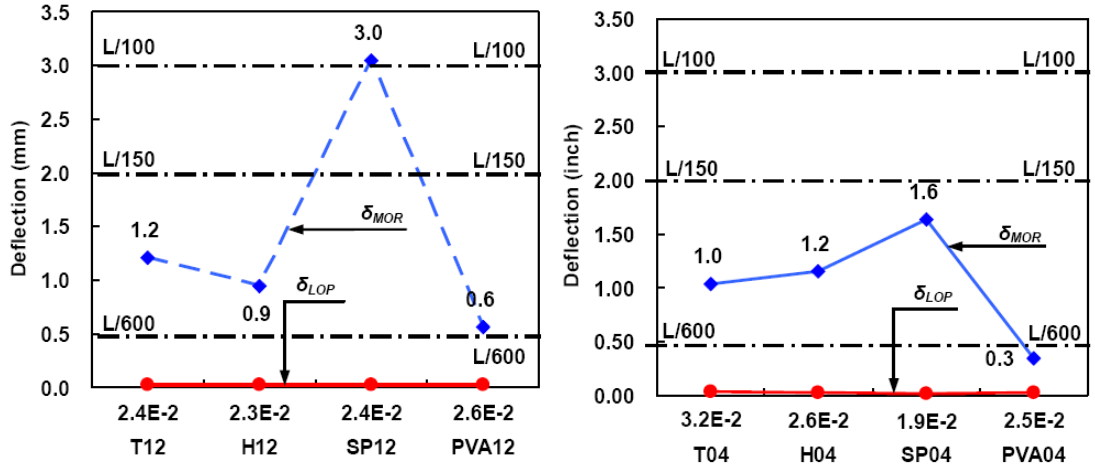

(a) $V_f = 1.2\%$ (b) $V_f = 0.4\%$

Fig. 4.8 – Effect of fiber type on deflection δ_{LOP} and δ_{MOR}

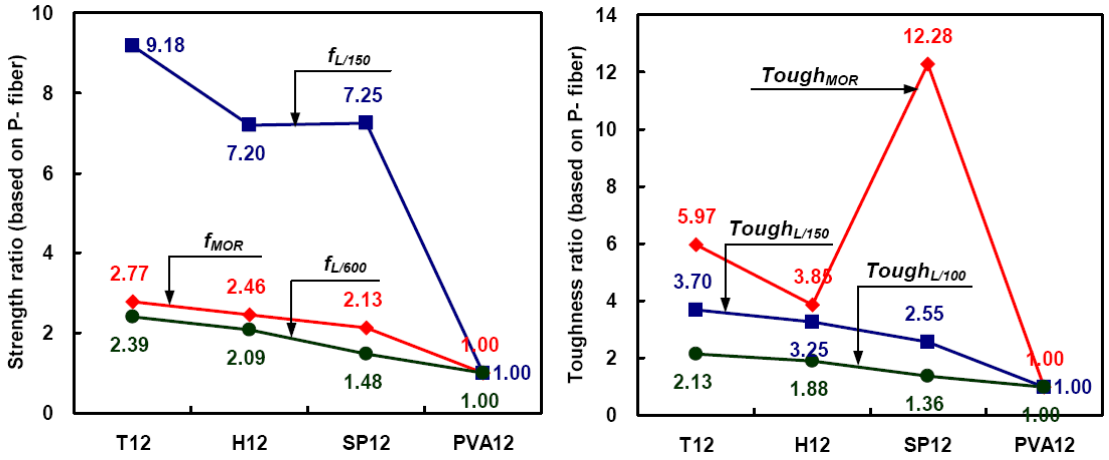

(a) Strength ratio (b) Toughness ratio

Fig. 4.9 – Strength and Toughness ratio based on PVA fiber

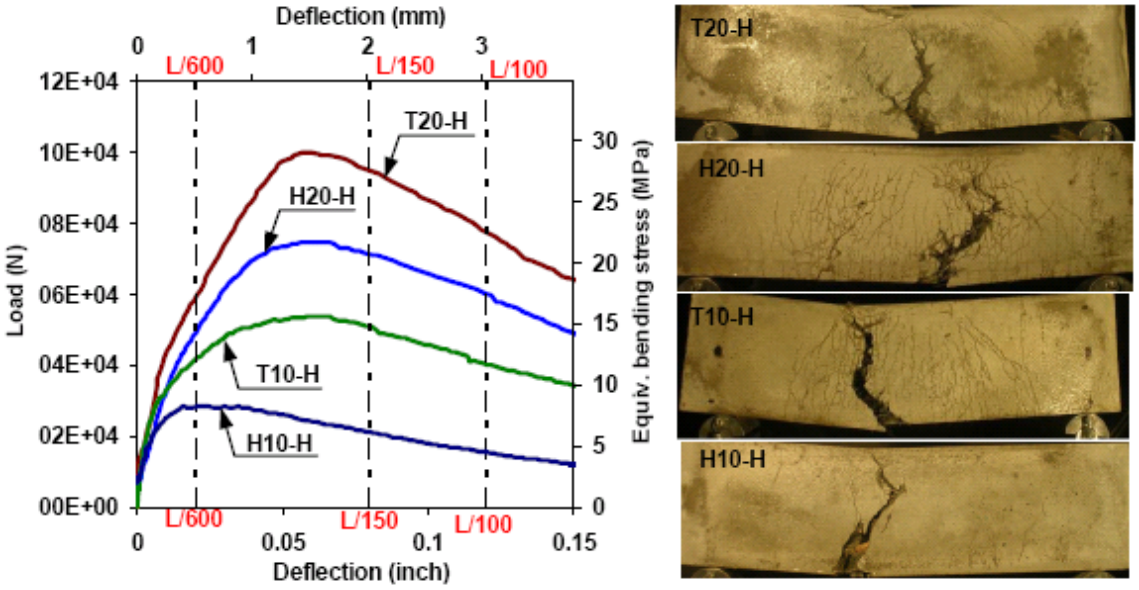

(a) Average load – deflection curves and cracking behavior

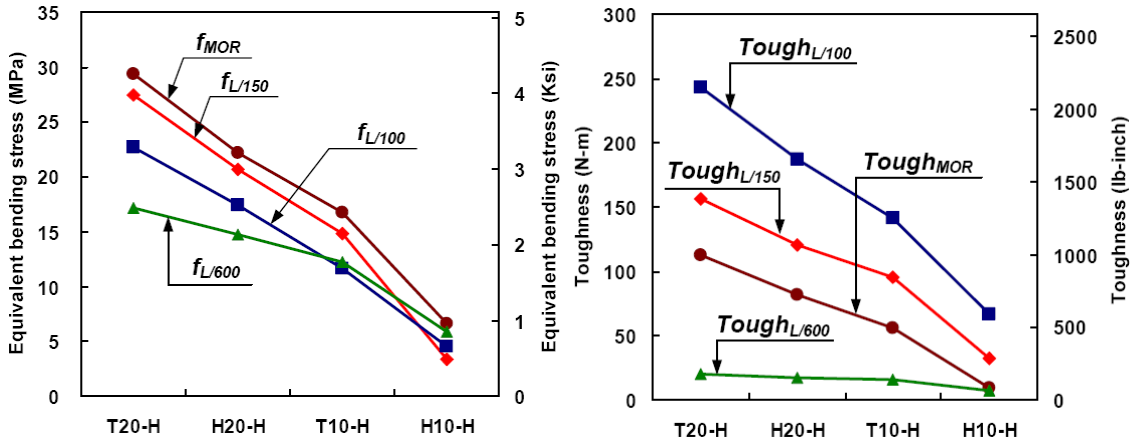

(b) Load carrying capacity (c) Energy absorption capacity

Fig. 4.10 – Bending test results with high strength matrix

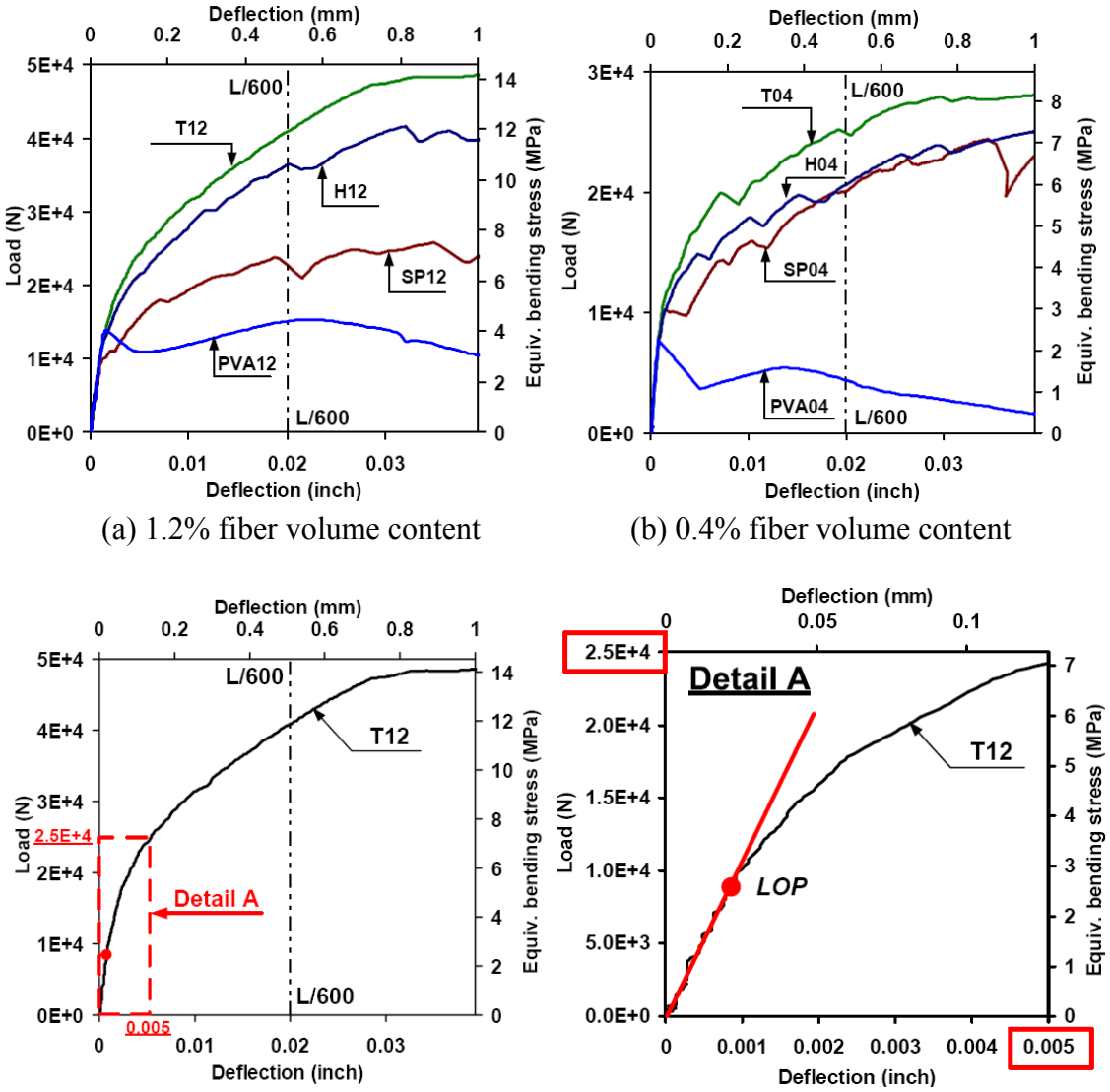

(a) 1.2% fiber volume content

(b) 0.4% fiber volume content

(c) Limit of Proportionality [*LOP*] in T12

Fig. 4.11 – Initial part of load – deflection curve

REFERENCES

ASTM C 1018 – 97, "Standard Test Method for Flexural Toughness and First – Crack Strength of Fiber Reinforced Concrete (using beam with third – point loading)," American Society of Testing and Materials, Oct. 1998, pp. 544-551.

ASTM C 1609/C 1690M – 05, "Standard Test Method for Flexural Performance of Fiber Reinforced Concrete (using beam with third – point loading)," American Society of Testing and Materials, Jan. 2006, pp. 1-8.

Balaguru, P., Narahari, R., and Patel, M., "Flexural Toughness of Steel Fiber Reinforced Concrete," ACI Materials Journal, Vol. 89, No. 6, Nov.-Dec. 1992, pp. 541-546.

Banthia, N. and Trottier, J.-F., "Test methods for flexural toughness characterization of Fiber Reinforced Concrete : Some concerns and a proposition," ACI Material Journal, Vol. 92, No. 1, Jan.-Feb. 1995, pp. 1-10.

Chandrangsu, K. and Naaman, A. E., "Comparison of tensile and bending response of three high performance fiber reinforced cement composites," in Print, HPFRCC4, Ann Arbor, USA, June 2003, pp. 259-274.

Gopalaratnam, S., Shah, S. P., Batson, G. B., Criswell, M. E., Ramakrishnam, V. and Wecharatana, M., "Fracture Toughness of Fiber Reinforced Concrete," ACI Materials Journal, Vol. 88, No. 4, July-Aug. 1991, pp. 339-353.

Naaman, A. E., "Toughness, Ductility, Surface energy and Deflection – Hardening FRC Composites," Proceedings of JCI workshop on ductile fiber reinforced cementitious composites (DFRCC) – Application and Evaluation, Japan Concrete Institute, Tokyo, Japan, Oct. 2002, pp. 33-57.

Naaman, A. E., and Reinhardt, H. W., "Proposed Classification of FRC Composites Based on their Tensile Response," Materials and Structures, Vol. 39, No. 5, June 2006, pp. 547-555.

Ozyurt, N., Mason, T. O., and Shah, S. P., "Correlation of fiber dispersion, rheology and mechanical performance of FRCs," Cement and Concrete Composites, Vol. 29, No. 2, Feb. 2007, pp. 90-79.

Soranakom, C., and Mobasher, B., "Correlation of tensile and flexural responses of strain softening and strain hardening cement composites," Cement and Concrete Composites, Vol. 30, No. 6, July 2008, pp. 465-477.

Soroushian, P. and Bayasi, Z., "Fiber-Type Effects on the Performance of Steel Fiber Reinforced Concrete," ACI Materials Journal, Vol. 88, No. 2, Mar.-April 1991, pp. 129-134.

CHAPTER V

LOADING RATE EFFECT ON PULLOUT BEHAVIOR OF DEFORMED STEEL FIBERS [4]

ABSTRACT

This chapter describes the results of single fiber pullout tests under various loading rates ranging from the static to the seismic level. Investigate the loading rate effect on single fiber pullout behavior provides a basis to better understand the effect of strain rate on the tensile properties of fiber reinforced cement composites. Two types of high strength deformed steel fibers [hooked and twisted fibers] known to have slip hardening behavior under static pull-out loading are evaluated. Experimental results reveal that the pull-out response of twisted steel fibers shows strong rate sensitivity that is dependent upon the compressive strength of the matrix. On the other hand, high strength hooked fibers did not show rate sensitivity under pull-out for the various matrices tested. The test results also showed the pull-out energy of twisted fibers increases with the matrix compressive strength and can be up to five times that hooked fibers.

5.1 INTRODUCTION

[4] D. Kim, S. El-Tawil, and A. E. Naaman, "Loading rate effect on pullout behavior of deformed fiber", ACI Materials Journal, Vol. 105, No. 6, Nov.-Dec. 2008, pp.576-584.

Naaman [1987] first defined high Performance Fiber Reinforced Cementitious Composites (HPFRCCs) as a class of composites that exhibit strain-hardening and multiple cracking responses under tensile loading. Advantages of HPFRCC include ductility, durability and high-energy absorption capacity compared with normal concrete and conventional Fiber Reinforced Concrete (FRC). Today, HPFRCC would be classified as tensile strain-hardening FRC composites [Naaman and Reinhardt, 1996 and 2006].

While numerous prior research studies have evaluated conventional FRC for seismic applications, the use of HPFRCCs in such applications is relatively recent. Canbolat et al. [2005] investigated the seismic behavior of HPFRCC coupling beams. They reported that HPFRCC allowed the transverse reinforcement for confinement to be eliminated, significantly simplifying the beam construction process. Parra-Montesinos et al. [2005] reported that the use of HPFRCC materials in the beam plastic hinge region allowed an increase in transverse reinforcement spacing to half the effective beam depth without adverse effects. Similarly the use of SIFCON (Slurry Infiltrated Fiber Concrete) in beam-column connections of precast frames allowed both strength and ductility demands to be met while eliminating the need for transverse reinforcement (Vasconez et al., 1998; Soubra et al., 1991, 1993). Chandrangsu and Naaman [2003] showed that HPFRCCs allow the development of a very effective plastic hinge mechanism in concrete bridge decks.

Most of the existing information on HPFRCC is based on its observed mechanical properties under static loading. A typical stress-strain response in tension obtained under low loading rate is shown in Fig. 5.1. Since the behavior of the fiber, the cement matrix,

and the bond between them is likely dependent upon the rate of loading, it is expected that the response of HPFRCC is also rate dependent. There is, however, very limited information on the rate dependent material response of HPFRCC.

Experimental and analytical investigations suggest that there is a direct relation between fiber pull-out and tensile stress-strain response. Indeed the model that leads to predicting the post-cracking tensile strength of the composite (Naaman 1972 or 1987) assumes general fiber pull-out and integrates the contribution of each fiber to the tensile resistance. Strong experimental evidence between fiber pull-out and tensile response was recently pointed out by Kim et al. [2007] who used high strength deformed steel fibers. They provided both single fiber pullout test data and composite tensile test data that showed that the equivalent bond strength based on the pullout work during a single fiber pullout test could be successfully used in calculating the number of cracks in a tensile specimen.

The objectives of the research reported in this chapter are: 1) to develop a fundamental understanding of the effect of loading rate on the pullout behavior of a single fiber; and 2) to establish if different pullout mechanisms make effect on the rate sensitivity in fiber pullout behavior of two high strength steel fibers, Hooked (H) and Twisted (T) fiber.

5.2 RESEARCH SIGNIFICANCE

Although fiber reinforced cement composites have been shown to significantly improve ductility, durability and load carrying capacity of buildings and other infrastructure components under static loading conditions, their performance under dynamic loading is not yet fully understood. In particular, it is not clear if HPFRCC

which undergo strain-hardening behavior in tension at quasi-static loading rate, can maintain their strain hardening behavior at higher strain rates. By investigating the pull-out behavior of a single fiber, and knowing its influence on composite tensile behavior, this research provides basic information necessary for developing a fundamental understanding of the dynamic response of HPFRCCs.

5.3 STRAIN RATE EFFECT ON FIBER PULLOUT BEHAVIOR

Very few studies have investigated the fiber pullout behavior under various loading rates. Gokoz and Naaman [1981] carried out fiber pullout tests under static ($v = 4.2 \times 10^{-3} cm/\sec$) and high loading rates ($v = 300 cm/\sec$) conditions for three types of fibers (smooth steel, glass, and polypropylene). They concluded that while PP fibers were very sensitive to the loading velocity, smooth steel fibers were insensitive to it. They also reported that the post-peak response of smooth steel fibers, whose pull-out behavior is essentially based on friction, is almost insensitive to loading velocity.

Banthia and Trottier [1991] investigated pull out resistance of deformed steel fibers (end hooked, crimped and I-shaped fiber) embedded in cement based matrices. A static ($v = 8.46 \times 10^{-4} cm/\sec$) pullout test was performed using an Instron testing machine, while dynamic ($v = 150 cm/\sec$) pullout response was investigated using a Charpy type pendulum impact tester. The study found that deformed steel fibers embedded in cementitious matrices generally sustain a higher load under impact than under static pullout and that the pullout energy is also greater under impact as long as the fiber pulls out and does not fail.

Yang and Li [2006] examined the rate dependence in Engineered Cementitious Composites (ECC) with PVA fiber. Single fiber pullout tests revealed a strong rate

dependency. The pullout loading rate ranged from $v = 10^{-4} cm/\sec$ to $v = 1\,\text{cm/sec}$. According to the study, a strong rate dependency in terms of chemical bond strength, G_d, was evident at the highest pullout speed and that G_d could be 5 times higher than the static values. The length of fiber embedded in the matrix was only 0.5 mm in order to prevent fiber breakage during pullout test; however, the fiber lengths used in their tensile specimens were 8 to 12mm.

5.4 PULLOUT MECHANISMS OF HOOKED AND TWISTED STEEL FIBERS

Naaman et al [1991] carried out experimental research on the bond-slip mechanisms of steel fibers using three types of steel fibers including smooth, crimped and hooked fibers. The single fiber pullout test revealed that deformed and hooked steel fibers show slip-hardening behavior under pull-out, while smooth steel fiber shows slip-softening behavior. An analytical model for the pullout behavior of smooth steel fiber was suggested by Naaman et al [1991]. This model considers only adhesion and friction in the bond stress-slip relation but does not include the mechanical component of bond.

Fig. 5.2 illustrates the typical pseudo-static pull-out response of high strength steel H-fibers (Hooked) and T-fibers (Twisted). Although the pullout behavior of both fibers is greatly dependent on the mechanical component of bond, their pullout mechanisms are very different. While H-fibers utilizes the plastic energy generated by two plastic hinges at the hooked end thus utilizing only a relatively small portion of fiber embedded length (Alwan et all in 1999), the pull-out mechanism of T-fibers is based on the untwisting torsional moment resistance of the fiber which is distributed throughout the fiber embedment length (Naaman in 1999 and 2003) as shown in Fig. 5.3. As will be discussed later on, these two different pullout mechanisms are the primary reasons for the different

pull-out rate sensitivity observed for the two fiber types.

In a typical pull-out test, adhesion and initial friction are activated first. The mechanical component of bond which is due to the mechanical deformation of the fiber such as the hook in an H-fiber, is triggered after adhesion and initial friction have been fully activated. Naaman and Najm [1991] used surface oiled hooked and indented fibers in pull-out tests to illustrate this mechanism. Let us call the point at which this occurs, the initiation of mechanical bond (IMB) as shown in Fig. 5.2. The slip at the IMB is generally very small and sometimes difficult to accurately pin-point even when a high rate of data acquisition is used. It definitely occurs following a change in the initial slope of the pull-out load versus slip curve. Because in this study, the slip at the IMB point was easier to identify for T-fibers, its value was taken the same for H-fibers as well. That is, the pull-out load at the IMB point for H-fibers was taken as the load corresponding to the given slip observed for T-fibers at their IMB point. This procedure is believed to introduce less subjectivity when describing the rate sensitivity of the IMB point. Another definition of the IMB point is the maximum contribution due to initial friction and adhesion prior to initiation of mechanical bond. After the IMB point, the mechanical component of bond is fully activated during fiber pullout and allows maximum pullout load to be reached as shown in Fig. 5.3. In addition, full slip capacity is defined as the slip at which the mechanical component of bond totally loses its capability (as illustrated in the photos in Fig. 5.3).

5.5 EXPERIMENTS

High strength H-fibers and T-fibers were embedded in three different mortar matrices (M) with low (1), moderate (2) and high (3) compressive strengths, leading to six basic

series of pullout specimens (M1H, M1T, M2H, M2T, M3H and M3T, as listed in Table 5.1). Matrix 1 has low compressive strength (28 MPa = 4 ksi), Matrix 2 has medium compressive strength (55.2 MPa = 8 ksi) and Matrix 3 has high compressive strength (84 MPa = 12 ksi) as provided in Table 5.2. Four different loading rates were applied in each series to investigate the effect of different rates and different matrices on the pullout behavior of H-fibers and T-fibers (Table 5.1). Table 5.2 provides the mortar mixture composition for the three matrices used and their average compressive strength. Fiber properties are given in Table 5.3, while Fig. 5.3 shows pictures of the H- and T-fibers used. The Twisted fiber used had a twist ratio leading to 2.36 ribs/cm (= 6 ribs/in).

A servo-hydraulic testing machine (MTS 810) was used to conduct the fiber pull-out tests for both the static tests and dynamic tests up to seismic loading rates. The pullout load speed for the static test was v = 0.018 mm/sec (= 0.0007 in/sec). This particular speed was selected to obtain a static strain rate of $\dot{\varepsilon} = 0.0001/\sec$ in companion composite tensile tests of dog-bone shaped specimens with 180 mm (= 7 in) gage length. The loading rate (v = 18 mm/sec = 0.7 in/sec) for the seismic rate was calculated using the same approach based on the assumption that the stain rate for earthquake loading is $\dot{\varepsilon} = 0.1/\sec$. It is clear that the ratio of the highest speed to the lowest speed is 1,000, i.e. 3 orders of magnitude.

5.5.1 Materials and specimen preparation

A Hobart type laboratory mixer was used to prepare the cement mix. Cement, fly-ash and sand were first dry mixed for about 2 minutes. Water mixed with superplasticizer and Viscosity Modifying Agent (VMA) was then added gradually and mixed for another 5 to 10 minutes. The cementitious mixture was carefully placed in a mold where the pull-out

fibers were pre-placed, and vibrated slightly using a high frequency vibrating table. Specimen casts were covered with plastic sheets and stored at room temperature for 24 hours prior to demolding. The specimens were then placed in a water tank for an additional 2 weeks, then removed and placed to dry in laboratory air conditions for 2 days prior to testing.

5.5.2 Test setup and procedure

The geometry of the fiber pull-out test specimen and the test setup are shown in Fig. 5.4. The embedment length of the fiber was 15mm (= 0.6 inch) and the fiber was precisely placed at the center of the specimen. The specimen's axis was located along the loading axis and the fiber was firmly gripped to prevent any slip in the gripping device.

5.5.3 Test Results

The pullout behavior of H- and T-fibers embedded in the three matrices (Matrix 1, Matrix 2 and Matrix 3) for the four different loading rates is illustrated in Fig. 5.5. At each loading rate and for each matrix composition, average values computed from at least 3 specimens of pull-out load at the IMB point, the maximum pullout load and the corresponding slip values are measured and summarized in Fig. 5.5 as well as Table 5.4. The dynamic increase factor (DIF), which is defined as the ratio of the measured dynamic load to the measured static load, is also computed and listed in Table 5.4.

From Fig. 5.4 and Table 5.4, it can be seen that the maximum pullout load value {160.8 N (= 36.15 lb) and 190.1 N (= 42.74 lb)} for H-fibers in Matrices 2 and 3 is higher than that in Matrix 1 {127.7 N (= 28.71 lb)}. Therefore, the pullout resistance of the H-fibers appears to be dependent on the compressive strength of the matrix. However, there is no noticeable rate effect on the single fiber pullout behavior in all three matrices.

Similarly, the maximum pull-out load of the T-fibers was significantly higher for Matrices 2 and 3 than that for Matrix 1. That is, it also increases with the compressive strength of the matrix. However, unlike the case of H-fibers, T-fibers show rate sensitive pullout behavior for all three matrices (Figs. 5.5b, 5.5d, and 5.5e).

The pullout behavior of the M1T series (Fig. 5.5b) exhibits the typical slip-hardening behavior of T-fibers with significant pullout energy. Moreover, the pull-out response is clearly rate sensitive. At the quasi-static loading rate (0.018 mm/sec = 0.0007 in/sec), the pullout load at the IMB point is 30.3 N (= 6.81 lb) and the maximum pullout load is 60.9 N (= 13.69 lb). The pullout load at the IMB point increases from 30.3 N (= 6.81 lb) under the quasi-static loading rate (0.018 mm/sec = 0.0007 inch/sec) to 60.2 N (= 13.53 lb) under the seismic loading rate (18 mm/sec = 0.7 in/sec). The maximum pullout load also increases from 60.9 N (= 13.69 lb) to 80.3 N (= 18.05 lb). Although both the pullout load at the IMB point and the maximum pullout load increase under seismic loading rate, the rate sensitivity of the pullout load at the IMB is higher than that of the maximum pullout load. In addition, the maximum pullout load of the M1T series under seismic loading rate is much lower than the maximum pullout load in the M2T and M3T series. The reason for the lower maximum pullout resistance in M1T is believed due to the matrix damage which occurs in the low strength matrix before full untwisting of the fiber takes place under pull-out.

The pullout behavior of T-fibers in Matrix 2 (Fig. 5.5d) also exhibits significant rate sensitivity in its initial response. Indeed, the IMB pullout load more than doubles as the loading speed increases; however, the maximum pullout load in the untwisting frictional phase does not increase in the same proportion, while its corresponding slip decreases.

This implies that the adhesive component of bond between steel fiber and matrix increases as the loading velocity increases, thus the adhesive bond strength, or elastic shear bond strength before debonding, is sensitive to the loading rate, while the frictional bond after initial slip is insensitive to the loading rate as observed in Gokoz and Naaman [1981].

Rate sensitivity was also found in the pullout behavior of T-fibers embedded in Matrix 3 (Fig. 5.5f). Under static loading rate (0.018 mm/sec = 0.0007 in/sec), the pullout load at the IMB point in Matrix 3 is much higher than those for Matrix 1 and Matrix 2. However, under seismic loading rate (18 mm/sec = 0.7 in/sec), it was observed that the pullout load at the IMB point for Matrix 3 is lower than for Matrix 2, but still more than double that for Matrix 1.

5.6 DISCUSSION AND EVALUATION OF EXPERIMENTAL RESULTS

In order to provide some quantitative comparison of the effect of loading rate on the single fiber pullout behavior, five quantities, namely the pullout load at the IMB point and maximum pullout load, pullout energy (and corresponding equivalent bond strength up to complete pull-out) and slip capacity for the four different loading rates were obtained from the test results and compared. In calculating equivalent bond strength at the IMB point, the fiber embedment length is taken as 15mm (=0.6 in) and the amount of slip as 0.4 mm (=0.016 in).

The pullout energy is calculated as the area under the pullout stress (that is the tensile stress induced in the fiber by the pull-out load) versus slip curve up to complete pull-out. Another quantity, the equivalent bond strength, is also computed from the pullout stress versus slip curve as shown in Eq. [5.1].

$$\tau_{eq} = \frac{2 \times PulloutEnergy \times d_f}{{L_f}^2} \quad [5.1]$$

where, d_f is the fiber diameter, L_f is the total fiber length and $L_f/2$ is the embedment length. The equivalent bond stress is thus a constant over the embedment length, and is proportional to the pull-out energy. This equivalent bond stress was successfully utilized to correlate single fiber pullout behavior and tensile behavior of fiber reinforced composites by Kim et al. (2007) (in Chapter II).

5.6.1 Rate Effect on IMB Pull-Out Load

The effect of loading rate on the pullout load at the IMB point is illustrated in Fig. 5.6. It is clear from the figure that there is virtually no rate sensitivity for the IMB pullout load for H-fibers for all three matrix types. Indeed, the DIF values for the pullout load at IMB under seismic loading rate (18 mm/sec = 0.7 in/sec) are around 1.00 for all three matrices. Unlike H-fibers, T-fibers show rate sensitivity for all three matrix types. The pullout load at the IMB point for the M1T series is 30.3 N under the static loading rate (0.018 mm/sec = 0.0007 in/sec) and 60.2 N (= 13.53 lb) under the seismic loading rate (18 mm/sec = 0.7 in/sec), i.e. the DIF of T-fibers embedded in Matrix 1 under the seismic loading rate is 1.98. T-fibers in Matrix 2 (M2T) have a DIF of 2.54 for the IMB point, whereas M3T has a DIF of only 1.18. Other than the fact there is sensitivity to the rate of loading, there appears to be no clear trend in how the DIF varies as the matrix strength increases.

5.6.2 Rate Effect on Pull-Out Work (or Energy) and Equivalent Bond Strength

The rate effect on the pullout energy and equivalent bond strength (as computed from Eq. 1) at complete fiber pullout is illustrated in Fig. 5.7 and also shown in Table 5.5. For

H-fibers the DIF for the pullout energy and equivalent bond strength under the seismic loading rate (18 mm/sec = 0.7 in/sec) is 0.99 for Matrix 1, 1.20 for Matrix 2 and 0.91 for Matrix 3. It is concluded that the pullout energy of H-fibers for all three different matrices is not rate sensitive. On the other hand, Fig. 5.7 illustrates that the pull-out energy of T-fibers is somewhat rate sensitive for all three matrices. The DIF are 1.29, 1.17 and 1.12 for Matrices 1, 2 and 3 respectively, at a loading rate 1.8 mm/sec (=0.07 in/sec). The trends are not very clear, however. For example, while M1T exhibited a DIF of 1.72 at 18 mm/sec (= 0.7 in/sec) loading speed, M3T had a DIF of only 0.89. M2T suffered premature fiber failures, which prevented computation of the corresponding DIF at 18 mm/sec (= 0.7 in/sec). Since fiber failures were not observed at lower speeds, it is inferred that the response of M2T is indeed rate sensitive. The rate effect on the pullout energy and equivalent bond strength at IMB point also is shown in Fig. 5.8 and Table 5.5. The same general trends as observed at pullout capacity are also observed at the IMB point.

5.6.3 Rate Effect on Slip Capacity

The rate effect on the slip capacity is illustrated in Fig. 5.9 and Table 5.6, which lists the load and slip values at slip capacity (see Fig. 5.2 for definitions). Clear differences between the slip capacities for H- and T-fibers can be noticed in Figs 5.5 and 5.9. In all three matrices, the average slip capacity of H-fibers is around 3.5mm (= 0.138 in), which is around a quarter of the fiber embedment length, while the average slip capacity of T-fibers is around 11 mm (= 0.433 in), which is about three quarters of fiber embedment length. No appreciable rate sensitivity in slip capacity is observed for both fiber types as shown in Fig. 5.9.

5.6.4 Pull-Out Energy Ratio

The ratio between the amounts of total pullout work (energy) up to complete pull-out for H- and T-fibers at different loading rates is illustrated in Fig. 5.10. As the loading rate increases, the pullout energy ratio increases for the low strength matrix (Matrix 1), while mixed results are obtained for the higher strength matrices (Matrices 2 and 3) suggesting lower rate sensitivity for those matrices. For Matrix 1, the ratio for seismic loading rate is 3.30 while it is 1.90 under quasi-static strain rate. For Matrices 2 and 3 the pull-out energy ratio between T- and H-fibers exceeds 4 and 5, respectively. It is observed that in all cases, T-fibers yield much higher pullout energy than H-fibers (between 2 to 5 times), with the higher values occurring either at higher strain rates or for high strength matrices. As indicated in Eq. [5.1] higher pull-out energy implies higher equivalent bond strength thus higher composite tensile strength and ductility.

5.6.5 Rate Sensitive Behavior of Twisted Fibers and its Advantages

Using a Split Hopkinson Pressure Bar system (SHPB), Vos and Reinhardt [1980] reported that while plain steel bars embedded in concrete showed no rate sensitivity, deformed steel bars with ribs showed high rate sensitivity under impact loading. They explained the discrepancy by highlighting the differences in the way bond resistance is mobilized in both types of bars. The bond strength of plain steel bars is mainly based on friction, which is known to have no or small rate sensitivity. On the other hand, the bond strength of deformed steel bars stems from mechanical resistance that leads to radial and longitudinal interface cracking during pull out, to which they attributed the observed load rate sensitivity.

During pull-out, properly designed T-fibers tend to un-twist while slipping creating a

torsional moment along the fiber length and inducing radial stresses. Excessive radial stresses will likely lead to radial and longitudinal interface micro-cracking along the embedded fiber length in a manner similar to what occurs around the ribbed bars in the Vos and Reinhardt [1980] study. It is therefore not surprising that T-fibers exhibit high loading rate sensitivity. Although both H- and T-fibers employ mechanical bond to improve bond strength, T-fibers induce radial and longitudinal interface cracking during pullout that is distributed along the entire embedded fiber length. On the other hand, H-fibers have only single end hooks, implying that the micro-cracking associated with deforming the hooks occurs in a localized zone, relatively small in comparison to the fiber embedded length, and hence the rate insensitivity of these fibers.

It was previously discussed that T-fibers have a higher pullout work under the seismic load rate compared to pseudo-static loading. It was also mentioned that Kim et al. [2007] have observed a strong correlation between single fiber pullout behavior and the tensile behavior of fiber reinforced cement composites (Chapter II). These two facts imply that enhancement in T-fiber performance under faster rate of loading will likely translate into improved performance under seismic loading rates at the structural level, especially for medium strength fiber reinforced cement composites. This hypothesis is investigated in Chapter VI.

5.7 CONCLUSIONS

This study investigated the rate of loading effect on the pullout behavior of two deformed high strength steel fibers, H-fibers and T-fibers. Four loading rates ranging from quasi-static to seismic, and three matrix compressive strengths (low to high) were used. Although both T- and H-fibers show slip-hardening behavior under pull-out due to

their mechanical bond, they exhibit different rate sensitivities. The following conclusions can be drawn from the limited experimental study that was conducted.

- High strength steel hooked fibers (H- fibers) showed no appreciable rate sensitivity when pulled out from all three matrices of low (28 MPa = 4 ksi), medium (55 MPa = 8 ksi) and high (84 MPa = 12 ksi) compressive strength. This was attributed to the fact that micro-cracking, from which the rate effect is thought to stem, is localized in a small region in the vicinity of the hooks and therefore does not have a chance to influence rate sensitivity in a significant way.
- High strength steel twisted fibers (T-fibers) showed rate sensitive pull-out behavior in all three matrices used. Different rate sensitivities were observed, with the highest sensitivity occurring in the medium compressive strength matrix. The observed rate sensitivity is attributed to the radial and longitudinal interface cracking that takes place along the entire embedded fiber length as the fibers untwist during pull out.
- T-fibers produce much higher single fiber pullout energy under the seismic loading rate than under the pseudo static loading rate. Moreover, the pull-out energy of T-fibers ranged from 1.90 to 5.15 times that of H-fibers for the loading rates considered, implying that T-fibers are much more efficient than H-Fibers in dissipating energy.

Since there is a direct correlation between fiber pull-out behavior and tensile stress-strain response of the composite, it is likely that the above general conclusions on pull-out behavior will translate into similar trends in rate sensitivity of fiber reinforced cement composites in tension. However, to ascertain such correlation, direct tensile tests are needed and are the subject of future publications by the authors.

Table 5.1–Matrix of pullout tests

	Hooked fiber	Twisted fiber	Loading rate	
			mm/sec	in/sec
Matrix 1	M1H	M1T	0.018	0.0007
			0.18	0.007
			1.8	0.07
			18	0.7
Matrix 2	M2H	M2T	0.018	0.0007
			0.18	0.007
			1.8	0.07
			18	0.7
Matrix 3	M3H	M3T	0.018	0.0007
			0.18	0.007
			1.8	0.07
			18	0.7

Table 5.2–Composition of matrix mixtures by weight ratio and compressive strength

Matrix	Cement (Type III)	Fly Ash°	Sand* (Flint)	Silica Fume	Super - Plasticizer	VMA**	Water	f_c', ksi (MPa)
Matrix 1	0.70	0.30	3.50	-	0.009	0.024	0.65	4 (28)
Matrix 2	1.00	0.15	1.00	-	0.009	0.006	0.35	8 (55)
Matrix 3	0.80	0.20	1.00	0.07	0.04	0.012	0.26	12 (84)

** Viscosity Modifying Agent, * ASTM 50-70, ° TYPE C

Table 5.3– Properties of high strength Hooked and Twisted fibers

Fiber Type	Diameter in (mm)	Length in(mm)	Density g/cc	Tensile strength ksi (MPa)	Elastic Modulus ksi (GPa)
Hooked	0.016 (0.4)	1.18 (30)	7.9	304 (2100)	29000 (200)
Twisted	0.012 (0.3)*	1.18 (30)	7.9	400 (2760)**	29000 (200)

* Equivalent diameter ** Tensile strength of the fiber after twisting

Table 5.4–Rate effect on Fiber Pullout Load

Loading rate [mm/sec]		0.018			0.18			1.8			18		
		LOAD		SLIP	LOAD		SLIP	LOAD		SLIP	LOAD		SLIP
		N	DIF[1]	mm	N	DIF[1]	mm	N	DIF[1]	mm	N	DIF[1]	mm
IMB pullout Load	M1T	30.3	1.0	0.40	33.1	1.1	0.40	36.5	1.2	0.40	60.2	2.0	0.40
	M1H	85.4	1.0	0.48	85.7	1.0	0.50	102.8	1.2	0.47	92.5	1.1	0.51
	M2T	68.4	1.0	0.40	97.3	1.4	0.40	135.3	2.0	0.40	174.0	2.5	0.40
	M2H	125.5	1.0	0.43	138.1	1.1	0.43	150.0	1.2	0.43	135.6	1.1	0.43
	M3T	122.0	1.0	0.40	135.0	1.1	0.40	128.0	1.0	0.40	144.1	1.2	0.40
	M3H	135.3	1.0	0.39	150.1	1.1	0.40	148.6	1.1	0.42	144.5	1.1	0.40
Maximum Pullout Load	M1T	60.9	1.0	8.27	70.3	1.2	9.12	71.6	1.2	6.87	80.3	1.3	6.55
	M1H	127.7	1.0	1.23	103.7	0.8	1.12	141.2	1.1	1.04	126.8	1.0	1.06
	M2T	155.8	1.0	11.14	153.5	1.0	9.17	182.7	1.2	2.05	207.4*	1.3	0.77**
	M2H	160.8	1.0	0.82	174.6	1.1	0.84	183.7	1.1	0.87	177.2	1.1	0.98
	M3T	139.2	1.0	1.08	168.7	1.2	2.00	163.6	1.2	3.07	175.3	1.3	1.50
	M3H	190.1	1.0	0.87	189.9	1.0	0.76	183.3	1.0	0.76	190.3	1.0	0.81

[1] DIF: Dynamic Increase Factor with respect to the 'static' case

* Pullout load at fiber breakage, ** Slip at fiber breakage

1 lb = 4.448 N, 1 inch = 25.4 mm

UP TO JMB Point

Table 5.5–Rate effect on Fiber pullout work and Equivalent bond strength

Loading rate [mm/sec]			0.018	0.18	1.8	18
	Pullout work [Mpa-mm]	M1T	161.9	168.8	183.6	187.1
		M1H	190.1	195.7	236.1	232.2
		M2T	293.0	391.2	556.2	741.4
		M2H	258.3	293.3	303.1	281.4
		M3T	558.1	565.0	551.7	545.6
		M3H	258.3	289.9	304.2	254.6
	Equivalent Bond strength [Mpa]	M1T	4.0	4.2	4.6	4.7
		M1H	6.3	6.5	7.9	7.7
		M2T	7.3	9.8	13.9	18.5
		M2H	8.6	9.8	10.1	9.4
		M3T	14.0	14.1	13.8	13.6
		M3H	8.6	9.7	10.1	8.5
COMPLETE PULLOUT	Pullout work [Mpa-mm]	M1T	7493.0	9754.0	9687.9	12919.4
		M1H	3947.1	3346.8	4015.3	3917.0
		M2T	21704.4	21995.6	25466.1	-
		M2H	5327.7	5512.9	6079.3	6371.1
		M3T	23155.1	27604.3	25967.0	20554.2
		M3H	5327.7	5424.3	5043.7	5198.4
	Equivalent Bond strength [Mpa]	M1T	5.0	6.5	6.5	8.6
		M1H	3.5	3.0	3.6	3.5
		M2T	14.5	14.7	17.0	-
		M2H	4.7	4.9	5.4	5.7
		M3T	15.4	18.4	17.3	13.7
		M3H	4.7	4.8	4.5	4.6

1 ksi = 6.9 MPa, 1 inch = 25.4 mm

Table 5.6–Rate effect on Slip capacity

Loading rate [mm/sec]		0.018		0.18		1.8		18	
		LOAD (N)	SLIP (mm)	LOAD (N)	SLIP (mm)	LOAD (N)	SLIP (mm)	LOAD (N)	SLIP (mm)
Maximum Slip Capacity	M1T	49.3	10.19	61.2	10.78	51.2	10.60	76.8	11.05
	M1H	71.5	2.95	60.3	3.28	82.0	3.03	66.9	3.24
	M2T	145.1	11.39	137.9	10.28	137.8	10.10	-	-
	M2H	66.2	3.69	77.4	3.47	84.2	3.44	82.7	3.48
	M3T	95.6	13.02	122.2	12.16	112.1	12.43	79.5	11.99
	M3H	82.6	3.53	77.1	3.61	77.5	3.52	75.3	3.77

1 lb = 4.448 N, 1 inch = 25.4 mm

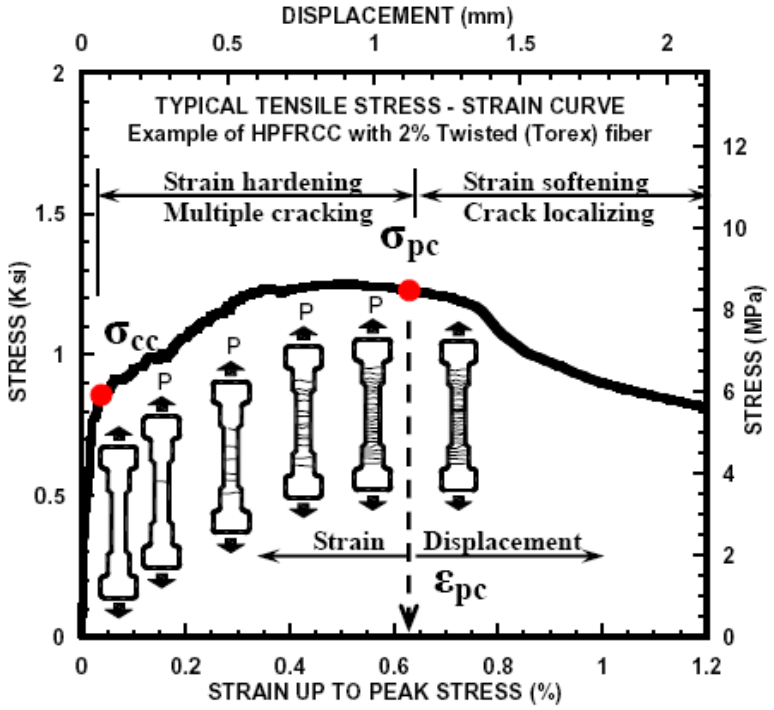

Fig. 5.1-Typical tensile stress-strain curve of HPFRCC

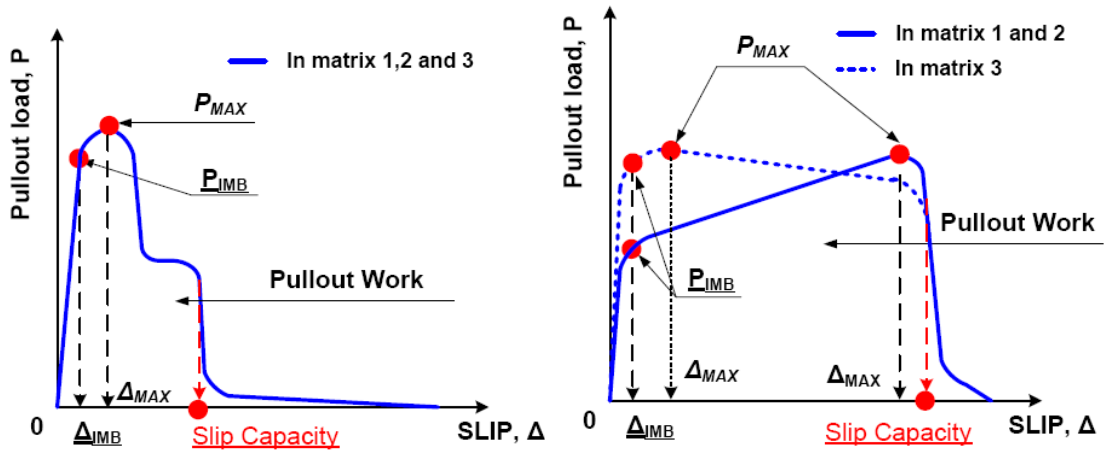

(a) Hooked Fiber (b) Twisted Fiber

Fig. 5.2-Pseudo static slip-hardening fiber pullout behavior

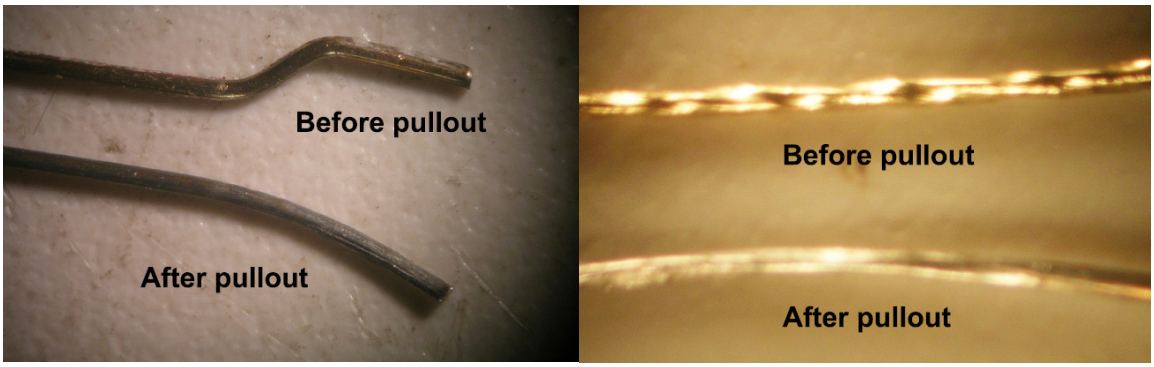

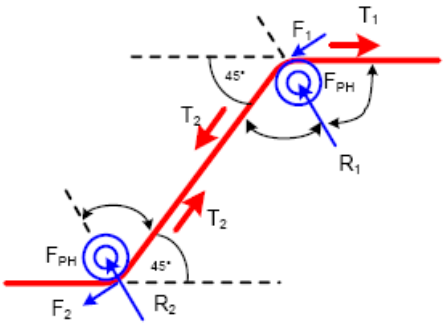

Line sketch of frictional pulley model
[Alwan et al, 1999]
(a) Hooked Fiber

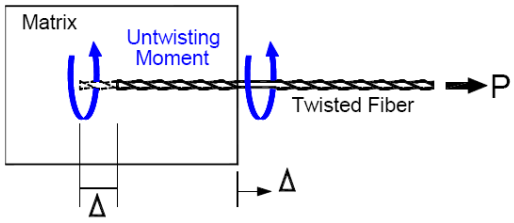

Pullout mechanism of Twisted fiber
[Sujiravorakul, C., 2001]
(b) Twisted Fiber

Fig. 5.3-Before and after pullout photos and mechanisms for Hooked Fiber and Twisted Fiber

1 inch = 25 mm

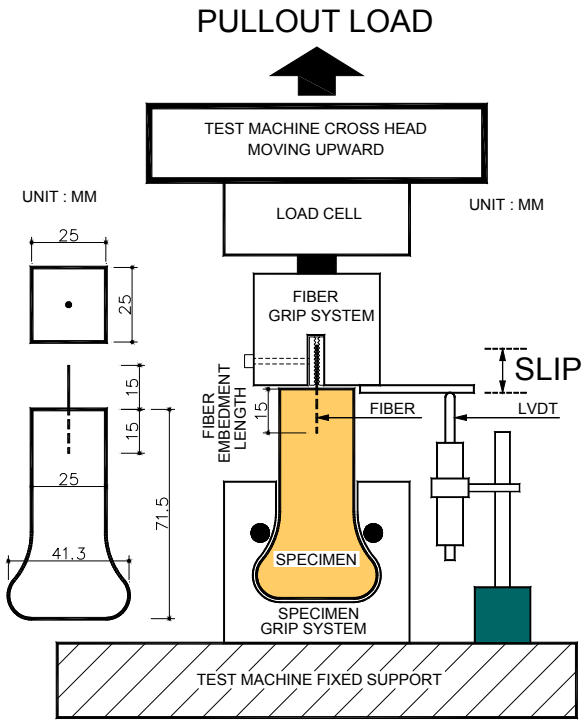

Fig. 5.4-Pull out test specimen and setup

1ksi = 6.9 Mpa, 1 lb = 4.448 N, 1 inch = 25.4mm

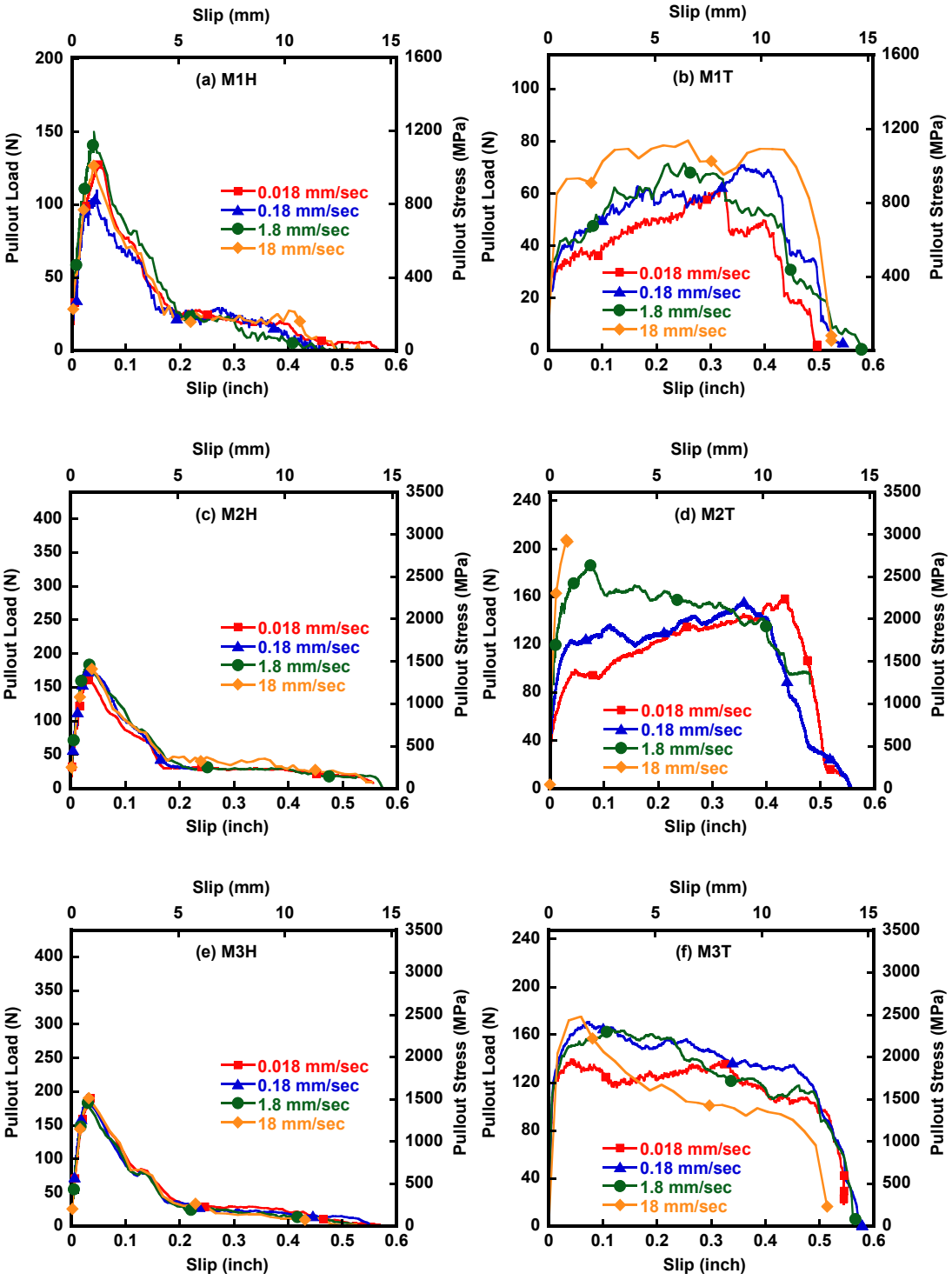

Fig. 5.5-Single fiber pull-out test results – Average curve

1 lb = 4.448 N, 1 inch = 25.4 mm

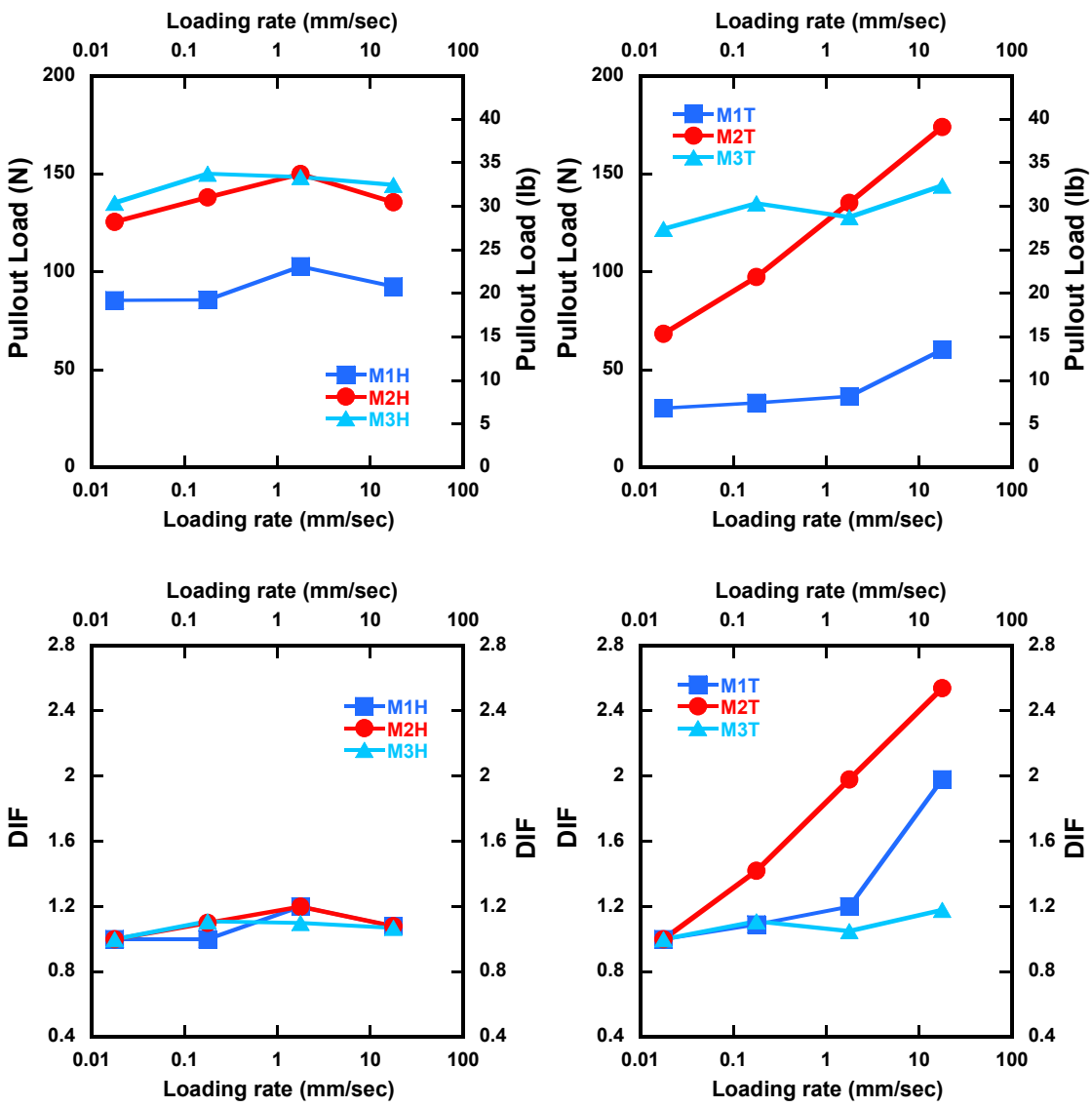

a) Hooked Fiber b) Twisted Fiber

Fig. 5.6-Rate effect on the Pullout Load at IMB point (Slip = 0.4mm)

1 ksi = 6.9 MPa, 1 inch = 25.4 mm

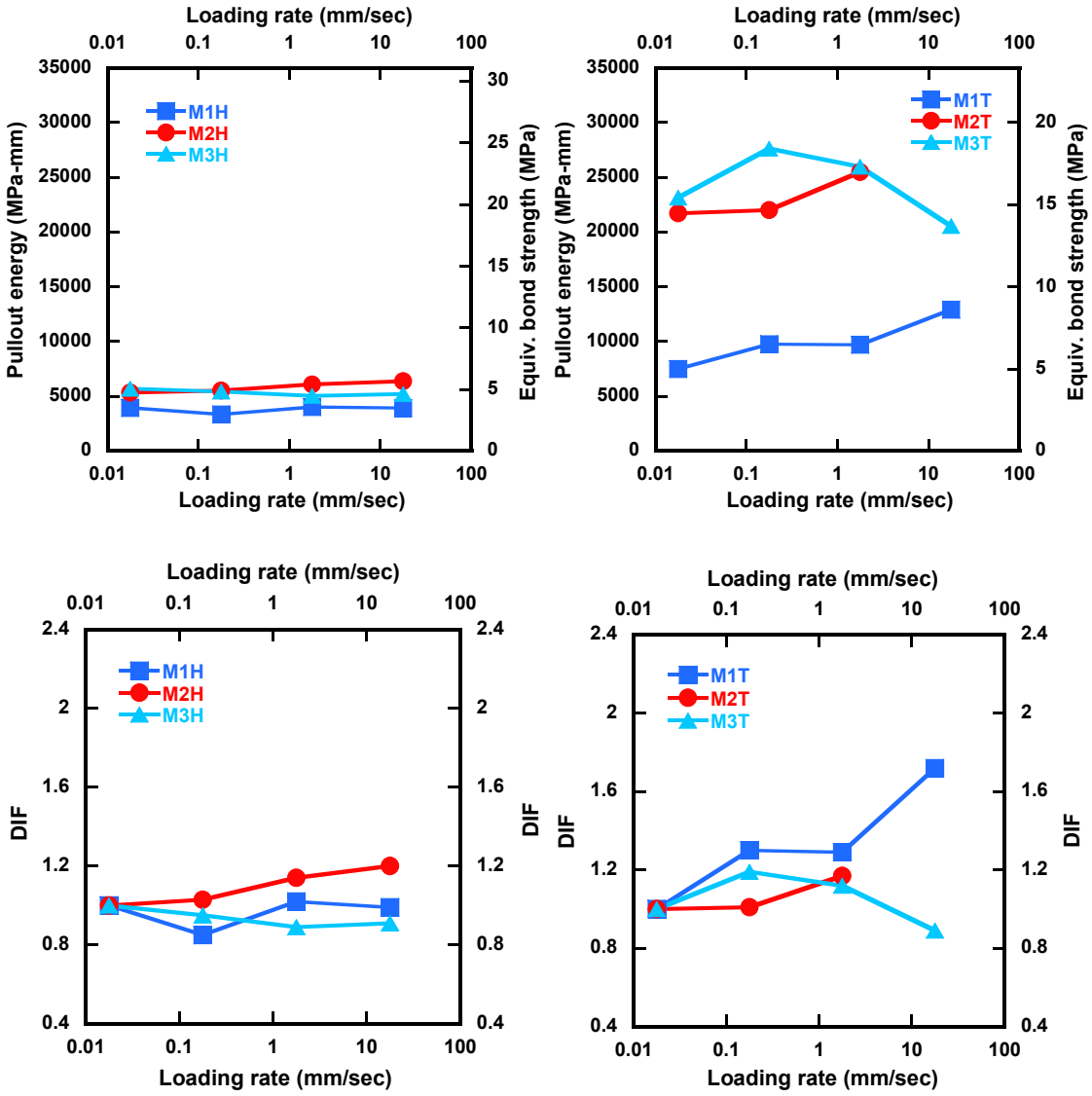

a) Hooked Fiber b) Twisted Fiber

Fig. 5.7-Rate effect on the Pullout Energy and Equivalent bond strength at complete pullout

1 ksi = 6.9 MPa, 1 inch = 25.4 mm

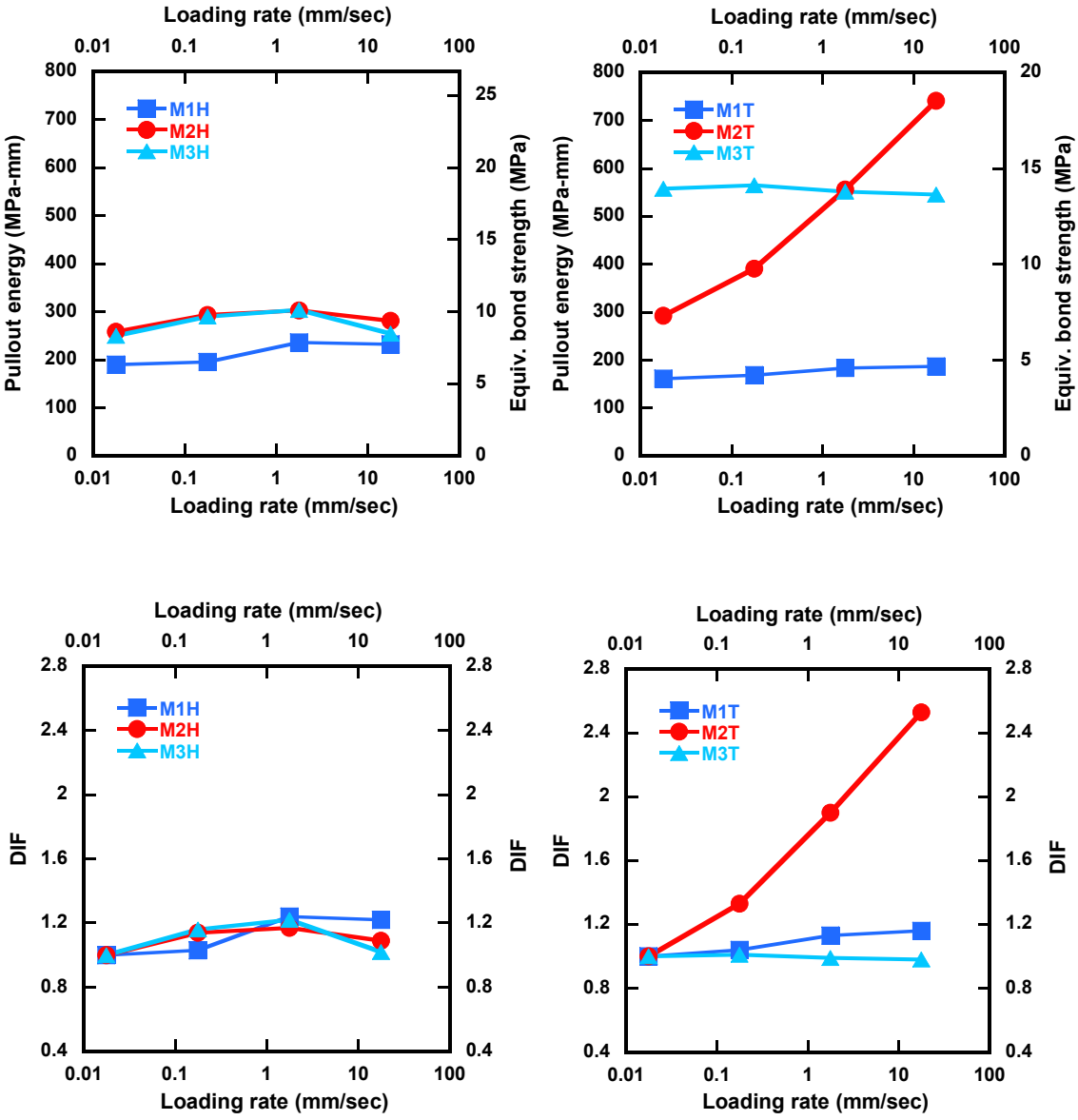

a) Hooked Fiber b) Twisted Fiber

Fig. 5.8-Rate effect on the Pullout Energy and Equivalent bond strength at IMB point (Slip = 0.4mm)

1 inch = 25.4 mm

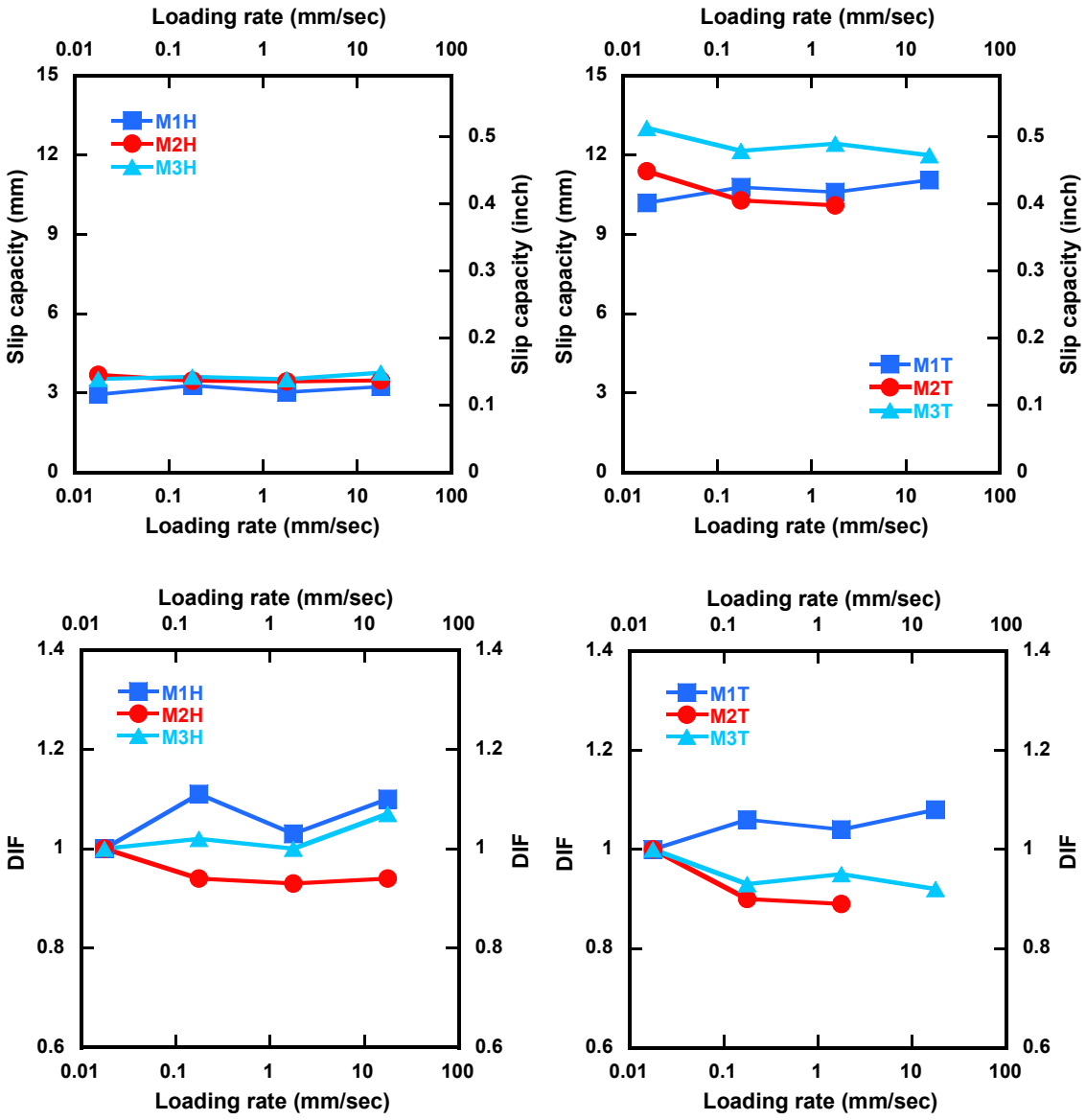

a) Hooked Fiber b) Twisted Fiber

Fig. 5.9-Rate effect on Slip capacity

1 inch = 25.4 mm

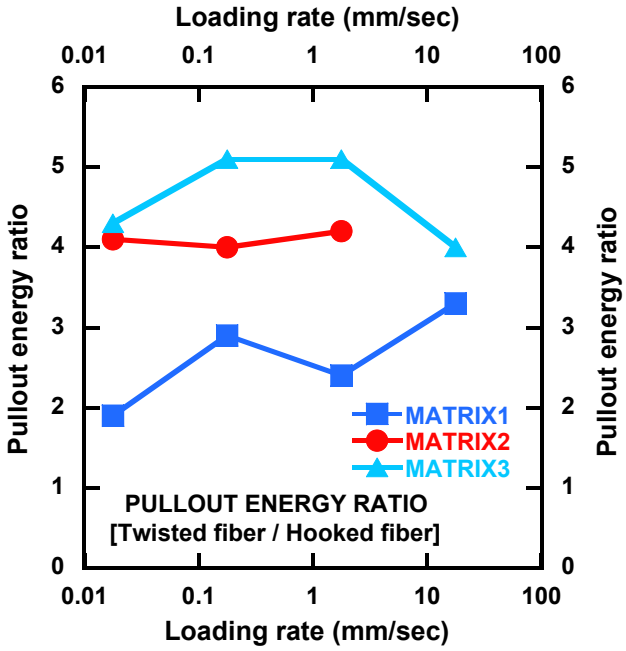

Fig. 5.10- Ratio of Pullout Energy of Twisted and Hooked fiber up to complete pull-out

REFERENCES

Alwan, J. M. Naaman, A. E., and Guerrero, P., "Effect of Mechanical Clamping on the Pull-out Response of Hooked Steel Fibers Embedded in Cementitious Matrices.," Concrete Science and Engineering, Vol. 1, Mar. 1999, pp. 15-25

Banthia, N. and Trottier, J. -F. "Deformed steel fiber – cementitious matrix bond under impact," CEMENT and CONCRETE RESEARCH, V. 21, 1991, pp. 158-168.

Canbolat, B. A., Gustavo, J. P. and Wight, J. K., "Experimental study on Seismic behavior of HPFRCC coupling Beams," ACI structural journal, Vol. 102, No. 1, Jan.-Feb. 2005, pp. 159-166.

Chandrangsu, K., and Naaman, A.E., "Comparison of Tensile and Bending Response of Three High Performance Fiber Reinforced Cement Composites," in High Performance Fiber Reinforced Cement Composites (HPFRCC-4), A.E. Naaman and H.W. Reinhardt, Etidors, RILEM Proceedings, Pro. 30, Cachan, France, 2003, pp. 259-274. .

Gokoz, U. and Naaman, A. E., "Effect of Strain Rate on the Pull-Out Behavior of Fibers in Mortar," International Journal of Cement Composites, Vol. 3, No. 3, Aug. 1981, pp. 187-202.

Kim, D., El-Tawil, S. and Naaman, A.E, "Correlation between single fiber pullout behavior and tensile response of FRC composites with high strength steel fiber", in High Performance Fiber Reinforced Cement Composites (HPFRCC-5), H.W. Reinhardt and A.E. Naaman, Editors, RILEM Proceedings , Pro 53, Cachan, France, 2007, pp. 67-76.

Naaman, A. E., "Engineered Steel Fibers with Optimal Properties for Reinforcement of Cement Composites," Journal of Advanced Concrete Technology, Japan Concrete Institute, Vol. 1, No. 3, November 2003, pp. 241-252.

Naaman, A. E., "Fibers with slip-hardening Bond," in High Performance Fiber Reinforced Cement Composites – HPFRCC 3," H.W. Reinhardt and A.E. Naaman, Editers, RILEM Pro 6, RILEM Publications S.A.R.L., Cachan, France, May 1999, pp. 371-385.

Naaman, A. E., Namur, G. G., Alwan, J. M., and Najm, H., "Fiber pullout and Slip. I : Analytical Study," Journal of Structural Engineering, ASCE, Vol. 117, No. 9, pp. 2769-2790, 1991

Naaman, A.E, "A Statistical Theory of Strength for Fiber Reinforced Concrete," Ph.D. Thesis, Massachusetts Institute of Technology, 1972, 196 pages

Naaman, A.E., "High Performance Fiber Reinforced Cement Composites," Concrete Structures for the future, IABSE Symposium, Paris, France, September 1987, pp. 371-376

Naaman, A.E., and Najm, H., "Bond-slip Mechanisms of Steel Fibers in Concrete," ACI Materials Journal, Vol. 88, No. 2, April 1991, pp. 135-145.

Naaman, A.E., and Reinhardt, H.W., "Characterization of High Performance Fiber Reinforced Cement Composites," Proceedings of 2nd International Workshop on HPFRCC, Chapter 41, in High Performance Fiber Reinforced Cement Composites:

HPFRCC 2, A.E. Naaman and H.W. Reinhardt, Editors, RILEM, No. 31, E. & FN Spon, London, 1996, pp. 1-24.

Naaman, A.E., and Reinhardt, H.W., "Proposed Classification of FRC Composites Based on their Tensile Response " Materials and Structures, Vol. 39, page 547-555, 2006.

Parra Montesinos, G., J. P., Sean, W. U. and Shih-ho, C., "Highly Damage-Tolerant Beam-Column Joints Through use of High-Performance Fiber-Reinforced Cement Composites," ACI Material Journal, Vol. 102, No. 3, May-June 2005, pp. 487-494.

Soubra, K., Wight, J.K., and Naaman, A.E., "Cyclic Response of Cast-in-Place Connections in Precast Beam-Column Subassemblages," ACI Structural Journal, Vol. 90, No. 3, May-June, 1993, pp. 316-323.

Soubra, K., Wight, J.K., and Naaman, A.E., "Fiber Reinforced Concrete Joints for Precast Construction in Seismic Areas," ACI Structural Journal, Vol. 88, No. 2, March-April 1991, pp. 214-221.

Sujiravorakul, C., "Development of High Performance Fiber Reinforced Cement Composites Using Twisted Polygonal Steel Fibers," Ph.D. thesis, University of Michigan, Ann Arbor, Feb. 2001. pp. 230.

Vasconez, R.M., Naaman, A.E., and Wight, J.K., "Behavior of HPFRC Connections for Precast Concrete Frames under Reversed Cyclic Loading," PCI Journal, Vol. 43, No. 6, Nov.Dec. 1998, pp. 58-71.

Vos, E. and Reinhardt, H. W., 'Bond resistance of deformed bars, plain bars and strands under impact loading', Report No. 5-80-6, Department of Civil Engineering, Delft University of Technology, The Netherlands, Sept. 1980.

Yang, E. and Li, V. C., "Rate dependence in Engineered Cementitious Composites," in Proceedings, Proceedings of International RILEM Workshop on HPFRCC in Structural Applications, Published by RILEM SARL, pp. 83-92, 2006.

CHAPTER VI

RATE-DEPENDENT TENSILE BEHAVIOR OF HIGH PERFORMANCE FIBER REINFORCED CEMENTITIOUS COMPOSITES [5]

ABSTRACT

High Performance Fiber Reinforced Cementitious Composites (HPFRCC) show strain hardening behavior accompanied with multiple micro-cracks under static tension. The high ductility and load carrying capacity resulting from their strain hardening behavior is expected to increase the resisting capacity of infrastructure subjected to extreme loading situations, i.e. earthquake, impact and blast. However, the promising high performance of HPFRCCs is based on their static tensile behavior, and there is very little information about the rate effect on HPFRCC. This experimental study investigated tensile behavior of HPFRCC using High strength steel fibers (High strength Hooked fiber and Twisted fiber) under various strain rates ranging from static to seismic rates. The test results indicated that the tensile behavior of HPFRCC using Twisted fiber shows high rate sensitivity while that using Hooked fiber shows no rate sensitivity. The rate sensitivity in Twisted fibers is also dependent upon both fiber volume fraction and matrix strength,

[5] D. Kim, S. El-Tawil, and A. E. Naaman, "Rate-dependent tensile behavior of high performance fiber reinforced cementitious composites", Materials and Structures, ISSN 1359-5997 (in print), 1871-6873 (online), May 21, 2008

which influences the interface bond properties.

6.1 INTRODUCTION

The demand has never been greater for tougher, more ductile materials to improve the behavior of civil engineering structures under rapid and severe loading, such as blast, impact and earthquakes. A particularly promising class of materials for such applications is high performance fiber reinforced cementitious composites (HPFRCCs), which exhibit a 'high performance' response in tension, i.e. strain hardening response after first cracking, extreme tensile ductility, both of which lead to improved durability and high energy absorption capacity. HPFRCCs, as first defined and developed by Naaman (1987), can now achieve high performance behavior through the use of a relatively low volume fraction (usually 2% or less) of short, randomly oriented steel or polymeric fibers. At the present time, HPFRCCs are classified as *tensile strain-hardening* fiber reinforced cementitious composites (FRCC) (Naaman and Reinhardt, 1996 and 2006).

In order to achieve *tensile strain-hardening behavior*, various approaches have been tried and used by many researchers. One well established example is SIFCON (slurry infiltrated fiber concrete) and its similar derivative SIMCON (slurry infiltrated mat concrete) which were developed during the late 1970's and 1980's (Lankard (1985), Krstulovic-Opara (1997)). Engineered Cementitious Composites [ECC] is also one family of HPFRCC. ECC utilize about 2% PVA fiber to produce strain hardening behavior with 3-4 MPa tensile strength; their strain capacity may be relatively high but is dependent on the size of the specimen and the method of testing. Value as high as 3% to 4% were reported (Li and Wang (2006) and Yang et al (2007)). Newer forms of HPFRCC include Ultra High Performance Fiber Reinforced Cement [UHPFRC]

composites which are characterized at the mechanical level by a very high compressive strength (practically in the range of 150–200MPa); however, to develop strain hardening behavior in tension, they require 5-11 % fiber contents by volume, mostly smooth steel fibers (Rossi (2005), Habel et al (2006), Graybeal (2007)). Very little information is available to describe the entire stress-strain response of UHPFRCC in direct tension using reasonably large size specimens. As of this writing, the tensile strength achieved by UHPFRC using 2% high strength steel fibers by volume, is around 11 MPa and its strain capacity at maximum stress is close to 0.5% (Kim et al. (2007)). In this research, high strength deformed steel fibers which show slip hardening behavior under single pullout testing are used to obtain tensile strain hardening behavior of the composite. It was shown earlier that the slip hardening behavior which leads to high pullout energy (or work) is a critical condition for the strain hardening behavior of FRC composites. (Kim et al. (2007))

The promise of HPFRCCs for dynamic loading application stems from their observed good response under static loading. However, very little research has been conducted to investigate if their good static response translates into improved dynamic response and damage tolerance. The objective of this paper is therefore to address this gap and provide information about the dynamic response of two types of HPFRCC, namely: HPFRCCs with high strength Hooked (H-) and Twisted (T-) fibers. H-fibers and T-fibers are employed in this research because their slip hardening behavior is believed to be a key factor in obtaining 'high performance' strain hardening behavior at the composite level for relatively *low* fiber volume fractions. Indeed, the author (Kim et al. (2007)) previously showed that a strong correlation exists between slip hardening behavior in

single fiber pullout and strain hardening behavior in tension. In addition, they demonstrated that strain hardening behavior can be achieved by using only 1% to 2% fibers by volume.

The overall goal of the research reported in this chapter is to develop a fundamental understanding of the effect of strain rate on the tensile behavior of HPFRCCs using high strength steel fibers and to provide experimental test data for strain rates that range from pseudo-static to seismic. In addition, the effects of fiber type, fiber volume fraction and matrix strength on the rate sensitivity are also investigated.

6.2 RESEARCH SIGNIFICANCE

This research provides information about the effect of strain rate on the tensile behavior of HPFRCC with high strength steel H- and T-fibers. The research investigates rate effect on the first cracking strength, post cracking strength, strain capacity and general cracking behavior as a function of fiber type, fiber volume fraction and matrix strength. It is observed that a strong correlation exists between rate sensitivity in single fiber pullout behavior and rate sensitivity at the corresponding HPFRCC composite level. This realization provides a means for developing a fundamental understanding of the factors that influence global rate sensitivity and, eventually, a means for tailoring the dynamic response of HPFRCC as a function of fiber pull-out behavior.

6.3 STRAIN RATE EFFECT ON FRCC

Fiber reinforced concrete or cement composites differ from HPFRCC in that FRCC response is not considered ‘high performance’, because it does not exhibit strain hardening response in tension. Nevertheless, FRCCs are widely perceived as tougher than regular mortar or concrete and their response under impact loading has been investigated

and reported by many researchers during the last twenty years.

Nammur and Naaman (1986) investigated strain rate effects on the tensile properties of fiber reinforced concrete. They reported that the pre-cracking strength as well as the strain at peak stress both increase with increasing strain rates and the post-cracking strength of fiber reinforced concrete also increases with strain rate. However, they also observed that the displacement at failure decreases with increasing strain rates. Körmeling and Reinhardt (1987) investigated high strain rate effects on FRCC with steel fibers in uniaxial tension. There was a significant increase in tensile strength of plain and steel fiber reinforced concrete due to high strain rates. The fracture energy and strain at maximum stress also increased at higher strain rates.

Banthia et al. (1993) also reported that FRCC were found to be stronger and tougher under impact and that the improvements were more pronounced at higher fiber volume fractions. They used a modified charpy pendulum machine to perform high strain rate testing with three types of fibers (Carbon, Steel and Polypropylene). In related research, Banthia et al. (1996) concluded that fiber reinforcement is indeed effective in improving fracture energy absorption under impact, however, the improvement is dependent on fiber type and geometry but is not as pronounced as observed under static conditions. Fiber types used in that experimental test program were hooked-end, crimped and twin cone steel fibers.

Other researchers who have investigated the dynamic response of FRCC include Rostásy and Hartwich (1985), Körmeling and Reinhardt (1987), Suaris and Shah (1982), Gopalaratnam and Shah (1986), Lok and Zhao (2004), Sun-Wei et al. (2005). These researchers, along with the others discussed above have showed that the mechanical

properties and rate sensitivity of FRCC are dependent upon the fiber type, fiber volume fraction and matrix strength (composition), which influences the bond between fiber and matrix.

6.4 STRAIN RATE EFFECT ON HPFRCC

To the best knowledge of the authors, no studies have been reported on the effect of strain rate on the tensile behavior of strain-hardening HPFRCC using high strength deformed steel fibers. However the effect of strain rate on the flexural behavior of CRC (compact reinforced concrete), a particular form of UHPFRC, was investigated by Bindiganavile et al (2002) using a drop weight impact testing method. CRC demonstrated a significantly higher energy absorption capacity in comparison to normal FRCC. There are, however, a few references on the rate sensitive behavior of HPFRCC with polymeric fibers, i.e. ECC. For example, Yang and Li (2005) reported strong rate dependence in ECC. They performed a uniaxial tensile test with different strain rate ($\dot{\varepsilon} = 10^{-5} \sim 10^{-1} / \sec$) to investigate the rate dependency by using a hydraulic testing machine. Douglas and Billington (2005) also examined rate dependence in ECC for seismic applications. Cylindrical specimens of ECC were subjected to monotonic compression, monotonic tension, and reversed-cyclic tension and compression at varying strain rates. They reported that while tensile strength increases with strain rate, the ductility decreases under seismic loading rate. In addition, tensile strength increased by 12% and the modulus of elasticity increased by 22%.

In contrast to the findings of Yang and Li (2005) and Douglas and Billington (2005), Maalej et al. (2005) reported that the tensile strain capacity in their tests was insensitive to strain rate. Theirs were tests on a hybrid-fiber ECC (1.5 vol. % polyethylene and 0.5

vol. % steel fibers). They did, however, note that the tensile strength increased with increasing strain rate.

6.5 CORRELATION BETWEEN SINGLE FIBER PULLOUT BEHAVIOR AND TENSILE BEHAVIOR

A typical pseudo-static tensile stress–strain curve for HPFRCC is shown in Figure 6.1. The strain hardening response, where the maximum post-cracking strength, σ_{pc}, is higher than the first cracking strength, σ_{cc}, is clear in the figure. In a typical HPFRCC, the post-cracking strength is directly dependent on the average bond strength at the fiber matrix interface, which is assumed to be a constant over a relatively small level of slip. Assuming that the bond strength remains a constant over the entire embedment length, Kim et al. (2007) suggested that an equivalent bond strength, τ_{eq}, could be calculated from the pullout energy obtained from a single fiber pullout test. (Chapter II)

By using the following equations suggested by Naaman [1970, 1972, 1987, 2000], the first cracking strength [Eq. 6.1] and post cracking behavior [Eq. 6.2] in the tensile behavior of HPFRCC can be calculated by using the equivalent bond strength. In addition, crack spacing (number of cracks within the gage length) shows strong dependency on the equivalent bond strength (Kim et al. (2007) and Chapter II).

$$\text{First cracking strength}: \ \sigma_{cc} = \sigma_{mu} \times \left(1 - V_f\right) + \alpha \times \tau_{eq} \times V_f \left(L_f / d_f\right) \qquad [6.1]$$

$$\text{Post cracking strength}: \ \sigma_{pc} = \Lambda \times \tau_{eq} \times V_f \left(L_f / d_f\right) \qquad [6.2]$$

Where, V_f = fiber volume fraction, L_f = fiber length, d_f = fiber diameter, σ_{mu} = tensile strength of matrix, τ_{eq} = equivalent bond strength, α = factor equal to the product of several coefficients for considering average stress, random distribution and fiber

orientation, λ = factor equal to the product of several coefficients for considering average pullout length, group reduction, orientation effect.

In the original formulation of Eqs. 6.1 and 6.2 the average bond strength over a given slip was used instead of the equivalent bond strength. In this study, the equivalent bond strength was defined using Eq. 6.3 which is based on the pullout work during the single fiber pullout test.

$$\tau_{eq} = \frac{8 \times PulloutEnergy}{\pi d_f L_f^{\,2}} \qquad [6.3]$$

If the equivalent bond strength is sensitive to the loading rate, i.e. if the pullout energy is different according to the applied loading speed, then the tensile behavior of HPFRCC is also expected to be rate sensitive because both first cracking strength and post cracking strength are basically functions of the equivalent bond strength as described in Eq. 6.1 and Eq. 6.2. However, for the cracking strength, the influence of bond is very small because the response is primarily dominated by the matrix (Eq. 6.1).

6.6 RATE EFFECT ON SINGLE FIBER PULLOUT BEHAVIOR

Single fiber pullout tests (Kim et al. (2008) and Chapter V) of both high strength steel H-fibers and T-fibers show slip hardening behavior as depicted in Fig. 6.2. This slip hardening behavior is key to achieving strain hardening behavior at the composite level. Kim et al. (2008) investigated the effect of rate sensitivity on the equivalent bond strength as defined in Eq. 6.3. For the loading rates applied, which varied from pseudo-static up to seismic as specified later on, the test results showed that T-fibers are sensitive to the loading rate in the single fiber pullout test. In contrast, H-fibers exhibited no rate sensitivity in the same type of test. Kim et al. (2008) also concluded that the observed

rate sensitivity in T-fibers was dependent on the surrounding matrix strength and theorized that interface adhesion, friction and hardness all play a role in the observed rate sensitivity. A different observation regarding rate sensitivity in H-fiber pull out response was reported by Banthia and Trottier (1991) who used a modified pendulum test method to generate loading speeds of up to 1500 mm/sec. In their tests, H- fibers showed maximum dynamic pull-out loads ranging from 1.38 to 4.58 times higher than those under quasi-static pullout.

6.7 EXPERIMENTAL PROGRAM

An extensive experimental program was undertaken to investigate the sensitivity of the tensile response of HPFRCC to strain rate. The main experimental parameters were: type of high strength steel fibers (H-fibers and T-fibers are both used), fiber volume fractions (two volume fractions of $V_f = 1\%$ and $V_f = 2\%$ were used), and matrix strength (3 matrices having low [28 MPa], medium [56 MPa] and high [84 MPa] compressive strength were used). The matrices employed are designated M1, M2 and M3, which correspond to low, medium and high strength matrices, respectively.

A total of twelve series of tensile test specimens were prepared and tested as shown in Table 6.1. The first two letters in the series names designates the matrix type (M1, M2 or M3), the third letter is the type of fiber (T-fibers of H-fibers) and the fourth letter is the volume fraction (corresponding to 1% or 2%). For example, M1H1 implies an HPFRCC specimen with matrix M1 and H-fibers with 1% volume fraction.

Four different loading rates were applied in each series in order to investigate the rate effect on tensile behavior. The slowest rate was 0.0178 mm/sec. For a specimen gage length of 178 mm (7 inches), this implies a strain rate of $\dot{\varepsilon} = 0.0001/\sec$, which

nominally corresponds to a pseudo-static loading rate. The highest loading rate was 17.8 mm/sec, which implies a strain rate of $\dot{\varepsilon} = 0.1/\sec$ that nominally corresponds to seismic loading. In between these two extremes were loading rates of 0.178 and 1.78 mm/sec, i.e. each loading rate is faster than the former by a factor of 10. The difference between the fastest and slowest rates was therefore 3 orders of magnitude. At least three specimens for each loading rate in each test series were tested, i.e. 144 specimens in total (12 series × 4 loading rates × 3 specimens) in this experimental program. A hydraulic servo-controlled testing machine (MTS-810) was used to conduct the tensile tests.

6.7.1 Materials and specimen preparation

The matrix mix composition and compressive strength are given in Table 6.2 and the main properties of the fibers are provided in Table 6.3. Note the very high tensile strength of the fibers used. Figure 3 shows the fiber shape before and after the single fiber pullout test.

A Hobart type laboratory mixer was used to prepare the mix. Cement, fly-ash and sand were first dry mixed for about 2 minutes. Water mixed with superplasticizer and Viscosity Modifying Agent (VMA), which helps ensure a uniform fiber distribution, was then added gradually and mixed for another 5 to 10 minutes. When the mortar started to show adequate flowability and viscosity, both of which are necessary for the good workability and uniform fiber distribution, fibers were dispersed carefully by hand in the mix. The cementitious mixture with uniformly distributed fibers was carefully placed in a mold and slightly vibrated using a high frequency vibrating table. Specimen casts were covered with plastic sheets and stored at room temperature for 24 hours prior to demolding. The specimens were then placed in a water tank for an additional 2 weeks. All

specimens were tested in a dry condition at the age of 16 days including 2 days for drying.

6.7.2 Test setup and procedure

The geometry of the specimen (bell-shaped ends) and the test set up are shown in Fig. 6.4. Two embedded layers of steel wire mesh are used to reinforce both ends of the specimen to avoid failure outside of the gage length. The gage length of the dog bone type tensile test specimen is 178mm (= 7 inch). Two OPTOTRAK markers (for non contact displacement measurement) were attached to the surface of the specimen. Traditional Linear Variable Displacement Transducers (LVDTs) were not used because their sampling rate was not adequate enough for measuring deformation of the specimen under the fastest loading rate. The displacement of the two markers attached on the surface of the tensile specimen was obtained from three cameras in the OPTOTRAK system and used for calculating deformation of the specimen. Note that preliminary static tests confirmed good agreement between the data reported by the OPTOTRAK system and those simultaneously recorded by two LVDTs attached to the same specimen. The tensile load history was obtained from the load cell of the test machine and synched with the non-contact displacement measurements.

6.7.3 Test Results

The following parameters are sufficient for describing the tensile behavior of HPFRCC; first cracking strength (σ_{cc}), elastic modulus prior to cracking or equivalently the strain at first cracking, post cracking strength (σ_{pc}), strain capacity, which is the strain value at post cracking strength (ε_{pc}) and the number of cracks within the gage length. The average crack width at post cracking strength is estimated by using the strain

capacity and equivalent number of cracks within the gage length. Table 6.4 shows the test results including the four basic parameters ($\sigma_{cc}, \sigma_{pc}, \varepsilon_{pc}$ and number of cracks). All the values given in Table 6.4 are averaged values from least three specimens. A Dynamic Increase Factor (DIF), which is the ratio between dynamic response and static response, is computed for each quantity to effectively illustrate the strain rate effect on each parameter. The DIF values are also listed in Table 6.4.

The average tensile stress–strain curves for each series with T-fibers for the four different strain rates are plotted in Fig. 6.5. Series with insufficient specimens, e.g. due to specimen damage during handling or where failure did not occur in the gage length during testing, are not considered in the analysis and are not shown in the plots. The highest rate sensitivity generally occurs in series with 1% fibers, especially in the M2T1 (Fig. 6.5b) and M3T1 (Fig. 6.5c) series. On the other hand, the lowest rate sensitivity generally occurs in series with 2% fibers, and especially in M3T1 (Fig. 6.5f) series.

In order to demonstrate that the rate sensitive behavior of M2T1 and M3T1 series is a real material characteristic and that it does not stem from test variance, individual test results for both series are plotted in Fig. 6.6 and Fig. 6.7, respectively. It is clear from both figures that in spite of some variability in test results, the strain rate effect is indeed perceptible. It is also obvious that under the seismic strain rate, T-fiber reinforced specimens yield higher tensile strength, load carrying and energy absorption capacity without losing much strain capacity compared to specimens loaded under a pseudo-static strain rate.

In sharp contrast to specimens in the M2T1 and M3T1 series, all H-fiber series do not show rate sensitive behavior regardless of fiber volume fraction and matrix type as shown

in Fig. 6.8. This clear difference in rate sensitive behavior between the H-fibers and T-fibers was also observed in the single fiber pullout test as shown in Fig. 6.2 by Kim et al. (2008) and in Chapter V. These results suggest that there is a link between the rate sensitive response of a single fiber under pull-out and the HPFRCC composite. Nevertheless, while the correlation is strong for H-fibers, it is not as clear for T-fibers, where series with 2% volume fractions did not exhibit rate sensitivity despite the rate sensitive pull out response of the fibers.

An important observation is that all test series maintained their 'high performance' response for all loading rates, i.e. strain hardening was observed for all loading rates. This is true for H-fiber as well as T-fiber series. This issue will be discussed in more detail farther below.

Fig. 6.9 shows the observed cracking patterns for the four different loading rates for test series M3T1 and M3H1. The most obvious difference between Fig. 6.9(a) and 6.9(b) is the difference in cracking pattern, especially number of cracks, between the T-fiber specimens and the H-fiber specimens. In general, the former exhibits many more cracks than the latter. The effect of strain rate on cracking patter is, however, difficult to discern from the figure. It appears that rate of loading has little discernable influence and that the number of cracks in M3T1 increases slightly as the strain rate increases.

6.8 EVALUATION OF EXPERIMENTAL RESULTS

The numerical results in Table 6.4 along with the plots in Figures 6.10, 6.11 and 6.12 quantify the effect of 3 parameters, namely fiber type, fiber volume fraction and matrix strength, on the load rate sensitivity of HPFRCC. Plotted in Figures 6.10 through 6.12 are series averages as well as test ranges to provide an indication of the level of test

variability. All three parameters of interest appear to be interdependent and an attempt is made below to discuss their influences by comparing the effect of loading rate on the first cracking strength, post cracking strength, strain capacity and number of cracks for corresponding HPFRCC series.

6.8.1 Effect of Fiber Type

In general, the test results show that HPFRCC specimens with T-fibers are generally sensitive to strain rate, whereas their counterparts with H-fibers are generally not. The level of sensitivity of T-fiber reinforced specimens depends on matrix type and fiber content. Fig. 6.10 contrasts between the performance of M2T1, which exhibited the highest level of sensitivity among all the series, and the corresponding H-fiber series, M2H1. The first cracking strength of M2T1 under the seismic rate is 5.82 MPa which is significantly higher than the static value, 2.91 MPa (the corresponding DIF is 1.98). On the other hand, the corresponding DIF for M2H1 is 1.2. Although there appears to be some strain rate effect for M2H1 in this case, the variability in results (Fig. 6.10a) is large enough to potentially mask this effect and makes it difficult to determine if there is indeed a true strain rate effect. Rate effect is primarily due to fiber.

The DIF of post cracking strength at the seismic rate for M2T1 is 1.73 whereas the corresponding DIF for M2H1 is 1.4. Again, the variability in results and trend in Fig. 10b do not strongly support the conclusion that there are significant strain rate effects for HPFRCC with H-fibers. However, the trend for T-fibers of strength increase with increasing strain rate is clear in Fig. 6.10b.

The effect of strain rate on strain capacity is not clear for either type of fiber. As shown in Fig. 6.10 (c) M2T1 series shows a slight decrease in average strain capacity

while M2H1 shows a slight increase. However, the variability in the test data indicates that the average trends may not be accurate and that there is likely no effect on strain capacity. A similar conclusion can be reached regarding the number of cracks (Fig. 6.10d).

The general trends discussed above hold for corresponding H- and T-fiber series with the other two matrices (M1 and M3), even though the rate sensitivity of T-fiber specimens is not as pronounced as in the M2 specimens.

6.8.2 Effect of Fiber Volume Fraction

Since H-fibers did not exhibit appreciable rate sensitivity for the two volume fractions considered, the following discussion focuses only on specimens with T-fibers, where the effect of fiber volume fraction on the rate sensitivity is shown in Fig. 6.11. M2T1 and M2T2 series are chosen for comparison because M2T1 shows clear rate sensitivity while M2T2 shows little or no rate sensitive behavior. For the seismic strain rate, the DIF for first cracking strength of M2T1 specimens 1.998, which is much higher than the DIF value of M2T2 specimens (1.08). The same trend, i.e. significant rate sensitivity at the lower volume fraction, is present for the post cracking strength. However, given the variability and trends shown in Fig. 6.11(c) and 6.11(d), both the strain capacity and number of cracks, respectively, do not seem to be much influenced by the loading rate.

6.8.3 Effect of Matrix Strength and Composition

Plots of DIF versus strain rate for first cracking strength, post cracking strength, strain capacity and number of cracks for the M1T1, M2T1 and M3T1 series are compared in Fig. 6.12 to highlight the effect of matrix compressive strength and composition on composite rate sensitivity. Figure 6.12(a) shows that the highest rate sensitivity for first cracking strength occurs in matrix M2, while the lowest occurs in M1. The same trend

can be seen in Fig. 6.12b for post cracking strength. Nevertheless, while a strong rate effect of Matrix strength on σ_{cc} and σ_{pc} was observed, no clear tendency can be observed for strain capacity (Fig 6.12(c)). It does appear from Fig. 6.12(c) that the strain capacity decreases slightly as strain rate increases regardless; however, the reduction is small enough that it is within the variability of the test results and cannot therefore be confirmed.

Fig. 6.12(d) appears to show that there is a significant rate effect on the number of cracks for specimens with M1 and M3 matrices, and almost none for specimens with M2 matrices. The trend for M1 and M3 is opposite. For example, while specimens with M3 matrices showed a marked increase in the number of cracks with increasing strain rate, those with M1 showed a marked decrease. In drawing conclusions from the last statement, however, readers should note that there was large variability observed in the number of cracks, and that the crack counting process itself is subjective because of the difficulty of ascertaining the presence of a crack after unloading.

6.8.4 Discussion of Test Results

Several general trends can be discerned in the test data presented:

1) Specimens with H-fibers are generally not sensitive to strain rate effects, while specimens with T-fibers exhibit some rate sensitivity;

2) The rate sensitivity in T-fiber reinforced specimens is greatest in specimens with the medium strength matrix (M2) and for the lower volume fraction; and

3) For T-fiber reinforced specimens, the strain capacity seems to be mostly unaffected by increasing strain rate, while the number of cracks exhibit widely varying trends depending on the matrix strength.

Clearly, the rate sensitivity of fiber pullout response plays a role in the sensitivity of the composite to strain rate. For example, it appears that the lack of rate sensitivity of H-fibers during pullout (as observed in Kim et al. (2008) and Chapter V) translates into composite response that is also insensitive to strain rate. The opposite is also true, that is, the rate sensitivity of T-fiber pull out behavior likely influenced the composite's sensitivity to strain rate. This premise is supported by the fact that specimens with M2 matrix are more sensitive than those with either M1 or M3 matrices, which correlates well with fiber pull out response as described in Kim et al. (2008) and Chapter V. In related research, Kim et al. (2008) and Chapter V showed that T-fiber pull-out behavior exhibit the greatest rate sensitivity in the medium compressive strength matrix (M2), second highest sensitivity in M1 and lowest in M3. In other words, the pullout rate sensitivity directly translates into sensitivity of the composite as observed in this paper. Kim et al. (2008) attributed the observed rate sensitivity in T-fiber pullout to the radial and longitudinal interface cracking that take place along the entire embedded fiber length as the fibers untwist during pull out.

However, the rate sensitivity of T-fiber pullout response did not uniformly translate into rate sensitivity for all series. The fact that series with 2% volume fraction showed little rate sensitivity unlike those with 1% volume fraction, implies that mechanisms other than pull out are likely controlling the response of the composite at higher volume fractions. The results in this paper therefore suggest that these mechanisms, which are being activated at higher volume fractions, are not rate sensitive in themselves implying that the composite is not fully optimized to take advantage of the strain rate effect. It is possible for instance that the group effect, which occurs when a group of fibers interact

together during pull out, is not as rate sensitive as single fiber pull out, which could dilute or eliminate rate sensitivity. It is also possible that at high composite post-cracking tensile strength, some fibers fail at higher strain rates instead of pulling out.

6.9 CONCLUSIONS

This study investigated the strain rate effect on the tensile behavior of HPFRCC using two deformed high strength steel fibers, namely Hooked fibers and Twisted (Torex) fibers. The strain rate ranged from pseudo static to seismic. By comparing previously published single fiber pull out test results to new composite test results described in this paper, it was shown that there is strong correlation between the rate sensitive behavior of HPFRCC composites and single fiber pullout response. The composite test results, as did the previous single fiber pull out test results, confirmed that the rate sensitivity of HPFRCC in tension depend on fiber type, volume fraction and matrix strength (or composition). The tests showed that the tensile behavior of HPFRCC with Twisted fibers is sensitive to the strain rate, while Hooked fiber reinforced specimens show no rate sensitivity. It was also observed that lower fiber volume fraction (V_f=1%) reinforced specimens show higher sensitivity than higher fiber volume fraction (V_f=2%) reinforced specimens. Further, the rate sensitivity seems to increase with matrix compressive strength up to a certain strength level, but then drops again. For instance, specimens using matrix 1 (28Mpa or 4ksi) showed the lowest strain rate sensitivity, while matrix 2 (56 MPa or 8 ksi) showed the highest strain rate sensitivity. Matrix 3 (84 MPa or 12 ksi) was more sensitive than matrix 1 but less than matrix 2 indicating that there is a limit to the observed trend. First cracking and post cracking strength are sensitive to the strain rate, but no clear trend could be identified for the strain capacity at post cracking strength.

Table 6.1–Matrix of tensile tests

	Hooked fiber		Twisted fiber		Loading rate
	$V_f = 1\%$	$V_f = 2\%$	$V_f = 1\%$	$V_f = 2\%$	
Matrix 1	M1H1	M1H2	M1T1	M1T2	0.0178 mm/sec
					0.178 mm/sec
					1.78 mm/sec
					17.8 mm/sec
Matrix 2	M2H1	M2H2	M2T1	M2T2	0.0178 mm/sec
					0.178 mm/sec
					1.78 mm/sec
					17.8 mm/sec
Matrix 3	M3H1	M3H2	M3T1	M3T2	0.0178 mm/sec
					0.178 mm/sec
					1.78 mm/sec
					17.8 mm/sec

Table 6.2–Compositions of matrix mixture by weight ratio and compressive strength

Matrix	Cement (Type III)	Fly ash	Sand (Flint)	Silica Fume	Super - Plasticizer	VMA	Water	$f_c^{'}$, ksi (MPa)
M1	0.70	0.30	3.50	-	0.009	0.024	0.65	4 (28)
M2	1.00	0.15	1.00	-	0.009	0.006	0.35	8 (56)
M3	0.80	0.20	1.00	0.07	0.04	0.012	0.26	12 (84)

Table 6.3– Properties of high strength Hooked and Torex fibers

Fiber Type	Diameter in (mm)	Length in(mm)	Density g/cc	Tensile strength ksi (MPa)	Elastic Modulus ksi (GPa)
Hooked	0.015 (0.38)	1.18 (30)	7.9	349 (2300)	29000 (200)
Twisted (Torex)	0.012 (0.3)*	1.18 (30)	7.9	400 (2760)**	29000 (200)

* Equivalent diameter ** Tensile strength of the fiber after twisting

Table 6.4– Rate effect on the tensile parameters of HPFRCC

With matrix 1

Test Series	Strain rate	First cracking strength		Post Cracking Strength		Strain Capacity		Number of cracks	Average Crack Width	
	/sec	Mpa	DIF	Mpa	DIF	%	DIF	EA	μm	DIF
M1H1	0.0001	1.921	1.000	3.128	1.000	0.372	1.000	22	30	1.000
	0.001	1.477	0.769	2.125	0.679	0.308	0.827	6	102	3.434
	0.01	1.553	0.808	2.346	0.750	0.311	0.837	11	59	2.004
	0.1	1.587	0.826	2.753	0.880	0.233	0.628	11	32	1.083
M1H2	0.0001	2.933	1.000	4.844	1.000	0.443	1.000	32	25	1.000
	0.001	2.921	0.996	4.384	0.905	0.295	0.665	34	15	0.612
	0.01	3.450	1.176	3.857	0.796	0.267	0.602	23	24	0.950
	0.1	3.574	1.219	4.800	0.991	0.383	0.865	25	26	1.024
M1T1	0.0001	2.636	1.000	3.191	1.000	0.351	1.000	32	20	1.000
	0.001	2.065	0.784	2.990	0.937	0.253	0.722	4	98	4.804
	0.01	2.774	1.052	3.287	1.030	0.195	0.557	11	40	1.967
	0.1	2.784	1.056	3.874	1.214	0.292	0.832	13	66	3.243
M1T2	0.0001	3.669	1.000	5.136	1.000	0.331	1.000	46	16	1.000
	0.001	3.688	1.005	5.710	1.112	0.448	1.353	40	21	1.342
	0.01	4.122	1.124	5.267	1.026	0.265	0.800	43	12	0.768
	0.1	4.168	1.136	4.970	0.968	0.229	0.693	34	13	0.806

With matrix 2

Test Series	Strain rate	First cracking strength		Post Cracking Strength		Strain Capacity		Number of cracks	Average Crack Width	
	/sec	Mpa	DIF	Mpa	DIF	%	DIF	EA	μm	DIF
M2H1	0.0001	3.050	1.000	3.243	1.000	0.386	1.000	5	144	1.000
	0.001	3.643	1.195	4.653	1.435	0.384	0.994	8	111	0.771
	0.01	2.767	0.907	4.296	1.325	0.506	1.312	6	148	1.032
	0.1	3.665	1.202	4.554	1.404	0.469	1.214	7	114	0.795
M2H2	0.0001	3.882	1.000	5.589	1.000	0.483	1.000	16	56	1.000
	0.001	3.888	1.001	5.265	0.942	0.303	0.626	10	51	0.918
	0.01	4.076	1.050	4.738	0.848	0.267	0.552	6	70	1.242
	0.1	4.526	1.166	6.348	1.136	0.538	1.114	9	104	1.864
M2T1	0.0001	2.914	1.000	4.441	1.000	0.397	1.000	17	42	1.000
	0.001	-	-	-	-	-	-	-	-	-
	0.01	4.503	1.545	6.097	1.373	0.258	0.650	9	49	1.158
	0.1	5.824	1.998	7.671	1.727	0.242	0.609	17	26	0.621
M2T2	0.0001	5.773	1.000	8.740	1.000	0.523	1.000	47	20	1.000
	0.001	5.060	0.876	9.340	1.069	0.589	1.126	40	26	1.347
	0.01	4.586	0.794	9.048	1.035	0.561	1.071	35	28	1.447
	0.1	6.245	1.082	9.644	1.103	0.693	1.325	43	29	1.488

With matrix 3

Test Series	Strain rate	First cracking strength		Post Cracking Strength		Strain Capacity		Number of cracks	Average Crack Width	
	/sec	Mpa	DIF	Mpa	DIF	%	DIF	EA	μm	DIF
M3H1	0.0001	4.299	1.000	5.207	1.000	0.301	1.000	15	37	1.000
	0.001	4.041	0.940	4.681	0.899	0.249	0.825	19	27	0.736
	0.01	5.049	1.174	5.644	1.084	0.525	1.743	19	51	1.393
	0.1	5.451	1.268	6.362	1.222	0.431	1.430	13	62	1.669
M3H2	0.0001	5.143	1.000	7.562	1.000	0.387	1.000	27	29	1.000
	0.001	5.566	1.082	7.615	1.007	0.362	0.935	27	24	0.826
	0.01	5.427	1.055	6.734	0.891	0.424	1.093	19	40	1.373
	0.1	5.658	1.100	7.673	1.015	0.443	1.143	22	37	1.268
M3T1	0.0001	4.264	1.000	5.499	1.000	0.616	1.000	23	49	1.000
	0.001	5.055	1.186	6.882	1.251	0.619	1.005	34	32	0.665
	0.01	5.697	1.336	7.491	1.362	0.496	0.806	32	27	0.557
	0.1	6.017	1.411	7.576	1.378	0.530	0.861	33	29	0.592
M3T2	0.0001	6.997	1.000	10.778	1.000	0.452	1.000	39	21	1.000
	0.001	-	-	-	-	-	-	-	-	-
	0.01	7.227	1.033	10.693	0.992	0.487	1.077	35	25	1.160
	0.1	6.918	0.989	11.008	1.021	0.571	1.263	32	34	1.609

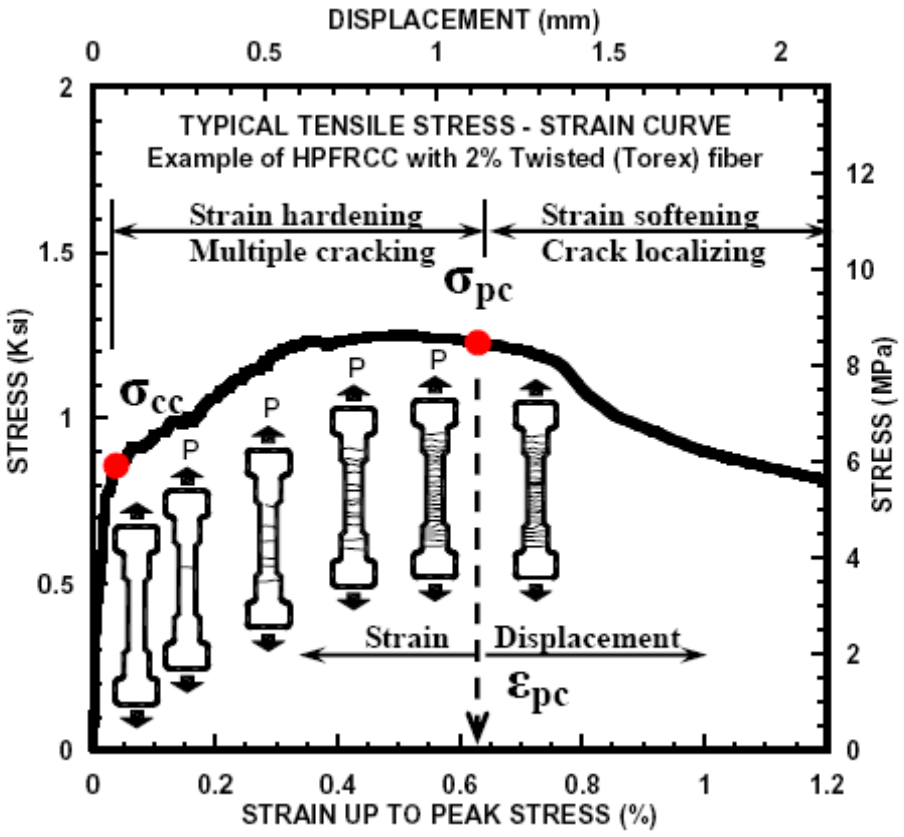

Fig. 6.1-Typical tensile stress-strain curve of HPFRCC using Twisted (Torex) fiber

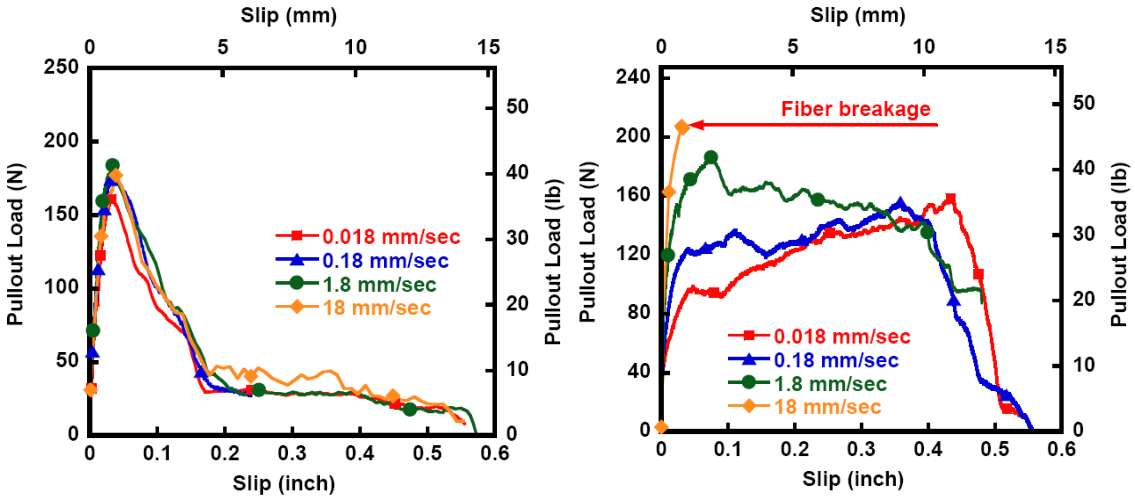

(a) H- Fiber in M2 (b) T- Fiber in M2

Fig. 6.2-Rate effect on single fiber pullout behavior

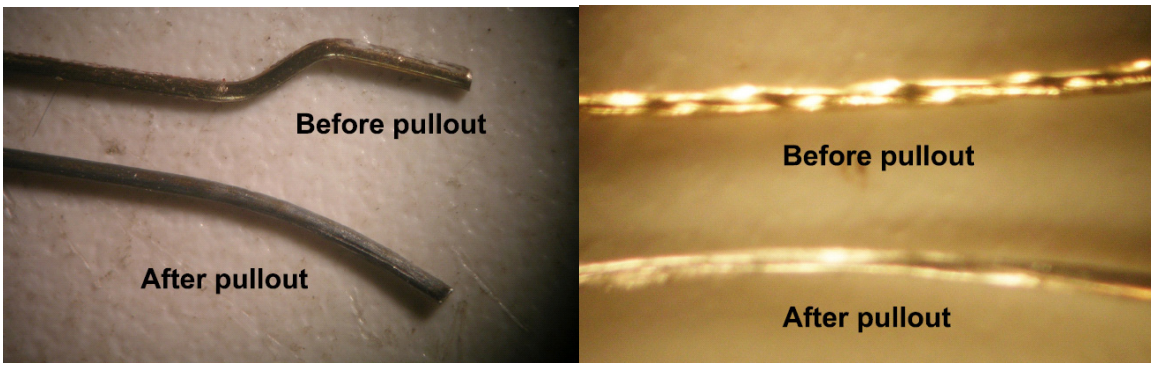

(a) Hooked Fiber (b) Twisted Fiber

Fig. 6.3-Photos for Hooked Fiber and Twisted Fiber after fiber pullout

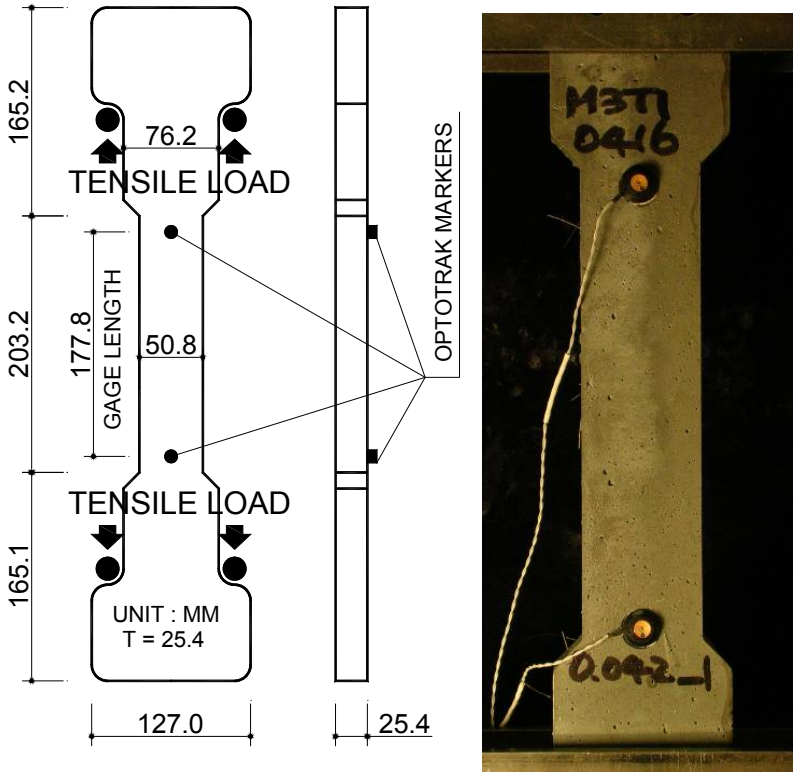

Fig. 6.4-Tensile test specimen and setup using OPTOTRAK

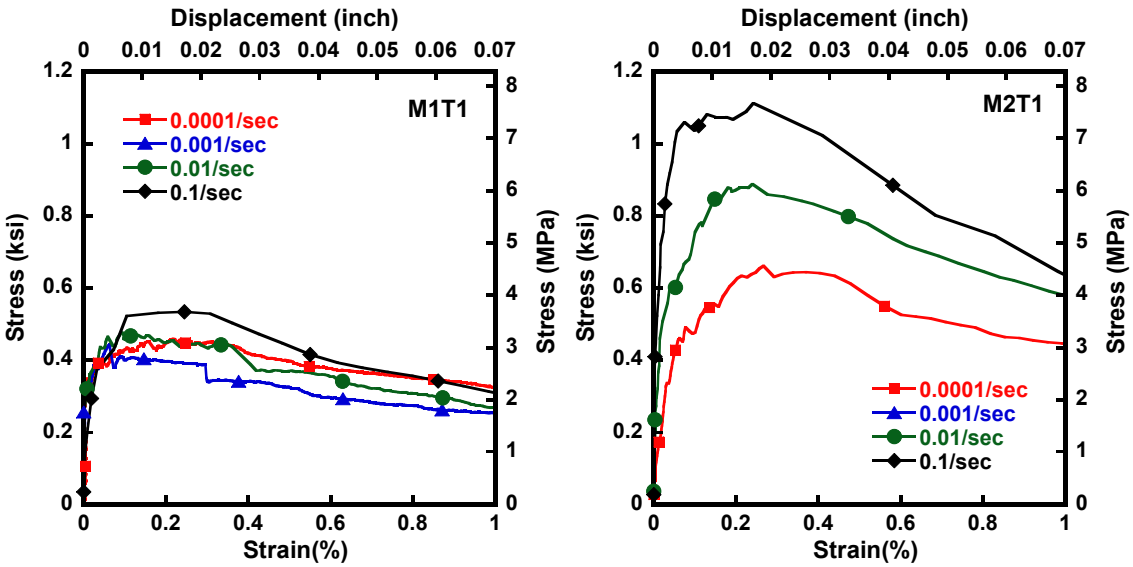

a) M1T1

b) M2T1

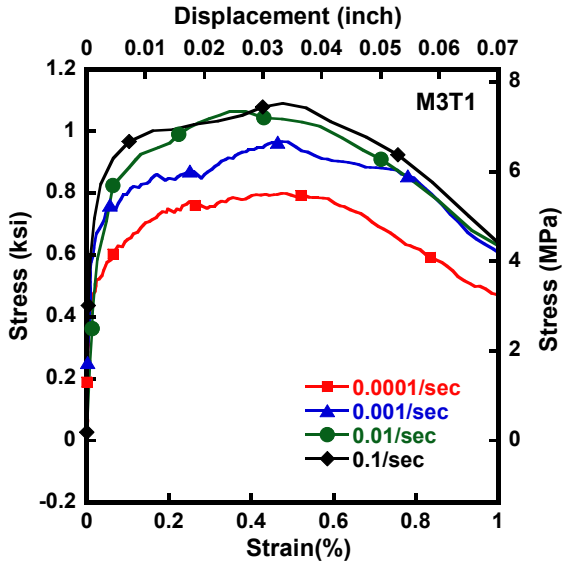

c) M3T1

Fig. 6.5 – Rate effect on the tensile behavior of HPFRCC using Twisted (Torex) fiber (Continued)

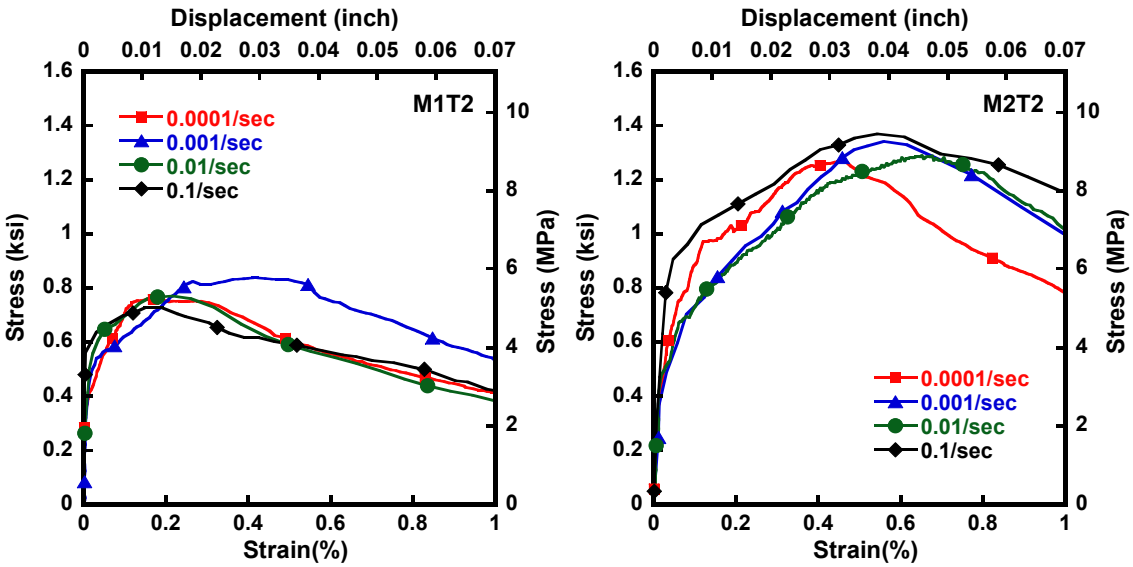

d) M1T2

e) M2T2

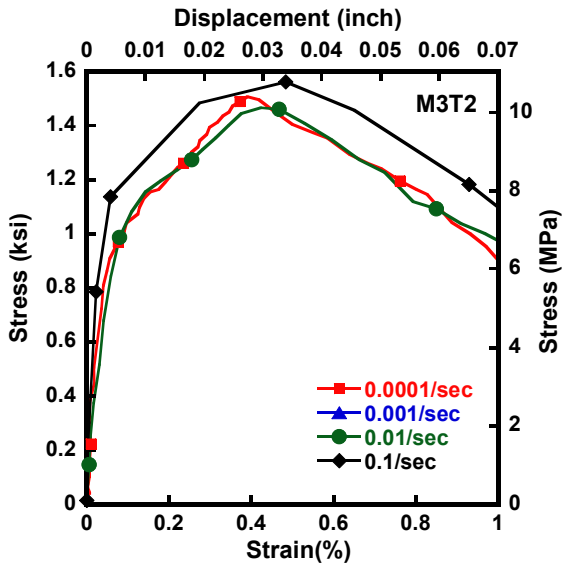

f) M3T2

Fig. 6.5 – Rate effect on the tensile behavior of HPFRCC using Twisted (Torex) fiber

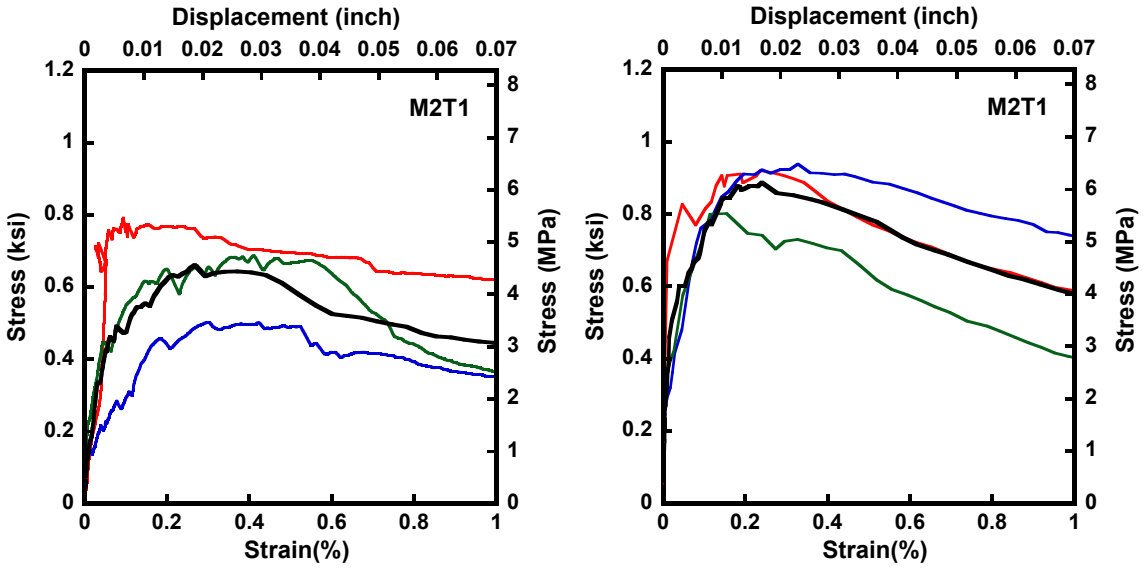

a) Strain rate : 0.0001 /sec b) Strain rate : 0.01 /sec

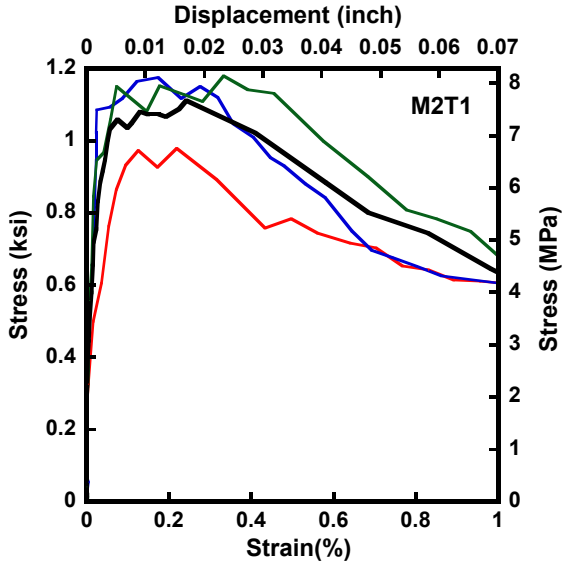

c) Strain rate : 0.1 /sec

Fig. 6.6– Rate sensitive tensile behavior of M2T1 series

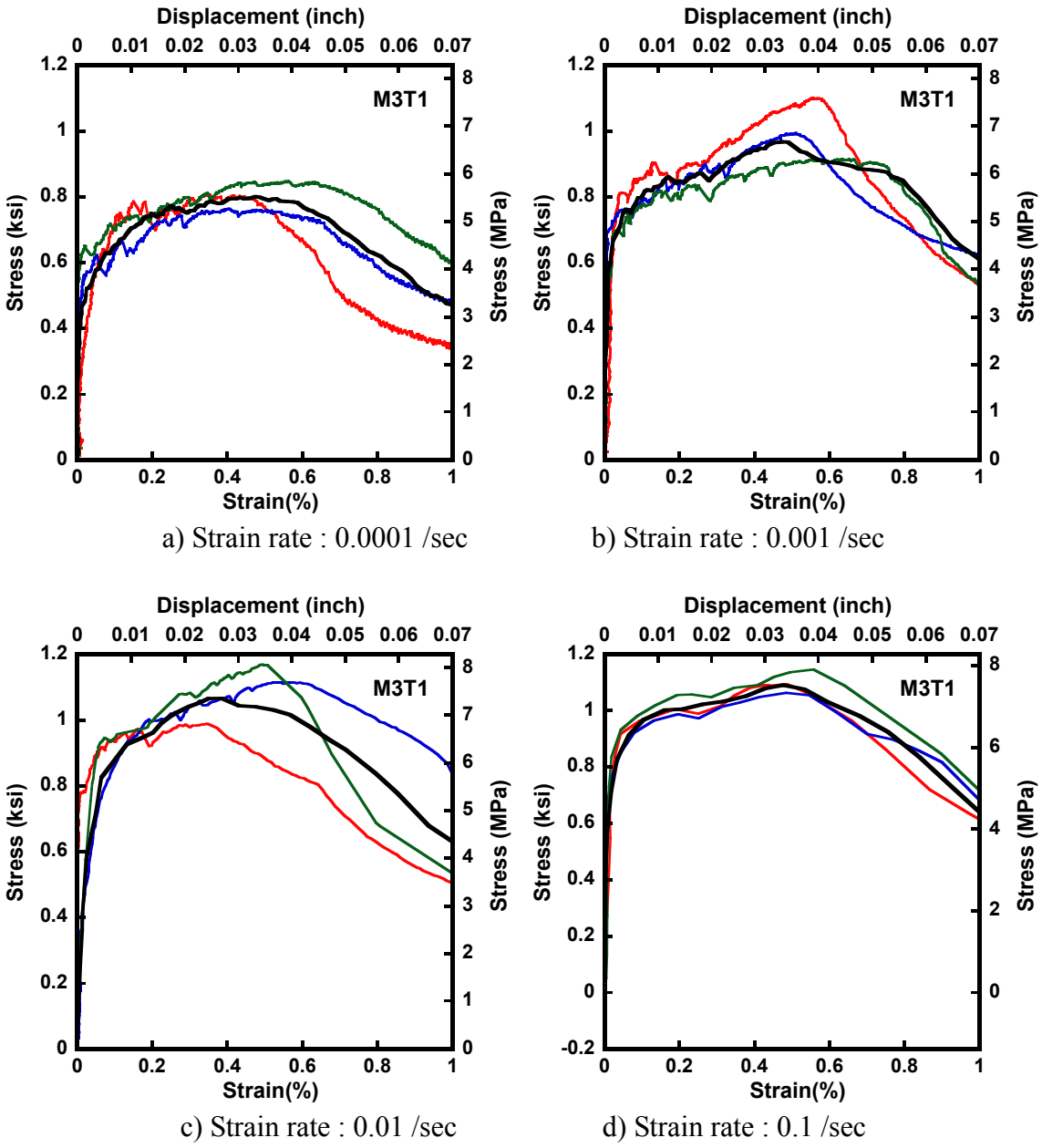

a) Strain rate : 0.0001 /sec

b) Strain rate : 0.001 /sec

c) Strain rate : 0.01 /sec

d) Strain rate : 0.1 /sec

Fig. 6.7– Rate sensitive tensile behavior of M3T1 series

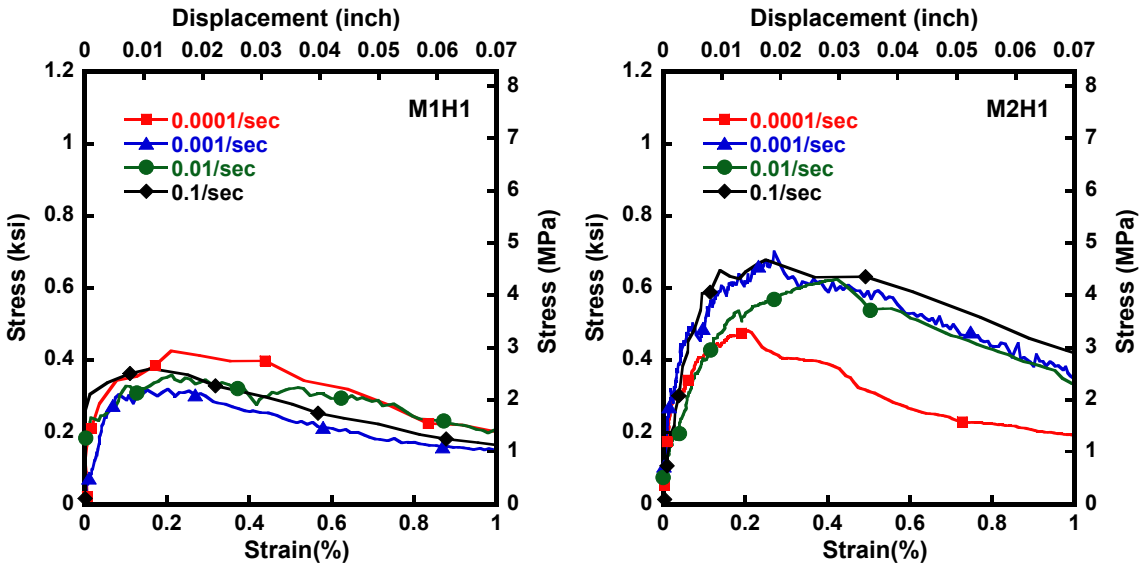

a) M1H1

b) M2H1

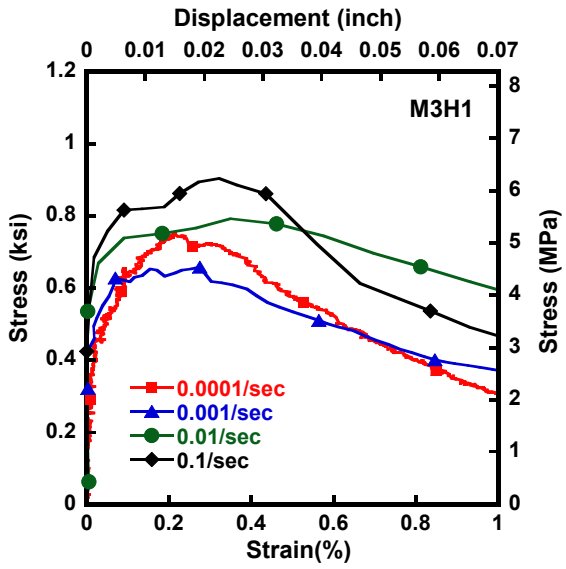

c) M3H1

Fig. 6.8 – Rate effect on the tensile behavior of HPFRCC using Hooked fiber (Continued)

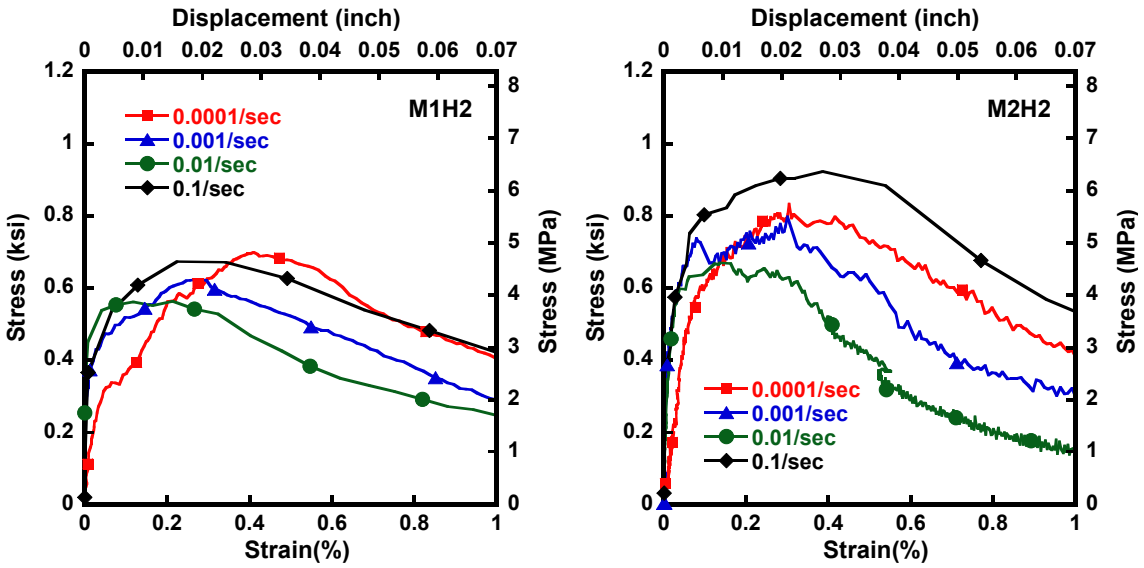

d) M1H2

e) M2H2

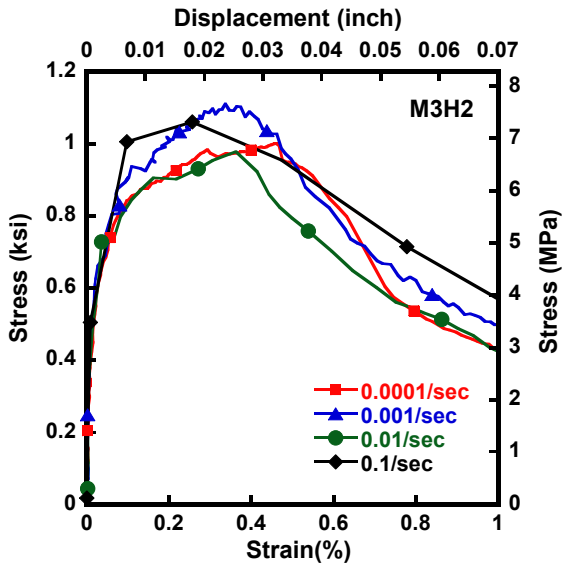

f) M3H2

Fig. 6.8 – Rate effect on the tensile behavior of HPFRCC using Hooked fiber

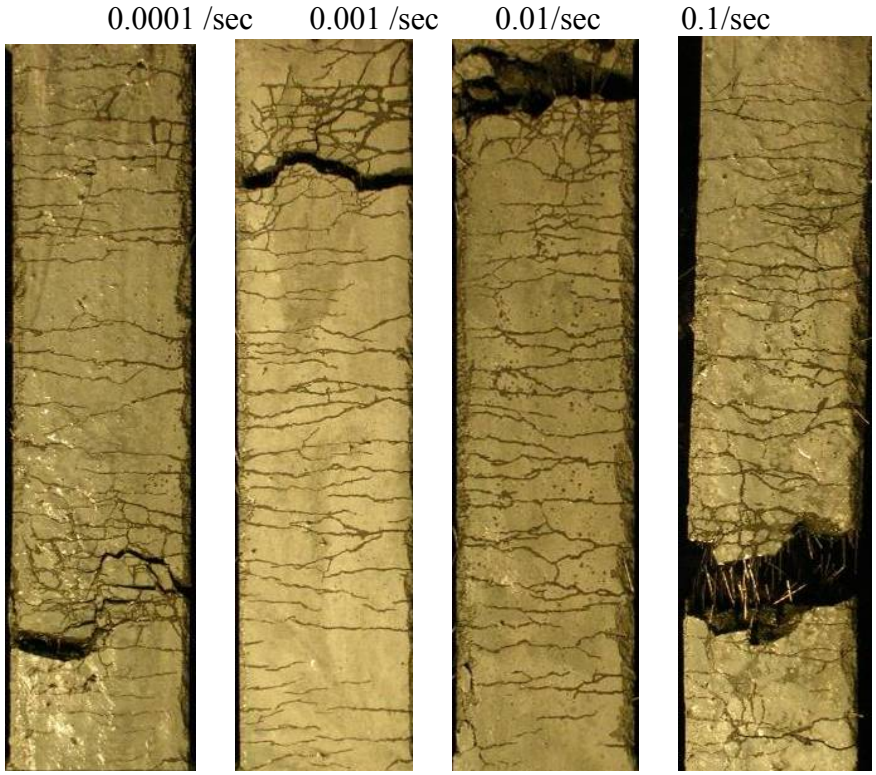

a) M3T1 Series

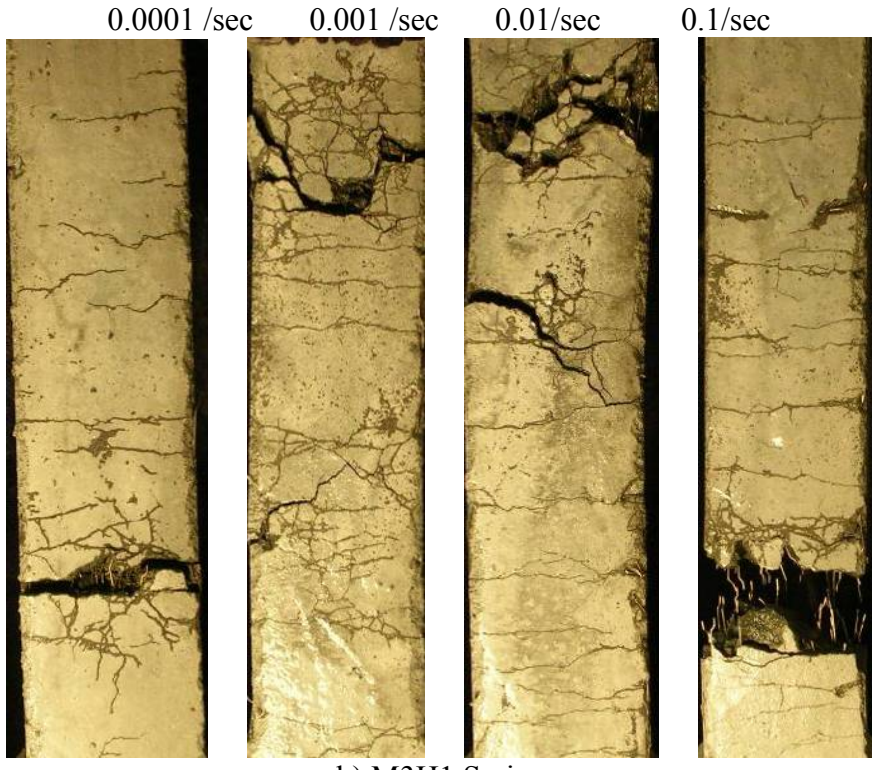

b) M3H1 Series

Fig. 6.9 – Cracking patterns under four strain rates in M3T1 and M3H1 series

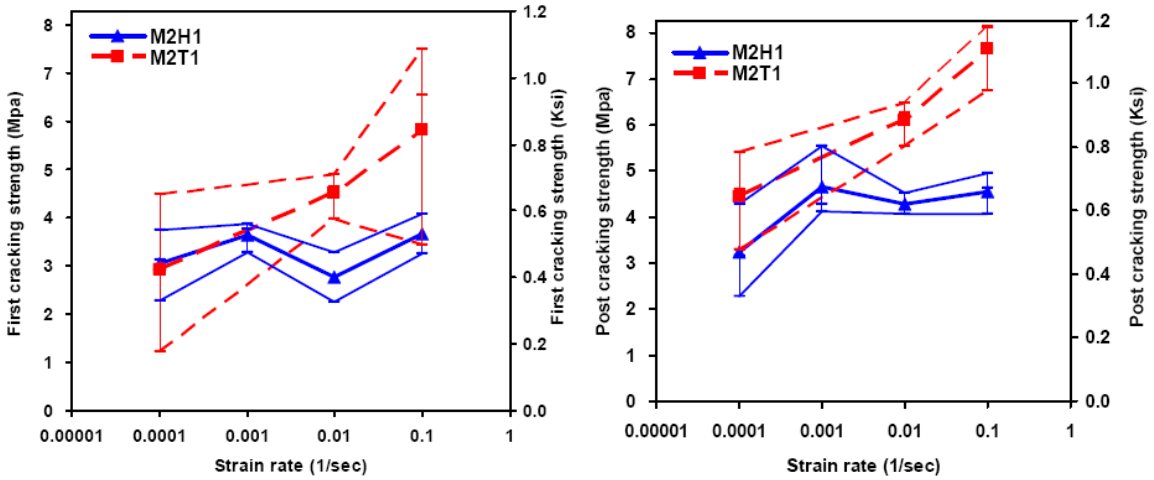

a) First Cracking Strength

b) Post Cracking Strength

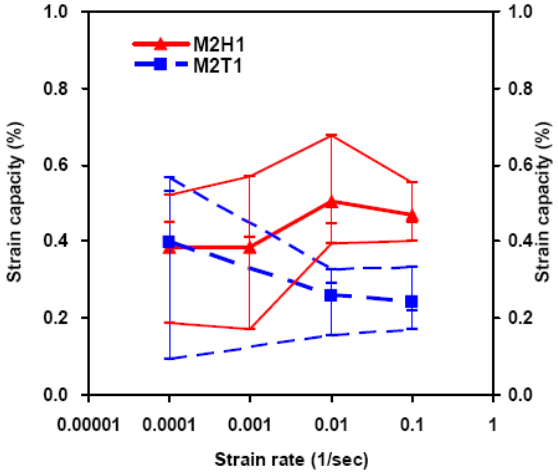

c) Strain Capacity

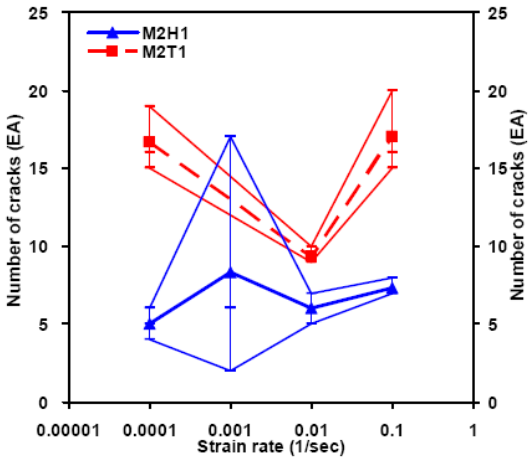

d) Cracking behavior

Fig. 6.10 – Effect of fiber type on Rate sensitivity, M2T1 and M2H1 series

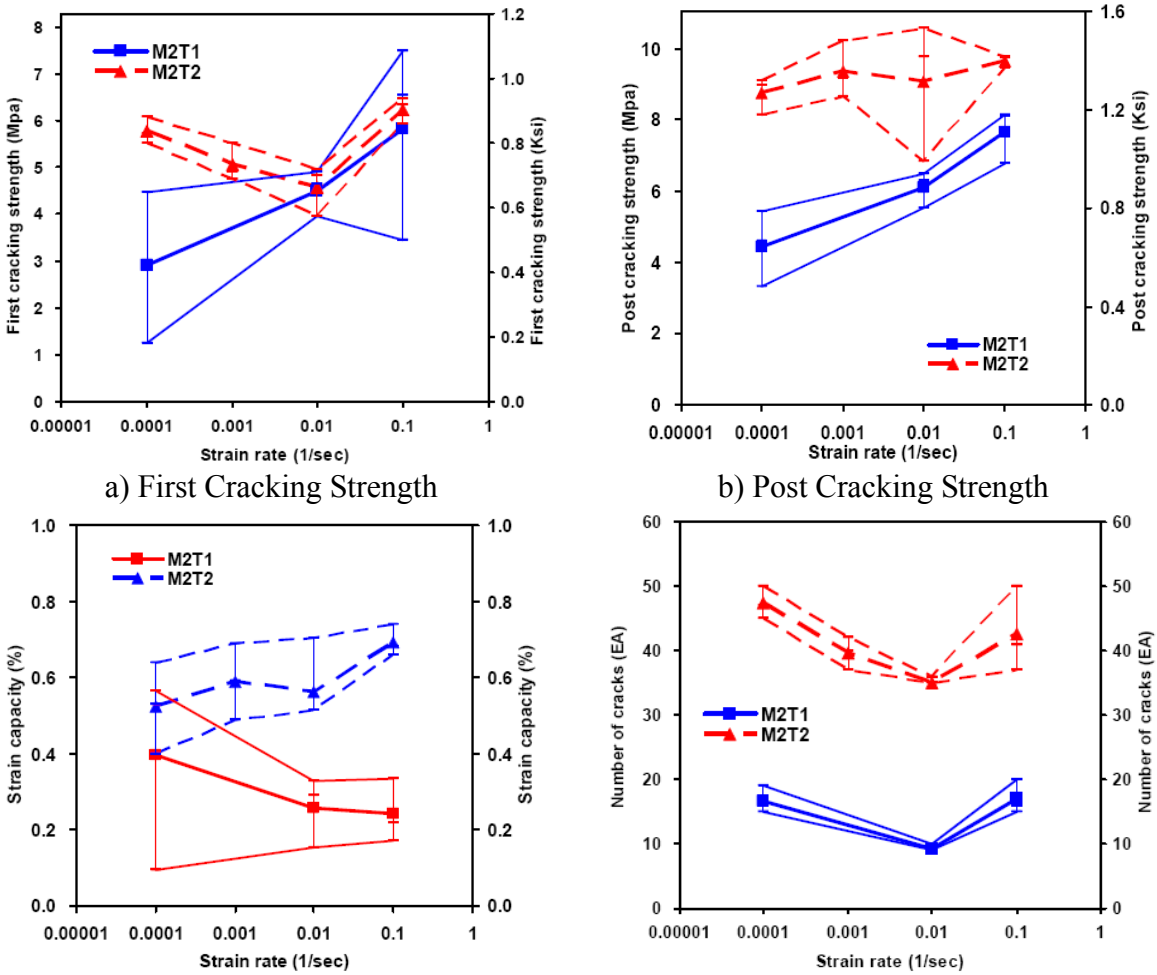

a) First Cracking Strength

b) Post Cracking Strength

c) Strain Capacity

d) Cracking behavior

Fig. 6.11 – Effect of fiber volume fraction on Rate sensitivity, M2T1 and M2T2 sereis

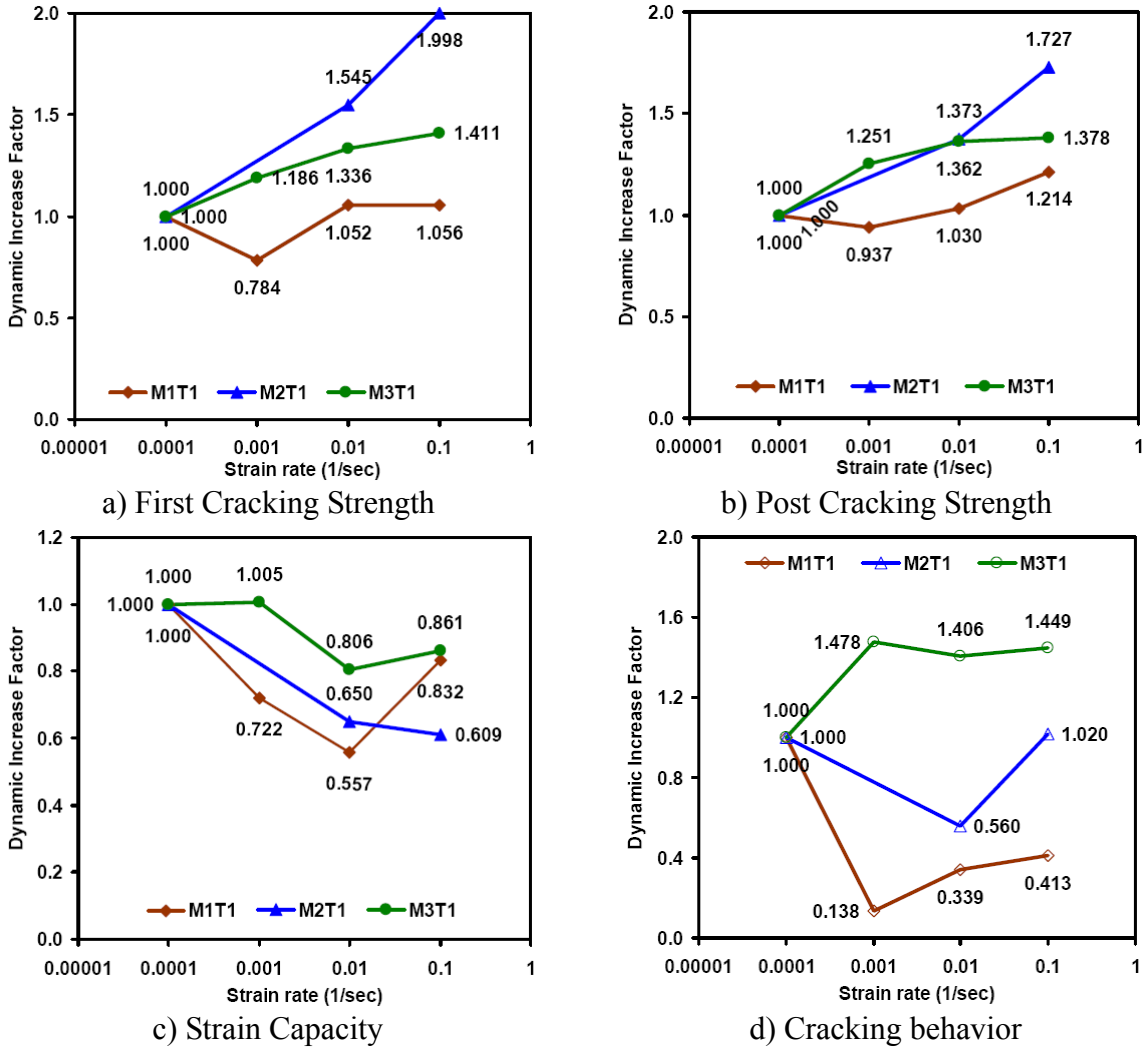

a) First Cracking Strength

b) Post Cracking Strength

c) Strain Capacity

d) Cracking behavior

Fig. 6.12 – Effect of Matrix composition (strength) on Rate sensitivity, M1T1, M2T1 and M3T1 series

REFERENCES

Banthia, N., and Trottier, J.-F., "Deformed steel fiber – cementitous matrix bond under impact," Cement and Concrete Research, V.21, 1991, pp.158-168.

Banthia, N., Chokri, K., Ohama, Y. and Mindess, S., "Fiber-Reinforced Cement Based Composites Under Tensile Impact," Advanced cement based materials, 1993, 1, pp. 131-141.

Banthia, N., Mindess, S. and Trottier, J.-.F, "Impact resistance of steel fiber reinforced concrete," ACI Materials Journal, V93, No. 5, Sep.-Oct. 1996, pp472-479

Bindiganavile, V., Banthia, N., and Aarap, B., "Impact response of Ultra-High Strength Fiber-Reinforced cement composite," ACI Materials Journal, V.99, No.6, Nov.-Dec. 2002, pp.543-548.

Douglas, K. S. and Billington, S. L. "Rate dependence in High-performance fiber reinforced cement-based composites for seismic application," in Proceedings, HPFRCC-2005 International Workshop, Honolulu, Hawaii, USA, 2005

Gopalaratnam, V.S. and Shah, S.P., "Properties of Steel Fiber Reinforced Concrete Subjected to Impact Loading," ACI Materials Journal, Vol. 83, No. 14, Jan.-Feb. 1986, pp. 117-126.

Graybeal, B. A., "Comparative behavior of Ultra-High-Performance Fiber – Reinforced Concrete," ACI Materials Journal, V.104, No. 2, March-April 2007, pp.146-152.

Habel, K., Viviani, M., Denarie, E., and Brühwiller, E., "Development of the mechanical properties of an Ultra-High Performance Fiber Reinforced Concrete (UHPFRC)," Cement and Concrete Research, Vol. 36, Issue 7, July 2006, pp. 1362-1370.

Kim, D., El-Tawil, S. and Naaman, A.E, "Correlation between single fiber pullout behavior and tensile response of FRC composites with high strength steel fiber", in Prints, HPFRCC5, Mainz, Germany, July 10-13, 2007, pp. 67-76.

Kim, D., El-Tawil, S. and Naaman, A.E, "Loading rate effect on pullout behaviour of deformed steel fibers", submitted to ACI Materials Journal in 2007.

Kim, D., Naaman, A.E. and El-Tawil, S., "High Tensile Strength Strain-Hardening FRC Composites with Less Than 2% Fiber Content," Proceedings of the Second International Symposium on Ultra High Performance Concrete Kassel, Germany, March 05-07, 2008.

Körmeling, H. A. and Reinhardt, H. W. "Strain rate effects on steel fiber concrete in uniaxial tension," International Journal of Cement Composites and Lightweight Concrete, V. 9, No. 3, 1987, pp. 197-204

Krstulovic-Opara, N. and Malak, S., "Micromechanical Tensile behaviour of Slurry Infiltrated Continuous-Fiber-Mat Reinforced Concrete (SIMCON)," ACI Mat. Journal, 94(5), Sep.-Oct. 1997, pp. 373-384.

Lankard., D. R., "Slurry Infiltrated Fiber Concrete (SIFCON) : Properties and Applications," Very high strength cement based materials, Vol. 42, Materials Res. Society, Pittsburgh, 1985, pp. 277-286.

Li, V.C., and Wang, S., "Microstructure Variability and Macroscopic Composite Properties of High Performance Fiber Reinforced Cementitious Composites", Probabilistic Engineering Mechanics, Volume 21, Issue 3, July 2006, pp201-206.

Lok, T. S. and Zhao, P.J., "Impact response of steel fiber-reinforced concrete using a split hopkinson pressure bar," Journal of materials in civil engineering, Jan-Feb 2004, pp54-59

Maalej, M., Quek, S. T. and Zhang, J. " Behavior of Hybrid-Fiber Engineered Cementitious Composites Subjected to Dynamic Tensile Loading and Projectile Impact," Journal of Materials in civil engineering, V. 17, No. 2, April 1, 2005, pp. 143-152.

Naaman, A.E, "A Statistical Theory of Strength for Fiber Reinforced Concrete," Ph.D. Thesis, Massachusetts Institute of Technology, 1972, 196 pages.

Naaman, A.E., "Ferrocement & Laminated Cementitious Composites", Techno Press 3000, Ann Arbor, Michigan, 2000

Naaman, A.E., "High Performance Fiber Reinforced Cement Composites," Concrete Structures for the future, IABSE Symposium, Paris, France, September 1987, pp. 371-376

Naaman, A.E., "Reinforcing Mechanisms in Ferrocement," M.S. Thesis, Massachusetts Institute of Technology, Civil Engineering Department, 1970, 152 pages.

Naaman, A.E., and Reinhardt, H.W., "Characterization of High Performance Fiber Reinforced Cement Composites," Proceedings of 2nd International Workshop on HPFRCC, Chapter 41, in High Performance Fiber Reinforced Cement Composites: HPFRCC 2, A.E. Naaman and H.W. Reinhardt, Editors, RILEM, No. 31, E. & FN Spon, London, 1996, pp. 1-24.

Naaman, A.E., and Reinhardt, H.W., "Proposed classification of HPFRC composites based on their tensile response," Materials and Structures, RILEM, Vol. 39, No. 5, June 2006, pp. 547-555

Nammur, G.G. and Naaman, A.E., "Strain Rate Effects on Tensile Properties of Fiber Reinforced Concrete," Proceedings of MRS Symposium on "Cement Based Composites: Strain Rate Effects on Fracture," S. Mindess, Editor, Materials Research Society, Vol. 64, Pittsburgh, 1986, pp. 97-118.

Rossi, P., "Development of new cement composite materials for construction," Proceedings of the Institution of Mech. Engineers, Part L, Jnl. of Materials: Design and Applications, 219(1), 2005, pp. 67-74.

Rostásy, F. S. and Hartwich, K., "Compressive strength and deformation of steel fiber reinforced concrete under high rate of strain," International Journal of Cement Composites and Lightweight Concrete, V. 7, No. 1, 1985, pp. 21-28

Suaris, W. and Shah, S.P., "Strain-rate effects in fiber-reinforced concrete subjected to impact and impulsive loading," Composites, April 1982, pp. 153-159

Sun W., Jiao C. and Lai J., "Behavior of steel fiber reinforced high and ultra-high strength concrete at high strain rate," in Proceedings, HPFRCC-2005 International Workshop, Honolulu, Hawaii, USA, 2005

Yang, E. and Li, V. C. “Rate dependence in Engineered Cementitious Composites,” in Proceedings, HPFRCC-2005 International Workshop, Honolulu, Hawaii, USA, 2005

Yang, E.H., Yang, Y. and Li, V.C., "Use of High Volumes of Fly Ash to Improve ECC Mechanical Properties and Material Greenness" ACI Materials Journal, Vol. 104, No. 6, Nov.-Dec., 2007, pp. 620-628.

CHAPTER VII

NEW IMPACT TEST SYSTEM USING ELASTIC STRAIN ENERGY [6]

ABSTRACT

This chapter describes a new test system that relies on sudden strain energy release to subject specimens to rapid loading. The new system is cheap-to-build, smaller than existing systems, can be used to test large-sized specimens and can be conveniently adjusted to achieve a broad range of strain rates. The theoretical potential of the device is discussed and equations that describe the operation of the system are developed and used to identify influential variables. A computational simulation model of a prototype system is then described and exercised to quantitatively explore the influence of the key variables. A prototype device that was built to demonstrate proof-of-concept is also introduced and its capabilities, especially its ability to test specimens in both tension and compression, are discussed.

[6] D. Kim, S. El-Tawil, and A. E. Naaman, "New impact test system using elastic strain energy", International Journal of Impact Engineering, (to be submitted)

7.1 INTRODUCTION

The demand has never been greater for tougher, more ductile materials to improve the behavior of civil engineering structures under rapid and severe loading, such as blast, impact and earthquakes. A primary hurdle that impedes rapid development of such materials is cheap, safe and accurate testing techniques that can be used to characterize high-strain-rate material response. Most existing methods for high-strain-rate testing require large equipment (e.g. drop-weight test or Split Hopkinson Pressure Bar), are expensive and, in some cases, risky to operate. As a result of these limitations, high-strain-rate testing remains highly specialized and can only be conducted in a few labs around the world.

Existing high rate test systems can be categorized into 4 classes based on the way the impact effect is generated: 1) systems based on potential energy (PE), where a large mass swings or falls from a specified height to strike a specimen at low speed (e.g. Charpy, Izod and Drop Weight methods); 2) systems based on kinetic energy (KE), where a small mass is propelled at high speed to impact a specimen (e.g. Gas Gun Method); 3) systems that utilize hydraulic machines (HM) to deform a specimen at medium speeds; and 4) systems based on stress wave propagation (SWP), in which a stress wave is propagated through a long bar to impinge upon a specimen (e.g. Split Hopkinson Pressure Bar, SHPB).

PE systems require much vertical clearance, a special foundation and can only achieve moderate strain rates. The maximum strain rate achieved by this method is reported to be 10^0 s^{-1} to 10^1 s^{-1} (Bischoff and Perry 1991). In KE systems, an explosively propelled striker mass is propelled towards a specimen to impart rapid loading. Alternatively, the same effect can be achieved by accelerating a specimen and colliding it

with a stationary anvil, e.g., Grote et al. (2001). KE methods can generate very high strain rates, e.g. Grote et al. report strain rates up to 10^4 s^{-1}. The primary challenge in KE methods is obtaining high quality measurements during the extremely short duration of the experiments. They are also somewhat dangerous to operate because they involve the use of explosives or compressed gas. HM testing using well-designed test machines can create high quality test data. However, the strain rates achieved using such methods is usually quite low, on the order of 10^{-1} to 10^0 s^{-1}. They are also generally expensive and cumbersome to reconfigure.

SWP systems (such as the SHPB) require long test setups to ensure 1-D stress wave propagation. In most practical SWP setups, the stress wave is initiated by an explosively propelled striker mass or by a suddenly released force. To successfully test concrete (and other nonhomogeneous materials) under high strain rate in a SHPB, the specimens must have a certain minimum size dictated by the characteristic size of the constituents of concrete, e.g., aggregate. The specimen must be several times the characteristic size of the aggregate so that the results are not adversely influenced by the size effect. On the other extreme, the diameter of the specimen must be as small as possible to reduce the overall length of the equipment, since lateral dispersion of the propagating uniaxial shock wave could distort the test results if the bars are too stocky. These two conflicting requirements, a specimen with as large a diameter as possible and testing bars that are as short as possible for a given diameter, create practical problems for SHPB testing of concrete. For example, to test a 75 mm diameter cylindrical specimen, a SHPB would have to be 10 - 12 m long, which is prohibitively long for most labs.

The objective of this chapter is to describe a new test system that was recently

proposed by the authors to overcome the combined limitations of traditional high strain rate systems, especially for testing concrete. In the proposed system, the internal strain energy accumulated in an elastic bar is suddenly released generating controlled, high strain-rate loading onto a specimen. The new system is similar to a stretched elastic cord, which when released at one end, can create a short duration, but quite painful impact on the person holding the other end of the cord. In the new system, the elastic cord is replaced with a high strength prestressing steel bar operating in the elastic range. As shown later on, the system can be conveniently controlled by a set of parameters. This system is hereafter identified as Strain Energy Impact Test Systems or SEITS.

7.2 PREMISE OF SEITS

Fig. 7.1 shows a schematic of how SEITS is intended to work. Fig. 7.1a shows the components of the system in its initial stage. Load is applied to a short pull bar, which then transmits the force through a coupler to the energy bar where elastic strain energy is stored (Fig. 7.1b**).** The energy bar is prevented from movement by a support and is maintained continuously in contact with the specimen, to the extent possible, as it is being stretched. The coupler is specially designed to suddenly release (e.g. through brittle fracture of a notched mechanical coupler) when a specified load is exceeded, as shown in Fig. 7.1c. When the coupler fractures, a pulse is directed into the specimen. If there is no gap between the specimen and the energy bar, which may be difficult to achieve in practice, the stress wave will be guided directly into the specimen. Alternatively, if a gap exists between the energy bar and specimen, SEITS becomes a kinetic energy device, in which the entire energy bar is launched towards the specimen. As will be shown later on, as long as the gap is small, both situations are theoretically equivalent. In other words, the

proposed system bridges the SWP and KE categories previously identified. Once a pulse is delivered to the specimen, instrumentation such as piezo-electric dynamic load cells and laser displacement measurement device can then be used to obtain the specimen's stress-strain properties as in other existing impact testing systems. Information about instrumentation follows later.

To demonstrate the theoretical capacity of the system consider an energy bar 50.8 mm diameter, 1.5 m long and subjected to 690 MPa tensile stress. The amount of stored strain energy is 3672 N-m. The required drop height to achieve the same amount of potential energy is 16.2 m, if an impactor with the same weight as the energy bar (23.1 kg) is used in the drop weight method. It is clear that the size of proposed system is much smaller than that of an equivalent drop weight system.

The proposed system shares some attributes with two existing systems. However, there are also fundamental differences that make SEITS unique. The first is a device patented by Keener et al. (1997, US Patent 5,677,494), where the energy stored in a breaker specimen is exploited to produce an impact action. SEITS differs from this device in two critical ways. First, SEITS uses an energy bar to store and release the energy needed for impact and to control the strain rate. The method proposed by Keener et al. relies instead on the energy stored in the breaker specimen, which could be orders of magnitude less than the energy stored in SEITS's energy bar. Keener et al. also claim that the impact load and accumulated energy may be increased by increasing the size of the starter specimen. However, that will necessitate a larger testing machine with a higher capacity frame and load cell. In contrast, the energy stored in the energy bar of SEITS can be increased or decreased by simply changing the bar characteristics as explored later

on in the paper. Another similar set-up was developed by Cadoni et al. (2006) to investigate the tensile behavior of concrete at high rate loading. They modified a SHPB by attaching a prestressing bar in front of the incident pressure bar. The Modified Hopkinson Bar (MHB), as Cadoni et al. (2006) called their system, employs the prestressing bar under tension instead of gas gun to generate a stress wave into the incident pressure bar. While MHB resolves some of the difficulties and dangers of operating a gas gun, it still suffers from the same key problem of a traditional SHPB, i.e. large size. The small size of SEITS is a major benefit over MHB.

7.3 WAVE PROPAGATION EQUATIONS FOR SEITS

Fig. 7.2a shows a schematic of the energy bar before it is deformed. At time, $t=t_1$, the bar tip is pulled through a displacement, $w(L,t_1)$, where L is the bar length (Fig. 7.2b). When the bar is released (Fig. 7.2c), a compressive stress wave travels through the bar and into the specimen. Force equilibrium in a differential element in the energy bar is shown in Fig. 7.3. This can be expressed as:

$$F_1 + F_m = F_2 \qquad [7.1]$$

where, $F_1 = AE\dfrac{\partial w_1}{\partial x}$, $F_2 = AE\dfrac{\partial w_2}{\partial x}$, $F_m = Adx\rho\dfrac{\partial^2 w_1}{\partial t^2}$, w_1 is the displacement at the top of the differential element, w_2 is the displacement at the bottom of the differential element, E is the modulus of elasticity of the bar and A is the section area of the bar The force, F_m, is the inertial force in the differential element. Substituting these quantities into Eq. 7.1, assuming that $w_2 = w_1 + \dfrac{\partial w_1}{\partial x}$ and simplifying the results:

$$C^2\frac{\partial^2 w_1}{\partial x^2} = \frac{\partial^2 w_1}{\partial t^2} \qquad [7.2]$$

where $C = \sqrt{\frac{E}{\rho}}$, is the speed of the stress wave in the bar. Eq. 7.2 represents the well-known wave equation, which has a general solution to the homogeneous wave equation as follows (Stronge 2000):

$$w(x,t) = \frac{1}{2}\left[f(x - Ct) + g(x + Ct)\right] \qquad [7.3]$$

where f and g are arbitrary functions representing waves that are traveling forward and backward as t increases.

Eq. 7.2 can be also expressed as:

$$\left(C\frac{\partial w}{\partial x} + \frac{\partial w}{\partial t}\right)\left(C\frac{\partial w}{\partial x} - \frac{\partial w}{\partial t}\right) = 0 \qquad [7.4]$$

Thus, the relation between the strain (ε) and particle velocity (V) can be established as follows:

$$\frac{\partial w}{\partial t} = C\frac{\partial w}{\partial x} \rightarrow V = C\varepsilon = \sqrt{\frac{E}{\rho}}\frac{\sigma}{A} \qquad [7.5]$$

where, $V = \frac{\partial w}{\partial t}$, $\varepsilon = \frac{\partial w}{\partial x}$ is the strain and σ is the corresponding stress in the bar.

7.4 INFLENTIAL VARIABLES AFFECTING PERFORMANCE OF SEITS

Eq. 7.5 is instructive in that it shows what variables are influential for SEITS. It is clear that the impact velocity (and therefore the strain rate) produced by the proposed system can be controlled by changing the energy bar's *material properties* and *prestress level*. Clearly materials with high modulus of elasticity and low density have the potential to produce higher strain rates, as does a higher prestress level.

To investigate the effect of bar geometry, consider the two elastic bars shown in Fig.

7.4. Both bars are assumed to have the same volume. As shown in Fig. 7.4, Bar 1, denoted by subscript 1 in all relevant variables, has a larger diameter D_1 and shorter length L_1 than Bar 2, denoted by subscript 2. The bars are subjected to corresponding forces P_1 and P_2 such that they both store the same amount of strain energy (*SE*). The strain energy stored in both bars is calculated by using Eq. 7.6 and 7.7, and the velocity of the stress wave in both bars is estimated by using Eq. 7.8 and 7.9 as follows:

$$\text{Strain energy in Bar 1}: SE_1 = \frac{P_1^2 L_1}{2EA_1} = \frac{\varepsilon_1^2 EA_1 L_1}{2} \quad [7.6]$$

$$\text{Strain energy in Bar 2}: SE_2 = \frac{P_2^2 L_2}{2EA_2} = \frac{\varepsilon_2^2 EA_2 L_2}{2} \quad [7.7]$$

$$\text{Stress wave velocity in Bar 1}: V_1 = C\varepsilon_1 \quad [7.8]$$

$$\text{Stress wave velocity in Bar 2}: V_2 = C\varepsilon_2 \quad [7.9]$$

Invoking volume equivalence and equating 7.6 and 7.7 leads to:

$$\varepsilon_2 = \varepsilon_1 \quad [7.10]$$

which implies that the strain in both bars is the same. According to Eq. 7.8 and 7.9, Eq. 7.10 implies that the stress wave velocity will be identical in both cases even though the two bars have different geometric shapes. Therefore, the geometry of the energy bar has no influence on the velocity of the impact head.

7.5 EQUIVALENCE OF STRESS WAVE PROPAGATION AND KINEMATIC ENERGY APPROACHES

Consider an elastic energy bar subjected to a tensile stress $\sigma = E\varepsilon$. Applying the principle of conservation of energy and assuming no energy loss implies that elastic strain energy stored in the energy bar will be instantaneously transferred into kinetic energy upon bar release. The elastic strain energy (*SE*) stored in the elastic energy bar with

volume V is

$$SE = \frac{1}{2}\frac{AL}{E}\sigma^2 \qquad [7.11]$$

The kinetic energy (*KE*) of the bar is

$$KE = \frac{1}{2}MV_b^2 = \frac{1}{2}(AL \times \rho)V_b^2 \qquad [7.12]$$

where *L* is the length of bar, *A* is the section area of bar, *M* is the mass of bar, ρ is the density of bar and V_b is the instantaneous bar velocity. Equating Eq. 7.11 and 7.12 and simplifying leads to

$$V_b = \sqrt{\frac{E}{\rho}}\varepsilon = C\varepsilon \qquad [7.13]$$

which is identical to Eq. 7.5 implying that the stress wave and kinetic energy approaches are equivalent when applied to SEITS.

7.6 FINITE ELEMENT MODELING OF SEITS

Prior to building a prototype (as described later on in this chapter), the viability of the proposed impact test system was investigated through explicit finite element analysis, conducted using the commercial code LS-DYNA. The purpose of this analysis was to quantify the effect of bar material properties and stress level in the energy bar at the point of strain energy release on the achievable strain rate. Eight node solid elements are used to model the system and interpenetration between parts in the system is prevented using the contact features in LS-DYNA. Tensioning of the elastic bar is performed by applying displacement control at the end of the pull bar. A friction coefficient $\mu = 0.2$ is assigned between the specimen and the load cells and a failure strain criterion is applied to the coupler to permit sudden bar release when a critical stress is reached in the energy bar.

Three different types of materials are used to represent the energy bar, namely prestressing (PS) steel, aluminum alloy and titanium alloy. This is done to investigate the effect of the energy bar material on the achievable strain rate. ASTM A29 Grade C1045 steel is used for the load cell, coupler and test frame. Aluminum is used for the test specimen in the SHPB simulation. The properties of the materials employed in the simulations are shown in Table 7.1. The time step used in this simulation is automatically determined within LS-DYNA to ensure stability of the dynamic simulations and is less than 0.0001 sec. Fig. 7.5 shows details of the model employed in the analysis, while Fig. 7.6 shows the specimen crushing as a result of impact loading.

Fig. 7.7 shows sample results from the simulation including the stress history obtained from both load cells and the strain history of the specimen. In this simulation, PS steel is used as the material for the energy bar. By averaging the stress values obtained from both cells, the specimen stress is calculated. In the process of averaging both load cell stress histories, a time interval is considered for the stress wave to transfer from the top load cell to the bottom load cell.

$$\sigma_{SPECIMEN}(t) = \frac{1}{2} \times \left(\sigma_{LC\_UPPER}(t + \Delta t) + \sigma_{LC\_BOTTOM}(t) \right) \qquad [7.14]$$

where, Δt is the time interval for the stress wave to travel from the top load cell to the bottom load cell. The data in Fig. 7.7 can be combined to draw the stress-strain curve of the specimen (aluminum) as shown in Fig. 7.8. The simulation demonstrates that SEITS can generate a powerful enough impulse to rapidly crush the specimen.

The effect of using various types of material for the energy bar is summarized in Table 7.2 and Fig. 7.9. For an assumed stress level at energy release of 517.5 MPa, it is clear from the simulations that the impact velocity is strongly influenced by the material

of the energy bar. For example, the computed impact velocity for PS is 12.9 m/sec, while it is 37.7 m/sec for aluminum. Clearly, the presence of the specimen slows down the computed impact speed as a result of the interaction that takes place between the specimen and bar. The reduction in impact speed is computed to be more than 50% in all three simulations. The maximum strain rate (computed for the ½ inch aluminum specimen) is also displayed in Table 7.2. Clearly, the aluminum energy bar is most efficient and is able to produce strain rates in excess of 1000 sec^{-1}.

The influence of stress level (at energy release) in the energy bar on the velocity of the impact head is also investigated using the same finite element model for the PS energy bar. The effect of two stress levels, 517.5 MPa and 655.5 MPa, are compared in Fig. 7.10, where it is clear stress level is also an influential variable. When the stress level is 655.5 MPa, the impact velocity approaches 17.8 m/sec., while it is about 12.7 m/sec when the stress level is 517.5 MPa. The simulation results in this section clearly show that SEITS can be easily tuned to provide various strain rates by replacing the energy bar with another of a different material or simply by changing the stress level in the bar at the energy release point.

7.7 SEITS PROTOTYPE FOR COMPRESSIVE AND TENSILE TESTS

With the confidence gained through the simulation model, a prototype of SEITS was recently built. The SEITS prototype is composed of an impact head, an energy bar, a coupler, a pullout bar, and a jack as shown in Fig. 7.11. Piezo-electric dynamic load cells (222,411N range, 0.1mV/4.44822N) and a high frequency laser displacement sensor (10kHz, +/- 25mm measuring range) are used to measure the response of the specimen. Fig. 7.12 demonstrates the impact process (in compression) on a mortar specimen having

compressive strength of 48 MPa (50.8 mm diameter). The average velocity in this preliminary test is measured to be 5 m/sec by analyzing the sequential photos recorded by the high-speed camera.

The SEITS prototype can also be used to investigate the tensile behavior of cementitious materials. The geometry of the test set-up is shown in Fig. 7.13. Hat-shaped tensile specimens are selected for this type of test as shown in Fig. 7.13 and 7.14d. The load histories are obtained from the two piezoelectric dynamic load cells placed between the specimen and the top of the two supports as shown in Fig. 7.13. The deformation of the specimen is obtained by measuring the movement of Point A at the bottom of specimen by using the laser sensor (Fig. 7.13). Fig. 7.14 shows sample test results for a test of a cementitious composite. Load and displacement histories measured from piezoelectric dynamic load cells are shown in Fig. 7.14a and the high frequency laser sensor are shown in Fig. 7.14b, respectively. Fig. 7.14c shows the stress strain curve obtained for the specimen, while the failure shape of the specimen tested is shown in Fig. 7.14d. Clearly, the geometry of the tensile specimen needs further modification to prevent bending failures at the specimen ends from influencing the results, i.e. to ensure uniform stress and/or strain state. However, this sample test result is shown to demonstrate that SEITS can be used to investigate the tensile response of large-sized cementitious specimens, albeit with a different geometry than shown in Fig. 7.14d, under high rate loading.

7.8 SUMMARY AND CONCLUSIONS

A new technique for generating a rapid loading pulse is proposed. The new system, named Strain Energy Impact Test System [SEITS], releases stored elastic strain energy in

an ‘energy bar’ to achieve high strain rate loading. The proposed system has several advantages over traditional impact test systems such as the Drop Weight method and Split Hopkinson Pressure Bar technique. In particular, while small, SEITS can still be used for large-sized specimens and can be easily controlled by changing the energy bar’s material or stress level in the energy bar. The theoretical potential of the device was discussed and equations that describe the operation of the system were developed and used to identify key variables that control SEITS’ performance. Computational simulation models of the system were used to confirm predictions from the theoretical models and to study how the system interacts with specimens. It is shown that that when an aluminum alloy is used for the energy bar, an impact velocity of 30.8 m/sec can be achieved in the simulation presented in this chapter. This translates into a strain rate in excess of 10^3 sec^{-1} on the aluminum alloy specimen used in the simulation. A prototype device that was built to demonstrate proof-of-concept was also introduced and its capabilities, especially its ability to test specimens in both tension and compression, were demonstrated. It was shown that the prototype, which is about 1.5 m in size, could generate a strong enough pulse to destroy a 48 MPa concrete specimen (50.8 mm diameter) in compression. It was also shown that tension tests on large sized cementitious specimens could be conducted using SEITS.

Table 7.1- The properties of the materials employed in the simulations

	Energy bar			Set-up	Specimen	Coupler
	PS Steel	Aluminum alloy	Titanium alloy	Steel	Pure aluminum	Steel
Modulus of elasticity E (MPa)	200100	70000	115996	200100	70000	200100
Poisson's ratio ν	0.28	0.33	0.32	0.28	0.33	0.28
Strength σ_u (MPa)	828	552	966	828	276	552 (or 621)
Density ρ (t/m^3)	8.027	2.690	4.484	8.027	2.690	8.027
Failure Strain ε_u	-	-	-	-	0.15	0.08

Table 7.2- Effects of material properties of elastic bar on impact velocity

	STEEL	ALUMINUM	TITANIUM
Energy bar stress at release (MPa)	517.5	517.5	517.5
Strain energy in unit volume (N-mm/mm^3)	0.669	1.911	1.152
Energy bar strain at release	0.00259	0.00739	0.00446
Modulus of elasticity E (MPa)	200100	70000	115996
Density ρ (t/m^3)	8.027	2.690	4.484
Wave velocity $C = \sqrt{E/\rho}$ (m/sec)	4992	5100	5083
Theoretical impact velocity, $V = C\varepsilon$ with no specimen (m/sec)	12.9	37.7	22.7
Maximum Impact velocity (m/sec) from simulation without specimen	12.7	30.8	22.4
Maximum Impact velocity (m/sec) from simulation with specimen	5.5	16.9	9.24
Maximum strain rate from simulation with specimen (1/sec)	433	1085	771

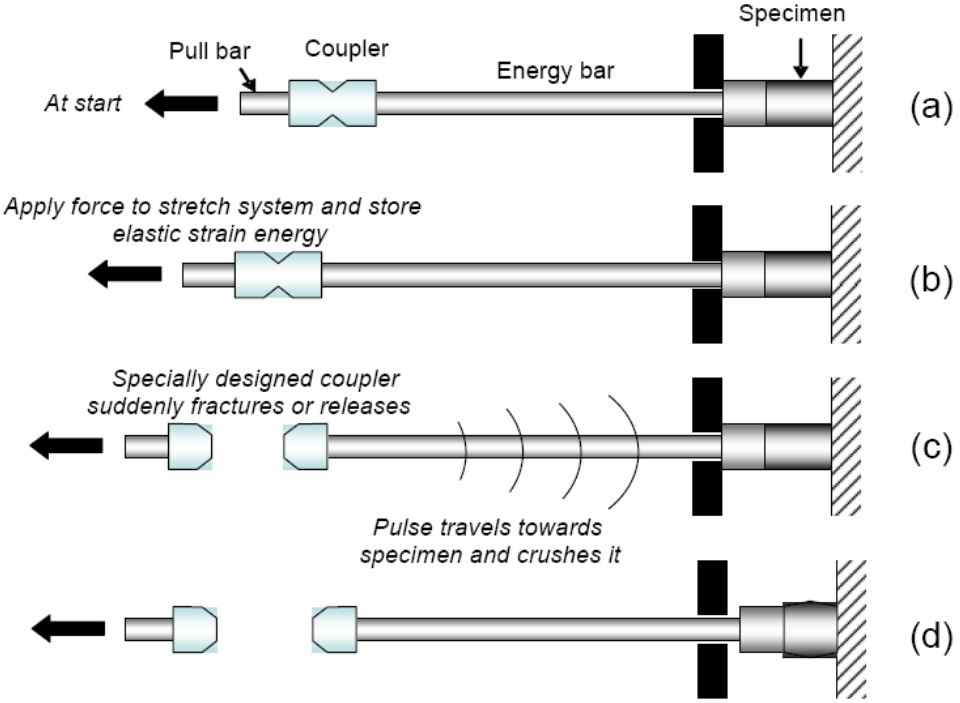

Fig. 7.1- Schematic showing operation of proposed test system

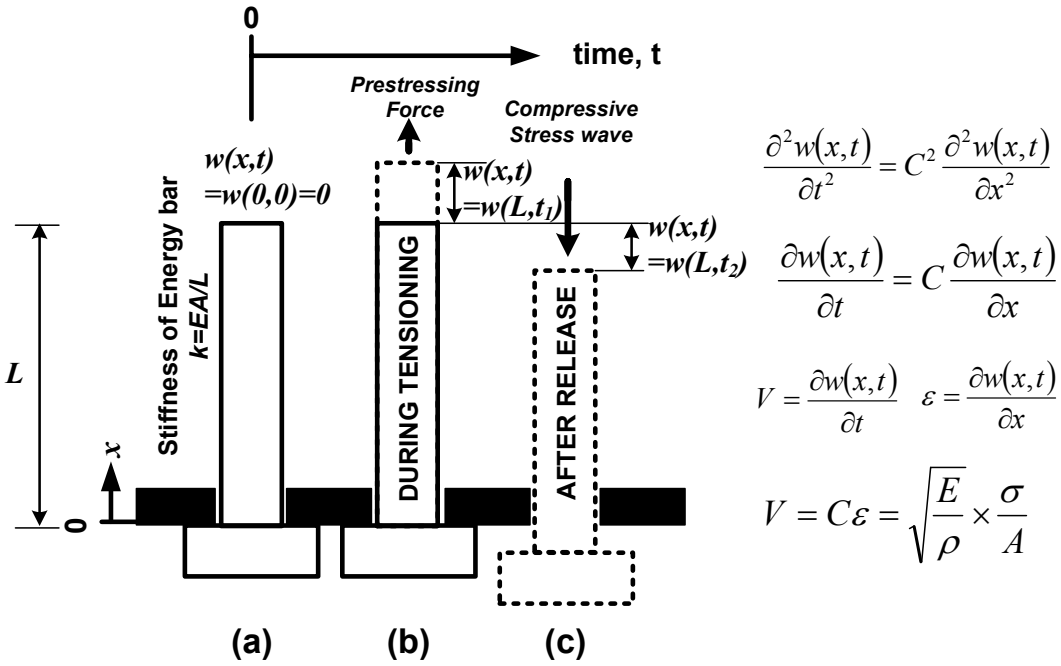

Fig. 7.2- Governing equations for proposed setup

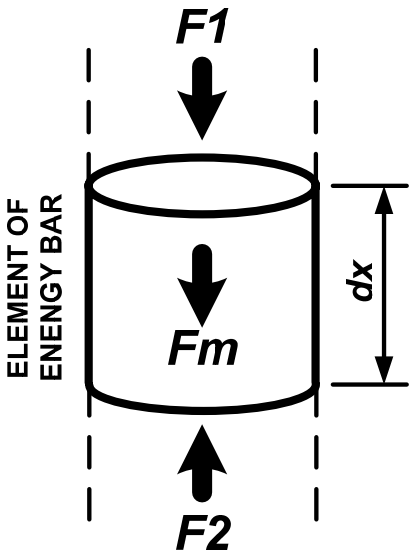

Fig. 7.3- Forces acting on a differential element

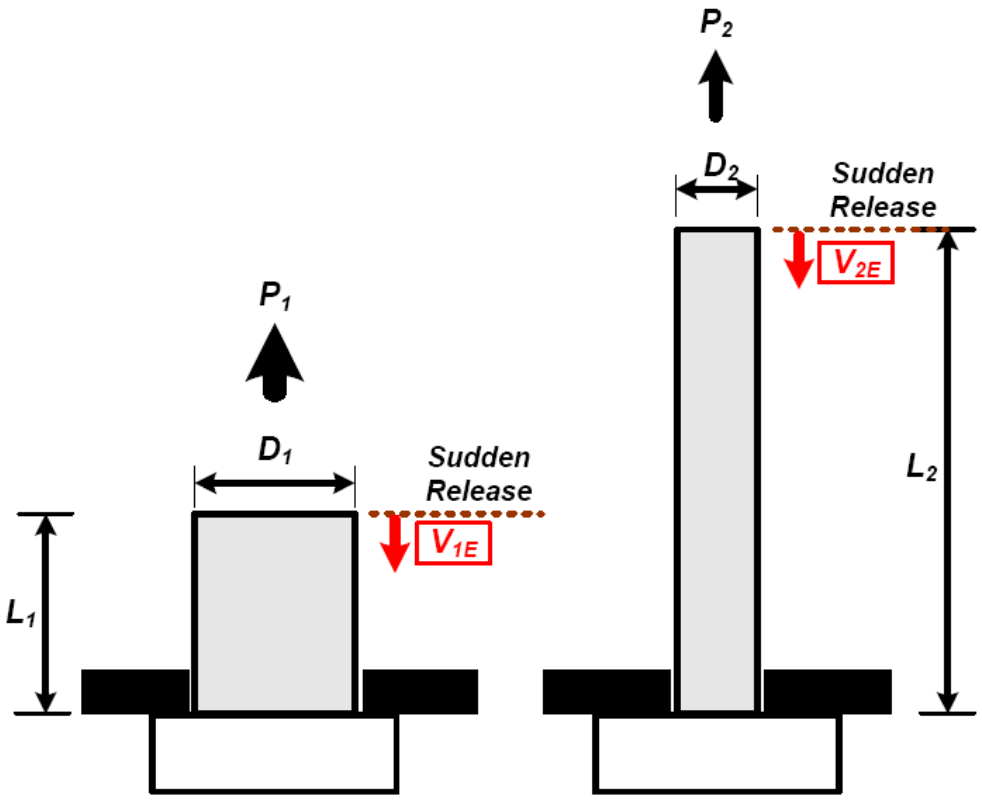

(a) Bar 1 (b) Bar 2

Fig. 7.4- Two elastic bars with different geometry

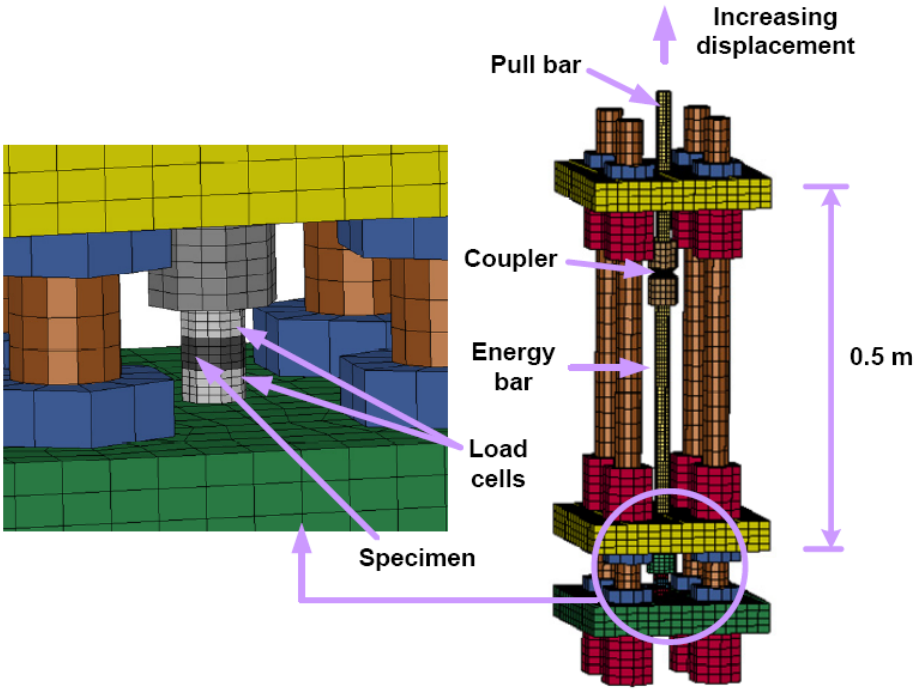

Fig. 7.5- Finite Element Model of SEITS

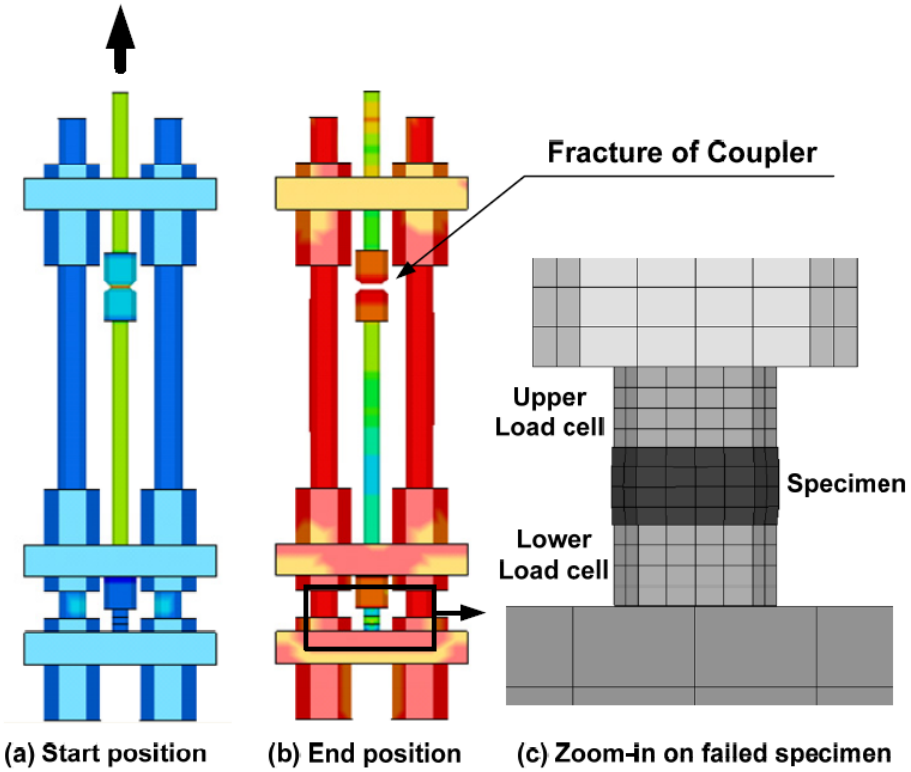

Fig. 7.6- Simulation results for SEITS

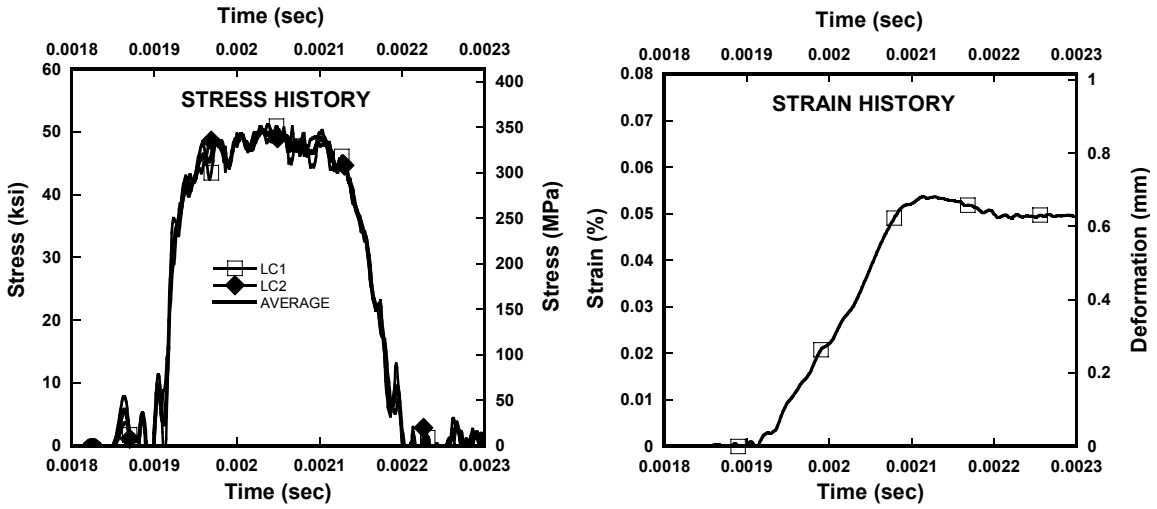

a) Stress history b) Strain history

Fig. 7.7- Stress and strain history results from simulation

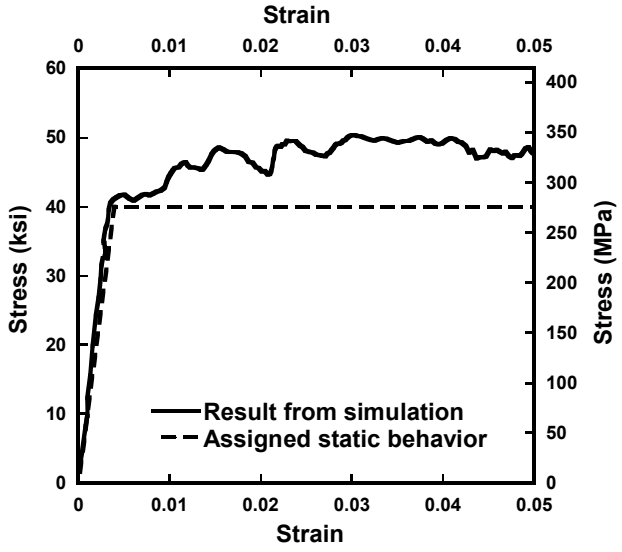

Fig. 7.8- Stress and strain curve of specimen (Aluminum) with PS steel bar

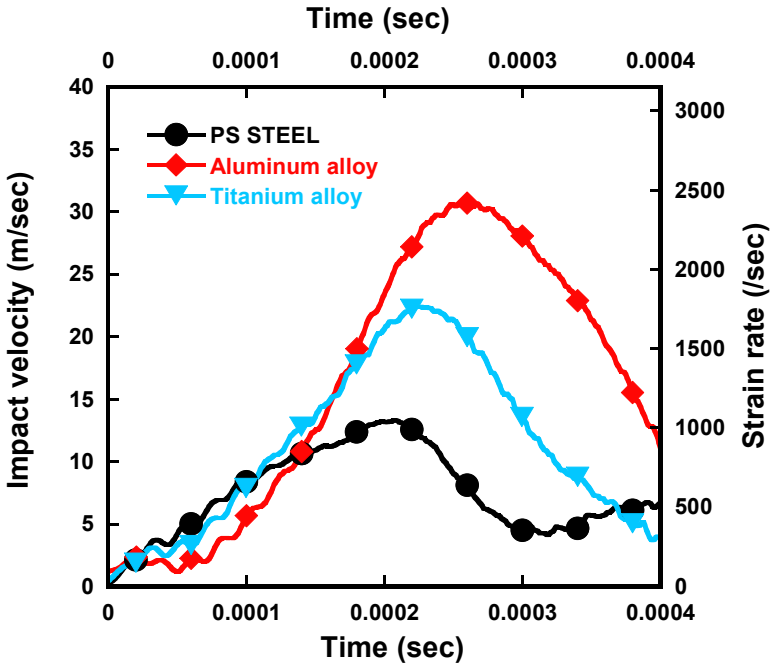

(a) without specimen

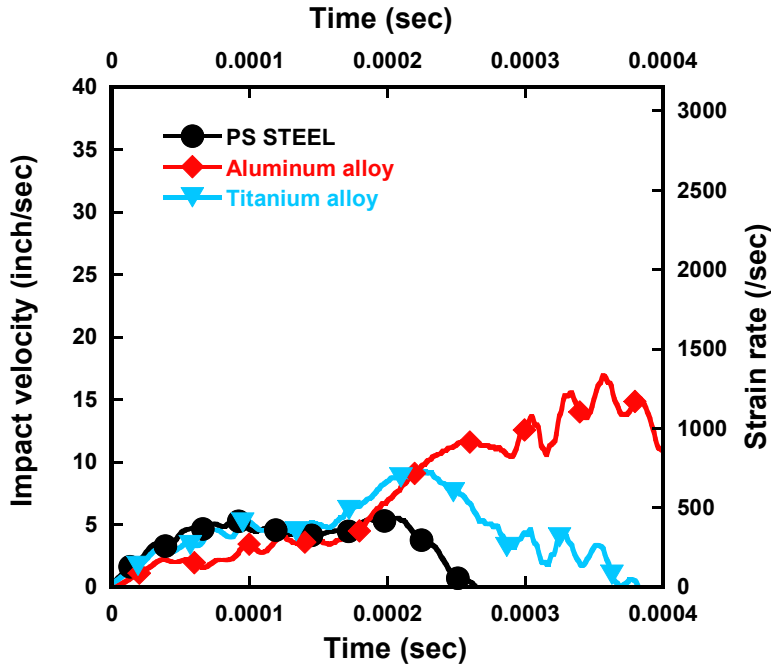

(b) with specimen

Fig. 7.9- Effect of bar material on impact velocity

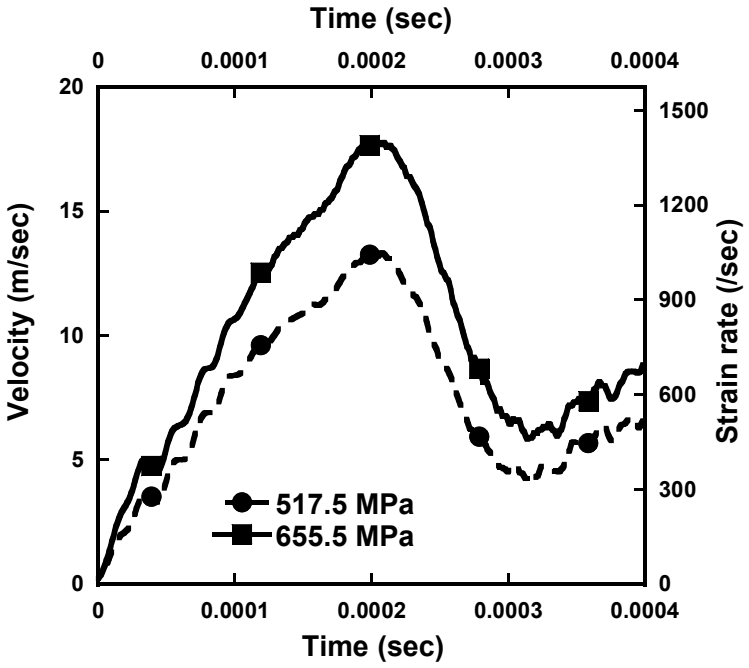

Fig. 7.10- Effect of stress level of energy bar on impact velocity (without specimen)

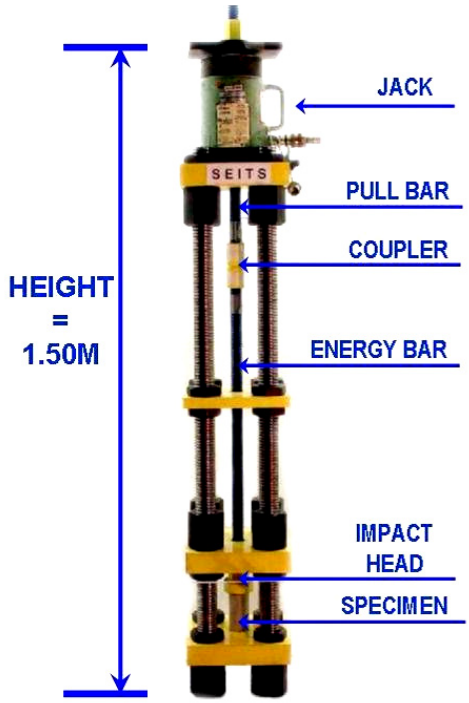

Fig. 7.11- Prototype of proposed method, Strain Energy Impact Test System [SEITS]

Time : 0 sec Time : 0.001 sec Time : 0.002 sec Time : 0.003 sec Time : 0.004 sec

Fig. 7.12- Progression of damage as a specimen is impacted in SEITS

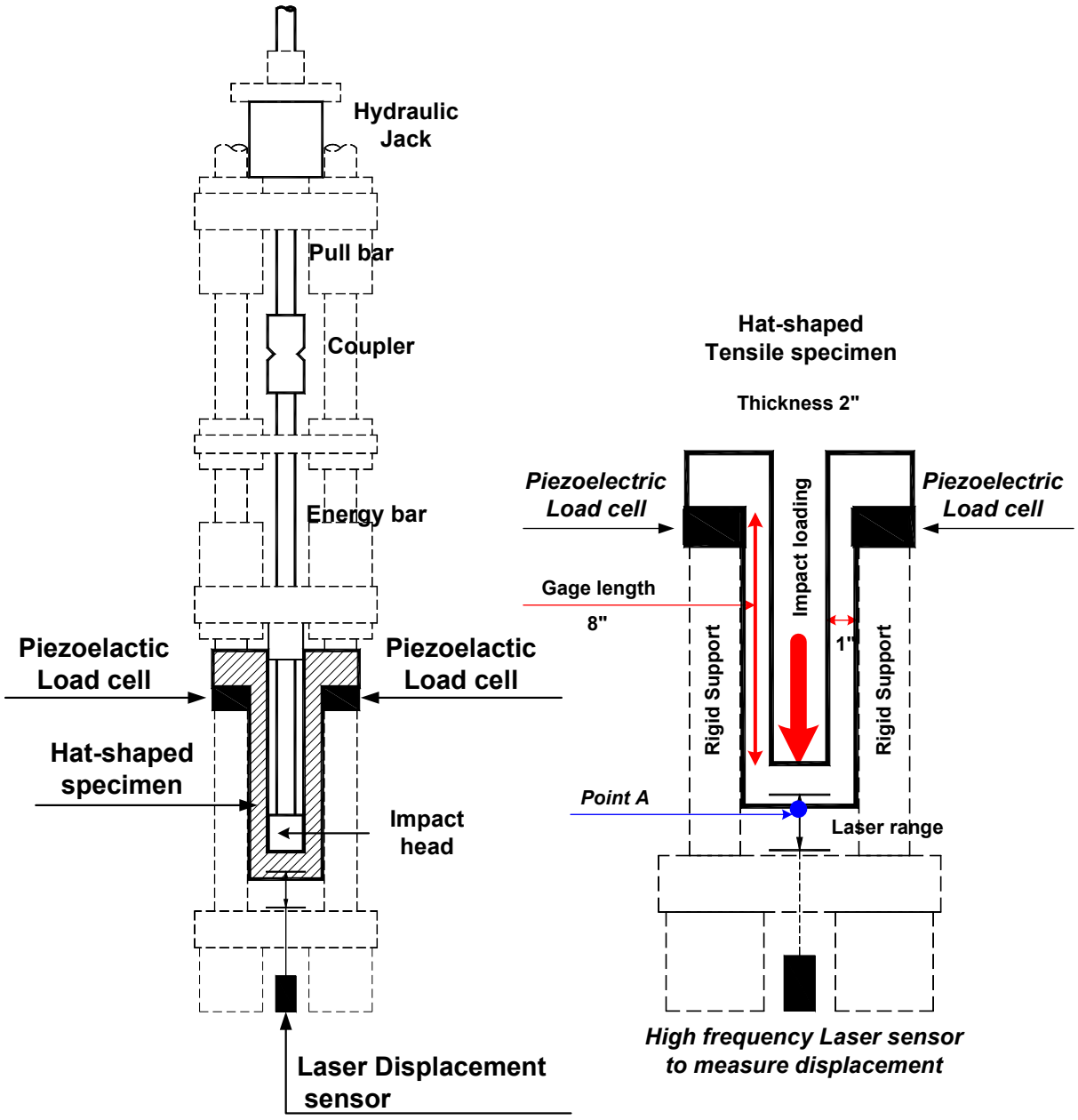

Fig. 7.13- Instrumentation for a tensile test

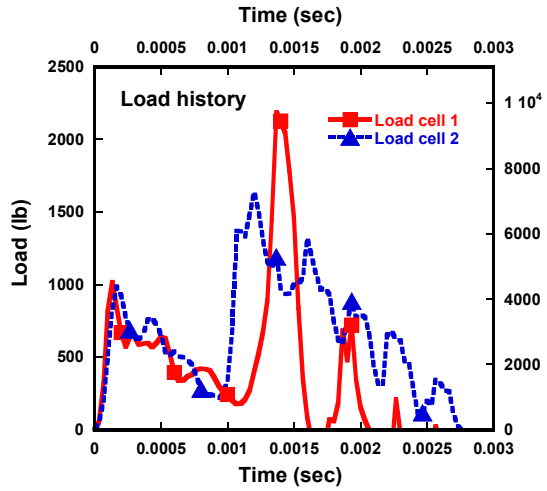

(a) Load history

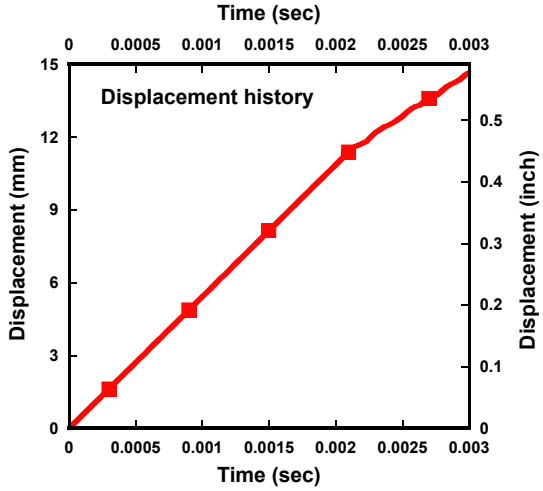

(b) Displacement history

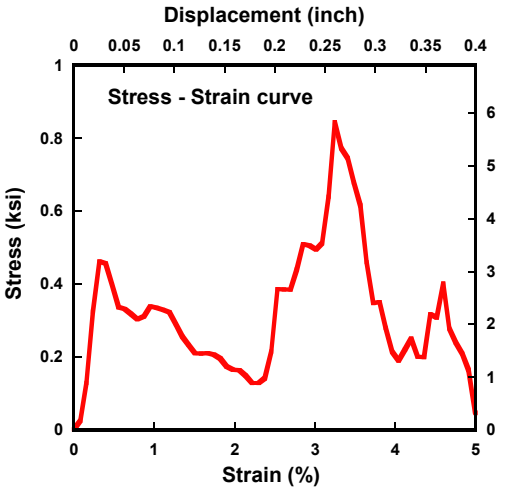

(c) Stress – strain curve

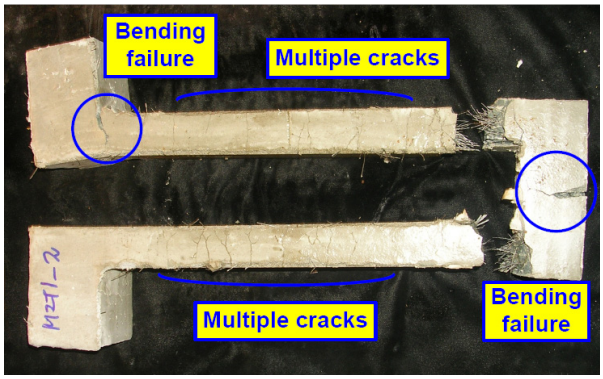

(d) Failure shape

Fig. 7.14- Preliminary tension test results using SEITS

REFERENCES

Bischoff, P. H. and Perry, S. H., "Compressive behavior of concrete at high strain rates," Materials and Structures, Vol. 24, 1991, pp. 425-450.

Bischoff, P. H. and Perry, S. H., "Impact behavior of plain concrete loaded in uniaxial compression," Journal of engineering mechanics, V. 121, No. 6, June, 1995, pp. 685-693

Cadoni, E., Albertini, C., and Solomos, G., "Analysis of the concrete behavior in tension at high strain rate by a modified hopkinson bar in support of impact resistant structural design," J. Phys. IV France, Vol. 134, 2006, pp. 647-652.

Elfahal, M. M., Krauthammer, T., Ohno, T., Beppu, M. and Mindess, S., "Size effect for normal strength concrete cylinders subjected to axial impact," International journal of Impact Engineering, Vol. 31, 2005, pp. 461-481

Grote, D. L., Park, S. W. and Zhou, M., "Dynamic behavior of concrete at high strain rates and pressures : 1. experimental characterization," International Journal of Impact Engineering, Vol. 25, 2001, pp. 869-886.

Gupta, P., Banthia, N. and Yan, C., "Fiber reinforced wet-mix shotcrete under impact," Journal of Materials in civil engineering, Vol. 12, No. 1, February 2000, pp. 81-90.

Keener, S. G., Thrash, C. P., and Mechlenburg, J. T., "Method for high strain rate testing of specimens," US Patent 5677494, Oct. 14, 1997

Naaman, A. E. and Gopalaratnam, V. S., "Impact Properties of Steel Fiber Reinforced Concrete in Bending," International Journal of Cement Composites and Lightweight Concrete, Vol. 5, No. 4, November 1983, pp. 225-233.

Stronge, W. J., "Impact mechanics," Cambridge University Press, 2000, pp. 146-172.

CHAPTER VIII

SOURCE OF STRENGTH ENHANCEMENT FOR CEMENT-BASED MATERIALS UNDER HIGH RATE COMPRESSIVE LOADINGS [7]

ABSTRACT

The Split Hopkinson Pressure Bar [SHPB] technique has been commonly used to investigate concrete compressive response under high strain rate. However, there appears to be a lack of agreement in the literature about a number of critical issues pertaining to this test method. In this paper, computational simulation models are employed to critique the technique and obtain a better understanding of it. Influential parameters are identified and attempts are made to shed light on some controversial issues surrounding the interpretation of high strain rate test data. The results show that significantly different strain rates can be obtained from the same SHPB test depending on the method used to estimate the strain rate value. Furthermore, comparing the results of simulations with pressure-independent and pressure-dependent constitutive material models show that strength increases associated with strain rate are strongly, but not totally, reliant upon the confinement introduced by lateral inertial effects and the frictional condition at the

[7] D. Kim, S. El-Tawil, and A. E. Naaman, "Numerical simulation of Split Hopkinson Pressure Bar test methods for concrete under compression", International Journal of Impact Engineering, (to be submitted)

interface between the pressure bars and the specimen. Based on these observations, it is argued that the so-called 'rate-enhanced' models that explicitly account for strength increases as a function of strain rate should not be used in numerical simulations that already account for the effects of lateral confinement, since such models would tend to double-count the strain rate effect.

8.1 INTRODUCTION

There is a common belief that high strain rate causes cement-based materials, such as concrete and mortar, to become stronger in compression and that this effect is inherently a material property. The tests on which this rationale is based show that the dynamic increase factor (DIF), defined as the ratio of the dynamic strength to the quasi static strength, for concrete in uniaxial compression is relatively insensitive to strain rates up to what is known as the transition strain rate. Ross et al. (1989) reported that the transition rate is between 60 s^{-1} and 80 s^{-1} for compression, while CEB (1998) suggested that the transition rate is 30 s^{-1}. Strain rates higher than the transition rate lead to large increases in the measured dynamic strength (Ross et al. 1989, Tedesco and Ross 1993, Ross et al. 1995 and 1996, Malvar and Crawford 1998, Klepaczko 2003). The effect of strain rate on material properties other than strength, such as axial strain at maximum strength, volumetric strain, energy absorption capacity, and elastic modulus was discussed by Bischoff and Perry (1995).

The number of theories and explanations that have been put forth to explain published test data reflect the lack of consensus about the true reasons for strain rate effects in concrete. Nemat-Nasser and Deng (1994) suggested that the increase in compressive capacity with increasing strain rate could be a consequence of the generation and

dynamic growth of interacting, compression-induced tensile micro cracks. Ross et al. (1995, 1996) noted that strain rate sensitivity is strongly dependent on moisture in concrete and attributed the effect to the added inertial effects of water and the increased fracture toughness of wet concrete over dry concrete. Donze et al. (1999) summarized two reasons for rate sensitivity that are commonly cited in the literature, namely the viscoelastic nature of hardened cement paste, and the time-dependent nature of crack growth. Friction between the specimen and loading head, as well as longitudinal and transverse inertial effects, are also widely thought to be influential factors.

Based on a numerical study, Li and Meng (2003) showed that friction, if not significantly reduced by using a lubricant between the specimen and load head, could cause substantial increases in strength that could be mistaken for strain rate effects. Using the same model, they also showed that strain rate sensitivity is strongly dependent upon the confining effect introduced by lateral inertial effects. The numerical results in Cotsovos and Pavlovic (2005) suggest that the strain rate effect is actually dependent upon general inertial effects, i.e., both longitudinal and transverse. This is also corroborated by numerical results in Donze et al. (1999) obtained through a discrete element model. Georgin and Reynouard (2003) discussed the strong influence of inertial confinement on the high strain rate response of concrete, but nevertheless suggested that concrete visco-plasticity can also play a role. In spite of their differences, the results and discussions presented in these 4 papers question the widely accepted view that the strain rate effect is, indeed, primarily a material property.

With the understanding that strain rate sensitivity is a material property, numerous practitioners and researchers have employed software packages that explicitly account for

the effect of strain rate in their constitutive models. Cotsovos and Pavlovic (2005) discuss the variety of strain rate dependent numerical models that exist in the literature, i.e. models based on plasticity theory, viscoplasticity, continuum damage mechanics, or a combination of these approaches. As previously discussed, recent studies are questioning the correctness of assuming that strain rate sensitivity is a material property, and therefore, whether strain rate dependent models in popular simulation software are rational (Li and Meng 2003, Cotsovos and Pavlovic 2005).

As is clear from the previous discussion, there appears to be a lack of general consensus about: 1) whether the experimentally observed strain rate effects are purely material responses; 2) what mechanisms are behind the observed responses; and 3) how to characterize high strain rate effects within numerical simulations. In addition, as will be discussed later on in the paper, there are significant differences in commonly used methods for processing high strain rate test data from the Split Hopkinson Pressure Bar (SHPB), which is widely used for testing concrete under high strain rate.

The objective of this paper is to clarify some of the previously outlined controversial issues through 3-D, high fidelity numerical simulations of the SHPB method. Other researchers, such as Donze et al. (1999), Li and Meng (2003), and Cotsovos and Pavlovic (2005) also conducted 3-D numerical simulations to investigate the rate effect on concrete response. The study reported herein differs from previous studies in that highly refined models of the entire SHPB testing system are created and exercised. This approach allows the development of a more detailed understanding, than previously achieved, of how interpreting the measured data influences the high strain rate response inferred from the tests.

Since the effect of confinement on compressive strength is central to this study, a short discussion of this topic is given first. The models used herein are then presented followed by a description of the SHPB theory and common techniques for processing SHPB test data. Finally, the SHPB simulations and the results drawn from them are presented and discussed.

8.2 THE EFFECT OF CONFINEMENT ON COCRETE AND MORTAR STRENGTH

Much research has been performed to understand the response of concrete under triaxial stress states. The most important difference in the behavior of concrete or mortar compared with metal is its strong dependence on lateral pressure; it is well known that the strength and ductility of concrete and mortar both increase with lateral confining pressure. Equation [8.1] is a well-known empirical formula that describes the effect of confinement pressure on the axial compressive strength of concrete (Macgregor and Wight, 2005).

$$\frac{f_{CC}^{'}}{f_{C}^{'}} = 1 + 4.1 \times \frac{f_{CON}}{f_{C}^{'}} \qquad [8.1]$$

where, $f_{CC}^{'}$ is the axial compressive strength of concrete under confining pressure f_{CON} and $f_{C}^{'}$ is the uniaxial compressive strength of concrete without any confinement.

Imran and Pantazopoulou [1996] performed an experimental program designed to characterize the behavior of concrete under multi-axial states of stress. They modified the level of confinement pressure and investigated the effect of confining pressure on the compressive strength. Different water cement ratios were used to produce concrete with three different unconfined compressive strength, including 21.2, 43.5 and 64.7MPa. As shown in Figure 8.1, their experimental results match well the strength computed using

Equation [8.1].

Candappa et al. [1999, 2001] investigated the effect of confining pressure on the behavior of high strength concrete. An extensive experimental program was performed in order to determine the effect of lateral confinement on the ductility of high strength concrete. Four levels of confining pressure, 4, 5, 8 and 12MPa, were applied to four concretes with unconfined compressive strengths of 41.9, 60.6, 73.1 and 103.3MPa. They reported that the multiplication factor associated with f_{CON} in Equation [8.1] was slightly more than the traditionally accepted value of 4.1. Their results are also plotted in Figure 8.1.

There are few studies on the confining pressure effect on mortar (that is concrete without large aggregates) behavior. A recent study by Schmidt and Cazacu [2006] showed that mortar, too, is strongly influenced by confining pressure. Their test results, which are plotted in Figure 8.1, indicate that it is reasonable to use Equation [8.1] to model the effect of confinement on mortar response.

8.3 CONSTITUTIVE MODELS USED IN SIMULATIONS

The simulations reported herein are conducted with two different material models: a J_2 model, and a modified Drucker-Prager (*D-P*) model. The former is a pressure independent constitutive model, while the latter is pressure dependent. The intent is to compare the high strain rate responses of both models to obtain a better understanding of the effect of lateral confinement, which generates high confinement pressures, on material behavior.

The J_2 model is a one-parameter model that uses shear strength to define yield of a material. The yield function of the model can be written as:

$$F(\sigma,k) = \sqrt{J_2} - k = 0 \qquad [8.2]$$

where, J_2 is the second invariant of the deviatoric stress tensor **S,** i.e. $J_2 = \frac{1}{2} S_{ij} S_{ij}$, and k is the yield strength under pure shear. The J_2 model is commonly used for representing metal response when used in conjunction with a perfectly plastic or hardening kinematic rule. Since this work is focused on mortar and concrete, and to ensure a fair comparison to *D-P* model results, the J_2 model used herein is assumed to be elastic-plastic up to a failure strain of 2%. Beyond this strain, the capacity is suddenly reduced to zero to signify crushing failure. The 2% strain value is chosen as a reasonable strain at which concrete no longer has any compressive capacity in compression.

The original *D-P* model is an extension of the J_2 model that accounts for the first invariant of the stress tensor, $I_1 = \sigma_{ii}$, i.e. it is pressure dependent.

$$F(\sigma,k) = \alpha I_1 + \sqrt{J_2} - k = 0 \qquad [8.3]$$

where α is the slope between I_1 and $\sqrt{J_2}$, and k is the intersection of the yield surface with the $\sqrt{J_2}$ -axis. Imran and Pantazopoulou (2001) modified the original *D-P* model to make it more suitable for modeling concrete response. In particular, their formulation could represent softening after the peak stress and could transition from softening response to elasto-plastic at sufficiently high confining pressures. Their proposed yield function is:

$$F(\sigma,k) = AkI_1 + B\sqrt{J_2} - kf_c^{'} + (1-r) f_c^{'} \left(1 - \frac{I_1}{I_{1,trans}} \right) \qquad [8.4]$$

where A and B are material parameters obtained from triaxial compression tests, which in this study, are obtained from Equation [8.1]. $f_c^{'}$ is the uniaxial compressive

strength and $I_{1,trans}$ indicates the level of confining pressure where the response changes from softening to perfectly plastic, defined based on information in Imran and Pantazopoulou (2001). The hardening and the softening parameters (k and r) are internal variables used to control the shape of the stress-strain response.

The modified *D-P* model, as described above, was implemented as a user-defined model in LS-DYNA (Hallquist, 2007) for the purposes of this research. In the implementation, a parabolic function was selected for the hardening parameter k, whereas the cosine function is used for the softening parameter r as shown in Fig. 8.2.

$$k = \left(\frac{2\sqrt{\varepsilon_p \varepsilon_{p,\max}} - \varepsilon_p}{\varepsilon_{p,\max}} \right)(1 - k_0) + k_0 \qquad [8.5]$$

$$r = \frac{1}{2} + \frac{1}{2}\cos\left[\frac{\pi(\varepsilon_p - \varepsilon_{p,\max})}{\varepsilon_{p,ult} - \varepsilon_{p,\max}} \right] \qquad [8.6]$$

where k_0 is the initial hardening parameter for the initial yield surface, ε_p is the effective plastic strain that measures the accumulation of the plastic strains (Chen, 1982) and is defined as:

$$\varepsilon_p = \int d\varepsilon_p = \int \boldsymbol{d\varepsilon^p} : \boldsymbol{d\varepsilon^p} \qquad [8.7]$$

where $\boldsymbol{d\varepsilon^p}$ is the incremental plastic strain tensor. As shown in Fig. 8.2, $\varepsilon_{p,\max}$, the maximum effective plastic strain, corresponds to the point where the hardening parameter reaches unity, i.e. the state of stress reaches its maximum capacity. $\varepsilon_{p,ult}$, the ultimate effective plastic strain, corresponds to the residual strength, i.e. where the softening parameter reaches zero. The material parameters k_0, $\varepsilon_{p,max}$, $\varepsilon_{p,ult}$ are obtained by fitting to the uniaxial, unconfined compressive response of specimens in Candappa et al. (1999,

2001).

To determine the direction of the plastic flow, a non-associative flow rule was implemented in this study. According to the triaxial compression test results in Smith et al. (1989), the plastic flow direction is not perpendicular to the yield surface and, if the associative flow rule is used, the volumetric strain will be over predicted. Furthermore, unlike steel that has a constant volumetric strain, the volumetric strain of concrete under uniaxial compression is not constant. It starts with contraction up to the maximum strength, followed by expansion after the peak. Hence, a non-associative flow rule based on the original *D-P* function is selected as the potential function in this study. Unlike the yield function, the parameters of the potential function are not constant, i.e., they depend on the effective plastic strain ε_p (Imran and Pantazopoulou, 2001).

$$g(\sigma) = a\frac{I_1}{3} + \sqrt{2J_2} - c \qquad [8.8]$$

where a is a slope of the flow direction and controls the amount of volumetric plastic strain and can be defined as:

$$a = \frac{a_u}{(1-\eta)}\left(\frac{\varepsilon_p}{\varepsilon_{p,\max}} - \eta\right) \qquad [8.9]$$

where a_u is the slope of flow direction under uniaxial loading condition and η is the ratio of $\frac{\varepsilon_p}{\varepsilon_{p,\max}}$ at zero volumetric strain that is also at the same point when the stress reaches its peak. The material parameters a_u and η are obtained from Imran and Pantazopoulou (2001).

The tension model is constructed by extending the compression yield surface to encompass the tension regime. Tensile response is modeled as linearly elastic up to the

peak tensile strength, followed by softening behavior. Additional detailed information on the material model can be found in Sirijaroonchai (2008).

8.3.1 Validation of the modified D-P Model

Concrete cylinder tests with various confining pressures were simulated in order to validate the implemented *D-P* model. The confined compression tests by Candappa et al (1999 and 2001) were selected for this purpose. The simulation model used in this exercise is shown in Fig. 8.4. The loading fixtures, which are simulated using steel plates, are placed at the top and bottom of the concrete. The friction coefficient between concrete and loading fixtures is assumed to be 0.3. A fixed boundary condition is enforced at the bottom nodes of the steel plates. For the triaxial simulations, the confining pressures are first applied to the circumferential layer of the concrete. Then, prescribed displacements are applied to the top steel plate. The summation of reactions at the bottom plate is used to calculate the stress on the specimen. Strain is measured from the change in length between the top and bottom nodes of concrete divided by the original height of concrete.

Fig. 8.5 compares between the measured stress strain curves and the response computed from models of the experimental setup. Clearly there are some differences in the general shape of the curves, especially in the post peak response at the highest confining levels. Nevertheless, the model reasonably predicts the strength enhancement associated with confinement for all confinement levels.

8.4 MODELING AND DISCUSSION OF THE SHPB TEST METHOD

The split Hopkinson Pressure Bar test system is based upon the following assumptions: (1) one dimensional wave propagation theory applies; (2) stress and strain in the specimen are uniform in the axial direction; and (3) specimen inertia and friction

effects are negligible. To successfully test concrete under high strain rate in a SHPB, the specimens (and therefore the SHPB) must have a certain minimum size dictated by the characteristic size of the constituents of concrete, e.g., aggregate. The specimen must be several times the characteristic size of the aggregate so that the results are not adversely influenced by the size effect. On the other extreme, the diameter of the specimen must be as small as possible to reduce the overall length of the equipment, since lateral dispersion of the propagating uniaxial shock wave could distort the test results if the bars are too stocky.

These two conflicting requirements, a specimen with as large a diameter as possible and testing bars that are as short as possible for a given diameter, create practical problems for SHPB testing of concrete. For example, to test a 75 mm diameter cylindrical specimen, a SHPB would have to be 10 - 12 m long. Furthermore, to ensure that inertial effects in the specimen are minimized, the length of the specimen is taken as small as possible; usually a concrete specimen is as long as its diameter. This implies that the behavior of the specimen could be affected by the confining effects due to friction at the specimen ends, an issue that will be evaluated and discussed later on in the paper.

Fig. 8.6 shows an overall schematic of the SHPB test system, while Fig. 8.7 shows details of its operation. When the stress wave, generated by the striker bar impact upon the incident bar, arrives at the interface between the incident bar and the specimen, a reflection stress wave is generated, which travels back towards the impact end. The remainder of the stress wave travels into the specimen, and a portion of it subsequently enters into the transmitter bar. The specimen's stress and strain histories are determined from the strains measured at strain gages A and B, located at the middle of the incident

and transmitter bars, respectively, as shown in Fig. 8.7.

The stress history of the specimen, σ_s, as computed from classical SHPB theory, is calculated by averaging the forces, at both ends of the specimen, which are computed from the strains measured at gages A and B as shown in Fig. 8.7:

$$\sigma_s(t) = \frac{F_{avg}(t)}{\pi D_S^{\,2}/4} \qquad [8.10]$$

where, D_s is the specimen diameter, and:

$$F_{avg}(t) = \frac{F_1(t) + F_2(t)}{2} \qquad [8.11]$$

$$F_1(t) = E_B \times \left[\varepsilon_I(t) + \varepsilon_R(t)\right] \times \frac{\pi D_B^{\,2}}{4} \qquad [8.12]$$

$$F_2(t) = E_B \times \varepsilon_T(t) \times \frac{\pi D_B^{\,2}}{4} \qquad [8.13]$$

where, ε_I and ε_R are the incident and reflected strains measured in the incident bar while ε_T is the strain measured in the transmitter bar. E_B, D_B are the bar elastic modulus and diameter, respectively.

The strain rate of the specimen is computed from the velocities imposed on both ends of the specimen.

$$\frac{d\varepsilon_s}{dt} = \frac{V_2 - V_1}{L_S} \qquad [8.14]$$

where, L_s is the specimen length, and:

$$V_1 = -C_O\left[\varepsilon_I(t) - \varepsilon_R(t)\right] \qquad [8.15]$$

$$V_2 = -C_O\varepsilon_T(t) \qquad [8.16]$$

where C_O is one dimensional stress wave velocity ($C_O = \sqrt{E_B/\rho_B}$), where ρ_B is the mass density of the bar material. The strain can then be obtained by substituting

Equations [8.15] and [8.16] into [8.14] and integrating with respect to time:

$$\varepsilon_S(t) = -\frac{C_0}{L_S}\int_0^t [\varepsilon_T(t) - \varepsilon_I(t) + \varepsilon_R(t)]dt \qquad [8.17]$$

If the specimen is assumed to deform uniformly during impact event, i.e., there are uniform strain, and therefore, stress fields within the specimen, then Equations [8.12] and [8.13] are equal, which results in:

$$\varepsilon_I(t) + \varepsilon_R(t) = \varepsilon_T(t) \qquad [8.18]$$

Substituting Equation [8.18] into Equation [8.17], the strain of the specimen simplifies to,

$$\varepsilon_S(t) = -\frac{2C_0}{L_S}\int_0^t \varepsilon_R(t)dt \qquad [8.19]$$

Equation [8.19] can be expressed in differential form as,

$$\frac{d\varepsilon_s}{dt} = -\frac{2C_0\varepsilon_R}{L_S} \qquad [8.20]$$

Furthermore, Equation [8.10], expressing the stress of the specimen, can be simplified into:

$$\sigma_S(t) = \frac{D_B^2 E_B}{D_S^2}\varepsilon_T(t) \qquad [8.21]$$

Grote et al. (2001) used Equation [8.20] to calculate strain rate, while Ross et al (1989, 1996) used a different method in which they first defined stress rate from the transmitter bar stress history:

$$\dot{\sigma} = f_{tn}/\tau \qquad [8.22]$$

where $f_{tn} = \sigma_T A_r$; f_{tn} is the maximum stress measured in the transmitter bar, τ is the time lag between the start of the transmitted stress wave and the maximum

transmitted stress, A_r is the area ratio such that $A_r = D_B^2 / D_S^2$, and E_S is the secant modulus of elasticity of the specimen under static loading. By assuming that E_S is independent of strain rate, the strain rate is computed by Ross et al (1989, 1996) from

$$\dot{\varepsilon} = \dot{\sigma} / E_S \qquad [8.23]$$

Although both studies employed the above described different methods in calculating the strain rate, both experimental studies used the same stress history measured from the transmitter bar (Equation [8.21]) in estimating the strength of the specimen, i.e., they assumed the uniform state of strain and stress in the specimen during the impact event.

8.5.1 Simulation model

The goal of the simulation studies of the SHPB test setup is to examine the previously discussed controversial issues pertaining to strain rate effects. To achieve these objectives, two SHPB models are created as shown in Fig. 8.8, corresponding to the SHPB experimental setups used by Ross et al. (1989, 1996) and Grote et al. (2001), respectively. Since Grote et al. (2001) did not provide information about the length of the pressure bars, a length of 1143 mm is assumed in the simulation. Furthermore, although Grote et al. (2001) reported that specimen aspect ratio did not appear to play a significant role in the measured strain rate sensitive behavior of mortar specimens, the effect of aspect ratio on rate sensitivity was nevertheless investigated in the current study. The Grote simulations are conducted using specimens with two aspect ratios, 1.0 (11.4 mm diameter, 11.4 mm length) and 0.5 (11.4 mm diameter, 5.7 mm length) in this study.

Eight-node hexahedron solid elements are used to model all parts of SHPB system and contact constraints are imposed to prevent interpenetration of the system components,

e.g., striker bar, incident pressure bar, transmitter pressure bar, and specimen. Several series of simulations are conducted with various striker bar velocities (ranging from 2.54 m/s to 33.02 m/s), and three friction coefficients, namely μ=0.1, μ=0.2 and μ=0.3. The strain rate and DIF values for μ=0.3, different impact speeds and material models are shown in Table 1, where the results of the simulations are based on Ross's SHPB set-up. Fig. 8.9 shows the stress wave histories from the incident and transmitter bars from the simulations using Ross's SHPB setup when the striker bar velocity is 10.16 m/s and the specimen aspect ratio is 1.0.

8.6.2 Strain rate computation

Table 1 shows the DIF at various strain rates computed using models employing both *D-P* and J_2 models for the SHPB setup by Ross et al. (1996). Three strain rates are presented in Table 8.1. The first two are computed using the methods proposed by Ross et al. (1996) and Grote et al. (2001), i.e., Equations [8.23] and [8.20], respectively. The third strain rate is calculated directly from the displacements of corresponding nodes at the interfaces between the two pressure bars and the specimen. In applying Ross' method to calculate strain rate, the secant modulus of elasticity at maximum strength under static loading was adopted in estimating strain rate based on the stress rate.

Two general observations can be made from Table 8.1: the strain rate increases as the striker bar velocity increases, and the DIF increases as the strain rate increases. Furthermore, for both *D-P* and J_2 models, there is a clear difference between the strain rates computed using Equations [8.20] and the strain rates computed using Equation [8.23]. The former estimates a larger strain rate than the latter. A close examination of Table 1 shows that Equation [8.20] used by Grote et al. (2001) matches the actual strain

rates better than Equation [8.23] used by Ross et al. (1996), which seems to significantly underestimate the actual rate.

8.5.3 Effect of material model on DIF

It is clear from Table 8.1 that specimens employing the J_2 Model show a small enhancement in strength with increasing strain rate, e.g., the DIF at strain rates up to 646 s^{-1} ranges between 1.06 and 1.39. The pressure dependent *D-P* Model, however, shows a strong dependence on strain rate, with the DIF exceeding 2.6 at the highest strain rates.

To judge the relative performance of *D-P* and J_2 models, the computed data is plotted versus the measured data for Ross' experiments in Fig. 8.10 and Grote's experiments in Fig. 8.11. To ensure consistency, Ross' method of data computation, Equation [8.23], is employed for the former in Fig. 8.10, while Grote's Equation [8.20], is used for the latter in Fig. 8.11. As previously mentioned, Grote's data is split into data for specimens with L/D of 1.0 and 0.5 (Figures 8.11a and 8.11b, respectively). It is clear from Figure 8.10 and 8.11(b) that the J_2 Model, as expected, does not follow the trends in the test data. In particular, there is only a mild increase in strength with increasing strain rate, and as a result, the J_2 model significantly underestimates the DIF at the highest strain rates. On the other hand, the D-P model shows a sharp increase in DIF with increasing strain rate, which reflects the general trend in the test data. Figure 8.11(a) is, however, not as conclusive, although this can be attributed to the limited experimental data points coupled with extreme scatter. For example the 3 circled data points correspond to about the same strain rate, but their DIF ranges from 1.4 to 2.4.

It is important to recall that the *D-P* Model used in this simulation was calibrated to static data only, i.e., it is not a so-called 'rate-enhanced' model, where the effect of strain

rate is taken into account in the constitutive model. Nevertheless, the model is still capable of capturing the general trends in the experimental data, suggesting that strain rate effect can be largely attributed to the pressure-dependent nature of concrete. However, some deviation in the computed data with respect to the test data, e.g., the two circled points in Figure 8.11b, suggests that other factors may also be contributing to DIF. As discussed next, friction between the specimen and SHPB bars can play an influential role. However, since it is not known what the coefficient of friction was in the Grote et al. (2001) tests, it is impossible to quantify the influence of this variable on the test data considered herein. It is also feasible that the specific cementitious material used by Grote et al. (2001) is more pressure sensitive than suggested by Equation 8.1, although this is unlikely given how well established Equation 8.1 is. Another possibility, of course, is that one of the previously described material-related explanations in the introduction could be contributing to strain rate sensitivity. However, whatever the mechanism, its effect is still smaller than that attributed to the pressure-dependent nature of concrete as embodied by Equation 8.1.

8.5.4 Effect of friction on DIF

The influence of the coefficient of friction (μ) on DIF is shown in Table 8.2 and Fig. 8.12. The simulation model of Grote's setup was used to produce this data. As shown in Table 8.2, even though μ has very little effect on static response, it has a significant influence on dynamic response. In particular, for a given striker bar velocity, an increasing DIF is obtained as μ increases. For example, the dynamic strength of the specimen, for 25.4 m/sec striker bar velocity, is 206.43 MPa for μ =0.3, 164.33 MPa for μ =0.2, and 132.29 MPa for μ =0.1, respectively. In addition, as the velocity of the striker

bar increases, the influence of μ appears to also increase.

8.6 SUMMARY AND CONCLUSIONS

Computational simulation models of two different SHPB setups were created and exercised to critique the SHPB technique and to investigate the effect of various influential parameters on the high strain rate response of mortar and concrete under compression. The developed models, which were validated by comparing their responses to static test data, were geared towards answering a number of questions, in particular: is the experimentally observed DIF a true material property or is it due to a structural effect, should rate enhanced models be used in high rate simulations, how should strain rate be measured and what is the role of friction? Based on the limited studies conducted, the following conclusions can be drawn for concrete or mortar subjected to high strain rate loading in compression:

- Comparisons between simulation data and Equation [8.20] show that the equation produces a reasonable estimate of strain rate. On the other hand, Equation [8.23] can significantly underestimate the actual strain rate. Care should therefore be exercised when selecting the method used for computing strain rate when using the SHPB technique.
- The numerical results show that friction can play an influential role in the observed strain rate effects for the specimen aspect ratios considered.
- Comparisons between the results of the *D-P* model, which is pressure dependent, and the J_2 model, which is pressure independent, clearly show that high strain rate loading on concrete specimens will create a significant dynamic strength enhancement effect

that can be attributed to: a) friction and lateral inertial effects, both of which create confinement effects; and b) the pressure dependent nature of mortar and concrete, which manifests confinement effects as an increase in the compressive strength. The evidence presented in this paper shows that, while pressure sensitivity appears to be responsible for the majority of the strength enhancement observed in the high strain rate tests considered, it may not account for all of it. Further experimental and simulation-based research is necessary to ascertain the specific contribution of the confinement effect.

- The fact that the DIF computed from the pressure-dependent *D-P* model, which was calibrated to static data, follows reasonably well the experimentally observed trends from two different test programs suggests that the so-called 'rate enhanced' models are not appropriate for conducting simulations that account for confinement effects. In particular, when used within models that account for distributed inertial effects, rate enhanced models will, in essence, incorrectly double-count the strain rate effect. This should not be construed to mean that 'rate enhancement' should not be used in less refined models, such as beam models, where the confinement effect associated with inertial or frictional effects are not directly captured.

Table 8.1- Summary of simulation results for SHPB using Ross's set-up (μ= 0.3)

Assigned Material Model	Vel. (m/s)	Incident Bar	Transmitted Bar	$\dot{\varepsilon}$ (1/s)			DIF
		σ_I (MPa)	σ_T (MPa)	Eqn. 20	Eqn. 23	From Simulation	$\frac{\sigma_T}{\sigma_S}$
D-P Model	Static	-	46.300	0.0001			1
	3.81	88.9	56.587	31	24	69	1.249
	5.08	118.3	58.325	84	36	92	1.288
	10.16	236.9	74.980	187	83	188	1.655
	15.24	355.7	86.237	265	102	286	1.904
	20.32	474.6	95.385	357	120	381	2.106
	25.40	594.0	104.795	460	131	487	2.313
	33.02	772.8	118.589	617	150	626	2.613
J2 Model	Static	-	46.000	0.0001			1
	3.81	89.4	48.565	50	16	72	1.056
	5.08	119.3	50.849	75	24	91	1.105
	10.16	238.7	59.582	167	62	185	1.295
	15.24	358.4	63.395	268	71	293	1.378
	20.32	478.3	63.985	392	75	394	1.391
	25.40	598.4	63.632	471	77	490	1.383
	33.02	778.9	61.901	625	78	646	1.346

σ_I : Peak stress value in the Incident stress history

σ_T : Peak stress value in the Transmitted stress history

Table 8.2- Effect of friction on peak strength and DIF (From the simulation based on Grote's SHPB set-up)

Velocity	μ=0.3		μ=0.2		μ=0.1	
	Strength	DIF	Strength	DIF	Strength	DIF
Static	46.30	1.00	46.30	1.00	46.26	1.00
2.54	86.98	1.88	72.14	1.56	56.57	1.22
7.62	103.70	2.24	91.67	1.98	76.90	1.66
12.70	130.57	2.82	111.15	2.40	93.24	2.02
17.78	167.71	3.62	133.49	2.88	108.09	2.34
25.40	206.43	4.46	164.33	3.55	132.29	2.86

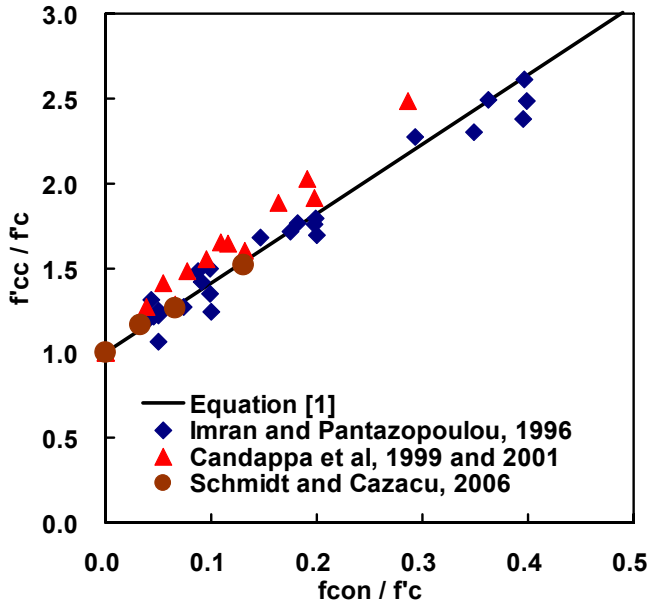

Fig. 8.1- Effect of confining pressure on the axial compressive strength of concrete and mortar

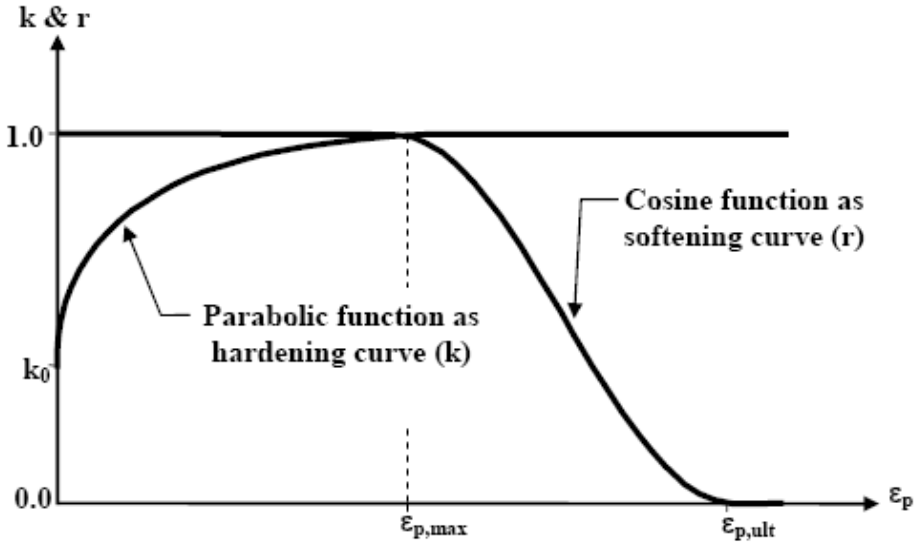

Fig. 8.2- Hardening and softening parameters as a function of effective plastic strain $\left(\varepsilon_p\right)$

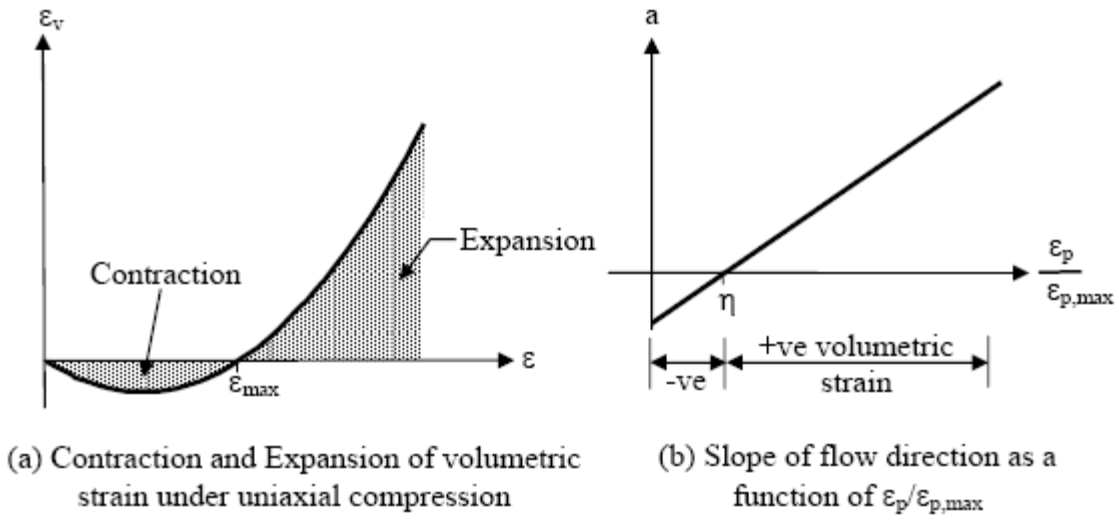

(a) Contraction and Expansion of volumetric strain under uniaxial compression

(b) Slope of flow direction as a function of $\varepsilon_p/\varepsilon_{p,max}$

Fig. 8.3- Amount of volumetric strain under uniaxial compression controlling by 'a' (Imran and Pantazopoulou, 2001)

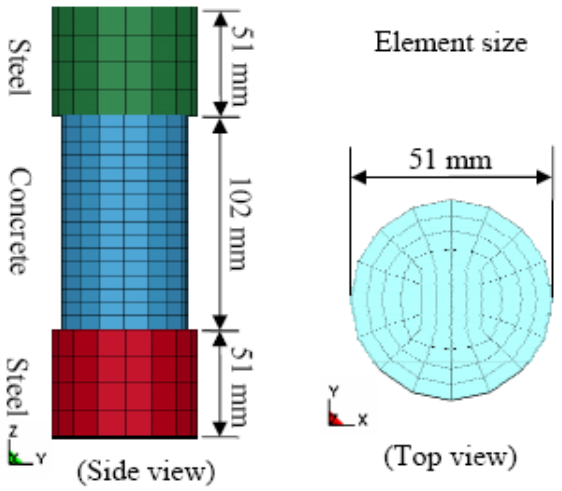

(a) Modeling for static load

Fig. 8.4- Static simulation model

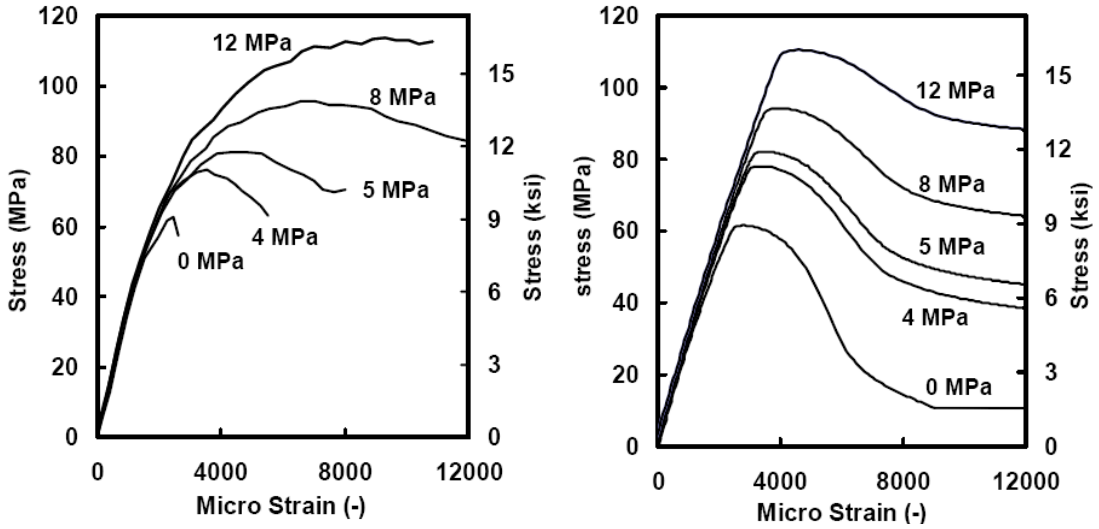

(a) Experimental Results by Candappa et al [1999, 2001] (b) Simulation Results

Fig. 8.5- Stress-strain responses of 60MPa-concrete under various confinements

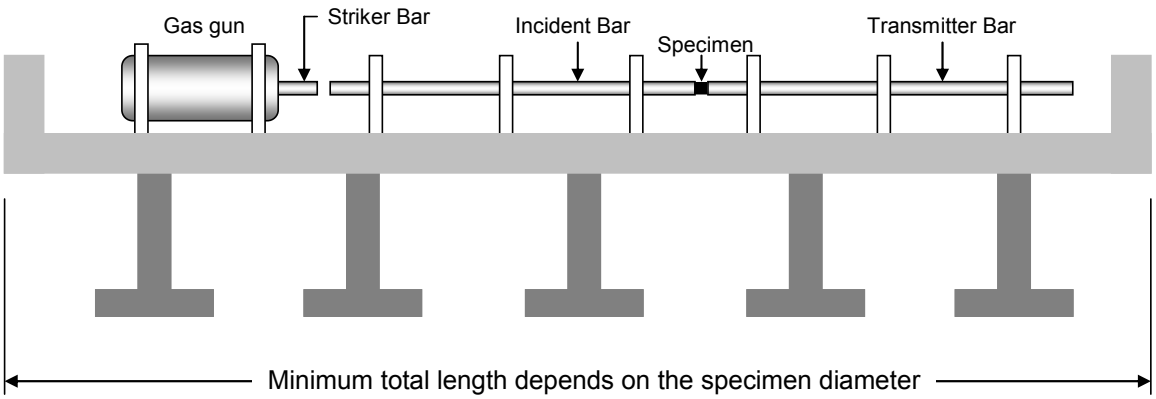

Fig. 8.6- Overview of SHPB test setup

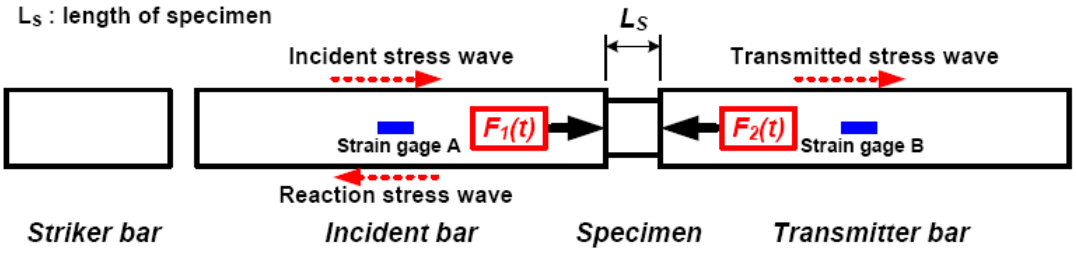

Fig. 8.7- Details of the SHPB setup

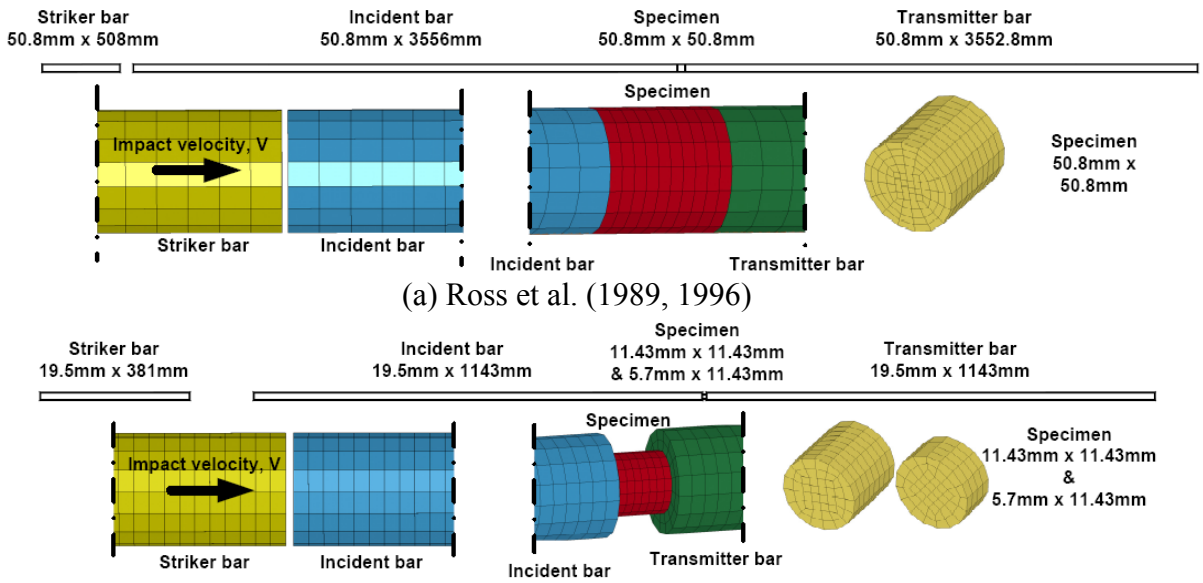

(a) Ross et al. (1989, 1996)

(b) Grote et al. (2001)

Fig. 8.8- Simulation models of SHPB test setups

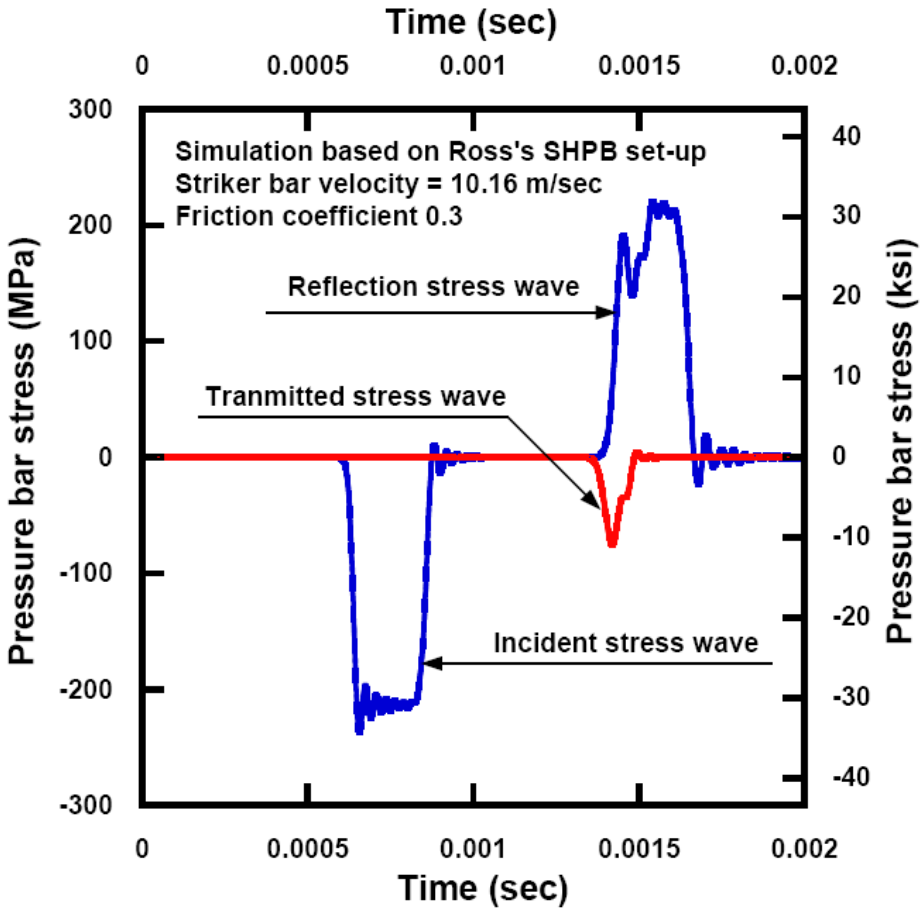

Fig. 8.9- Stress waves generated within Ross's SHPB test system simulation

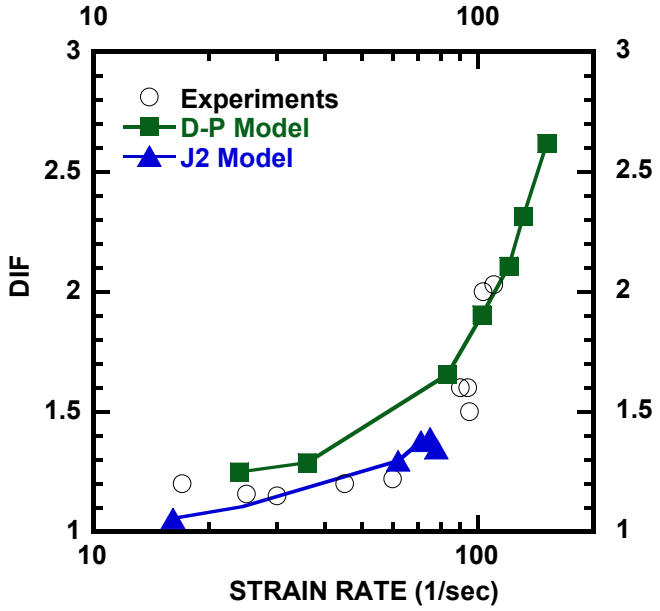

Fig. 8.10- DIF versus strain rate for Ross' setup

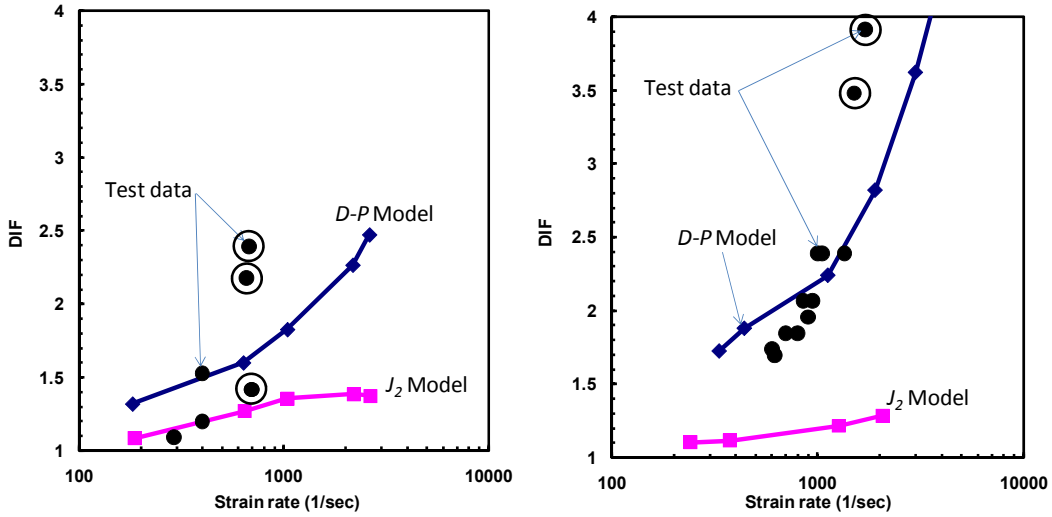

(a) L/D = 1.0 (b) L/D = 0.5

Fig. 8.11- DIF versus strain rate for Grote's setup

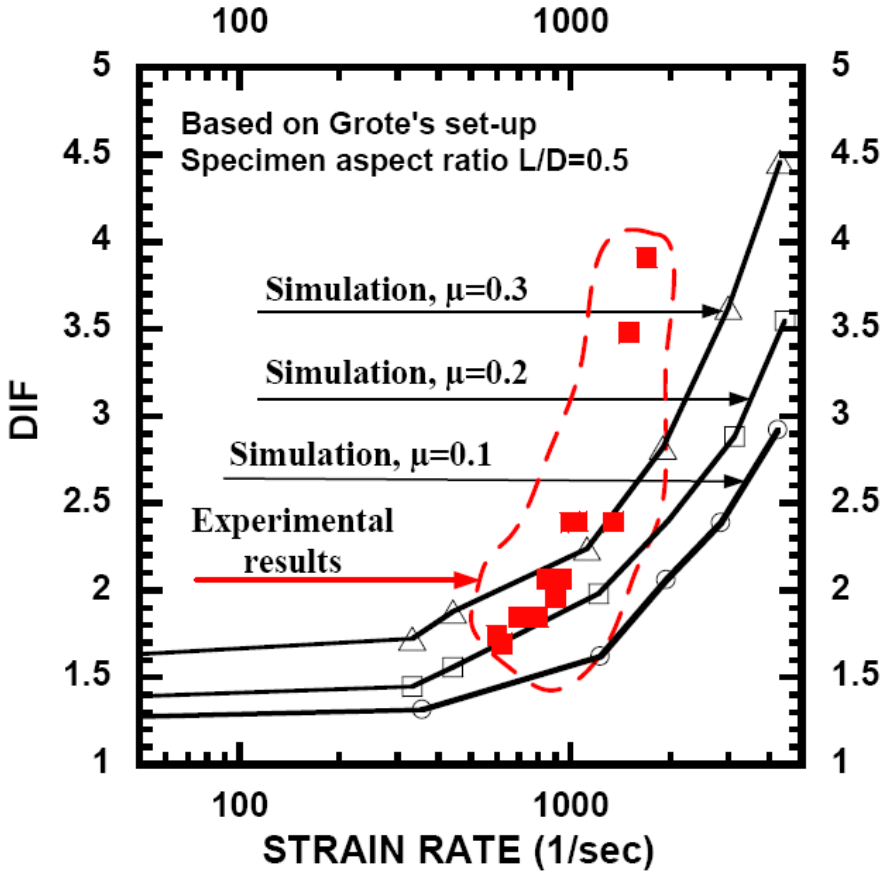

Fig. 8.12- Effect of friction on dynamic strength enhancement

REFERENCES

Bischoff, P. H. and Perry, S. H., "Impact behavior of plain concrete loaded in uniaxial compression," Journal of engineering mechanics, V. 121, No. 6, June, 1995, pp. 685-693

Candappa, D. C., Sanjayan, J. G. And Setunge, S., "Complete triaxial stress-strain curves of high strength concrete," Journal of materials in civil engineering, Vol. 13, No. 3, May-June 2001, pp. 209-215.

Candappa, D. C., Sanjayan, J. G. And Setunge, S., "Stress versus strain relationship of high strength concrete under high lateral confinement," Cement and Concrete Research, Vol. 29, Oct. 1999, pp1977-1982.

CEB., "Concrete structures under impact and impulsive loading," Bulletin d'information No. 187, Committee Euro-International du Beton, Lausame, France, 1998.

Chen, W.F., "Plasticity in reinforced concrete," McGraw-Hill Education, 474 p., 1982.

Cotsovos, D. M. and Pavlovic, M. N., "Numerical investigation of RC structural walls subjected to cyclic loading," COMPUT CONCRETE, 2005, Vol. 2, pp. 215-238.

Donze, F. V., Magnier, S. A., Daudeville, L., Mariotti, C. and Davenne, L., "Numerical study of compressive behavior of concrete at high strain rates," Journal of engineering mechanics, oct. 1999, pp. 1154-1163.

Georgin, J. F. and Reynouard, J. M., "Modeling of structures subjected to impact: Concrete behavior under high strain rates," Cement & Concrete Composites, Vol. 25, No. 1, Jan. 2003, pp. 131-143.

Grote, D. L., Park, S. W. and Zhou, M., "Dynamic behavior of concrete at high strain rates and pressures: 1. experimental characterization," International Journal of Impact Engineering, Vol. 25, 2001, pp. 869-886.

Hallquist, J. O., "LS-DYNA keyword user's manual," Livermore software Technology Corporation, 2007.

Imran, I. and Pantazopoulou, S. J., "Experimental study of plain concrete under triaxial stress," ACI Material Journal, V. 93, No. 6, Nov.-Dec. 1996, pp. 589-601.

Imran, I. and Pantazopoulou, S.J., "Plasticity model for concrete under triaxial compression," Journal of Engineering Mechanics, V. 127, No. 3, Mar. 2001, pp. 281-290.

Klepaczko, J. R., "On a very high rate sensitivity of concrete failure at high loading rates and impact," Proc. Int. Symp., Brittle Matrix Composites 7, ZTUREK RSI and Woodhead Publ., Warsaw 2003.

Li, Q. M. and Meng, H., "About the dynamic strength enhancement of concrete-like materials in a split Hopkinson pressure bar test," International journal of solid and structures, Vol. 40, 2003, pp. 343-360.

Macgregor, J.G. and Wight, J.K., "Reinforced concrete: mechanics and design," Pearson Prentice Hall, 1132 p., 2005, pp. 67.

Malvar, L. J. and Crawford, J. E., "Dynamic increase factors for Concrete," Twenty-eighth DDESB Seminar, Orlando, FL, august 1998

Nemat-Nasser, S. and Deng, H., "Strain-rate effect on brittle failure in compression," Acta metall. mater. V. 42, No. 3, 1994, pp. 1013-1024

Ross, C. A., Jerome, D. M., Tedesco, J. W. and Hughes, M. L., "Moisture and Strain rate effects on Concrete strength," ACI Materials Journal, V. 93, No. 3, May-June 1996, pp. 293-300.

Ross, C. A., Tedesco, J. W., and Kuennen, S. T., "Effects of strain rate on concrete strength," ACI Materials Journal, V92, No. 1, Jan.-Feb. 1995, pp. 37-47

Ross, C. A., Thomson, P. Y. and Tedesco, J. W., "Split-Hopkinson Pressure-Bar test on Concrete and Mortar in Tension and Compression," ACI Materials Journal, V. 86, No. 5, Sep-Oct 1989, pp. 475-481.

Schmidt, M. J. and Cazacu, O., "Behavior of cementitious materials for high strain rate conditions," Journal of Physics, V. 4, No. 134, 2006, pp. 1119-1124.

Sirijaroonchai, K., "Macro-scale plasticity model for high performance fiber reinforced cementitious composites," PhD. Dissertation, University of Michigan, Ann Arbor, 2008.

Smith, S. S., Willam, K. J., Gerstle, K. H., and Sture, S., "Concrete over the TOP, or Is There Life after Peak?," ACI Material Journal, Vol. 86, No. 5, Sep.-Oct. 1989, pp. 491-497.

Tedesco, J. W., Ross, C. A. and Kuennen, S. T., "Experimental and Numerical Analysis of High Strain Rate Splitting Tensile Tests," ACI Materials Journal, V. 90, No. 2, Mar-April 1993, pp. 162-169.

CHAPTER IX

SUMMARY, CONCLUSIONS AND FUTURE RESEARCH

9.1 SUMMARY AND CONCLUSIONS

The overall goal of this dissertation is to develop robust, tough and durable civil infrastructure under various extreme loading conditions such as earthquakes, impacts, and blasts through the use of HPFRCC. Much research has been performed to develop practical solutions to improve the response of civil infrastructure at both material and structural levels. However, most of the developed solutions are fundamentally based on the investigation under static loading condition not the high strain rate conditions that occur during extreme loading.

In this research, the development and application of an innovative construction material, HPFRCC, is proposed as one of solutions to reduce damage of civil infrastructure resulting from extreme load conditions. Many advantages, such as high load carrying capacity, energy absorption capacity, and durability, are expected from the unique strain hardening behavior of HPFRCC.

However, there is currently little information on the response of HPFRCC under such high strain rates although this information is vital for the practical application of

HPFRCC. In other words, it is necessary to investigate whether HPFRCC can maintain its distinctive and beneficial strain hardening behavior under higher strain rates. This research is geared towards answering this question and also towards understanding the influence of key parameters on HPFRCC response under high strain rate.

Four objectives, each of which is envisioned to serve the overall goal of this thesis, have been achieved. These are:

1) HPFRCC with high tensile strength (>10 MPa) and ductility (>0.5 %) was developed by using innovative slip hardening fibers with high slip capacity in a high strength mortar;

2) The strain rate effect on the behavior of HPFRCCs until seismic strain rate was investigated;

3) A new impact test system that employs suddenly released elastic strain energy was developed to enable impact testing for cementitious composites requiring large size specimen;

4) The source of strength enhancement for cement-based materials under high rate compressive loadings was investigated through computational simulation models.

Specific conclusions from this dissertation are divided into four parts according to the corresponding objectives.

9.1.1 Development of HPFRCCs with high strength and ductility by using less than 2% fibers by volume

Slip hardening high strength steel deformed, Twisted (T-) and Hooked (H-), fibers are used in developing HPFRCCs with high tensile strength and ductility. This development of HPFRCCs contains three tasks: 1) correlation between fiber pullout and tensile behavior of FRCC; 2) high tensile strength strain-hardening FRC Composites with less

than 2% fiber content; and, 3) comparative flexural behavior of four FRC Composites. Conclusions for these three tasks are as follows:

9.1.1.1 Correlation between single fiber pull-out and tensile response of composite

It is concluded that the slip capacity in fiber pullout behavior has a strong influence on the tensile behavior of HPFRCC. Although both T- and H- fiber shows slip-hardening pullout behavior, the extent of slip prior to bond softening (slip capacity) is very different due to their different mechanisms during pullout. The different slip capacity of two fibers is responsible for the different strain capacity and multiple cracking behavior in HPFRCCs. The following specific conclusions are drawn:

- The slip-hardening behavior with high slip before bond decay in fiber pull-out helps achieve strain-hardening behavior with higher strain capacity in tension and better multiple cracking developments.
- The large slip capacity of T-fiber, 76 % of the fiber embedment length on average, significantly increases the energy required to pull out the fiber.
- The high pull-out energy of T-fibers generates a high equivalent bond strength, which can be used to predict, with reasonable accuracy, crack spacing at crack saturation in strain-hardening FRC composites.
- T-fiber reinforced composites show very fine crack widths at saturated micro-cracking, and this very fine width is helpful to enhance durability.

9.1.1.2 High tensile strength strain-hardening FRC composites with less than 2% finer content

The following specific conclusions are drawn:

- T-fibers take better advantage of a higher strength matrix than H- fibers.

- In pullout tests, T-fibers lead to equivalent bond strength about 3 times that of the H-fibers, although both H- and T-fibers show slip-hardening behavior under pull-out due to their mechanical bond.
- In tensile tests, T-fiber is much more effective than H-fiber in terms of maximum tensile strength, strain capacity, and number of cracks within gage length.

9.1.1.3 Comparative flexural behavior of four FRC composites

The study on investigated the performance of four different types of fibers with two volume fraction contents (0.4% and 1.2%) in identical matrices. The four fiber types were high strength steel twisted (T -), high strength steel hooked (H -), high molecular weight polyethylene Spectra (SP -) and PVA fibers. The following specific conclusions are drawn:

- T-fiber specimens show the highest load carrying capacity. The order of performance in terms of equivalent bending strength, f_{MOR}, is observed to be as follows: T- > H- > SP- > PVA fibers.
- T-fiber specimens exhibit the highest energy absorption capacity at large deflections of $\delta_{L/150}$ and $\delta_{L/100}$. The order of performance at this deflection level is as follows: T- > H- > SP- > PVA fibers.
- Spectra (SP-) fibers generate the highest deflection capacity at maximum resistance, δ_{MOR}.
- Different cracking behavior is observed according to the types of fiber. The order of performance in terms of cracking behavior is as follows: T- > SP- > H- > PVA fiber.

9.1.2 Conclusions Related to Strain rate effect on HPFRCCs

This part of the study investigated the rate of loading effect on the pullout behavior of

two deformed high strength steel fibers, H-fibers and T-fibers, and the strain rate effect on the tensile behavior of HPFRCC using the same fibers. Four loading (strain) rates ranging from quasi-static to seismic and three matrix compressive strengths (low to high) were used. The following specific conclusions are drawn:

9.1.2.1 Loading rate effect on pullout behavior of deformed steel fibers

The study investigated the pullout behavior of two high strength deformed steel fibers, Hooked and Twisted fiber, under four different loading rates. The following specific conclusions are drawn:

- There is strong correlation between the rate sensitive behavior of HPFRCC composites and single fiber pullout response.
- T-fibers show favorable rate sensitive pull-out behavior in all three matrices, while H-fibers show no appreciable rate sensitivity during pull-out in all three matrices of low (28 MPa = 4 ksi), medium (55 MPa = 8 ksi) and high (84 MPa = 12 ksi) compressive strength. Different rate sensitivities of T- fibers are observed according to the matrix, with the highest sensitivity occurring in the medium compressive strength matrix.
- This rate sensitivity is attributed to micro cracking. During pullout, the micro cracking of H-fiber is localized in a small region near the hook while the micro cracking of T-fiber, the radial and longitudinal interface cracking, takes place along the entire embedded fiber length as the fibers untwist during pull-out.
- T-fibers produce much higher single fiber pullout energy under the seismic loading rate than under the pseudo-static loading rate. Moreover, the pull-out energy of T-fibers ranged from 1.90 to 5.15 times that of H-fibers for the loading rates considered, implying that T-fibers are much more efficient than H-Fibers in dissipating energy.

9.1.2.2 Rate-dependent tensile behavior of HPFRCC

The study investigated the tensile behavior of six HPFRCCs, using two types of fiber with three matrix compositions, under four different loading rates. The following specific conclusions are drawn:

- The tensile behavior of HPFRCC with Twisted fibers is sensitive to the strain rate, while Hooked fiber reinforced specimens show no rate sensitivity. First cracking and post cracking strength are sensitive to the strain rate, but no clear trend can be identified for the strain capacity at post cracking strength.
- The rate sensitivity of HPFRCC in tension depends on fiber type, volume fraction and matrix strength (or composition).
- Lower fiber volume fraction (V_f=1%) reinforced specimens show higher sensitivity than higher fiber volume fraction (V_f=2%) reinforced specimens.
- Tensile specimens using medium strength matrix (56 MPa or 8 ksi) show the highest strain rate sensitivity, while specimens using low strength matrix (28Mpa or 4ksi) show the lowest strain rate sensitivity. High strength matrix (84 MPa or 12 ksi) is more sensitive than low strength matrix but less than medium strength matrix.

9.1.3 Conclusions Related to New impact test system using elastic strain energy

This study developed an innovative impact test system, named Strain Energy Impact Test System [SEITS]. This new system utilizes elastic strain energy stored in an energy bar to generate an impact load, unlike the current impact test systems which employ potential and/or kinetic energy. The following specific conclusions are drawn:

- The impact test system developed belongs to a new category of impact system utilizing elastic strain energy instead of potential energy or kinetic energy.

- The developed impact test system does not require a large space to be installed unlike the traditional impact test systems; a huge space is required for Drop Weight and Split Hopkinson Pressure Bar. A prototype of the system demonstrates a strong impact-generating capacity with high velocity. The height of the prototype built is only 1.5m.
- The developed impact test system is inexpensive, safe and easy to operate.
- The developed impact test system can control impact velocity by changing the material of the energy bar and the capacity of the coupler.

The application of this new idea to generate impact load is not limited within cementitious composites. This system can be used in a broad material engineering area for the investigation of material response under impact.

9.1.4 Conclusions Related to Source of strength enhancement for cement-based material under high rate compressive loadings

This numerical study investigated several issues on the dynamic strength enhancement of mortar experimentally reported using Split Hopkinson Pressure Bar techniques. Whether the experimentally observed dynamic strength enhancement under high rate loading is a pure material property is questioned. The source of dynamic strength enhancement of mortar is investigated based on relevant simulation results, and two different methods used to estimate strain rates are compared and criticized. The following specific conclusions are drawn:

- The strain rate effect observed for mortar under compression is a combined effect of lateral inertial effects under high rate loading and pressure dependent material characteristic.
- The frictional condition between Split Hopkinson Pressure Bars and Specimen has an

influence on the obtained dynamic strength enhancement of the mortar specimen.

- Pressure from lateral inertia plays an important role in the experimentally observed strain rate effects. Although no additional DIF according to different strain rates are considered in the material model, the pressure dependent concrete plasticity (*D-P*) model generates almost the same level of strength enhancement compared with the experimental results. Therefore, many material models that consider strain rate effect additionally will double-count the strain rate effect.
- The strain rate, based on the measured stress rate, underestimates the strain rate, while the strain rate, based on reflected stress history, produces accurate strain rate.

9.2 RECOMMENDATIONS FOR FUTURE RESEARCH

The following research topics are recommended for further investigation, based on the results of the present study, to better understand the source of rate sensitivity, to explore the behavior of HPFRCC under higher rate loadings such as impact and blast by utilizing the developed impact test system, and to increase the practical application of the developed material (HPFRCC) and new impact test system (SEITS):

- High strain (loading) rate effects on fiber bond properties and tensile behavior of HPFRCC should be studied. Two experimental programs on high rate tests in both fiber pullout and at the composite level could be performed to investigate the response of HPFRCC under high strain rates.
- Development of new HPFRCC with very high tensile strength with high ductility. Based on the result that T- fibers take better advantage of a higher strength matrix, Ultra high strength mortar can be successfully used with 2% T- fiber by volume to produce a new ultra HPFRCC. This may require an optimized T- fibers geometry.

- The source of strain rate sensitive pullout behavior of T- fiber is not yet fully understood. A numerical study could be performed to investigate the source of rate sensitivity. Fiber pullout modeling could include three types of fiber such as smooth, hooked and twisted fibers.
- The source of physical bonding strength for steel fibers is not yet fully understood. A numerical study could be implemented to investigate the influence of matrix shrinkage, strength and stiffness on the physical bond and frictional bond property.